THE STUDY OF SOLAR PHOTOCATALYTIC PROCESSES IN OPTIMAL REACTOR CONFIGURATIONS BASED ON BENZOTRIAZOLES DEGRADATION

Radetić, Lucija

Doctoral thesis / Disertacija

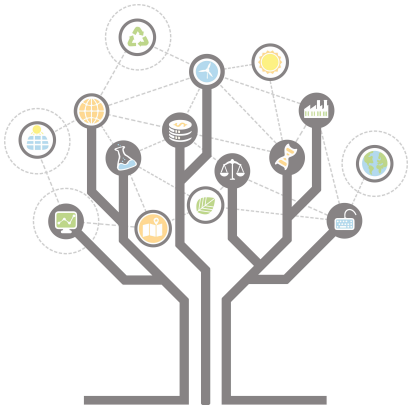
2023

Degree Grantor / Ustanova koja je dodijelila akademski / stručni stupanj: **University of Zagreb, Faculty of Geotechnical Engineering / Sveučilište u Zagrebu, Geotehnički fakultet**

Permanent link / Trajna poveznica: https://urn.nsk.hr/urn:nbn:hr:130:728749

Rights / Prava: In copyright / Zaštićeno autorskim pravom.

Download date / Datum preuzimanja: **2024-03-28**



Repository / Repozitorij:

Repository of Faculty of Geotechnical Engineering - Theses and Dissertations

DIGITALNI AKADEMSKI ARHIVI I REPOZITORIJI



University of Zagreb

Faculty of Geotechnical Engineering

Lucija Radetić

THE STUDY OF SOLAR PHOTOCATALYTIC PROCESSES IN OPTIMAL REACTOR CONFIGURATIONS BASED ON BENZOTRIAZOLES DEGRADATION

DOCTORAL DISSERTATION

Varaždin, 2023



University of Zagreb

Faculty of Geotechnical Engineering

Lucija Radetić

THE STUDY OF SOLAR PHOTOCATALYTIC PROCESSES IN OPTIMAL REACTOR CONFIGURATIONS BASED ON BENZOTRIAZOLES DEGRADATION

DOCTORAL DISSERTATION

Supervisor:

Ivana Grčić, PhD

Varaždin, 2023



Sveučilište u Zagrebu

Geotehnički fakultet

Lucija Radetić

ISTRAŽIVANJE PROCESA SOLARNE FOTOKATALIZE U OPTIMALNIM REAKTORSKIM IZVEDBAMA NA PRIMJERU RAZGRADNJE BENZOTRIAZOLA

DOKTORSKI RAD

Mentorica:

Izv. prof. dr. sc. Ivana Grčić

Varaždin, 2023.

INFORMATION ABOUT SUPERVISOR

Associate professor Ivana Grčić started her carrier at the Faculty of Chemical Engineering and Technology in Zagreb, where she obtained her PhD under the mentorship of prof. emeritus Natalija Koprivanac in the field of technical sciences, reaction chemical engineering. Her research interests focus on applying advanced oxidation technologies for the purification of wastewaters and airborne pollutants with an emphasis on reactor designing, mathematical modelling and nanomaterials application.

Throughout her carrier, she has constantly worked on her research improvement. As a scholarship holder of The British Scholarship Trust, she worked under the mentorship of prof. Gianluca Li Puma on developing mathematical models for photocatalytic decomposition of water-borne pollutants at the Department of Chemical and Environmental Engineering, University of Nottingham, UK. Within the Erasmus program, she collaborated as a guest scientist with Laboratoire de Génie des Procédés Plasmas et Traitement de Surface (LGPPTS) at Universite Pierre et Marie Curie (ENSCP/UPMC) in Paris and the Faculty of Chemistry and Chemical Technology at the University of Ljubljana. Over the years, she has actively participated in national and international projects and COST actions. She was awarded the Memorial Prize of Voya Kondic, the Young Chemical Engineer of the Society HDKI for a Contribution in the Field of Chemical Engineering, the Annual Award of the Society of University Teachers and Other Scientists in Zagreb for Scientific Research in the Field of Technical Sciences published in the academic year 2012/2013. The most recent one is the Fran Bošnjaković Prize for scientific achievements, the promotion of scientific discipline and profession, and the transfer of knowledge, especially the education of young professionals in the field of technical sciences. She is the winner of three gold medals for innovation at the ARCA fair. She is supervising students' master and PhD thesis. Continuous encouragement of students toward scientific work has resulted in winning two Rector's awards for students' research. Her current research is focused on the application of solar photocatalysis, detection of photocatalytic degradation by-products in water samples by hybrid Q-ToF (LC/MS) technique, air pollutant degradation confirmation by GC analysis, and synthesis of nanocomposites. Her bibliography includes over 60 scientific papers, 90 conference contributions, and one book chapter, all with over 700 citations.

Currently, she is a Vice-dean for Research at the Faculty of Geotechnical Engineering, where she is employed.

ACKNOWLEDGEMENTS

This work has been supported by the following project, “Waste & Sun for photocatalytic degradation of micropollutants in water” (OS-Mi), supported by the European Regional Development Fund, KK.01.1.1.04.0006.

"At the right time, I, the Lord will make it happen."
Isaiah, 60:22

It is hard to list all the people who have helped me to reach this goal. All of them have a special place in my heart.

Yet, I would like to express my gratitude to my mentor, associate professor Ivana Grčić, for motivating me to stay in science and opening new horizons in the research work. Furthermore, thank you for your patience regarding my 'time-framework' interpretation.

Also, I would like to express my gratitude to Professor Aleksandra Anić Vučinić, for having faith in me and giving me my first opportunity to work in science. Her decision directed me toward scientific work.

Furthermore, a special thank would go to Jan Marčec, for being my research partner throughout his entire study and an accomplice in experimental adventures.

As well, I would like to express my gratitude to my colleagues at work. You are more than just colleagues, you are friends and therefore, thank you for being supportive.

And to my family, mom and dad, sister and brothers, aunts and uncle, cousins and all good friends of mine… thank you for being by my side.

And lastly, but not less importantly, I would like to thank Johnny, for the best 'scientific' advice in situations when things are not going the way we would like them to happen.

ABSTRACT

This doctoral dissertation's main goal was to study the impact of the intensification factors on the efficiency and applicability of solar photocatalysis based on 1H-benzotriazole (1H-BT) degradation. Modelled pollutant 1H-BT was chosen due to its wide application in industrial and everyday life, for which it has been detected in natural waters from nano to microgram per litre concentrations.

For those purposes, a mathematical model was developed, and the intrinsic reaction rate constant was determined (k_i =3.54×10^{-10} s^{-1}W$^{-0.5}$m$^{1.5}$), as well as intensification factors due to photocatalyst modification (Y_{cat}=0.769) and reactor setup (Y_{RD}=25). Stated represents a base for further studies of new photocatalytic materials and their faster implementation in pilot and real-scale treatment systems. High-resolution analysis was used to identify six degradation products enabling the proposition of reaction pathways in correlation with different intensification approaches. Hydroxylation and benzene ring cleavage were proposed in the flat plate reactor (FPCR) setup. The addition of carbon nanotubes (CNT) enhanced the adsorption process, thus reducing toxicity due to hydroxylated products formed with titanium dioxide (TiO_2). On the other hand, nucleophilic addition on the triazole ring and its cleavage were proposed in the compound parabolic collector (CPC) reactor as state-of-the-art due to irradiation capturing. The addition of CNT enhanced the formation of superoxide radicals and their further reactions with the species in the system. Furthermore, based on the comparative life cycle assessment (LCA), photocatalysis under natural sunlight was proposed as optimal for different scaling.

.

KEY WORDS: 1H-benzotriazole, photocatalysis intensification, degradation mechanisms, life cycle assessment (LCA).

EXTENDED ABSTRACT

The intensive use of various compounds and the promotion of industrial and agriculture production are daily challenges for scientists and engineers. Consequently, removing micropollutants from waters has become one of humankind's priorities.

Accordingly, the efforts have been directed towards promising advanced oxidation processes (AOPs) based on the generation and use of radicals, powerful chemical species for the removal (oxidation/reduction) of substances that conventional oxidants cannot remove. One of the AOPs is heterogeneous photocatalysis. Radicals are formed after photocatalyst's excitations by photons with sufficient energy for electron/hole pair generation. For several decades, titanium dioxide (TiO_2) has been recognized as an efficient photocatalyst. However, modifications of TiO_2 are gaining importance due to the photocatalytic intensification in the visible spectra range. One such improvement is the one with carbon nanotubes (CNT).

Photocatalysts are either used in suspensions or immobilised on an inert support. Suspended photocatalysts tend to be more reactive. However, the use of an immobilised photocatalyst is more cost-effective and versatile due to the reusability issues. Namely, separating the photocatalyst from purified water is a complex and economically unprofitable process. Moreover, it is possible to overcome mass and photon transfer limitations due to immobilisation with an appropriate reactor design.

Furthermore, appropriate reactor design is essential due to the usability of incident irradiation and reactor applicability. Among the few reported optimal reactor designs, two different setups were considered hereby, a flat-plate cascade reactor (FPCR) and a compound parabolic collector (CPC) reactor. The FPCR was chosen since it mimics an outdoor system application which can be implemented at a low cost. Meanwhile, the CPC reactor was selected as the state-of-the-art in design regarding its favourable properties such as the highest effectiveness of irradiation capture in the reactor system.

Therefore, the main goal of this dissertation was to study the impact of the intensification factors on the efficiency and applicability of solar photocatalysis based on 1H-benzotriazole (1H-BT) degradation. The photocatalyst modification and reactor setup were selected as intensification factors. Modelled pollutant 1H-BT was chosen due to its wide application in industrial and

everyday life, for which it has been detected in natural waters from nano to microgram per litre concentrations.

Previous studies have proved direct photolysis of 1H-BT under UV light with the most efficient degradation in UV-C spectra. A more dominant role of 1H-BT removal in the natural environment is indirect photolysis or reaction with reactive transient species. Nevertheless, due to the insensitivity to visible light, 1H-BT is relatively long persistent in the environment. In surface waters, it is subjected to reactions with other species where more toxic compounds can be formed if there is no mineralization.

Recent studies have demonstrated the importance of radicals in 1H-BT removal reactions. Yet, a negative impact was reported when chlorine was used in the AOPs due to the generation of more harmful degradation products for the aquatic environment. To avoid such a scenario, an analysis with a high mass resolution, full-scan sensitivity, and mass accuracy provided by a hybrid Q-TOF LC/MS (quadrupole time of flight, liquid chromatography coupled with mass spectrometry) system is gaining attention in the detection of degradation products.

Accordingly, the following objectives were established: (i) a development of a mathematical model including irradiation terms and a rate of photon absorption over photocatalyst surface (local or global) and fluid dynamics in chosen reactors to obtain intrinsic reaction rate; (ii) determination of 1H-BT photocatalytic degradation pathways in correlation with different intensification approaches under neutral pH conditions and (iii) proposition of optimal parameters for accurate scale photocatalytic process based on comparative life cycle assessment (LCA) of various photocatalysis intensification approaches and the use of natural sunlight.

Based on the dissertation objectives, four hypotheses were formulated. The first hypothesis (H1) states that 1H-BT degradation is more effective with TiO_2/CNT photocatalyst under simulated solar light than TiO_2. The second hypothesis (H2) states that existing kinetic models with the local volumetric rate of photon absorption can be modified for 1H-BT degradation in FPCR and CPC reactors. The third hypothesis (H3) states that photocatalytic degradation products of 1H-BT degradation are negligible compared to ones obtained by photolysis alone. And the fourth hypothesis (H4) states that photocatalysis under natural irradiation with UV/vis intensified photocatalyst is optimal for scale-up and real-scale application based on the comparative LCA.

Therefore, regarding the first hypothesis and observed experimental data of 1H-BT concentration decreasing, it could be concluded that photocatalysis with TiO_2/CNT is not more efficient than photocatalysis with TiO_2 in both cases when FPCR and CPC reactors were applied. However, further analysis by the newest high-resolution techniques, a hybrid Q-TOF LC/MS, enabled the identification of degradation products formed during photocatalysis. With unique insight, it was possible to identify that modification of TiO_2 with CNT had triggered different 1H-BT degradation mechanisms in the CPC reactor. Also, the degradation product with the same fragmentation pattern as the 1H-BT can occur in the system due to triazole ring breakage. On the other hand, the reaction pathway of 1H-BT degradation in FPCR was governed by hydroxylation and benzene ring breakage. Furthermore, the larger surface of the immobilised photocatalyst in the FPCR (15.6x) compared to the CPC reactor demonstrated that photocatalysis is a surface phenomenon. Therefore, the addition of CNT increased adsorption.

Regarding the toxicity of degradation by-products, the adsorption was favourable in the FPCR since hydroxylated species pose a slightly greater negative impact on the environment. Therefore, it can be said that 1H-BT degradation is not necessarily more effective with TiO_2/CNT compared to TiO_2 under simulated solar light. However, from the aspects of reaction mechanisms, TiO_2/CNT contributes to photocatalysis enhancement and environmentally friendlier photocatalysis.

Regarding the second hypothesis, a kinetic model with mass balance was developed and successfully applied for 1H-BT degradation independently on reactor setup and different photocatalysts formulation. The introduction of intrinsic parameters enabled the determination of the intrinsic reaction rate constant for 1H-BT (k_i=3.54×10^{-10} s^{-1}W$^{-0.5}$m$^{1.5}$) applicable in all setups, while the contribution of a photocatalyst formulation and reactor setups was described with appropriate indexes, Y_{cat}=0.769 and Y_{RD}=25, respectively.

As was discussed in the dissertation, 1H-BT is subjected to photolysis under UV, namely UV-C light, while that is not the case with UV-A and UV-B light. However, with the assistance of photocatalysts, it is possible to degrade 1H-BT using UV/vis light and obtain less harmful degradation products.

And lastly, natural irradiation is favourable for the degradation process due to less energy consumption and the higher proportion of irradiation.

Therefore, the constant of the intrinsic reaction rate for 1H-BT was determined by which the first objective of this dissertation was achieved. Moreover, the mechanism's degradation pathways were proposed in correlation with different intensification processes. In the FPCR setup, hydroxylation is the dominant reaction pathway of benzene cleavage with emphasized adsorption when TiO_2/CNT is used. In the CPC reactor, the degradation pathway suggested nucleophilic addition reaction and triazole separation. As mentioned, the second objective of this dissertation was achieved. Finally, based on the comparative LCA, photocatalysis under natural sunlight was proposed as the optimum for scaling.

Therefore, the influence of various intensification factors on solar photocatalysis application was determined. The intrinsic reaction rate constant has enabled further studies of new photocatalytic materials and their faster implementation in pilot and real-scale treatment systems. The results contributed to the 1H-BT and other pollutants treatment considerations in other aquatic systems, such as groundwaters, and the proposed degradation pathways were suggested for a better aquatic toxicity understanding.

The LCA methodology was applied to study various photocatalysis intensification approaches. The most acceptable process from the environmental point of view for scale-up was proposed to be the usage of the CPC reactor under natural sunlight.

KEY WORDS: 1H-benzotriazole, photocatalysis intensification, degradation mechanisms, life cycle assessment (LCA).

PROŠIRENI SAŽETAK

Prekomjerna uporaba različitih spojeva te poticanje industrijske i poljoprivredne proizvodnje predstavljaju svakodnevne izazove za znanstvenike i inženjere.

Zbog toga je posebna pažnja usmjerena prema obećavajućim naprednim oksidacijskim procesima (NOP), koji se temelje na stvaranju i korištenju reaktivnih kemijskih spojeva za razgradnju (oksidaciju i/ili redukciju) tvari koje se ne mogu ukloniti konvencionalnim oksidansima. Heterogena fotokataliza jedan je od NOP-a gdje radikali nastaju uslijed ekscitacije fotokatalizatora s fotonima s dovoljno energije za stvaranje para elektron-šupljina. Već nekoliko desetljeća titan dioksid (TiO_2) je prepoznat kao učinkovit fotokatalizator, međutim njegove modifikacije dobivaju na značaju poradi povećanja fotokatalitičke aktivnosti u području vidljivog spektra. Jedna od takvih modifikacija je dodatak ugljičnih nanocjevčica (eng. *carbon nanotubes*, CNT).

Fotokatalizatori se koriste u suspenziji ili su imobilizirani na inertnom nosaču. Premda su fotokatalizatori u suspenziji reaktivniji od imobiliziranih, uporaba imobiliziranih fotokatalizatora je isplativija. Naime, zbog veličine čestica, izdvajanje fotokatalizatora iz pročišćene vode je složen i ekonomski neisplativ proces, dok se imobilizirani fotokatalizator može upotrijebiti višekratno. Nadalje, uz odgovarajući dizajn reaktora moguće je prevladati ograničenja prijenosa mase i fotona uslijed imobilizacije.

Odgovarajući dizajn fotokatalitičkog reaktora važan je poradi iskoristivosti upadnog zračenja i primjenjivosti reaktora. Među nekoliko utvrđenih optimalnih reaktorskih konfiguracija, razmotrene su dvije izvedbe: kaskadni reaktor pločastog tipa (eng. *flat plate cascade reactor*, FPCR) i reaktor s paraboličnim zrcalima (eng. *compound parabolic collector*, CPC). FPCR oponaša primjenu u prirodnom okruženju koja se može implementirati uz niske troškove. S druge strane, CPC reaktor je odabran kao „*state-of-the-art*" u dizajnu zbog najveće učinkovitosti zahvaćanja i usmjeravanja zračenja u sustavu reaktora.

Glavni cilj ove disertacije bio je istražiti utjecaj faktora intenzifikacije na učinkovitost i primjenjivost solarne fotokatalize temeljene na razgradnji 1H-benzotriazola (1H-BT). 1H-BT je odabran kao modelno onečišćivalo u istraživanju zbog svoje široke primjene u industriji i svakodnevnom životu, a upravo zbog toga je detektiran u prirodnim vodama u koncentracijama od nano do mikrograma po litri.

Dosadašnja istraživanja ukazala su na izravnu fotolizu 1H-BT-a pri UV spektru s najučinkovitijom degradacijom pri UV-C spektru zračenja. Dominantniju ulogu uklanjanja 1H-BT-a u prirodnom okolišu ima neizravna fotoliza ili reakcija s reaktivnim kratkoživućim česticama. 1H-BT je relativno dugo postojan u okolišu budući da se ne razgrađuje u vidljivom spektru zračenja. U površinskim vodama podložan je reakcijama s drugim tvarima pri čemu mogu nastati toksičniji spojevi ukoliko nema mineralizacije.

Nedavna istraživanja ukazala su na važnost sudjelovanja radikala u reakcijama razgradnje 1H-BT-a. Ipak, istraživanja su također ukazala na negativan utjecaj klora u NOP-ima zbog nastajanja štetnijih produkata razgradnje po vodeni okoliš. Poradi navedenog, pozornost je usmjerena prema analizi visoke razlučivosti, osjetljivosti i točnosti detektiranja masa koju omogućuje hibridni Q-TOF LC/MS sustav analize (eng. *quadrupole time of flight liquid chromatography/ mass spectrometry*, kvadrupolno vrijeme leta spregnuto s tekućinskom krmatografijom i masenom spektrometrijom).

Stoga, u ovoj doktorskoj disertaciji, cilj je bio istražiti kako faktori intenzifikacije, prvenstveno modifikacija fotokatalizatora, različit dizajn reaktora te upadno zračenje utječu na učinkovitost i primjenjivost solarne fotokatalize.

U te svrhe postavljeni su sljedeći ciljevi: (i) razviti matematički model uzimajući u obzir upadno zračenje i brzinu apsorpcije fotona na površini fotokatalizatora (lokalnu ili globalnu) te dinamiku fluida u odabranim reaktorima kako bi se dobila stvarna brzina reakcije; (ii) odrediti mehanizme fotokatalitičke razgradnje 1H-BT-a u korelaciji s različitim pristupima intenzifikacije procesa u uvjetima neutralnog pH te (iii) predložiti optimalne parametre za primjenu fotokatalize u realnim uvjetima na temelju usporedne procjene životnog ciklusa različitih pristupa intenziviranja fotokatalize, te korištenjem sunčevog zračenja.

Temeljem zadanih ciljeva, postavljene su četiri hipoteze: (H1) razgradnja 1H-BT-a s fotokatalizatorom TiO_2/CNT sa simuliranom sunčevom svjetlošću učinkovitija je u usporedbi s TiO_2; (H2) postojeći kinetički modeli s lokalnom volumetrijskom brzinom apsorpcije fotona mogu se modificirati i primijeniti za modeliranje razgradnje 1H-BT-a u FPCR i CPC reaktorima; (H3) fotokatalitički produkti razgradnje 1H-BT-a značajno su manje prisutni u odnosu na rezultate fotolize 1H-BT-a; i (H4) fotokataliza pri sunčevom zračenju s fotokatalizatorom aktivnim i u vidljivom dijelu spektra optimalna je za uvećanje procesa i

primjenu u realnim uvjetima na temelju usporedne procjene životnog ciklusa procesa (eng. *life cycle assessment*, LCA).

Dakle, što se tiče prve hipoteze, temeljem dobivenih eksperimentalnih podataka i smanjenja koncentracije 1H-BT-a može se zaključiti kako fotokataliza s TiO_2/CNT nije učinkovitija od fotokatalize s TiO_2 u oba slučaja primjene FPCR i CPC reaktora. Međutim, daljnja analiza najnovijom metodom visoke rezolucije, hibridnim Q-TOF LC/MS, omogućila je identifikaciju produkata razgradnje nastalih tijekom fotokatalize.

S novim uvidom bilo je moguće primijetiti kako je modifikacija TiO_2 s CNT-om pokrenula drugačiji reakcijski mehanizam u CPC reaktoru. Primjerice, uslijed raspada triazolnog prstena 1H-BT-a u sustavu se može pojaviti produkt razgradnje s istim fragmentacijskim uzorkom raspada kao 1H-BT. S druge strane, reakcijski put razgradnje 1H-BT-a u FPCR-u bio je vođen hidroksilacijom i raspadom benzenskog prstena. Veća površina imobiliziranog fotokatalizatora u FPCR-u (15,6x) u usporedbi s CPC reaktorom pokazala je da je fotokataliza površinski fenomen te je dodavanje CNT-a doprinijelo adsorpciji. S aspekta toksičnosti produkta razgradnje, adsorpcija pozitivno doprinosi budući da hidroksilirane tvari imaju nešto veći negativan utjecaj na okoliš. Stoga se može reći kako razgradnja 1H-BT-a nije nužno učinkovitija s TiO_2/CNT u usporedbi s TiO_2 pod simuliranim sunčevim svjetlom. Međutim, s aspekta reakcijskih mehanizama TiO_2/CNT doprinosi poboljšanju fotokatalize i ekološki prihvatljivijoj fotokatalizi.

Što se tiče druge hipoteze, razvijen je kinetički model s masenom bilancom te je uspješno primijenjen za razgradnju 1H-BT-a neovisno o postavkama reaktora i različitoj formulaciji fotokatalizatora. Uvođenje intrinzičkih parametara omogućilo je određivanje stvarne konstante brzine reakcije za BT (k_i=3.54×10^{-10} s^{-1}W$^{-0.5}$m$^{1.5}$) primjenjive u svim postavkama, dok je doprinos formulacije fotokatalizatora i postavki reaktora opisan odgovarajućim indeksima, Y_{cat}=0.769 and Y_{RD}=25.

Kao što je navedeno u disertaciji, 1H-BT je podložan fotolizi pod UV zračenjem, odnosno UV-C zračenju, dok to nije slučaj s UV-A i UV-B zračenjem. Međutim, pomoću fotokatalizatora i UV/vis zračenja moguće je razgraditi 1H-BT na manje štetne produkte razgradnje. Naposljetku, korištenje prirodnog zračenja poželjno je za proces razgradnje, zbog manje potrošnje energije kao i zbog većeg udjela zračenja.

Stoga je određena prethodno spomenuta stvarna konstanta brzine reakcije za 1H-BT, čime je postignut prvi cilj ovog rada. Štoviše, predloženi su mehanizmi razgradnje u korelaciji s različitim procesima intenzifikacije. Naime, dok je u FPCR-u hidroksilacija dominantan reakcijski put cijepanja benzena s naglašenom adsorpcijom kada je korišten TiO_2/CNT, u CPC reaktoru put razgradnje ide prema reakciji nukleofilne adicije i cijepanju triazolskog prstena. Time je postignut drugi cilj ovog rada. U konačnici, temeljem komparativne LCA, predložena je fotokataliza pod prirodnim sunčevim zračenjem kao optimalno rješenje za buduće skaliranje.

Ovim radom utvrdio se utjecaj različitih intenzifikacijskih faktora na učinkovitost solarne fotokatalize. Određivanje stvarne konstante brzine reakcije omogućit će daljnja proučavanja novih fotokatalitičkih materijala i njihovu bržu implementaciju u pilot i realnim sustavima obrade otpadnih voda. Predloženi mehanizmi razgradnje 1H-BT-a omogućili su utvrđivanje toksičnog utjecaja i razmatranje uklanjanja kako 1H-BT-a tako i drugih onečišćivala i u vodenim sustavima poput podzemnih voda gdje je utvrđena pojava istih.

LCA metodologija primijenjena je za proučavanje različitih fotokatalitičkih intenzifikacijskih pristupa te korištenje sunčevog zračenja u odnosu na umjetne izvore zračenja radi utvrđivanja najprihvatljivijeg s aspekta utjecaja na okoliš, što čini predloženi rad pionirskim u užem području inženjerstva okoliša.

KLJUČNE RIJEČI: 1H-benzotriazol, intenzifikacija fotokatalize, mehanizmi razgradnje, procjena životnog vijeka proizvoda.

CONTENT

Information about supervisor ..... *I*

Acknowledgements ..... *III*

Abstract ..... *V*

Extended abstract ..... *VI*

Proširenisažetak ..... *X*

1 Introduction **1**

2 Solar photocatalysis **3**

2.1 Heterogenous photocatalysis 4

2.2 Photocatalysts 5

2.2.1 Titanium dioxide (TiO_2) 7

2.2.2 Modifications of TiO_2 towards activity in visible light spectra 8

2.2.3 Modifications towards visible photoactivity with carbon nanotubes (CNT) 11

2.2.4 Immobilisation of photocatalysts 13

2.2.5 Reaction mechanisms 15

2.3 Reactor setups 17

2.3.1 Flat plate cascade reactor (FPCR) 21

2.3.2 Compound parabolic collector reactor (CPC) 21

3 Photocatalytic modelling **22**

3.1 Kinetics of heterogeneous photocatalytic reactions 22

3.2 Parameters affecting photocatalytic reactions 23

4 Benzotriazoles **27**

4.1 Properties and applications 27

4.2 Occurrence and impact on the environment 29

4.3 Removal methods of 1H-BT 32

5 Materials and methodology **36**

5.1 Materials 36

5.1.1 Photocatalysts 37

5.1.2 Irradiation sources 38

5.1.3 Reactors setup 39

5.2 Experiments setup 41

5.3 Analytical methods 42

5.3.1 UV/vis spectrophotometry 42
5.3.2 Quadrupole time of flight mass spectrometry coupled with liquid chromatography system (Q-TOF LC/MS) 45
5.3.3 Irradiance measurements 48
5.4 Kinetic model developments and reactor mass balance 49
5.5 Environmental impact estimation 51
5.5.1 Toxicity Estimation Software Tool (T.E.S.T.) 51
5.5.2 Ecological Structure Activity Relationships (ECOSAR) 52
5.6 Life cycle assessment (LCA) 53
6 Results and discussion 54
6.1 High-resolution analysis of 1H-BT and its degradation products 54
6.1.1 Identification and calibration of 1H-BT 54
6.1.2 Mechanisms and reaction pathways of 1H-BT photocatalytic degradation 55
6.2 Photocatalytic degradation of 1 H-BT 70
6.2.1 Impact of photocatalyst's modification on 1H-BT degradation intensification 70
6.2.2 Impact of different photocatalytic reactor setups on 1H-BT degradation intensification 72
6.2.3 Impact of different irradiation setups on 1H-BT degradation intensification 73
6.2.4 Modelling of Photocatalytic Degradation 74
6.3 Environmental impact estimation 76
6.3.1 Toxicity Estimation Software Tool (T.E.S.T.) 76
6.3.2 Ecological Structure Activity Relationships (ECOSAR) 77
6.4 Life cycle assessment (LCA) 79
6.4.1 Goal and scope 79
6.4.2 Inventory 80
6.4.3 Life cycle impact assessment (LCIA) 82
6.5 Perspectives for a scale-up in real systems 87
7 Conclusions 88
8 Literature 90
List of figures 115
List of tables 117
List of abbreviation 119
Annexes 122
Curriculum vitae 157

1 INTRODUCTION

Nowadays, a significant challenge for scientists and engineers is the removal of environmental pollutants. Intensive use of various compounds that improve people's daily lives (pharmaceuticals, pesticides, personal care products, etc.) promotes industrial and agricultural production. Every day, compounds are discharged from production systems or households into sewer systems, reaching wastewater treatment plants (WWTPs). However, conventional WWTPs, due to the compounds' structure, chemical, and physical properties, are insufficient to remove all pollutants. Accordingly, they are being released into water recipients as micropollutants, which pose a risk for more minor, primarily aquatic organisms and, consequently, humans [1–3].

Respectively, it is necessary to find an adequate solution for the complete removal of such pollutants from effluents to ensure the satisfactory quality of natural recipients. Therefore, efforts have been directed towards promising advanced oxidation processes (AOPs) and their possible application in WWTPs, one of which is heterogenous solar photocatalysis. The synergy of photocatalyst and photons initiate redox reactions necessary for the pollutant's degradation, which makes this technology the best available technique for air and water pollutant removal. In this regard, titanium dioxide (TiO_2) is among the most researched and widely applicable photocatalysts [4]. However, its modifications, such as using carbon nanotubes (CNT), are gaining importance to intensify photocatalytic activity in the visible (vis) spectra range [5,6].

Therefore, in this dissertation, the objective was to study the impact of the intensification factors on the efficiency and applicability of solar photocatalysis, namely by photocatalyst modification, reactor setup and irradiation. For those purposes, a mathematical model was developed to determine the intrinsic reaction rate constant, a base for further studies of new photocatalytic materials and their faster implementation in pilot and real-scale treatment systems. As a modelled pollutant, 1H-benzotriazole (1H-BT) was chosen due to its wide application in industrial and everyday life, for which it has been detected in natural waters from nano to microgram per litre concentrations.

Furthermore, the next objective was to determine 1H-BT's photocatalytic degradation pathways under natural pH conditions. Afterwards, correlate 1H-BT's photocatalytic degradation with various intensification approaches. Given results will contribute to the

1H-BT and other pollutants' treatment considerations in different aquatic systems, such as groundwaters, and the proposed degradation pathways to understand the aquatic toxicity.

And concluding objective was to propose optimal parameters for real photocatalytic process scale-up. Comparative life cycle assessment (LCA) of studied photocatalytic intensification approaches and natural sunlight was used. The most acceptable method for scale-up was discussed and proposed from the environmental point of view, making this research a pioneering work in the field of environmental engineering.

2 SOLAR PHOTOCATALYSIS

A set of processes by the name of AOPs, are based on the generation and use of reactive oxygen species, powerful chemical species, for the removal (oxidation/reduction) of substances that cannot be removed by conventional oxidants [7]. Reactive oxygen species, or radicals, include not only free radicals such as hydroxyl radical (•OH), superoxide radical ($\bullet O_2^-$) and hydroperoxyl radical ($\bullet HO_2$), but also molecular oxygen (O_2) and hydrogen peroxide (H_2O_2). However, radicals differ from molecules by the unpaired electron that enables them to be highly reactive. Under ideal conditions, due to the action of radicals, complete mineralization of the organic molecule occurs with the formation of water (H_2O), carbon dioxide (CO_2) and mineral acids [3,8,9].

Hydroxyl radical •OH, with a half-life of 10^{-10} s [3,10] is the most commonly used radical in AOPs. It is the most powerful oxidizing species after fluorine. Table 1 gives a review of commonly used oxidants along with the oxidation potential.

Table 1 Oxidation potential of a few oxidizing agents [11]

Oxidant	Oxidation potential, V
Fluor	3.03
Hydroxyl radical	2.80
Atomic oxygen	2.42
Ozone	2.07
Hydrogen peroxide	1.77
Permanganate ion	1.67
Chlore (IV) oxide	1.50
Hypochlorite	1.49
Chlor	1.36
Molecular oxygen	1.23

The literature reports different AOPs to remove persistent organic pollutants (POPs) in water [12]. However, during the last decades, heterogeneous photocatalysis has shown as the most promising one [4] from the economic and engineering aspect for industrial applications. Advantages such as degradation of pollutants, sustainability, requirements of no additional chemicals, [13] non-toxicity, and low-cost and long-term photostability [14–16] have been recognized.

Generally, photocatalysis can be conducted in different phases: gas, pure organic liquid or aqueous solutions [17] as homogeneous or heterogeneous systems. In homogeneous

photocatalysis, the reactant and photocatalyst are in the same phase, as in photo-Fenton systems, while in heterogeneous photocatalysis, the reactant and photocatalyst are in different phases [18]. Therefore, in this dissertation, the emphasis was on heterogeneous photocatalysis.

2.1 Heterogenous photocatalysis

The reaction mechanism of heterogenous photocatalytic degradation begins with reactants' transfer onto the photocatalyst's active sites, where diffusion and adsorption occur. In the meantime, photon-induced redox reactions occur, and desorption and diffusion of the oxidized/reduced by-products arise, enabling participation in new redox processes [19–21]. Given steps depend on the fluid dynamics and photocatalyst structure [19].

The photon-induced process principle crucial for the initiation of redox processes is based on the semiconductor valence band gap theory, where the semiconductor is the photocatalyst. When electrons (e^-) from the valence band (VB) are induced by the photons ($h\nu$) with energy equal to or higher than the photocatalysts band gap energy (E_g), electrons are being transferred into the conduction band (CB) whilst an electron-hole pair (e^-/h^+) is being formed [20,22,23]. The scheme of the process is given in Figure 1.

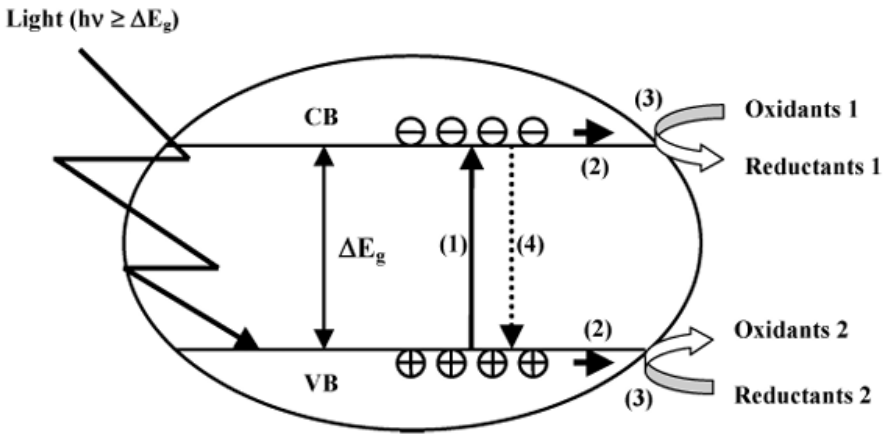


Figure 1. Schematic representation of the "band gap model." (1) Photoinduced electron-hole pair formation; (2) charge transfer onto the surface; (3) redox reactions; (4) recombination. VB and CB represent the valence band and conduction band, respectively [24]

The formation of electron-hole pairs can be generally written with Equation (1). While formed electrons are in the conduction band, positively charged holes remain in the valence band. Furthermore, in the presence of a fluid (liquid/gas), the adsorption of

molecules occurs. According to the redox potential of the adsorbent, electrons are transferred to the acceptor molecule (A) (2). At the same time, the hole remains with the donor (D) (3) [20,25].

Further recombination of electron/hole pairs releases energy in the form of heat. Positively charged holes in the valence band react with hydroxyl ions or water, thus creating hydroxyl radicals. Electrons from the conduction band react with oxygen molecules, thus creating superoxide radical anions [22].

$$\text{Photocatalyst} \xrightarrow{h\upsilon} e^- + h^+ \quad (1)$$

$$A_{ads} + e^- \rightarrow A^-_{ads} \quad (2)$$

$$D_{ads} + h^+ \rightarrow D^+_{ads} \quad (3)$$

2.2 Photocatalysts

Physical and chemical properties of the photocatalyst, and therefore its photoactivity, are dependable on the position of energy classes, mobility and an average lifetime of generated electron/ hole pairs, absorption coefficient and its synthesis [26].

An ideal photocatalyst should be chemically and biologically inert, photocatalytically stable yet active under solar irradiation, easily synthesized and used, inexpensive and harmless to humans and the environment [19,27]. In general, photocatalyst must have a crystalline structure since irradiation absorption and electron/hole pair generation is only possible in semiconductors with a spatially ordered crystal structure [19]. Furthermore, for a semiconductor to be a photocatalyst, it needs to participate in electron transfer onto adsorbed molecules, depending on the band gap energy of the semiconductor and the redox potential of the adsorbed molecule. For instance, the photocatalyst must have a redox potential higher than the redox potential of the $H_2O/\bullet OH$ pair, which is −2.8 V [28].

Most often, as photocatalysts, oxides and sulphides of metals such as TiO_2, ZnO, CeO_2, ZrO_2, SnO_2, Sb_2O_4, ZnS, WO_3, $BiVO_4$, Fe_2O_3 etc. are used [19,29]. Some of them are shown in Table 2 with corresponding band gap energy values.

Table 2. Semiconductors with corresponding band gap energy values [30]

Semiconductor	**Band gap energy in the aqueous electrolyte at pH 1 (eV)**
TiO_2	3.2
ZnO	3.2
WO_3	2.8
CdS	2.5
GaP	2.3
Fe_2O_3	2.2
$CdSe$	1.7

Although they have a suitable band gap energy, not all semiconductors can be applicable photocatalysts [17]. For instance, semiconductors CdS and GaP can absorb the visible part of the irradiation, during which radicals are formed on their surface. However, after multiple cycles of photocatalysis, stated semiconductors are subject to decomposition and formation of toxic products along the process, wherefore their use is avoided [30].

Furthermore, it can be seen that the valence band redox potential of TiO_2 is more positive than the ($\bullet OH/OH^-$) redox couple, meaning adsorbed water and hydroxyl groups can be oxidized to highly reactive hydroxyl radicals (Figure 2). Compared to the other semiconductors, that is not the case [24].

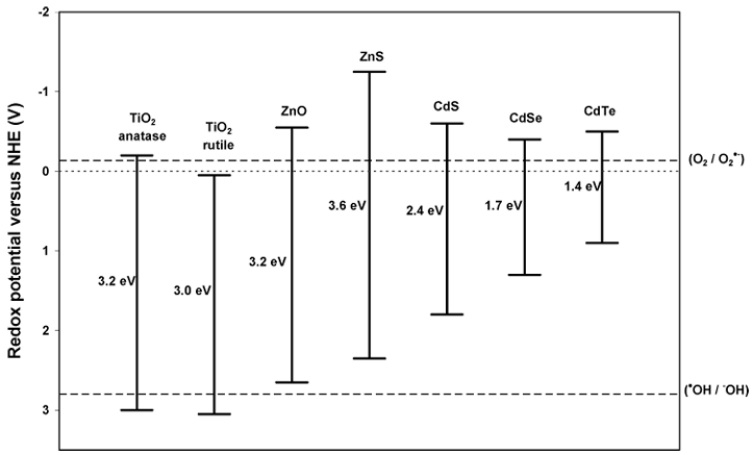


Figure 2. Band gaps with valence and conduction band gap edges of common semiconductors and standard redox potentials (versus NHE: normal hydrogen electrode) of the ($O_2/\bullet O_2^-$) and ($\bullet OH/OH^-$) redox couple [24]

Therefore, semiconductors' performance enhancement can be obtained in four primary ways: (i) formation of localized state just above the valence band or (ii) below the conduction band, (iii) usage of semiconductor with a low band gap, (iv) formation of colour centre in band gap and by (v) surface modification. Accordingly, used techniques

can be doped with metal/non-metal, co-doping with various combinations of donor and acceptor materials, sensitization, substitution, composite formation etc. [5].

2.2.1 Titanium dioxide (TiO_2)

Titanium dioxide is the most researched and used photocatalyst. It is non-toxic, photochemically and biologically stable, with high photoactivity and mineralization efficiency [3]. It can be found in three allotropic modifications: anatase, rutile and brookite [25]. The properties of allotropic transformations are shown in Table 3.

Table 3. Properties of anatase and rutile [25]

Property	Anatase	Rutile
Molecular weight (g/mol)	79.88	79.88
Melting point (°C)	1825	1825
Boiling point (°C)	2500-3000	2500-3000
Irradiation absorption (nm)	< 390	< 415
Mohr hardness	5.5	6.5-7.0
Refractive index	2.55	2.75
Dielectric constant	31	114
Crystal lattice	Tetragonal	Tetragonal
Lattice parameters (Å)	a = 3.78 c = 9.52	a = 4.59 c = 2.96
Density (g/cm^3)	3.79	4.13
The length of the Ti-O bond (Å)	1.94 (4) 1.97 (2)	1.95 (4) 1.98 (2)

The modification differences are reflected in the length of the structure bonds. Namely, the distance in the Ti-Ti bond in anatase is longer than in rutile, while the Ti-O bonds are shorter. Furthermore, allotropic modifications of TiO_2 have different band gap energies; 3.0 eV for anatase and brookite and 3.2 eV for rutile. For anatase, the potential of the conduction band is -0.51 V at pH 7, which enables the reduction of adsorbed oxygen, while the potential of the valence band is +2.69 V at pH 7, allowing the oxidation to of water and the formation of hydroxyl radicals. For rutile, the conduction band potential is -0.31 V at pH 7, so the rutile phase can't carry out oxygen reduction (-0.33 V) [31]. Furthermore, anatase shows higher photoactivity compared to other modifications. Due to these properties, TiO_2 is often used for photocatalytic purposes as a mixture of two allotropic modifications of anatase and rutile in a ratio of 80:20. Such combination shows the best photocatalytic performance, and it is known under the commercial name Degussa P25® [31] synthesized by the Aerosil (flame pyrolysis) process [32].

The good properties of TiO_2 P25 are elaborated with a redox potential of the rutile conductive band, which is more favourable than that of anatase. Furthermore, considering stated, the rutile phase acts as a sink for photogenerated electrons from the anatase conduction band, thus reducing the recombination rate and improving the photocatalyst's efficiency [25]. Similar conclusions were given in the research [33], where advantages of TiO_2 P25 were identified as a smaller energy gap in rutile which enables photoactivity in the visible part of the spectrum and stabilization of the recombination rate by transitioning electrons from higher energy level (rutile) to lower energy level (anatase).

Furthermore, photocatalytic properties depend on the dimensional forms of TiO_2 nanostructures (0D, 1D and 2D), which formation is governed by various synthesis methods (Table 4). The size, morphology, and structure of TiO_2 nanoparticles are precisely controlled by the precursor concentration, pH, temperature, purity of the used chemicals and synthesis time [34].

Table 4. Review of nanostructures and associated nanoparticle forms with the corresponding method of obtaining [34]

Nanostructure	Nanoparticle shape	Obtaining method
0D	Nanosphere	Solvothermal method, electrodeposition technique
1D	Nanofibers, nanorods, nanotubes	Electrospinning, hydrothermal method, electrochemical anodization method, sol-gel
2D	Different structures	Spin coating, Dip coating, chemical vapour deposition, atomic layer deposition

However, the main drawback of TiO_2 is its photocatalytic activity only in the UV range, representing only 3-5 % of the solar irradiation that reaches the earth's surface [3].

To overcome shortcomings, modifications have been made in order to intensify photocatalytic activity in the visible spectra range [5] since it accounts for the ~44 % of the overall irradiance [35].

2.2.2 Modifications of TiO_2 towards activity in visible light spectra

In recent years, a lot of efforts have been invested in the development of materials which are photocatalytically active under visible light spectra. Some proposed approaches are doping titania with metal and non-metal elements, dye sensitization, and semiconductor coupling [35]. An overview of the different methods can be seen in Table 5.

Table 5. Summary of TiO_2 modification approaches towards photoactivity in visible light spectra [35]

	TiO_2 doping	**Semiconductor coupling**	**Dye sensitisation**
Main elements/ compounds used	Non-metals (N, C, S, F) Metals: • Transitions such as Cu, Fe, Mn, Ni, V, Zn, Zr • Noble such as Ag, Au, Os, Pd, Pt, Ru, Rh, Ir • Rare Earth metals such as Sc, Y, La,	CdS, Fe_2O_3, CdS, ZnO, SnO_2, WO_3, V_2O_5, Bi_2S_3	Methylene blue, acid red 44, reactive red dye 198, eosin Y, merbromin, rhodamine B etc.
Drawbacks	Metal ions can also be a source of recombination centres for electrons and holes.	Possible disaggregation and/or dissolution during the photocatalytic reaction.	Possible oxidative degradation of the dye itself in the absence of organic pollutants. Desorption of dye molecules.

Modification by doping reduces the band gap between the valence and conduction band of the photocatalyst due to added 'impurities. Metal and non-metal as dopants have a remarkable impact on the crystal structure of the photocatalyst. The creation of new energy levels between the valence and conduction band caused by doping reduces the photocatalyst's band gap, thereby improving photoactivity in the visible spectra. While metal dopants give rise to a new band below the conduction band, nonmetals create a new band above the valence band, contributing to reduced recombination of electron-hole pairs and increasing photocatalytic degradation [5].

One of the modifications is to dope anatase to avoid the high recombination rate of electron/hole pairs. However, the photoactivity of doped TiO_2 depends on the dopant, its quantity, and the synthesis method. TiO_2 doping involves narrowing the band gap between the valence band O 2p and the conduction band Ti 3d, i.e. an intermediate energy class is created for electrons from the valence band (Figure 3) [4].

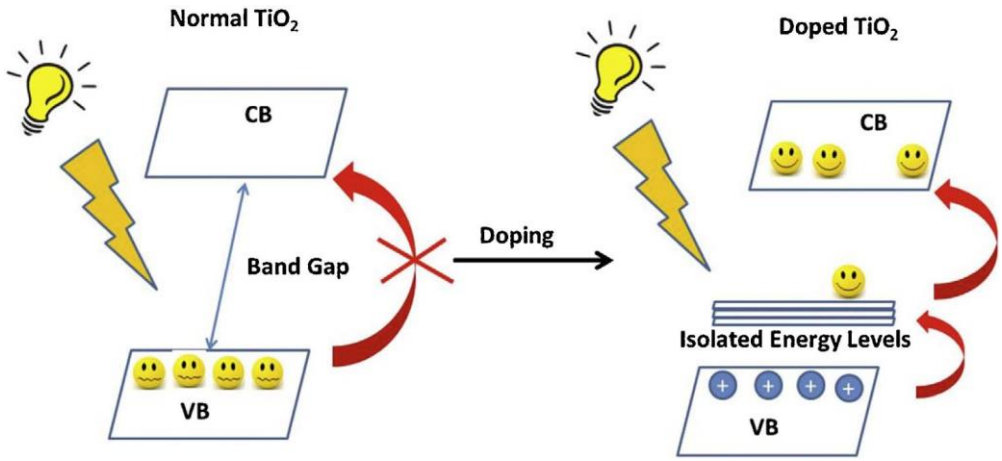


Figure 3. The principle of energy gap narrowing [4]

Moreover, TiO_2 doping with rare Earth metals, specifically with Ln, was reported in [36]. Results have shown that doping with Ln(III) increases surface "defects", apropos oxygen and Ti(III) vacancies which decreases the recombination rate of electron/hole pairs. Also, since Ln(III) has a larger ionic radius than Ti(IV), the specific surface area of the photocatalyst is increased. Furthermore, co-doping with metals such as Fe or Ag indicated improved photocatalyst activity.

On the other hand, doping of TiO_2 with non-metals, such as N, C, F, B, and I, has been discussed [37]. Thereby, possible methods are spraying, pulsed laser deposition, vacuum deposition, solvothermal, and sol-gel processes. Out of non-metallic doping, N doping proved to be the most effective. According to the study [38], the N atom is replaced by an O atom in the TiO_2 structure, thus forming an isolated energy class above the valence band. Irradiation with UV spectra excites electrons in the valence band and an isolated energy class, while irradiation with visible spectra excites only electrons in an isolated energy class. Moreover, due to the proximity of the energy states of N 2p and O 2p, the narrowing of the band gap zone improves the activity of N-doped TiO_2 in the visible spectra [39].

In addition, another study [40] states that the O atoms, located at the structure's boundaries, are stabilized in the presence of N. As a result of charge stabilization, the photocatalyst is active in the visible spectra. As an N source, a stream of pure nitrogen [41], ammonia [42], diethylenetriamine [43], EDTA [44], etc., can be used.

Semiconductor coupling or composite formation shows higher efficiency than its semiconductor. In a review study [5], it was reported about researches where TiO_2 was

coupled with CdS as a sensitizer for titania. Photodegradation under visible light irradiation was achieved for methylene blue and nitric oxide [45], as well as acid orange II [46].

Also, sensitization with dyes due to their absorption of visible light and redox properties improves the excitation process of a semiconductor and photocatalytic activity [5].

2.2.3 Modifications towards visible photoactivity with carbon nanotubes (CNT)

Improvements of desirable photocatalyst properties can be enhanced by creating combinations with other materials to create new composites or hybrids. As an attractive material, carbon nanotubes (CNT) have been recognized. Advantages such as chemical inertness, stability, good electrical properties (conductivity, electron storage capacity), high specific surface (>150 m^2/g), and high charge mobility [6,32,47] were recognized. Furthermore, the advantage of CNT over activated carbons is enhancing the specificity toward adsorbents by modification of CNTs' surface groups via acid treatment [32].

Composites of CNTs and metal oxides reduce the electron/hole pair recombination because of created barrier junction, the so-called Schottky barrier, where there is a space-charge separation region. While CNTs act as electron acceptors, semiconductors act as electron donors in the Fermi energy levels aligning process. Initially, the method was established with platinum and other noble metal interfaces [32,35].

Due to the larger CNT surface area, more electrons can reduce oxygen molecules to superoxide radicals, achieving a higher rate of organic degradation. Simultaneously, more holes are generated and, therefore, more hydroxyl radicals with the intensified hydroxyl groups production on the surface of the hybrid, hydrophilicity increases and the self-cleaning properties of the hybrid (Figure 4) [35].

Furthermore, within C-doped TiO_2, a shift towards the absorption of the visible spectra was noticed. Namely, C atoms are introducing a new C 2p energy level close to the valence band of TiO_2 (O 2p), increasing the active surface of the photocatalyst and an improvement in photocatalytic activity [47].

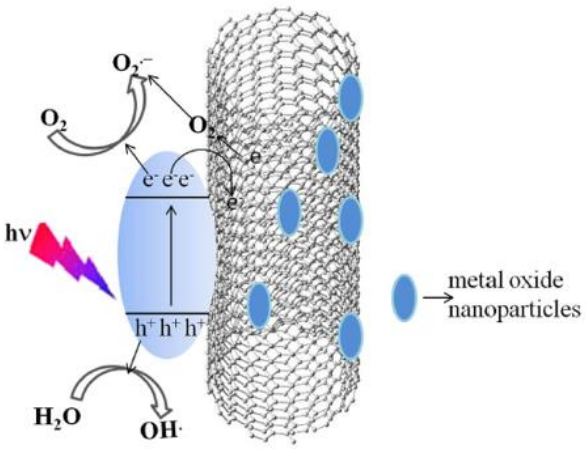


Figure 4. Schematic representation of the photocatalytic activity of a CNT semiconductor oxide [35]

For example, in the study [48], commercial TiO_2 was doped with CNT and caffeine was used as a model pollutant. In the study, photocatalysts with different mass fractions of CNTs were prepared. While all photocatalysts showed good photoactivity, some achieved complete caffeine removal. Therefore, doping with 20 % CNTs proved to be the best option. Moreover, in another study, modification of TiO_2 with CNTs demonstrated intensification of the pollutant's photocatalytic degradation [48,49].

A significant role in photocatalytic activity is the amount of CNT in a composite preparation with TiO_2. For example, an excess amount of TiO_2 reduces the ability of electron trapping by CNT due to a large gap between CNT and TiO_2 particles. Yet, excess of CNTs prevents effective UV absorption by the TiO_2. Therefore, an optimum percentage is necessary to obtain [35,50].

Also, using different TiO_2 precursors during the preparation of nanocomposites with CNTs plays a role. For example, the study [51] found that nanocomposite of anatase TiO_2 and CNT shows lower activity under visible illumination but higher activity under simulated solar illumination. However, the opposite was observed for P25 and rutile TiO_2, where CNTs significantly increased photocatalytic activity under visible illumination.

Good photocatalytic activity was demonstrated by using composites of ZnO and CNT for the degradation of dyes [35].

2.2.4 Immobilisation of photocatalysts

Photocatalysts can be suspended in a medium (i.e., water) or immobilised on an inert support. Even though the suspended photocatalysts tend to be more reactive than the immobilised version, with appropriate reactor design, it is possible to overcome mass and photon transfer limitations [52]. Namely, due to the particles' size, separating the photocatalyst from purified water is a complex and economically unprofitable process. Therefore, the use of suspension is limited to small laboratory systems. The use of an immobilised photocatalyst is, therefore, more cost-effective and reusable [32,53]. The main advantages and disadvantages of the two approaches are summarized in Table 6.

Table 6. Summary of main advantages and disadvantages of suspended and immobilised photocatalysts [35,54]

	Suspended photocatalysts	**Immobilised photocatalysts**
Advantages	Uniform photocatalyst distribution Few mass-transfer limitations Good illumination of photocatalysts Well-mixed particle suspension Ease of photocatalyst reactivation Low-pressure drops through the reactor	Easily applicable continuous operational mode Photocatalyst separation is not required Lower operational costs Improve in pollutant removal due to adsorptive properties of a support
Disadvantages	Required photocatalyst separation More expensive operational costs Aggregation of suspended particles under higher photocatalysts concentrations Harder to apply in a continuous operational mode Possible rate reduction due to light absorption and light scattering	Lowered photons absorption by photocatalysts Mass transfer limitations due to flow rate and photocatalysts film thickness Possible detachment of photocatalysts High-pressure drops Low surface-to-area ratios

Different materials have been used as a photocatalyst's support, from optically transparent to opaque. However, stated materials had to pose one of the characteristics: strong immobilisation of photocatalyst, no decrease in photoactivity due to immobilisation, adsorption properties toward pollutants, stability towards radicals' activity and large surface area. One of the most common support materials are glass, activated carbon, silica, polymers, and minerals such as pumice, alumina, quartz, zeolites, and even materials such as cellulose, fly ash, polyethene sheets, ceramic membranes, monoliths, glass slides, glass wool, anodised iron, optical fibres, etc. Among stated materials, glass is still preferred from an economical and engineering point of view [55].

Furthermore, the immobilisation method plays a significant role in determining photocatalytic activity. Some of the methods reported in the literature are sol-gel,

chemical vapour deposition (CVD), thermal treatment, electrophoretic deposition, and sol-spray methods [55].

For example, an eco-friendly immobilisation process is cold plasma discharge (CPD). Lately, it has been used as a pre-treatment process since it introduces new polar functional groups on the material, facilitating the immobilisation of the photocatalysts [56]. Moreover, among the most common immobilisation methods of today is polymer-assisted hydrothermal decomposition (PAHD), a combination of polymer-assisted deposition and hydrothermal methods. For example, nanocomposites of TiO_2 with graphene oxide [57] and Fe [58] were successfully synthesized on the glowing optical fibres with effective results regarding photocatalytic degradation. Another standard method is spray pyrolysis due to its low cost and eco-friendly nature. It doesn't require expensive equipment and is easily managed in the lab. The method involves the preparation of aerosol, which is then dispersed in the gas phase into droplets passed through the furnace [59].

However, the sol-gel method was considered the most suitable for synthesising nanocomposites and their immobilisation on inert carriers [32]. It is easy to use, does not require expensive equipment and is non-destructive [60]. As well, preparation is conducted at room temperature with high purity and homogeneity due to controllable stoichiometry [61].

As reported in the review [62], sol–gel process is primarily an economical and reasonable method for preparing TiO_2 photocatalyst. The surfactant-assisted sol–gel method has been used to avoid the precipitation of amorphous particles with uncontrolled structure. For example, a complex mixture of hydrochloric acid, DBS, xylene, and water with $TiCl_4$ and simple with DBS was prepared, and homogenous particle size and distribution were achieved. Furthermore, non-ionic surfactants such as Triton X-100, T80 and T20, with the assistance of acetic acid, were reported for the preparation of highly efficient nanostructured photocatalytic TiO_2 thin films [63].

Moreover, the sol-gel method has proved promising for the nanocomposite preparation of TiO_2 and CNT [64]. The higher photocatalytic activity was demonstrated with the same CNT content compared to the mechanically prepared mixture. The biggest challenge of CNTs' sol-gel coating is the dispersion of the CNTs in mediums such as alcohol with TiO_2 precursor. The most common precursors are various metal alkoxides, like titanium

isopropoxide or titanium butoxide [64,65] with alternatives such as titanium tetrachloride or titanium oxysulfate. However, their usage can be challenging since unmodified CNT are hydrophobic, and given precursors can be used in water [66].

Although the sol-gel method is the most common, there are reports on CNTs coating onto TiO_2 by hydrothermal method. Mostly titanium tetrachloride and titanium oxysulfate are used as raw materials, forming amorphous TiO_2 with anatase. The formed coating is further treated in the 300-500°C range to avoid CNT burnout and transformation of anatase to rutile [66]. As well, sputtering, CVD and atomic layer deposition were reported [67,68], such as electrospinning, impregnation, and calcination [69].

Immobilisation of nanocomposite TiO_2 and CNT onto glass substrate was reported by [64]. The sol-gel dip-coating prepared thin films with concentrations ranging from 1 % to 4 % by weight. Characterization measurements of nanocomposites confirmed the incorporation of CNTs into the film.

2.2.5 Reaction mechanisms

The mechanism of photocatalysis on the TiO_2 surface is suggested through a couple of phases [70]. A schematic representation is shown in Figure 5.

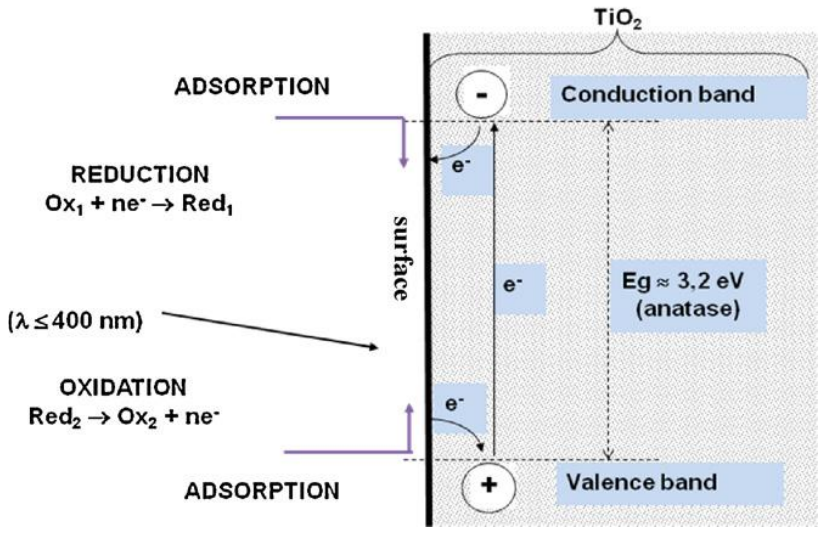


Figure 5. Schematic representation of electron/holes pairs formation on the photocatalyst [71]

When photons irradiate the TiO_2 surface, excitation of TiO_2 occurs, and electron/hole pairs are formed following Equations (4) to (6).

$$TiO_2 \xrightarrow{h\nu} TiO_2(e^-_{CB} + h^+_{VB}) \quad (4)$$

$$e^-_{CB} \rightarrow e^- \quad (5)$$

$$h^+_{VB} \rightarrow h^+ \quad (6)$$

Water and compound molecules are diffused and afterwards adsorbed onto the surface of TiO_2 as written by Equations (7) and (8).

$$Ti^{4+} + H_2O \rightarrow Ti^{4+} - H_2O \quad (7)$$

$$TiO_2 + R_1 \rightarrow R_{1(ads)} \quad (8)$$

Electron/hole pairs are captured onto the surface of TiO_2 by adsorption, Equations (9) to (13).

$$Ti^{4+} - OH^- + h^+ \rightarrow Ti^{4+} - \bullet OH^- \quad (9)$$

$$Ti^{4+} - H_2O + h^+ \rightarrow Ti^{4+} - \bullet OH^- + H^+ \quad (10)$$

$$R_{1(ads)} + h^+ \rightarrow R^+_{1(ads)} \quad (11)$$

$$Ti^{4+} + e^- \rightarrow Ti^{3+} \quad (12)$$

$$Ti^{3+} + O_2 \rightarrow Ti^{4+} - \bullet O_2^- \quad (13)$$

Electron/hole pairs can recombine on the surface or inside the photocatalyst, releasing heat (14).

$$e^- + h^+ \rightarrow heat \quad (14)$$

The oxidation process of adsorbed and free organic molecules with •OH radicals (15) – (18).

$$Ti^{4+} - \bullet OH + R_{1(ads)} \rightarrow Ti^{4+} + R_{2(ads)} \quad (15)$$

$$\bullet OH + R_{1(ads)} \rightarrow R_{2(ads)} \quad (16)$$

$$Ti^{4+}\text{-}\bullet OH + R_1 \rightarrow Ti^{4+} + R_2 \quad (17)$$

$$\bullet OH + R_1 \rightarrow R_2 \quad (18)$$

Initially, two reaction mechanisms were discussed to explain the enhancement of the photocatalytic properties of TiO_2 and CNT nanocomposites (TiO_2/CNT). According to the first (Figure 6.a), after TiO_2 excitation, photogenerated electrons are transferred into

CNTs, wherefore holes remain in TiO_2. In that way, charge recombination is reduced and redox processes prolonged [72]. However, according to the second approach (Figure 6.b), CNTs are seen as photosensitizers that transfer electrons to TiO_2 (19). Injection of photogenerated electrons into the conduction band of the TiO_2 enables the formation of superoxide radicals by adsorbing molecular oxygen (20). Afterwards, an electron from the valence band of the TiO_2 is transferred onto positively charged CNTs creating a hole (21) which then reacts with adsorbed water to form hydroxyl radicals (22) [61,66,69].

$$TiO_2/CNT \xrightarrow{h\upsilon} TiO_2^-/CNT^+ \quad (19)$$

$$TiO_2^-/CNT^+ + (O_2)_{ads} \rightarrow TiO_2/CNT^+ + \bullet O_2^- \quad (20)$$

$$TiO_2/CNT^+ \rightarrow TiO_2{}^+/CNT \quad (21)$$

$$TiO_2{}^+/CNT + (H_2O \leftrightarrows H^+ + OH^-)_{ads} \rightarrow TiO_2/CNT + H^+ + \bullet OH \quad (22)$$

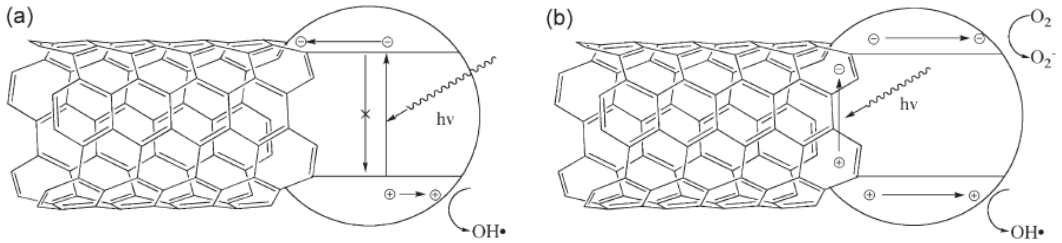


Figure 6. The proposed mechanisms for the CNT-mediated enhancement of photocatalysis. a) CNTs act as electron sinks and scavenge away the electrons hindering recombination. b) Photons generate an electron-hole pair in the CNT. Based on the relevant positions of the bands, an electron (or the hole) is injected into the TiO_2 generating an O_2^- or a $\bullet OH$ species. [32]

However, TiO_2/CNT nanocomposite systems are more complex. According to the review [32], two simultaneous contributions to the reaction mechanism were reported. The first was the formation of the C-O-Ti bond, which extends the light absorption, while the second was the electronic configuration of the CNTs [64]. Regarding photocatalysis, the electronic-band structure of CNTs is a more critical factor, as well as having as fewer defects in structure as possible [32].

2.3 Reactor setups

Today, photocatalysis is applied in various fields: water and air purification, the production of hydrogen and alternative fuels, the synthesis of organic compounds, etc. Depending on the application, it is necessary to design an adequate reactor system to best use the photocatalytic process [73,74].

Therefore, when designing a reactor, it is necessary to know the parameters affecting the process. Namely the source of irradiation, i.e. the illumination of the reactor, the geometry of the system (tubular, annular, plate, etc.), the material from which the reactor is made, the mode of operation (batch, flow) and other processes parameters such as fluid flow, mixing, etc. [73,75]. The photoreactor must be able to "collect" photons; thus, its surface must be fully irradiated. Furthermore, the material from which the reactor is made must transmit irradiation to the surface of the photocatalyst and must be stable and chemically inert. Photoreactors are often made of quartz or borosilicate glass, transmitting irradiation in the UV spectra [76].

Given that it is necessary to ensure good contact between the photocatalyst and the reactants, flow and mixing are also important parameters [77]. Better contact between photocatalyst and reactant is achieved when photocatalyst is used in suspended form. However, to achieve a technically more straightforward yet effective system, nowadays, research goes towards the immobilisation of photocatalysts on an inert carrier. In that case, it is important to how the photocatalyst is placed in the reactor system [78]. Some examples of photoreactors with suspended and immobilised photocatalysts can be seen in Table 7.

Table 7. Examples of photoreactors with suspended and immobilised photocatalysts [54]

	Suspended photocatalysts	**Immobilised photocatalysts**
Examples of reactors	Photocatalytic ultrafiltration Rotating drum Taylor vortex Fluidized bed Labyrinth bubble Hybrid low-pressure submerged membrane	Optical fibre Photocatalytic membrane Fixed bed Corrugated plate Rotating disk Carberry

When the photocatalyst is positioned towards the irradiation source, the increase of reaction constant is proportional to the increase of photocatalyst film thickness up to the saturation point, when film thickness has no further effect on the reaction constant. Under weak irradiation, a thinner film will achieve the same reaction constant as under stronger irradiation. Therefore, a thicker film (4-10 μm) is recommended. However, the irradiation intensity will decrease on its way to the photocatalyst's surface due to the absorption of photons by compounds in the solution. The result is a smaller quantity of absorbed photons and a smaller reaction constant compared to the case where the photocatalyst is

placed away from the irradiation source. In this case, the amount of photocatalyst is critical. If it is less than the optimal amount, fewer photons are absorbed, which leads to a lack of produced radicals. If it exceeds the optimal amount, the result is greater photon absorption. Still, the diffusion length increases at the same time, and there is faster recombination of electron/hole pairs [78]. On the following Table 8, an overview of reactors with immobilised TiO_2 is shown.

Table 8. Immobilised TiO_2 reactors throughput and degradation efficiencies [79]

Reactor type	Pollutant	Volume/ flow rate	Water matrix	Support	UV-A W/m²	Destruction percentage	Reactor size, m²	Treatment duration	Reference
One packed tube	BTEX	2.4 L/h	Pretreated groundwater	Silica gel	3.2	100	0.375	Single-pass mode	***[80]***
Packed CPC	Triclosan	21 L	Water-ethanol solution	porous stones	30	50.5	1.71	2 h	***[81]***
Packed CPC	Humic acids	50 L	Deionized water	Ahlstrom paper	-	100	1	12 h	***[82]***
Packed CPC	Amazil, acetamiprid, thiabendazole	8 L	Secondary treated municipal WW	Glass spheres	30	10-70	0.25	13.3 h	***[83]***
Packed CPC	15 emerging contaminants	10 L	Secondary treated municipal WW	Glass spheres	30	90	0.3	2.3 h	***[81]***
Packed CPC (Solwater)	F.coliforms, Enterococcus faccalis	20 L	Groundwater	Ahlstrom paper	30	100	1	6 h	***[84]***
Packed tubular	TOC	100 L/h	City water	Silica beads	-	Variable through 3 months	-	Single pass mode	***[85]***
TFFBR	TOC	1.5 L/h	pretreated landfill leachate	reactor surface	100	52	0.7	Single pass mode	***[86]***
TFFBR pilot plant	dyes	730 L	Well water	reactor surface	-	47	25	8 h	***[87]***
Fluidized bed shallow tank	Bisphenol A	1 L	Deionized water	ceramic carriers	30	100	0.0375	12-13 h	***[88]***
Floating bed shallow tank	Ammonia	5 L	Petrochemical plant effluent	Light expanded clay aggregate	30-45	59	0.071	21 h	***[89]***
Shallow tank	Phenol	1350 L	Tap water	Photospheres, steel mesh, filtercloth	330	50-80	1.8	15 h	***[90]***
Thin film cascade	Benzoic acid	7 L	Deionized water	reactor plates	17.4	30	1.68	3	***[91]***
Step reactor	Pesticide mixture	25 L	Tap water	Ahlstrom paper	30	80	1	4.5 h	***[92]***
Pebble bed	Dyes	10 L	Simulated dyehouse effluent	pebbles	18.9	15	0.234	5 h	***[93]***
Flat packed bed	E. Colli	1 L	Deionized water	quartz sand	3.7	No complete sterilization	0.07	1.6 h	***[94]***

2.3.1 Flat plate cascade reactor (FPCR)

During the 1990s, the design of solar photocatalytic reactors started to develop toward non-concentrating systems, apropos immobilised photocatalysts upon which the fluid flows. Open configuration of the reactor allowed usage of all incoming irradiance, however, with the risk of evaporation of volatile compounds and possible release of photocatalyst particles. Nonetheless, these reactors were used for the localized wastewater problem solution due to the low-cost investment and high surface requirement [35]. A flat-plate cascade reactor (FPCR) mimics an outdoor system application which can be implemented at a low cost [95]. Industrial scaling of the FPCR has drawbacks, such as the usage of UV transmissive glazing, which increases the costs and limited water film thickness necessary for initiating the degradation process. Nevertheless, the FPCR can be used as an innovative passive water protection in real outdoor systems [79]. The geometry of the cascade reactor is favourable to the mass transfer limitations due to the usage of immobilised photocatalysts [96]. However, the water film thickness is a limiting factor [79]. It was reported that similar degradation reaction rates to those obtained with slurries systems were possible and comparative for the FPCR reactor with immobilised photocatalyst (TiO_2 onto nonwoven paper coated with PC500 using an inorganic SiO_2 binder) [97].

2.3.2 Compound parabolic collector reactor (CPC)

On the other hand, as an optimal reactor, a compound parabolic collector reactor (CPC) is recommended [49] as the state-of-the-art design due to the highest effectiveness of irradiation capture in a reactor system. Furthermore, turbulent flow conditions, no overheating, no vaporisation of contaminants, no solar tracking, collection of both direct and diffuse radiation, low cost, weatherproof properties, and high optical efficiency are some of the few additional advantages [35]. Therefore, its application on a larger scale has been recognized as technically and economically feasible [98].

As a reactor setup, it was successfully applied for hazardous chemicals or water pathogens from landfill leachate, olive mill, and urban wastewater [35].

3 PHOTOCATALYTIC MODELLING

3.1 Kinetics of heterogeneous photocatalytic reactions

The photocatalysis can be described as a change in the chemical reaction rate when a semiconductor or photocatalyst absorbs a quantum of irradiation. A heterogeneous system can be presented as photo-adsorption/desorption and photoexcitation processes [26]. The adsorption of molecules on a semiconductor in an aqueous solution can be explained by Langmuir-Hinshelwood (LH) and Eley-Rideal (ER) mechanisms. The most often used one is the LH mechanism [20]. The LH mechanism explains the interactions of charge carriers with adsorbed molecules, which participate in chemical reactions on the surface of the photocatalyst. Equations (23) to (25) are a simplified presentation of the reaction mechanism [20]:

$$A + S \leftrightarrow AS_{ads} \quad (23)$$

$$B + S \leftrightarrow BS_{ads} \quad (24)$$

$$AS_{ads} + BS_{ads} \leftrightarrow Products \quad (25)$$

where A and B are the reactants and S is the surface of the photocatalyst. It also explains the kinetics of reactions on the surface of the photocatalyst. There are two main assumptions of the LH model [26]: (i) adsorption equilibrium is established all the time, and the rate of a chemical reaction is lower than the rate of adsorption/desorption; (ii) it is assumed that the reaction occurs between adsorbed molecules whose concentration on the surface is in equilibrium with the concentration of the substance in the fluid, so the determining rate of a chemical reaction is on the surface of the photocatalyst.

The ER mechanism explains the interaction between molecules and centres on the photocatalyst surface, which initiate chemical processes. Here, only one reactant is adsorbed, while the other participates in the reaction without adsorption. Stated is described with Equations (26) and (27) [26].

$$A + S \leftrightarrow AS_{ads} \quad (26)$$

$$AS_{ads} + B_g \leftrightarrow Product \quad (27)$$

Furthermore, in the past study [28], it was elaborated that the photocatalytic reaction does not take place in the fluid mass but at the boundary phase, where the transfer of substances

by diffusion can have an impact on the adsorption of molecules on the photocatalyst surface and thus determine the rate of the chemical reaction.

3.2 Parameters affecting photocatalytic reactions

The rate of chemical reactions can be affected by several parameters, such as the photocatalyst's mass, irradiation wavelength and flow, initial reactant concentration, temperature and pH [71].

The photocatalyst's mass is proportionally related to the rate of a chemical reaction. Given is expressed with the chemical reaction constant *k* and the number of active centres on the surface of the photocatalyst n_T, which is shown by the equation (28) [20]:

$$r = k * n_T = k * d * m * S_{BET} \quad (28)$$

where *d* is the average density of active centres on the photocatalyst surface, *m* is the mass of the photocatalyst, and S_{BET} is the specific surface area of the photocatalyst.

When a photocatalyst is used as a suspension, its mass is most commonly defined as a concentration. Overall, determining the optimal photocatalyst concentration is necessary. If the concentration is too high, the turbidity of the suspension due to the scatter effect prevents the irradiation penetration, thus reducing the effectiveness of photocatalysis [30]. Furthermore, in the study [99], it was elaborated that at high concentrations of TiO_2, hydroperoxyl radicals are formed (29) - (30).

$$\bullet H + \bullet HO \rightarrow H_2O_2 \quad (29)$$

$$H_2O_2 + \bullet OH \rightarrow H_2O + \bullet HO_2 \quad (30)$$

Therefore, the optimal mass concentration of TiO_2 suspension is recommended in the range of 0.15 – 8 g/L [99] or 0.2 – 2.5 g/L when the light path is several centimetres long [20].

When the photocatalyst is immobilised on the support, the optimal concentration of the photocatalyst's mass is defined as the optimal thickness of the film layer [70,99]. It is because thicker films are more suitable for photocatalytic oxidation. However, increasing the film thickness increases the resistance of substances' transfer through the photocatalyst, favouring the recombination of electron/hole pairs [28].

The effective irradiation wavelength for photocatalysis depends on the photocatalyst's band gap energy E_g. For example, TiO_2, which has E_g = 3.02 eV n, must have the wavelength $\lambda \leq 400$ nm [20]. However, the gap of E_g does not affect the photocatalytic decomposition if the wavelength of the incident irradiation is sufficient to excite the electrons. Therefore, lamps of various designs are often used as irradiation sources in closed reactors. In addition to the type of lamp, its position in the reactor is also essential, as it is necessary to ensure uniform illumination of the system [28].

The initial concentration of reactants in the system significantly affects the kinetics of the photocatalytic reaction. As already stated, the kinetics follows the LH mechanism with an expression for the chemical reaction rate (31) [20]:

$$r = k\theta = k(\frac{KC}{1 + KC}) \tag{31}$$

where k is the chemical reaction constant and θ is the photocatalyst surface coverage which can be further described with expression defining K as the equilibrium adsorption constant and C as the reactant concentration.

For highly diluted systems ($C < 10^{-3}$ M), KC becomes << 1, and the reaction is pseudo-first order, while at concentrations > 5×10^{-3} M (KC >> 1), the rate of the chemical reaction is the highest, and it is zero order [20].

According to the study [28], the rate of pollutant degradation is inversely proportional to its initial concentration. Namely, there is a limited number of active sites on the surface of the photocatalyst, and at higher pollutant concentrations, all free sites are filled. Therefore, a further increase in the initial concentration does not affect the conversion.

In general, photocatalytic reactions do not depend significantly on temperature. Therefore, the process is attractive for water and air purification because it is not necessary to supply and consume additional energy for the system. The real activation energy (E_t), according to the real chemical reaction constant, is equal to zero. In contrast, the apparent activation energy (E_a) is of very small values in the temperature range 20°C $\leq \theta$°C $\leq$ 80°C. However, at low temperatures (-40°C $\leq \theta$°C $\leq$ 0°C), primarily for gaseous systems, the activity decreases. The photocatalyst and photocatalysis activity is reduced at temperatures higher than 70-80°C. It is attributed to the reduced solubility of oxygen

[20]. The study [100] observed that an increase in temperature promotes the recombination of electron/hole pairs and desorption of adsorbed reactants, thus reducing the efficiency of the photocatalytic process. Namely, it follows the LH mechanism, by which lower temperature favours adsorption since it is a spontaneous exothermic process.

As well, the rate of the chemical reaction is proportional to the irradiation flux Φ [20]. It indicates the nature of the photocatalyst to be activated under the irradiation source. There are two regimes where the photocatalytic process can occur regarding the irradiation flow [99]. The irradiation flow of the first order includes the process where the incident irradiation intensity is up to 25 mW/cm^2. At higher intensities, the order of the process changes, favouring the recombination of electron/hole pairs, while at lower intensities, the chemical reaction of the pairs dominates.

A typical photon flux of 1 mW/cm^2 provides the order of 1 incident photon per surface atom per second. As aqueous-phase photocatalysis has apparent quantum efficiencies routinely in the order of one-tenth to several percent, the apparent turnover frequency, F, is one event per 30–1000 s, which is slow compared to the usual kinetic rate of the order of 10^8 s^{-1} in liquid phases. In consequence, equilibrium is assumed and constant (k_r) contains the irradiance dependence, typically in the form given by Equation (32):

$$r = k_r = k_{r0} I^n; \quad 0.5 < n < 1.0 \tag{32}$$

where $n = 1$ corresponds to reaction dominance while $n = 0.5$ corresponds to electron-hole recombination dominance.

The solution's pH, especially in suspension systems, affects the photocatalysis on the charge of the particles, the size of the aggregates, and the position of the valence and conduction bands [30]. In the pH range of 4 – 10, the rate of the chemical reaction does not depend on the pH. However, the pH can affect the process if photocatalysis is used to purify industrial waters, which can be acidic or alkaline. For example, in acidic solutions, the surface of TiO_2 can be protonated (33), or in alkaline solutions, deprotonated (34) [100].

$$TiOH + H^+ \rightarrow TiOH_2^+ \tag{33}$$

$$TiOH + OH^- \rightarrow TiO^- + H_2O \tag{34}$$

In acidic pH (pH < 6.9), the TiO_2 surface is positively charged, while in alkaline (pH > 6.9), it is negatively charged. The pH at which the surface of the photocatalyst is uncharged is called the pH of the isoelectric point (pH_{IET}). TiO_2 pH_{IET} is 4.5 – 7, and P25 6.25 – 6.6. Therefore, P25 is positively charged in an acidic medium (33) while negatively charged in an alkaline medium (34) [70]. According to the study [100], TiO_2 has a more substantial oxidizing effect at lower pH, but at very low pH conditions, the reaction rate decreases due to excess H^+ ions.

The oxygen molecule is a strong electrophile, and if the concentration of oxygen increases, there is a possible decrease in recombination. For the complete mineralization of organic matter, the presence of oxygen is necessary. However, at high oxygen concentrations, hydroxylation of the surface of the photocatalyst occurs, resulting in a reduction of active centres and the success of photocatalysis decreases [28]. According to the study [30], oxygen molecules can participate in the formation of reactive oxygen species, e.g., superoxide, hydrogen peroxide, hydroxyl radical, prevention of reduction reactions, stabilization of by-products, mineralization and photocatalytic reactions.

4 BENZOTRIAZOLES

Benzotriazoles (BTs) are a group of heterocyclic compounds widely used in industrial activities and domestic life. The most used compound in this class is 1H-benzotriazole (1H-BT) [101]. BTs application varies from corrosive inhibition in de-icing fluids to application in bleaching, antifogging and antifungal agents [102–105]. Moreover, during synthesising of dyes, drugs, and fungicides, BTs are formed as intermediates [101]. About 9,000 tons are produced annually, with China being the largest producer [106,107]. In addition, airports have been detected as hot spots of the BTs releasement in the environment [101,108].

Since BTs are chemically stable and highly soluble compounds, their removal by WWTPs is insufficient [109]. Therefore, BT's residuals were detected mainly in aquatic environments in nano to microgram per litre concentrations. Even though reported acute toxicity is generally low, considerable residual levels were found in various organisms (plants, invertebrates, fish etc.), revealing a potential risk. Endocrine-disrupting effects, hepatoxicity and neurotoxicity are some of the impacts of sublethal dosages and bioaccumulation effects [101,102].

4.1 Properties and applications

The 1H-benzotriazole (1H-BT) is an organic compound composed of a benzene ring joined to a five-membered ring containing three nitrogen atoms. Depending on the position of the hydrogen atom bonded with nitrogen, the compound can be written as 1,2-H benzotriazole, depending on the source. However, it was calculated and experimentally confirmed by NMR analysis that the 1H structure is more energetically stable than the 2H structure [110]. Accordingly, the structure of 1H-BT is shown in Figure 7.

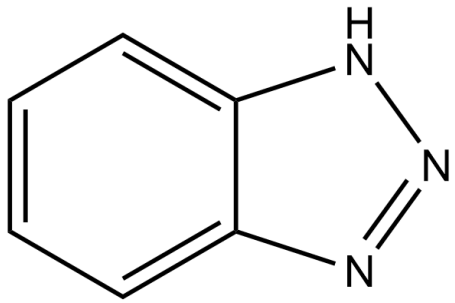


Figure 7. Structural formula of 1H-benzotriazole [111]

The 1H-BT acts as a weak acid with a pK_a value of 8.2, but at the same time as a weak base ($pK_a < 0$). Consequently, 1H-BT is soluble in an aqueous solution of sodium carbonate or 1 M hydrochloric acid, representing two possibilities for separating 1H-BT from mixtures. Furthermore, an electron donor forms complex organic structures, while an electron acceptor stabilizes carbanions [112]. The basic chemical and physical properties of 1H-BT are shown in Table 9.

Table 9. Properties of 1H-benzotriazole [111]

Property	
Molecular formula	$C_6H_5N_3$
Molecular mass	119.12 g/mol
Occurrence	crystals/ powder
Colour	colourless
Odour	None
Boiling point	355°C
Melting point	100°C
Solubility	In water 1-5 g/L at 23°C

Since their discovery by chemist Alan Katritzky, BTs have had a wide range of applications. Their application can be found in polymer engineering, metallurgy, technology, medicine, etc. [106,107].

The most effective application of BT derivatives is in material engineering. One of its roles in this area is corrosion inhibition on copper alloys. Copper alloys corrode during their usage, such as in heat exchangers, desalination devices, WWTPs, the chemical industry, etc. Coating of copper alloys with 1H-BT enables the creation of a diffusion barrier between 1H-BT and material surface. Namely, the 1H-BT molecule joins with the copper atom due to free nitrogen electrons [113].

Furthermore, according to the USA regulation, 1H-BT is allowed to be used as an indirect food additive. Namely, it is permitted to use 1H-BT as a surface coating onto rolling foil or sheet, provided that the total quantity of the coating residue on the metal object in the unchanged form in which it comes into contact with food does not exceed 0.015 mg/in^2 of metal contact with food [114].

In polymer materials, 1H-BT is used as a UV absorber. Polymeric materials are subject to degradation due to the absorption of UV radiation. To avoid degradation, various organic and inorganic molecules are used as UV filters that have a high absorption

coefficient in the UV spectrum. These molecules transform the absorbed radiation into a less harmful one before it reaches the substrate. For a molecule to be a UV filter, it must have strong and broad UV absorption zones, a short excitation time, and be photostable. Some of the most commonly used molecules are 2-(2'-hydroxy-5'methylphenyl)benzotriazole, better known under the commercial name Tiruvin P and its derivative Mexoryl XL. Their photostability is explained by intramolecular proton transfer in the excited state [113]. Therefore, as stabilisers for degeneration and yellowing reduction, BTs are used in everyday plastics, paint, building materials, automobile components, skin creams and shampoos [108].

It has been proven that compounds based on BTs inhibit the growth of microorganisms. Therefore, they are used in medicine as antibiotics, antifungals, antiparasitics and antivirals. Furthermore, their use as antitumor drugs is possible. Several BT derivatives have shown this property, such as Vorozole and 4,5,6,7-tetrabromobenzotriazole, an inhibitor of protein kinase CK2 [113].

4.2 Occurrence and impact on the environment

As can be seen, BTs are widely used and, therefore, easily transferred into the environment. The most common recipient is water, which BTs reach through sewage and drainage channels from WWTPs [115]. 1H-BTs have been detected at the inlet and outlet of WWTPs, typically in concentrations of several hundred ng/L to tens of thousands of ng/L [116]. It has been estimated that approximately 30 % of the total 1H-BT input into wastewater is due to dishwashing machines' discharge [108]. An overview of the studies' results reported in [102] and shown in Table 10 demonstrates the removal of 1H-BT and significant contractions still released into the environment.

Table 10. Concentrations of 1H-BT before and after WWTPs in different countries [102]

State	Influent (ng/L)	Effluent (ng/L)	Sludge (ng/L)	Reference
Greece	516-2632	14-548	76-412	***[117,118]***
Germany	5890-44000	3470-20000		***[106,119–122]***
Switzerland	13000-75000	11000-100000		***[123]***
Australia	4778-6634	2206-3300	1.45-120	***[124,125]***
UK		840-3605		***[126]***
Spain	76.5-36200	26.7-16933	0.5-27.1	***[127–130]***
India	34.5-167	10.8-42	6.3-18.9	***[131]***
China	204	155-553	17.2-198	***[132–134]***
Netherlands		8000		***[135]***

Hence, a great emphasis has been placed on the BTs monitoring and occurrence in waters. The study [136] analysed 35 polar POPs from 27 European countries. 1H-BT was found in 94 % of samples, with a maximum concentration of 7.99 μg/L. Furthermore, in follow-up research [137], the pollution of the Danube River and its tributaries were studied. The highest concentration of 1H-BT was determined in the Vah River in Slovakia (~ 1.55 μg/L) and the lowest in the countries of Eastern Europe, Serbia, Romania, and Bulgaria (< 40 ng/L).

Moreover, high concentrations of BTs were found in groundwaters. One of the first studies about BTs detection in groundwaters was conducted in 1997 near an airport in the USA [138] with a maximum detected concentration of 126 mg/L. According to the study [139] in Europe, which included 164 groundwater samples from 23 countries, the maximum concentration of 1H-BT in the samples was 1.03 μg/L. Meanwhile, a concentration of 280 ng/L in Australia was detected in groundwaters near Adelaide [124].

The number of publications is small regarding the presence of BT in air and soil. However, due to the use of 1H-BT in de-icing fluids, the highest concentrations in soil and air are expected nearby airports [108]. For example, along the abandoned airport runway in Oslo, snow disposal sites and sediments nearby drainages 0.33 mg/kg, 0.66 mg/kg and 13 mg/kg were reported, respectively [140]. In China, sediments from the Songhua and Saginaw Rivers were investigated, and 1H-BT was detected in several hundred ng/g concentrations [141]. Similar findings were reported for the sediments from the Ariake Sea in Japan, where 6.3 ng/g of 1H-BT was detected [142]. Furthermore, 1H-BT was identified in indoor dust samples from the USA, Japan, Korea, and China. Among 158 samples, the highest individual sample concentration of 200 ng/g was detected in China [143].

As a persistent and biologically active substance, 1H-BT is easily (bio)accumulated in the tissues of plants and animals [144]. There are several studies on the topic of bioaccumulation. In follow-up research [145,146], the 1H-BT occurrence was analysed in lettuce and strawberries. The presented results in Table 11 revealed the presence of 1H-BT on a nanoscale. Namely, 1H-BT is structurally similar to the indole molecule (it has only one N atom on the five-membered ring), which participates in the biochemical processes of tryptophan metabolism. Therefore, authors [145,146], assumed that 1H-BT mimics the indole molecule and, in that way, is being incorporated into plant cells.

Table 11. Concentrations of 1H-BT in fruits and vegetables [145,146]

Part of the plant	**Concentration BT (ng/g)**
Lettuce leaf	153
Strawberry root	61.9
Strawberry fruit	44
Strawberry stalk	16.6

On the other hand, the presence of 1H-BT in fish tissue was researched by follow-up studies [147–149] of China's Yangtze and Pearl rivers. The highest concentration of 1H-BT in wild fish was 2.95 μg/L, primarily identified in the liver due to its detoxifying role.

Regarding its impact on smaller organisms, different authors indicated the toxicity of 1H-BT and its derivatives. In research [150] impact of 1H-BT and 5-methylbenzotriazole (5-MBT) on two species of planktonic crustaceans from the genus Daphnia (*Daphnia Magna, Daphnia Galeata*) and two species of primary producers (*Desmodesmus suspicious, Lemna minor*) was studied following OECD guidelines. Slow growth and an impact on the reproduction system have been observed. Namely, a hormonal imbalance occurs due to the similarity in structure between 1H-BT and phytohormones. In daphnids, it was observed that smaller organisms (*D. galeata*) are less resistant to the effect of 1H-BT and 5-MBT.

Another research [151] studied the impact of 1H-BT derivatives containing a methyl group on luminescent bacteria. The authors reported that BT derivatives containing a methyl group are more toxic than 1H-BT. Furthermore, the impact of 1H-BT and its derivatives 4-tolitriazole (4-TTri) and 5-tolitriazole (5-TTri) on zebrafish (*Danio rerio*) larvae was studied [152]. It was reported that 1H-BT and its derivatives had moderate toxicity to larvae. Moreover, it is essential to point out that a particular substance's toxicity depends on its bioaccumulation in the larva's organism. Thus, 4-TTri has the highest value of acute toxicity (LC_{50} = 59 mg/L), the longest retention time and more complex biotransformation pathways in contrast to 1H-BT and 5-TTri.

When discussing impacts on human health, they are not sufficiently researched yet. However, the accumulation of 1H-BT, due to its abundance in the environment, is occurring. Namely, due to its polarity, 1H-BT is excreted from the human body through urine. For example, BT and its derivate 5-MBT were detected in human urine samples; 9.78 ng/ml and 3.37 ng/ml, respectively [108]. Furthermore, research [153] revealed the

presence of BTs in human urine samples across several countries: China, the USA, India, Korea, Japan, Greece and Vietnam. As a result, 1H-BT was identified in all samples, ranging from a few hundred ng/L to a maximum of 24.5 μg/L (China).

4.3 Removal methods of 1H-BT

When pollutants reach the environment, their persistence depends on their photolysis susceptibility. Due to the insensitivity to visible light, 1H-BT is relatively long and persistent in the environment. Previous studies have proved direct photolysis with a first-order kinetic reaction mechanism of 1H-BT under UV light. The most efficient degradation is in UV-C spectra since maximum absorption of 1H-BT is detected at 254 nm [102]. However, a more dominant role of 1H-BT removal in the natural environment is indirect photolysis or reaction with reactive transient species. Therefore, sunlight photolysis is relevant for 1H-BT degradation in surface waters [104]. However, more toxic compounds can be formed without mineralization [101].

Regarding conventional treatment processes, the degradation of 1H-BT and its derivatives was studied by hybrid MBBR (Moving Bed Biofilm Reactor) technology, MBR and activated sludge technology.

The removal of 1H-BT and its derivatives by hybrid MBBR technology was investigated in the research [154]. The hybrid MBBR system consisted of two aerated reactors with activated sludge and a settling tank. During the 34 days of the experiment, COD decreased by 87 % and NH_4-N by 98 %. Furthermore, most of the 1H-BT was already removed in the first reactor, while the second was used for additional water purification. Namely, in the second reactor, COD was 24 mg/L while NH_4-N was 1 mg/L. Therefore, by metabolic biodegradation, the hybrid MBBR technology partially removed 1H-BT and its derivatives. While 1H-BT was the easiest to biodegrade, 4-TTri proved to be the most challenging derivate to remove. Another research [155] studied optimal conditions for removing 5-TTri by conventional activated sludge and MBR technology. Both technologies proved successful for 5-TTri removal.

In the study [156], the biological degradation of 1H-BT, 5-TTri and 4-TTri by activated sludge from a membrane bioreactor and conventional technology was studied. Aerobic biodegradation of the compounds at different concentrations in a laboratory and scale-up environment was tested. The fastest biodegradation was recorded for 5-TTri, regardless

of its initial concentration (0.53-31.2 mg/L), followed by 1H-BT with an initial concentration of 1.03 mg/L. However, the increase of 1H-BT initial concentration negatively affected the removal process by activated sludge. The most resistant BT derivate to remove was 4-TTri. After 105 days, changes in concentration were not recorded. Analysis of the activated sludge revealed that Alpha- and Betaproteobacteria had played a vital role in the degradation of 1H-BT and its derivatives.

Meanwhile, recent studies have demonstrated the importance of radicals in 1H-BT removal, including photolysis with hydrogen peroxide (H_2O_2) [105,157] or chlorination [103] assistance, cavitation [158,159], Fenton processes [160,161], ozonolysis [122,162,163], electrochemical oxidation [164] and photocatalysis [101,157].

Photolysis alone is not an efficient method to remove 1H-BT. Therefore, applying H_2O_2 has been demonstrated as an efficient removal for BTs and benzothiazoles. However, the removal efficiency depends on the applied concentration of H_2O_2, reactor design, irradiation, water matrix and chemical properties of the target micropollutants [105].

The impact of chlorination on the 1H-BT degradation was investigated by the study [103]. It revealed a synergetic effect on the removal of 1H-BT compared to UV-A photolysis or chlorination alone due to the generation of hydroxyl radicals and reactive chlorine species. Even though identified degradation products were less toxic than 1H-BT, other studies [165,166] have shown the negative impact of chlorine in AOPs due to the generation of more harmful degradation products for the aquatic environment.

During the cavitation process, radicals are formed during the collapse of bubbles/cavities and the releasement of a large amount of energy in short intervals [7]. For example, in the study [158], ultrasound (665 kHz, 500W) was used to remove 5-MBT. After 2 hours of process, 97 % of 5-MBT was successfully removed. Alongside, 32 by-products were identified. Another study [159] of 1H-BT degradation by ultrasound revealed that the increase in the ultrasound power is positively correlated with 1H-BT removal. In contrast, the rise of 1H-BT initial concentration negatively correlates with the removal rate.

Another AOPs, the Fenton process, was also studied to remove 1H-BTs. The Fenton process is based on the oxidation of Fe(II) ions by H_2O_2 to Fe(III), most often under pH 3. The reduction of Fe(III) to Fe(II) forms hydroperoxyl radicals and protons necessary for pollutants' degradation [12]. For example, in the study [160], degradation of 1H-BT

depending on different concentrations of 1H-BT, H_2O_2 and zero-valent iron (Fe^0) under pH 3 was researched. The results indicated that degradation of 1H-BT increases until reaching optimal conditions. The highest removal rate of 1H-BT (70 %) was achieved with an initial concentration of 15 mg/L with 0.10 g/L of Fe^0 and 1.5 mmol of H_2O_2. In another study [161], the degradation of 1H-BT by photolysis and photo-Fenton was researched. Photolytic degradation was negligible, proving 1H-BT stability. Meanwhile, degradation by a modified photo-Fenton process with ethylenediamine-N,N'-disuccinic acid (EDDS) at the ratio Fe(III):EDDS:H_2O_2 = 0.1:0.2:0.3 mM confirmed that the degradation rate depends on the water matrix content. During the 30 minutes experiment, 100 % of 1H-BT was removed when a model solution was used, while less than 30 % was removed from synthetic wastewater.

Furthermore, as one of the strongest oxidizing agents, ozone (O_3) is often used in industry [12,167]. Compared with the conventional activated sludge method in WWTPs, removing 1H-BT, 4-TTri and 5-TTri by ozonolysis proved to be an effective method since nearly 100 % of all three compounds were removed [122].

Moreover, electrochemical oxidation was studied to remove 1H-BT [164]. The mechanism is based on the oxidation of water on the electrode's surface, during which hydroxyl radicals are formed on the anode's surface [168]. Conclusions of the study [164] reported that the best results were achieved with a higher electric density for a longer time of the experiment. Namely, after 150 min, 97.9 % of 1H-BT was removed in the presence of sulfuric acid as an electrolyte.

And finally, the removal of 1H-BT or its derivatives by photocatalysis was researched. The overview of the studies is shown in Table 12. Depending on the preparation of the photocatalyst, different results were obtained during the analysis. Most of the studies were based on the removal of 1H-BT from an aqueous solution in the presence of a photocatalyst in a suspension. Although this method showed the best results (removal of 1H-BT above 90 %), it presents a problem from the engineering point of view due to the separation of photocatalyst particles from the solution. Therefore, emphasis is given to the studies using immobilised photocatalysts. In two studies [169,170], 1H-BT was removed in the presence of a photocatalyst immobilised on a carrier. However, the reactors used were smaller dimensions.

Table 12 Overview of the studies researching the removal of 1H-BT by photocatalysis [171]

	Photocatalyst	Photocatalyst's synthesis	Photocatalyst's usage	Concentration	Type and intensity of the lamp source	Experiment length	Removal efficiency	Reference
1	α-Fe_2O_3-Bi_2S_3 with graphene doping	Solvothermal method	Suspension 0.5 g/L	1H-benzotriazole 20 mg/L	36 W LED lamp	300 min	98 %	***[172]***
2	BiOBr in the form of nanoplates and nanospheres	Deposition	Suspension 0.5 g/L	1H-benzotriazole 1 mg/L	800 W Xe lamp	180 min	~90 %	***[173]***
3	Ta_2O_5/$PtCl_2$ nanoplates	Chemical vapour deposition	Suspension 0.5 g/L	1H-benzotriazole 10 mg/L	880 W/cm2 Xe lamp	120 min	94 %	***[174]***
4	TiO_2 P25 Evonik	Commercial photocatalysts	Suspension 1 g/L	1H-benzotriazole 0.1-0.5 mM	6 W UVC	90 min	50 % - 99 %	***[175]***
5	BiOI	Hydrolysis	Suspension 0.5 g/L	1H-benzotriazole 10 mg/L	28 W Fluorescent lamp	90 min	do 80 %	***[176]***
6	TiO_2 nanorods with Fe_2O_3 and FeOOH doping	Hydrothermal method	Calcination	1H-benzotriazole 5 mg/L	15 W Fluorescent lamp	60 min	do 8 %	***[170]***
7	Gd_2YSbO_7/$ZnBiNbO_5$	Solvothermal method	Suspension 0.75 g/L	1H-benzotriazole 0.04 mmol/L	500 W Xe lamp	150 min	~99 %	***[177]***
8	TiO_2 Merck (100 % anatase) TiO_2 P25	Commercial photocatalysts	Suspension 0.5 g/L	1H-benzotriazole, Tolytriazol and Tinuvine P 10^{-4} M	18 W Fluorescent lamp	120 min	do 100 %	***[101]***
9	TiO_2 with Cu doping	Hydrothermal method, anodization, electrodeposition, and spin coating	Electrochemical anodization	1H-benzotriazole 5-30 mg/L	15 W Fluorescent lamp	75 min	do 80 %	***[169]***

5 MATERIALS AND METHODOLOGY

5.1 Materials

The contamination of water with BTs was simulated with a model solution of 1H-benzotriazole (1H-BT; 99 %, ACROS ORGANICS). The initial concentration was 10 ppm. A working solution with a concentration of 50 ppm was prepared, and diluted as needed, depending on the experiment. Distilled water was used in the experiments; purified in the laboratory by the Hydrolab device (HLP Plus V10).

In respect of analytical methods, chemicals of LC/MS (liquid chromatography/mass spectrometry) purity grade were used; ultrapure water (H_2O, LC/MS, Honeywell), methanol (MeOH, LC/MS grade, Honeywell), formic acid (FA, 99 %, Fisher Chemicals) for the preparation of mobile phases. Mobile phases A and B were used for the separation of the compounds by liquid chromatography; H_2O+0.1 % FA (V/V) and MeOH+0.1 % FA (V/V), respectively. The mobile phase D, H_2O: MeOH=60:40 (V/V), was used to elute and condition the system. When required, isopropanol (ACS reagent, Grammol) was used for needle washing and system cleaning.

The stock solution for the reference mixture (Bottle A, Reference mix) was prepared according to the procedure proposed by the manufacturer and was consequently used. A stock solution ($V = 1L$) was prepared with 950 ml of acetonitrile (ACN, LC/MS, Honeywell) and 50 mL of ultrapure H_2O. In a prepared solution, 0.1 ml of ammonium trifluoroacetate ($TFANH_4$, 100 mM, T.T.T.), 0.2 ml of purine (5 mM, Agilent) and 0.5 ml of hexakis phosphazine (HP-0921, 2.5 mM, Agilent) were added.

The mass spectrometry calibration mixture (Bottle B, Tune mix) was used without dilution, according to the manufacturer's instructions *(ESI-L Low concentration tuning mix; contains CAS #: 107-43-7; 3336-58-1; 957-13-1; 186817-57-2; 58943-98-9; 16059-16-8; 3830-74-8; 186043-67-4; 186406-47-3; 186406-48-4; 186406-49-5; 368-66-1: 915-76-4; diluted in ACN (HPLC grade) and deionized water).*

5.1.1 Photocatalysts

In the research, two photocatalyst formulations were studied (Figure 8):

- TiO_2 or commercial titanium dioxide (Evonik, Aeroxid®, TiO_2 P25, 30 nm, 56 m^2/g, 75:25 anatase to rutile mas' ratio) and
- TiO_2/CNT, a nanocomposite of TiO_2 P25 and multiwalled carbon nanotubes, (CNT, Sigma-Aldrich, 50-90 nm, >95 % carbon) in a ratio of 10:1 (w:w).

Both photocatalysts were immobilised on a glass fibre mesh (Kelteks, Karlovac, Croatia, density 480 g/m^2) of defined dimensions according to the reactor's setup needs by the modified sol-gel procedure previously described in the paper [49].

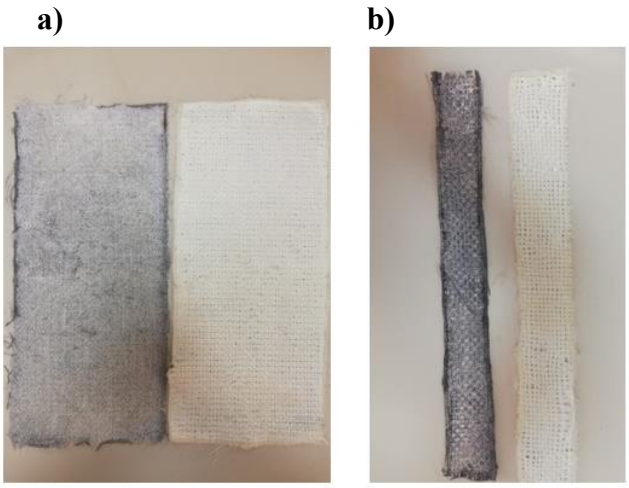


Figure 8. The image of photocatalysts: TiO_2 photocatalytic film on glass fibre mesh (white) and TiO_2/CNT photocatalytic film on glass fibre mesh (black) for a) the FPCR and b) CPC reactor

According to the procedure, the photocatalyst (TiO_2 or TiO_2/CNT) was added to a solution of distilled water and ethanol (p.a. 96 %, Grammol) with a volume ratio 1:1 and stirred for 15 minutes, during which the pH is adjusted to 1.5 with the addition of acetic acid (Kemika, Zagreb, Croatia). The homogenization of the solution is then performed by the ultrasonic probe for 2 minutes (30 W, 20 kHz). After sonication, tetraethoxysilane (TEOS, Sigma-Aldrich, Germany) was added, and the solution was stirred for 1 hour at 50°C. Meanwhile, glass fibre mesh was cut to prepare supports for the immobilisation. For the FPCR, six meshes were prepared with dimensions 25×50 cm, three for the TiO_2 immobilisation and three for the TiO_2/CNT immobilisation. Accordingly, four meshes were prepared for the CPC reactor with dimensions 48×2.5 cm, two by two for TiO_2 and TiO_2/CNT immobilisation, respectively. Next, supports were cleaned with ethanol, treated for 5 minutes with 10M NaOH and rinsed with

deionized water. Finally, pretreated supports were dipped in the immobilisation solution 4 times in a row and then dried at 70°C for 30 minutes. After an additional week of immobilised photocatalysts' drying at room temperature, the procedure was completed.

Characterization was performed by using: scanning electron microscopy (FEG SEM Quanta 250 FEI microscope), Raman spectroscopy (HORIBA Jobin Yvone T64000 spectrometer with a 532.5 nm, solid-state laser excitation) and diffuse reflectance spectroscopy (DRS, Perkin-Elmer Lambda 35). Additional information were described in more detail in the previously published paper [49].

5.1.2 Irradiation sources

A custom-made panel with three full spectra lamps (JBL, Neuhofen, Germany, Solar Ultra linear fluorescent lamps: Color, Tropic and Nature, T5, 145 cm, nominal power 80 W) and corresponding reflective mirrors (JBL, Neuhofen, Germany, Solar Reflect 146) was used as the first light source in the set of experiments (Figure 9). Photometrical data of the lamps provided by the manufacturer are given in Table 13.

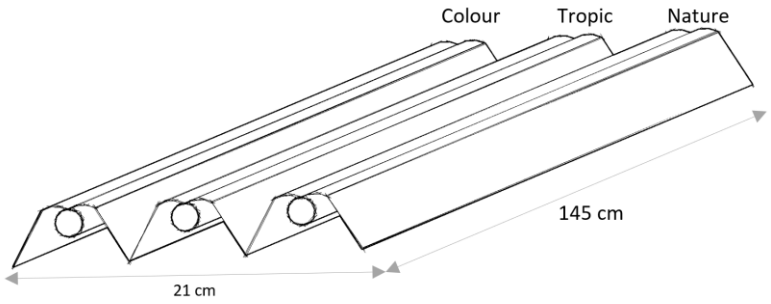


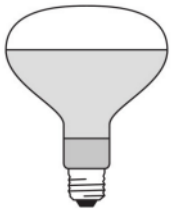
Figure 9. A scheme of the custom-made panel with three full spectra lamps and corresponding reflective mirrors

Table 13. Photometrical data of the first irradiation source - ultra linear fluorescent lamps

Type of ultra-linear fluorescent lamp	Lumen	Colour temperature
Colour	2450	Not known
Tropic	3900	4000 K
Nature	5000	9000 K

Compact fluorescent lamps (Ultra vitalux UV-A 300W, E 27) with UV-A and UV-B spectra were used in the set of experiments as a second light source. Technical data provided by the manufacturer are shown in Table 14.

Table 14. Technical data of the second irradiation source - compact fluorescent lamp

	Property	Value
	Radiated power 315…400 nm (UVA)	13.6 W
	Radiated power 280…315 nm (UVB)	3 W
	Beam angle	30°
	Dimensions & weight	D = 127 mm L = 185 mm

5.1.3 Reactors setup

Two types of reactor setups, a flat plate cascade reactor (FPCR) and a compound parabolic collector (CPC) reactor, were studied in the research. The model solution was continuously recirculated in both setups by a peristaltic pump Rotarus Smart 30 under constant laminar flow. The reactors were set up horizontally concerning the irradiation source at a 10 cm distance.

The FPCR setup consisted of three cascades (50 × 25 ×4 cm) made from resistant polycarbonate material. The height distance between cascades was 50 cm. The experimental setup (Figure 10) also included a sampling tank, peristaltic pump, and irradiation source. The custom-made panel with three full spectra lamps is shown as an irradiation source on the scheme.

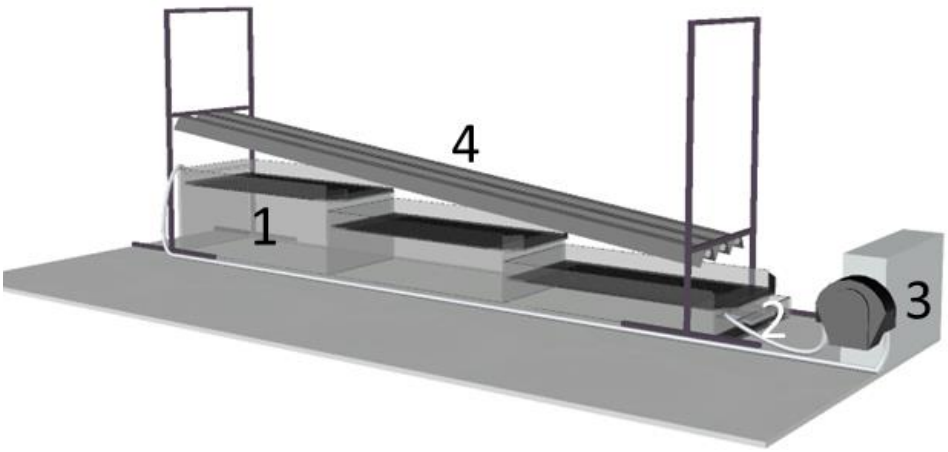


Figure 10. Scheme of the experimental setup for the FPCR reactor (1-reactor with a photocatalyst, 2-sampling tank, 3-peristaltic pump, and 4-irradiation source, custom-made panel).

The CPC reactor (Figure 11) setup consisted of two parallel quartz tubes (L = 50 cm, D_{outer} = 3 cm, D_{inner} = 2.7 cm) connected with a PTFE U-tube of the same inner dimension to avoid changes in flow rates. Each quartz tube was placed in a compound parabolic mirror of highly reflective alumina (JBL, Neuhofen, Germany, Solar Reflect 50).

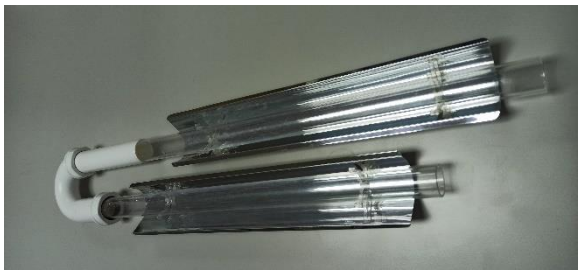


Figure 11. The setup for the CPC reactor (2 quartz tubes connected with a PTFE U-tube placed in a compound parabolic mirror)

The experimental setup consisted of the CPC reactor, sampling tank placed on a magnetic stirrer, peristaltic pump, and irradiation source. A schematic and lab experimental setups are given in Figure 12. The custom-made panel with three full spectra lamps is shown as an irradiation source.

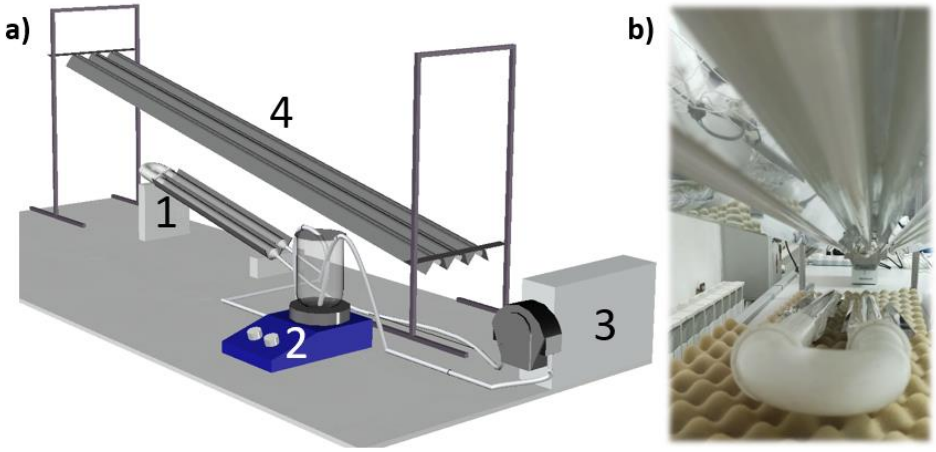


Figure 12. Representation of the scheme a) and lab b) experimental setups for the CPC reactor. The scheme numbers represent 1-CPC reactor with a photocatalyst, 2-sampling tank & magnetic stirrer, 3-peristaltic pump, and 4-irradiation source (custom-made panel).

In Figure 13, both reactors with compact fluorescent lamps as irradiation sources are shown. Each cascade was irradiated with one, while the CPC reactor was irradiated with two compact fluorescent lamps.

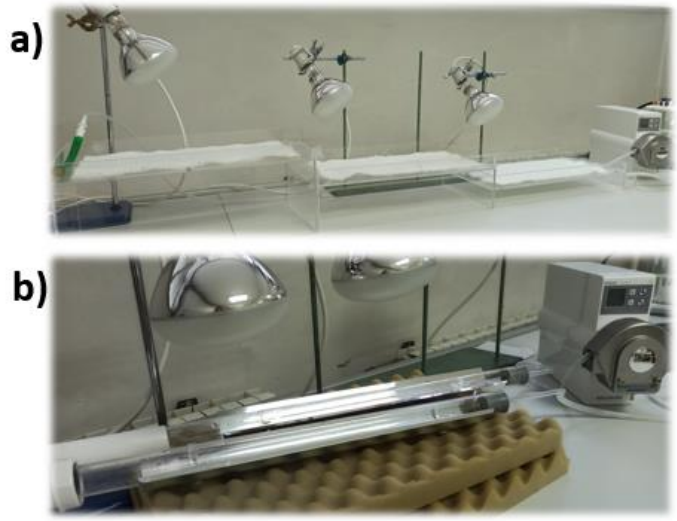


Figure 13. Experimental setups of a) the FPCR and b) the CPC reactor with compact fluorescent lamps as the irradiation source

5.2 Experiments setup

Each experiment started with recirculating the model solution for 30 minutes without irradiation to achieve sorption equilibrium (marked with a time interval of -30 min). Afterwards, the experiments were conducted under irradiation for 240 minutes. Samples were continuously collected during the experiments in defined time intervals (-30, 0, 15, 30, 45, 60, 90, 120, 150, 180, 210 and 240 minutes) and were stored in vials (2 ml). Before storing, each sample was filtered (0.22 μm, Chromafill) due to the requirements of the analytical method.

The same methodological approach was applied in all experiments. An overview of the planned experiments in correlation with the varied intensification approaches can be seen in Table 15. Determination of the photolytic 1H-BT degradation was analysed as the reference measurement. All experiments were conducted in triplets, and average values were reported.

Table 15. Overview of the planned experiments

No.	**Photocatalysts**	**Irradiation**	**Reactor**	**Type and purpose of the measurement**	
1	/	Sources 1…n	FPCR	Photolysis	Determination of the photolytic degradation in 240 minutes. Represent reference measurement.
2					
3			CPC		
4					
5	TiO_2	Sources 1…n	FPCR	Photocatalysis	Determination of the photocatalytic degradation in 240 minutes. Determination of decrease in initial 1H-BT concentrations and an increase/decrease of 1H-BT degradation products.
6					
7			CPC		
8					
9	TiO_2/CNT	Sources 1…n	FPCR		
10					
11			CPC		
12					

5.3 Analytical methods

The decrease of 1H-BT concentration was determined by UV/vis spectrophotometry (Avantes AvaLight-DH-S-Bal spectrometer, Lafayette, USA).

The degradation products of 1H-BT were determined by hybrid quadrupole time-of-flight mass spectrometry coupled with liquid chromatography system (Q-TOF LC/MS) (Agilent 6530 C Accurate Mass Q-TOF LC/MS System with LC system Agilent 1260 Infinity II, Santa Clara, California, USA) as well as their respective concentrations.

5.3.1 UV/vis spectrophotometry

Ultraviolet-visible (UV/vis) spectrophotometry has been a widely used technique for quantifying and identifying compounds. It is relatively easy to use, cost-effective and fast. Therefore, it is a good starting point for quick-checking experiments [178,179].

5.3.1.1 Working principle

The working principle is based on the molecule's absorption of UV/vis light. Wavelength is usually expressed in nanometres with a UV range from 100 to 400 nm and a visible range from approximately 400 to 800 nm. A light of a known wavelength and intensity is directed through the sample. After passing through, the final intensity is measured by a detector. By comparing the incident irradiation (I_0) and the transmitted irradiation (I), the amount of light absorbed by the sample at that particular wavelength can be easily calculated. According to Beer-Lambert law (35), the absorption can be written as follows:

$$A = \log_{10}(I_0/I) = \epsilon c L \qquad (35)$$

where A is absorbance, ε is the molar absorptivity (L/mol·cm), c is the concentration of the dissolved compound (mol/L), and L is the path length (cm). Different compound concentrations can be determined when a calibration curve of the interest compound is set up [179].

5.3.1.2 Method setup

Therefore, concentrations of 1H-BT were determined by UV/vis spectrophotometer (Figure 14) at the maximum wavelength (λ_{max}) 256 nm (Figure 15) according to the literature [157,180].

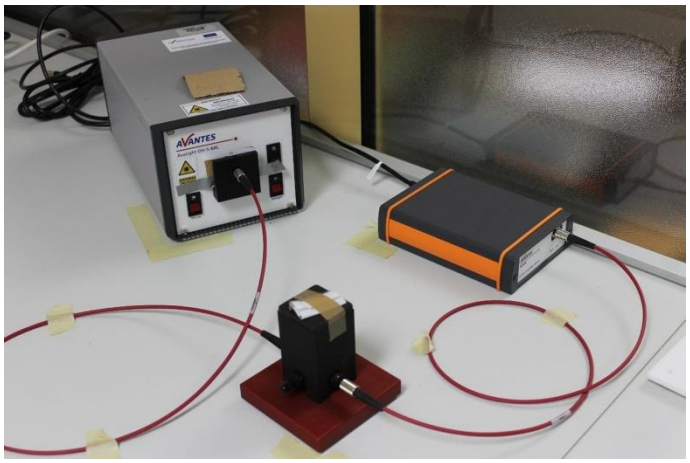


Figure 14. UV/vis spectrophotometer (Avantes AvaLight-DH-S-Balspectrometer)

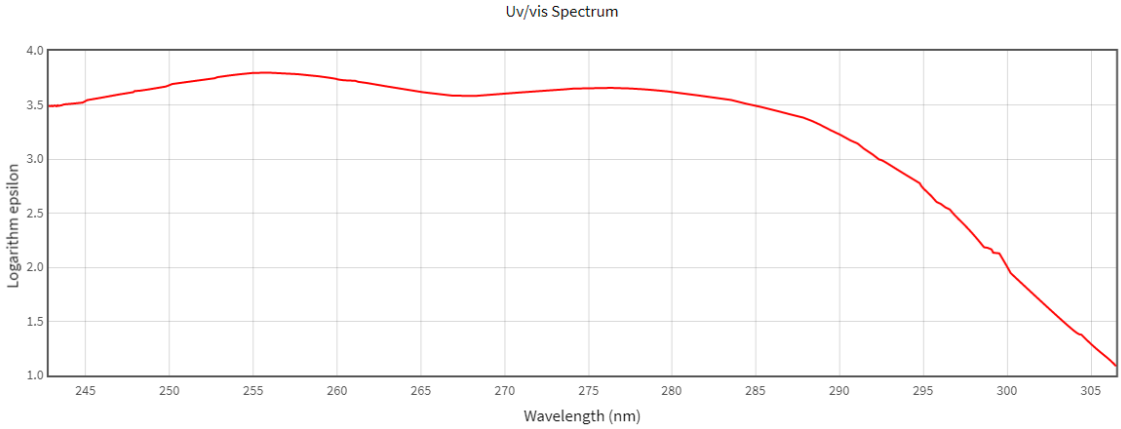


Figure 15. UV/vis spectra of the 1H-BT with a maximum peak at 256 nm [181]

To determine 1H-BT concentrations, the calibration curve (Figure 16.a) was developed with 5 points (0.01, 0.05, 0.5, 1.5, 2.5 and 3.5 ppm) for the lowest 1H-BT concentration of interest (C_0=3.5 ppm) (Figure 16.b) and additional 5 points calibration with the highest 1H-BT concentration of interest (C_0=10 ppm). Concentrations were calculated according to equation (35) and expressed in an appropriate unit. Open-source SpectraGryph 1.2.15 and MS Office Excel 365 were used for the calculations.

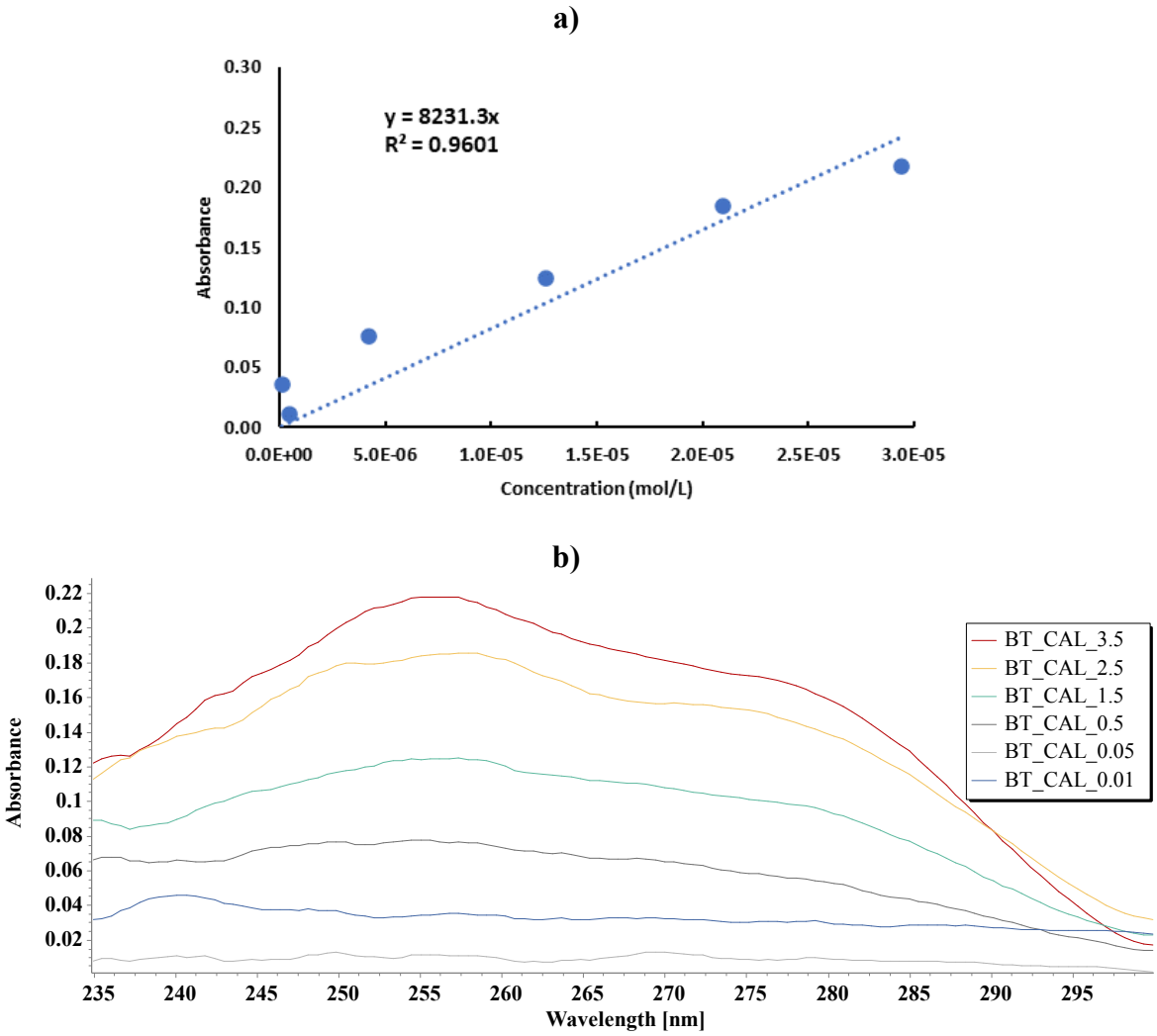


Figure 16. Determination of 1H-BT calibration curve a) based on the UV-vis spectrogram b) with five points

5.3.2 Quadrupole time of flight mass spectrometry coupled with liquid chromatography system (Q-TOF LC/MS)

A new window of opportunity for the detection of polar organic contaminants has opened with the evolution of high-accuracy mass spectrometry with high resolution coupled with liquid chromatography [182], such as hybrid Q-TOF LC/MS.

Detection of known and unknown compounds in the same sample has become possible. Data processing is usually done by one of the three approaches: target analysis, suspect screening, and non-target screening. While reference standard is necessary for the target analysis, that is not true with suspect screening. Instead, it can be performed based on available information, mainly accurate mass, precursor ion and isotope information which can be calculated from the molecular formula of the compound of interest. On the other hand, non-target screening is performed when no reference standard or information is known [182,183]. Nowadays, combining approaches such as target and suspect screening are commonly used due to economic and time-saving points of view [183].

Furthermore, more precise detection of degradation products and proposals of reaction's mechanism pathways has become possible. A couple of approach options are used for that purpose. First, the assumption of not having a degradation product in blank or zero samples is common for all approaches. Afterwards, either a non-target screening with a combination of MS and MS/MS data is used, or a combination of target and suspect screening can be used [165].

5.3.2.1 Working principles

Liquid chromatography in tandem with mass spectrometry (LC/MS) is a powerful analytical technique that combines liquid chromatography's resolving power with the detection specificity of mass spectrometry. While liquid chromatography separates sample components, a mass spectrometer creates and detects charged ions. Therefore, LC/MS data can be used for information gathering about the molecular weight, structure, identity and quantity of specific sample components [184].

Improving analytical performances, mainly selectivity and sensitivity of mass spectrometry, is achieved by performing tandem mass spectrometry (MS/MS) by using two mass spectrometers, quadrupole and time-of-flight (Q-TOF). The precursor ions are selected by quadrupole based

on m/z ratios, which are further fragmented in the collision cell (hexapole) into product ions and detected by time-of-flight (TOF). The TOF principle involves the separation of ions based on the time necessary for the ions to travel through a flight tube with a known length and reach the detector. While ions with lower m/z travel faster, ions with larger m/z ratio travel slower. Agilent 6530 Q-TOF LC/MS (Figure 17) is an example of such a device [185].

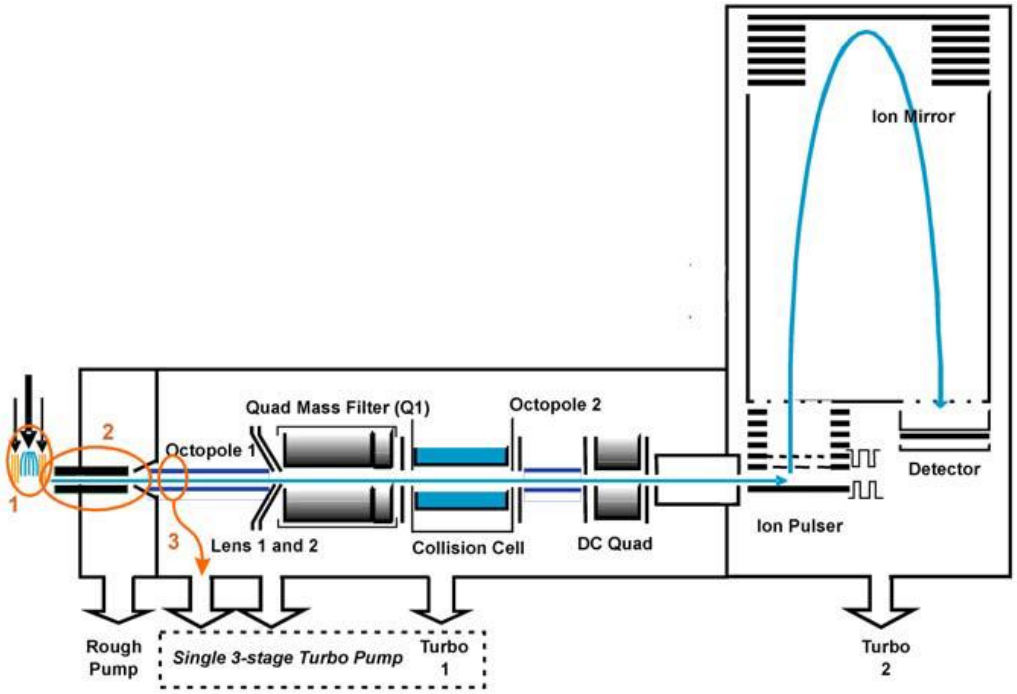


Figure 17. Scheme of Agilent 6530 Q-TOF LC/MS [185]

Ions are generated by electrospray ionization (ESI), where the analyte is simultaneously ionized and desolvated from the liquid matrix (Figure 18). The principle of ESI includes the formation of ions, nebulization, desolvation and ion evaporation. Depending on the analyte and solvent chemistry, ions can be generated prior to nebulization. However, if that is not the case, a strong electric charge on the surface of the spray droplets can induce necessary ionization during other steps. During the aerosol generation or nebulization, the sample solution enters the spray chamber through a nebuliser needle. In contrast, nebulizing gas enters the spray chamber concentrically through a tube that surrounds the needle. The combination of strong shear forces generated by the nebulizing gas and the strong voltage (2–6 kV) in the spray chamber draws out the sample solution and breaks it into droplets. With droplet dispersion, ions of one polarity preferentially migrate to the droplet surface due to electrostatic forces. As a result, the sample is simultaneously charged and dispersed into a fine spray of charged droplets. Because the sample solution is not heated when the aerosol is created, ESI does not thermally decompose analytes. Before the ions can be mass analysed, the solvent is removed by nitrogen in the form

of heated drying gas. Evaporation of solvent decreases the droplet diameter. When the force of the Coulomb repulsion equals that of the droplet's surface tension, the droplet explodes, producing smaller charged droplets subject to further evaporation. This process repeats itself, and droplets with a high density of surface charges are formed. These ions are attracted to and pass through a capillary sampling orifice into the ion optics and mass analyser [185].

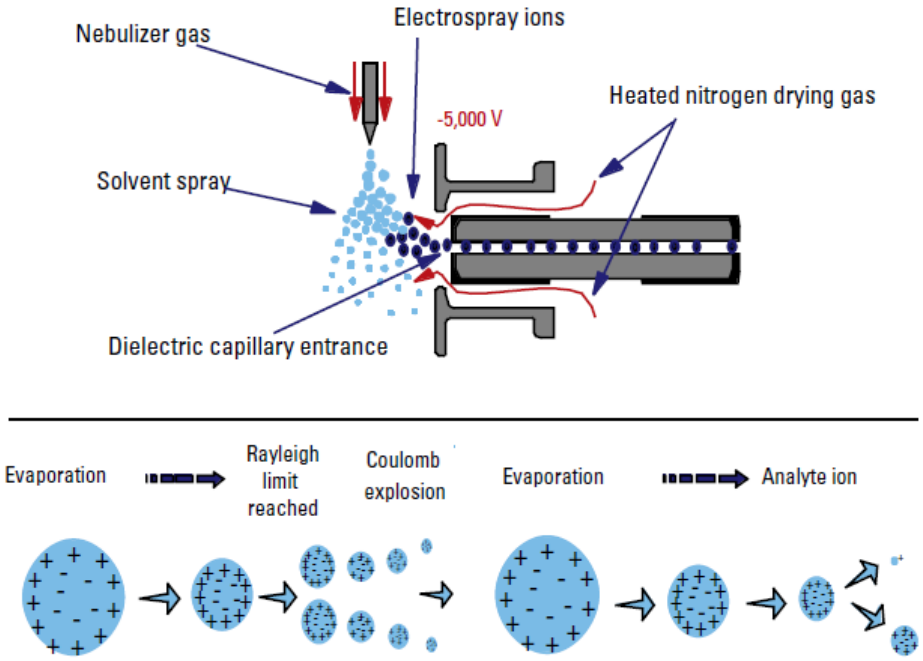


Figure 18. The scheme of API-ESI [184]

Before each analysis, Q-TOF needs to be calibrated and tuned. While calibration is assigning accurate masses based on the known masses of standard compounds, tuning is the process of quadrupole adjusting [185].

5.3.2.2 Method setup

Prior to each analysis, LC column C-18 (Poroshell 120 EC-C18, 3.0 x 100 mm, 2.7 µm, Agilent Technologies, Santa Clara, USA) was equilibrated with the intended solvent. The given was made by running a sample method without sample injection. Also, the method's duration was slightly longer to achieve equilibration after each sample run. After finishing the worklist for the day, the column was conditioned. During the sample run, the column was heated to 30°C. Then, a gradient was set up with two mobile phases, ultrapure H_2O and MeOH, with the addition of 0.1 % FA. The gradient duration was 20 minutes, where elution of 99 % MeOH and 1 % H_2O was achieved continuously for up to 8^{th} minutes, and the ratio was maintained for up to 12^{th} minutes. Immediately after, at 12:01 and up to 20 minutes, a ratio of up to 1 % MeOH

and 99 % H_2O was achieved. During the method, the flow rate was 0.4 mL/min. BT was determined at 8 ±1.5 min in positive mode with a fragmentation energy of 175 V.

During the analysis, ion source parameters for Dual AJS ESI were: gas temperature 250°C, drying gas 11 L/min, nebulizer 35 psig, sheet gas temperature 350°C and sheet gas flow 11 L/min. In addition, the voltage capillary was set to 3500 V, the nozzle voltage was to 1000 V and the fragmentor voltage was set to 175 V.

A standard tune solution was used for the tunning, while for the mass calibration, the following masses were chosen 112.050873 and 922.009758.

All samples were scanned in positive MS mode. A combination of target and suspect screening was used to detect 1H-BT concentrations and degradation products.

5.3.3 Irradiance measurements

The UV intensities were determined at the photocatalysts' surface by UVX radiometer (Figure 19.a, UVP Products, Analytik Jena US LLC, Upland, CA) fitted with corresponding longwave UV-A UVX-36 (range 335-385 nm), midrange UV-B UVX-31 (range 280-340 nm) and shortwave UV-C UVX-25 (range 210-280 nm) sensors (Figure 19.b) of ± 5 % accuracy. The total irradiance was measured by the Solarimeter HT204 (Figure 19.c).

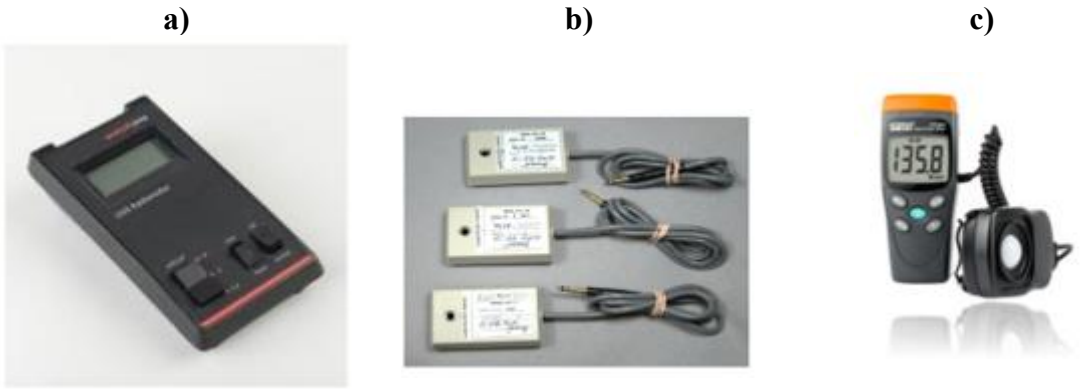


Figure 19. Devices for the irradiation measurements; a) UVX radiometer with b) sensors and c) Solarimeter HT204

5.4 Kinetic model developments and reactor mass balance

The basic equation for the rate of a chemical reaction is written as follows:

$$r = -k[X]^n \tag{36}$$

where r is the chemical reaction rate, k is the approximate rate constant of a chemical reaction and $[X]$ is the concentration of pollutant, while n is reaction order.

The equation (36) was modified by introducing intrinsic parameters related to the photocatalytic degradation of pollutants; the absorption coefficient of the photocatalyst TiO_2 μ (m^{-1}) and incident irradiation $I_0(Z,W)$ (Wm^2), respectively. Thereby, m represents the order of the reaction depending on the absorption of radiation, which in conditions of good illumination is 0.5.

$$r_i = -k_i(\mu I_0(\mathrm{Z,W}))^{\mathrm{m}}[\mathrm{X_i}]^{\mathrm{n}} \tag{37}$$

When the term k is replaced with $k_i(\mu I_0(T,H))^m$ in equation (37), the approximate rate constant of a chemical reaction k, becomes independent of the conditions of irradiation and the used photocatalyst, i.e. the intrinsic degradation rate constant k_i of pollutant (i). Since the experiments were conducted in conditions with a certain proportion of UVA and UVB radiation, the intrinsic parameters were additionally listed as follows:

$$r_i = -k_i\left(\left(\mu I_0(Z,W)\right)_{UVB} + \left(\mu I_0(Z,W)\right)_{UVA}\right)^m [X]^n \tag{38}$$

The intensification of the pollutant degradation process due to the modification of the TiO_2 photocatalyst with CNT was quantified by introducing the index Y_{cat} into the equation (38):

$$r_i = -k_i Y_{cat}\left(\left(\mu I_0(Z,W)\right)_{UVB} + \left(\mu I_0(Z,W)\right)_{UVA}\right)^m [X]^n \tag{39}$$

The specified index Y_{cat} can be used to determine the improvement of the activity of the modified TiO_2 photocatalyst with CNT in the UV and visible radiation spectrum.

The impact of different reactor designs on the intensification of the pollutant degradation process was quantified by introducing the Y_{RD} index into equation (38):

$$r_i = -k_i\left(Y_{RD}\left(\left(\mu I_0(Z,W)\right)_{UVB} + \left(\mu I_0(Z,W)\right)_{UVA}\right)\right)^m [X_i]^n \tag{40}$$

where Y_{RD} is introduced as an additional intrinsic parameter. Since the dissertation investigates the degradation of pollutants using CPC and FPCR reactors, Y_{RD} can be written as:

$$Y_{RD} = \frac{I_0(CPC)}{I_0(FPCR)} = \frac{I_0 + I_{ref}}{I_0} = 1 + \psi^g \quad (41)$$

From the aspect of the reactor's illumination, the design of the CPC reactor is more optimal than FPCR. That is, the total incident radiation in the CPC reactor, in addition to the incident radiation inside the reactor, also consists of the reflected radiation in the reaction space (due to the parabolic mirrors), while in the FPCR, the total incident radiation is equal to the incident radiation inside the reactor. Here, Y_{RD} is determined by semi-empirical models, but it is possible to determine it by different ray optics models if the reflectivity of the material (ψ) and the total number of rays (g) inside the reactor are known values.

Furthermore, considering that the experiments in CPC and FPCR were set up as flow reactors with recirculation, equations (38),(39) and (40) were combined with the corresponding material balance equation. Since during the experiment, the output flow from the reactor is mixed with the reaction mixture in the recirculation tank, and this leads to different input concentrations at different reaction times, the following equation was used:

$$V_{tank} \frac{d[X_i]_{tank}^{out}}{dt} = Q\left([X_i]_{tank}^{in} - [X_i]_{tank}^{out}\right) \quad (42)$$

in combination with equation (43) for the CPC reactor or equation (44) for the FPCR reactor.

$$v\frac{d[X_i]}{dZ} = r_i(Z,t) \quad (43)$$

$$v\frac{d[X_i]}{dZ} = r_i(Z, W, t) \quad (44)$$

The numerical simulation was performed in such a way that the reaction space was divided into small intervals ΔZ. A very small-time increment (Δt) equal to the space-time of the reactor ($\tau = V_R/Q$)) was introduced. The material balance in the reactor was solved at the time *t*. The simulations were carried out in the Excel program interface.

The rate constant of the decomposition reaction k_i, ($s^{-1}w^{-0,5}m^{1,5}$) was determined by trial and error by fitting the experimental values to the minimum variance model.

5.5 Environmental impact estimation

Protection of human health and the environment, in general, is very important, particularly concerning exposure to anthropogenic chemicals. However, considering the progress of the chemical industry, it is hard to conduct traditional ecotoxicity testing for each chemical. Testings are most often expensive, time-consuming, and reliant on a large number of animal subjects. Therefore, *in silico* approaches were developed to overcome stated challenges. Regulatory support contributed to developing tools for ecotoxicity assessments, such as Quantitative Structure-Activity Relationships (QSARs) and chemical category methods. QSARs methods are mathematical models derived from a training set of model chemicals. Different chemical and physical properties in combination with conducted *in vivo* studies with similar compounds are used for the training sets as descriptors. One of the tools based on the QSARs methodology are softwares such as the Toxicity Estimation Software Tool (T.E.S.T.) and Ecological Structure Activity Relationships (ECOSAR) Predictive Model developed by USA Environmental Protection Agency [186,187].

Therefore, environmental impact estimation, i.e., the ecotoxicological impact of the identified degradation products of 1H-BT during photocatalysis, was assessed via stated open-source tools.

5.5.1 Toxicity Estimation Software Tool (T.E.S.T.)

The Toxicity Estimation Software Tool (T.E.S.T.) enables users to quickly estimate acute aquatic toxicity of chemicals based on the QSARs methodologies and an overall pool of 797 2-dimensional descriptors [188]. In the software framework, acute aquatic toxicity values can be estimated by several QSARs methodologies: hierarchical clustering method, single model method, group contribution method, nearest neighbour method, and consensus method [189].

The following toxicity endpoints can be estimated by T.E.S.T.:

1. 96-h fathead minnow LC_{50} (concentration of the test chemical in water in mg/L that is lethal to 50 % of exposed fathead minnows after 96 hours),
2. 48-h *Daphnia magna* LC_{50} (concentration of the test chemical in water in mg/L that is lethal to 50 % of exposed *Daphnia magna* after 48 hours),
3. 48-h *Tetrahymena pyriformis* IGC_{50} (concentration of the test chemical in water in mg/L that results in 50 % growth inhibition to *Tetrahymena pyriformis* after 48 hours),

4. Oral rat LD_{50} (amount of chemical in mg/kg body weight that is lethal to 50 % of rats after oral ingestion),
5. Bioaccumulation factor (ratio of the chemical concentration in fish to that in water at a steady state),
6. Developmental toxicity (binary indication of whether or not a chemical can interfere with 24 normal developments of humans or animals),
7. Ames mutagenicity (a compound is positive for mutagenicity if it induces revertant colony growth in any strain of *Salmonella typhimurium*) [188].

The consensus method was used in this dissertation since predicted toxicity is estimated by taking an average of all possible predicted toxicities from the other QSAR methods. Four endpoints were discussed, oral rat $LD_{50,}$ bioaccumulation factor, developmental toxicity, and ames mutagenicity.

5.5.2 Ecological Structure Activity Relationships (ECOSAR)

The Ecological Structure Activity Relationships (ECOSAR) Class Program is another predictive system for aquatic toxicity estimation. In the program framework, a chemical's acute (short-term) and chronic (long-term or delayed) toxicity on fish, aquatic invertebrates, and aquatic plants can be estimated by using Structure-Activity Relationships (SARs). Database for the SARs is built from publicly available data, such as the ECOTOX database, which comprises of 130 structural classes [186,187].

5.6 Life cycle assessment (LCA)

According to ISO 14040, life cycle assessment (LCA) is defined as the "compilation and evaluation of the inputs, outputs and potential environmental impacts of a product system throughout its life cycle" [190]. Therefore, due to its quantitative character, LCA represents a powerful tool for comprehensively and systematically analysing a product's environmental burdens during the different stages of its lifespan [191,192]. Apart from product assessment, individual processes or services can be a subject of LCA. The oldest and most common approach is cradle-to-grave, which includes processes from raw material extraction towards end-of-life. However, in the meantime, depending on the LCA usage, variations in the approach were developed.

Due to its quantitative approach, LCA is suitable for assessing chemical processes' environmental impact. It considers energetic and engineering aspects, while the other methods are more oriented towards chemical characteristics [193]. Mainly is applied as comparative LCA when different AOPs are discussed. It is applicable to the energy scenario developing, especially when considering artificial lamps and natural Sun usage [194]. Moreover, LCA helps provide knowledge about the hotspots, i.e., the pros and cons from the environmental point of view of different AOPs. For example, removal of 1 μg of 17α-ethinylestradiol from the total environmental impact point of view, the most suitable AOPs are in the following order solar photolysis>UV-A>UV-C>solar/Fe>UV-A/TiO_2>UV-C/H_2O_2>solar Fe/H_2O_2 [191].

Beside, LCA was recognized as a powerful tool for the environmental performance assessment of nano products and their toxicological impact [192,195].

The LCA methodology includes four phases: defining (1) goal and scope, where main intention, hypothesis and data source are defined; (2) inventory analysis or data collection; (3) impact assessment, where potential environmental impacts are identified and characterized and (4) interpretation of the results [194].

6 RESULTS AND DISCUSSION

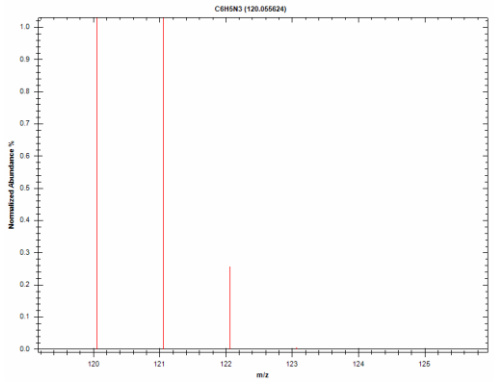
6.1 High-resolution analysis of 1H-BT and its degradation products

6.1.1 Identification and calibration of 1H-BT

The identification of compounds by high-resolution analysis (Q-TOF LC/MS) was performed according to the knowledge of ion fragmentation distribution and analysis mode. Therefore, the 1H-BT ion fragmentation distribution in positive mode was calculated using the Isotope Distribution Calculator (Agilent MassHunter Workstation Data Analysis Core 10.1). Results are shown in Table 16. For identification by manufacturer's software Agilent Qualitative Analysis 10.1, the first two ions were used, the precursor ion m/z=120.0556 and the fragment ion m/z= 121.0581.

Table 16. Mass spectra of 1H-BT with ion distributions in positive mode obtained by Isotope Distribution Calculator

m/z	Abundance (% largest)	Abundance (% sum)
120.0556	100	92.67
121.0581	7.65	7.09
122.0604	0.26	0.24



Furthermore, for 1H-BT quantification, calibration with five points (10, 8, 6, 4 and 2 ppm) was performed (Annex 1). The obtained calibration curve is shown in Figure 20. Data were processed by the software Agilent MassHunter Quantitative Analysis 10.1., as well as 1H-BT concentration determination in the samples (Annex 2 - Annex 5).

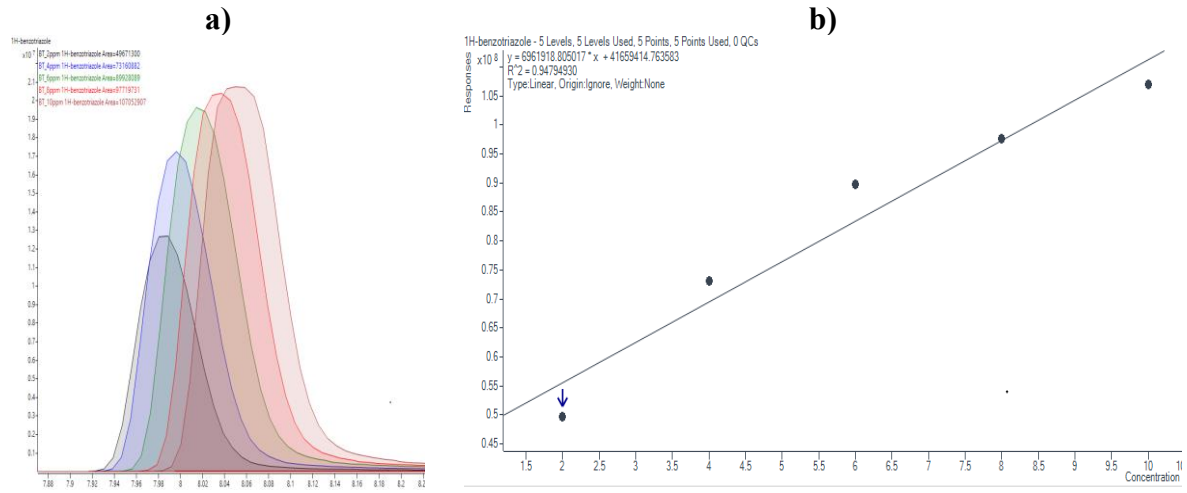


Figure 20. Chromatographs with extracted peaks of 1H-BT (a) and associated calibration curve with five points (10, 8, 6, 4 and 2 ppm) (b)

6.1.2 Mechanisms and reaction pathways of 1H-BT photocatalytic degradation

A detailed study of reaction mechanisms and pathways has developed following the evolution of high mass resolution, full-scan sensitivity and mass accuracy, such as hybrid Q-TOF systems [196]. As a result, identifying a wide range of possible reaction pathways, such as oxidation, alkylation, and hydroxylation, was enabled. For instance, during the conventional wastewater treatment by activated sludge, 4-MeBT and 5-MeBT, as well as 4- and 5-OHBT, were identified as degradation products [197]. Similar was observed in the study [198], where two isomers of hydroxy and methoxy 1H-BT were identified after biological treatment of 1H-BT.

In nature, 1H-BT is subjected to photolysis according to pseudo-first-order reaction, especially in surface waters due to reaction with reactive transient species [102,104,199]. While 36 degradation products were identified after photolysis of 6 common BTs under UV/vis light [104], 7 degradation products were identified under UV-C light [199]. The central role in degradation plays hydroxylation either of a benzene ring or triazole ring. It was reported more toxic compounds could be formed if there is no mineralization [101], even with a high rate of mineralization (>80 %) [199]. Thereby, aside from other reactive species, irradiation intensity also impacts the toxicity of formed degradation products [102].

Meanwhile, AOPs have been recognized as promising methods for 1H-BT removal. Apart from the detection of concentration decrease, recent studies have been on 1H-BT degradation product identification. The decomposition of 1H-BT was monitored in a laboratory-prepared wetland

with artificial solar irradiation in dispersed TiO_2 (anatase) presence. As a result, the main degradation products of 1H-BT were identified as hydroxylated derivatives [200].

Furthermore, applying the UV/chlorination process indicated the promotion of 1H-BT removal by ●OH radicals. At the same time, 10 degradation products were detected after chlorination [165], while 6 degradation products were detected after UV-C/chlorination [166], and 5 degradation products were detected after UV-A/chlorination [103]. The first pathway route resulted from hydroxylation and benzene ring cleavage. Then, another route resulted from chlorination, during which hydrogen atoms on the benzene ring were substituted with chlorine atoms. However, ecotoxicity tests have revealed high toxicity due to forming intermediates with chlorine [165,166]. The aforementioned emphasizes the problem of 1H-BT detection in underground water since water is captured and processed by chlorination for residential use.

On the other hand, decreased toxicity was observed when the UV-A/chlorination process was applied since degradation was more influenced by ●OH radicals than ●Cl [103]. Opposite reports indicate that the presence of UV-A light in the chlorination process enhances degradation toward less harmful products. In contrast, chlorination itself and the synergy of UV-C light and chlorination contribute to the formation of more toxic degradation products. Similar differences in degradation pathways of 1H-BT under UV-A and UV-C light were observed during photolysis [102].

Meanwhile, degradation of 1H-BT by ozonolysis involves the electrophilic addition of O_3 on the benzene ring, followed by further cleavage in the first pathway [162,163]. The second pathway includes hydroxylation of the benzene ring, which can continue by benzene ring cleavage or toward the third pathway of triazole opening [162].

Moreover, two degradation pathways were proposed when the photo-Fenton process was used for the degradation of 1H-BT in the batch system under visible light with the aid of α-Fe_2O_3/Bi_2S_3 and graphene. The first involved cleaning the triazole ring due to a reaction with h^+ followed by a reaction with •OH and benzene ring cleavage, while the second hydroxylation of the benzene ring and its opening, as well as triazole opening, forming intermediates with two amino and carbonyl groups [172].

Improved photocatalytic degradation of 1H-BT was observed by photocatalysis with BiOBr under UV/vis light in comparison with TiO_2 P25. Four main degradation products were identified, and three possible pathways were suggested. The first one followed reports

[172,201] where triazole ring opening was initiated by h^+ and followed by N_2 releasement. However, according to the other two pathways, identified degradation products were formed by intermediate coupling comprising degradation products with two benzene rings and amine groups, suggesting further degradation towards H_2O, CO_2 and NH_4^+ [173]. A similar mechanism pathway was proposed in [202]. The degradation of 1H-BT by $BiSnSbO_6$ in the batch system under visible light was analysed. However, triazole opening was triggered by a combination of h^+ and $\bullet O_2^-$. A higher impact of $\bullet O_2^-$ in 1H-BT degradation was reported due to the photocatalyst mechanism. 1H-BT was excited by visible light irradiation, which enhanced its adsorption onto the photocatalyst. The transfer of e^- onto the conduction band enabled the reduction of O_2.

In another study [177], degradation products of 1H-BT were reported. $Gd_2YSbO_7/ZnBiNbO_5$ was used in the batch system under visible light as a photocatalyst. Overall, 9 degradation products were formed by oxidation and methylation reactions of the triazole ring, breaking down 1H-BT towards smaller molecules that react with other organic groups up towards CO_2 and H_2O.

Likewise, in a batch system with TiO_2 P25 under UV-C light, 8 degradation products were identified with main reaction pathways, which included a series of additions, substitutions, and cleavages of the phenyl structure induced by hydroxyl radicals. The detected loss of nitrogen in mass balance was attributed to the formation of molecular nitrogen. Also, a lower mineralization rate was attributed to the volatilization of intermediate HCHO before its mineralization into HCOOH or CO_2 [157]. A Similar was observed in the study [101] of 1H-BT degradation products with TiO_2 in suspension under UV-A light. Hydroxylation of the aromatic ring with preferential 5 and 7 C positions as the most active sites was observed in acidic conditions (pH 3). Thus, the first step of degradation involved triazole ring opening. Eventually, most degradation products were mineralized to H_2O, CO_2, and NH_3. Lower photocatalytic degradation at pH 6 was observed and associated with the aggregation of photocatalyst particles [101]. At pH 7 highest degradation efficiency of 1H-BT was observed [157]. The importance of the irradiation source in the reaction mechanism and the benefit of the photocatalyst's immobilisation to avoid agglomeration was reported. Furthermore, both studies [101,157] have proposed hydroxyl radicals as promising for the rapid removal of 1H-BT without the formation of toxic degradation products, despite incomplete mineralisation.

The following scheme presents an overview of proposed reaction mechanisms discussed in described literature in Figure 21. For listed degradation products, with the aid of the Isotope Distribution Calculator software, ion fragmentation distribution in positive mode was calculated (Annex 6). The above was used to extract degradation products' ion chromatographs (EIC). Further, the presence of a compound was verified by the MS spectrum, which allowed an approximation of concentrations. For identified degradation products, EIC and MS spectra can be found in supplement materials (Table 17). Finally, sufficient concentrations of degradation product for detection were covered by analysing samples with $[1H\text{-}BT]_0$=10 ppm.

Table 17. An overview of supplement materials regarding the identification of degradation products

	FPCR_TiO_2	**FPCR_TiO_2/CNT**	**CPC_ TiO_2**	**CPC_ TiO_2/CNT**
EIC	Annex 7	Annex 12	Annex 17	Annex 22
	Annex 8	Annex 13	Annex 18	Annex 23
	Annex 9	Annex 14	Annex 19	Annex 24
	Annex 10	Annex 15	Annex 20	Annex 25
MS	Annex 11	Annex 16	Annex 21	Annex 26

Furthermore, during the experiments conducted with different irradiation setups, namely compact fluorescent lamps, heat generation was observed, which caused visible water evaporation in the open design of FPCR, while in closed CPC reactor setup, an additional parameter affected the photocatalysis. Therefore, in further discussion, only the results of photocatalytic degradation under liner lamps were discussed.

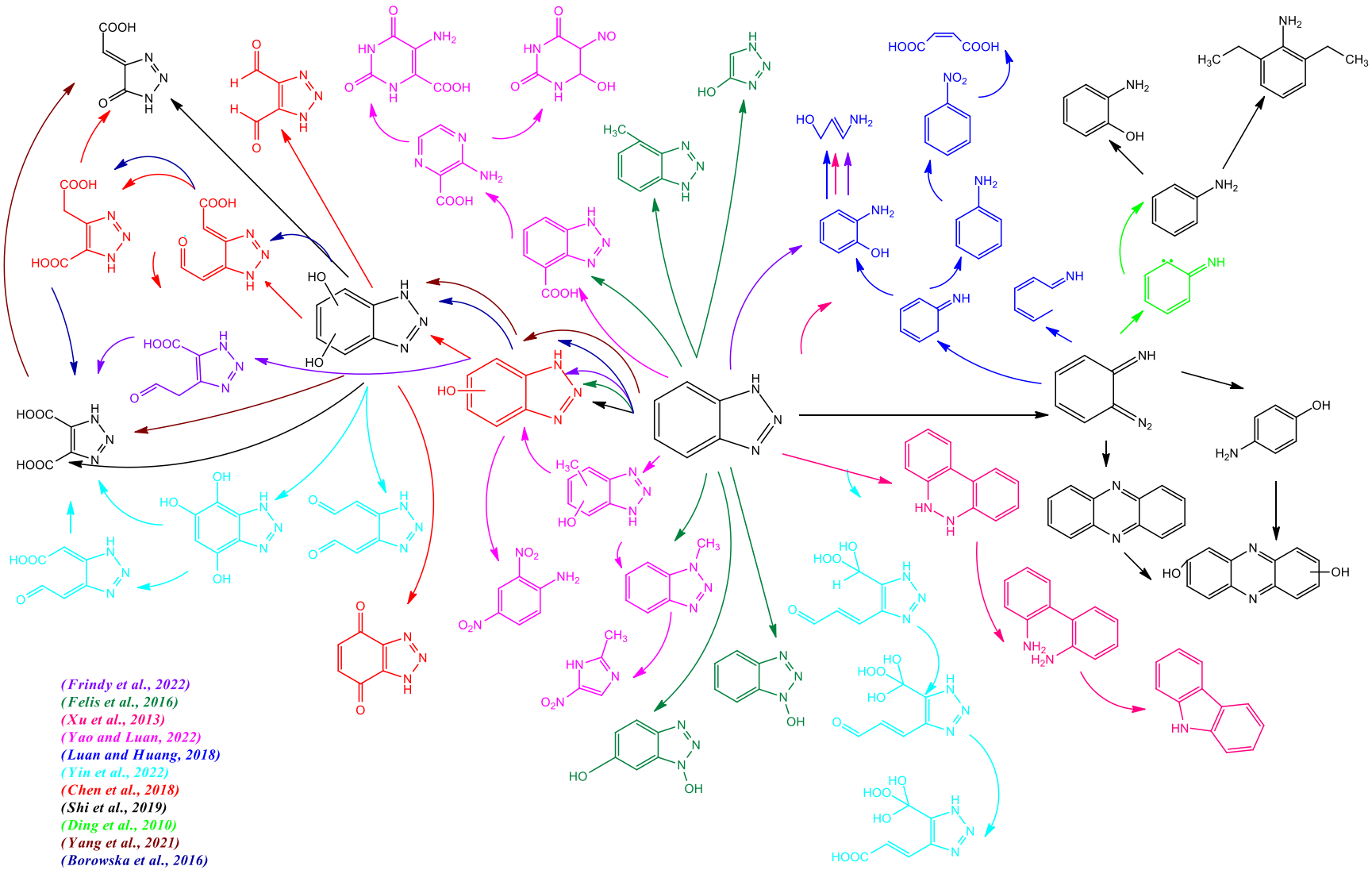


Figure 21. Overview of proposed 1H-BT degradation pathways reported in literature [102,109,157,166,172,173,177,200–203]

During the photocatalytic degradation of 1H-BT by immobilised TiO_2 and TiO_2/CNT in both reactors, FPCR and CPC, 4 degradation products m/z=136.0505, m/z=152.0455 and m/z=168.0404 were identified by EIC (with two fragment ions). Additionally, the degradation product m/z=150.0298 was identified only during the photocatalysis in FPCR, both by TiO_2 and TiO_2/CNT. Similarly, the degradation product m/z=186.0509 was identified only during the photocatalysis in the CPC reactor with both photocatalysts formulations.

However, not all reported structures listed in overviewed literature (Figure 21) were confirmed by the MS spectrum. The first degradation product $C_6H_5N_3O$ (m/z=136.0505), was confirmed during photocatalysis in FPCR (Annex 11.a, Annex 16.a), which was not the case for the CPC reactor. On the other hand, the second degradation product $C_6H_5N_3O_2$ (m/z=152.0455) was confirmed during the photocatalysis in all four instances (Annex 11.b, Annex 16.b, Annex 21.a, Annex 26.a). Moreover, the third degradation product $C_6H_5N_3O_3$ (m/z=168.0404), was not confirmed only during the photocatalysis in FPCR_TiO_2/CNT. Nevertheless, even though it was detected after photocatalysis in the FPCR and CPC with TiO_2 (Annex 11.c, Annex 21.b, Annex 26.b), the abundances were smaller than the abundance in CPC_TiO_2/CNT. Furthermore, during the photocatalysis in FPCR_TiO_2/CNT and CPC_TiO_2 degradation products $C_6H_3N_3O_2$ (m/z=150.0298), $C_6H_7N_3O_4$ (m/z=186.0509) and $C_8H_7O_4$ (m/z=168.0428) were confirmed, respectively (Annex 16.c, Annex 21.c).

Overall, 6 different m/z values of degradation products were identified, having 4 m/z values of degradation products discussed for each setup (FPCR_TiO_2, FPCR_TiO_2/CNT, CPC_TiO_2, CPC_TiO_2/CNT). An overview is shown in Table 18, Table 19, Table 20, and Table 21, respectively.

Table 18. Identified degradation products of 1H-BT during photocatalysis by FPCR_TiO_2 (degradation products confirmed by EIC – green, degradation products confirmed by MS – approximated concentration - ppm)

Time, min	$C_6H_5N_3O$ m/z=136.0505 RT:6.5 min| RT:6.7 min		$C_6H_5N_3O_2$ m/z=152.0455 RT:5.1 min| RT:5.9 min		$C_6H_5N_3O_3$ m/z=168.0404 RT:5.4 min| RT:6.3 min		$C_6H_3N_3O_2$ m/z=150.0298 RT:6.2 min
-30							
0							
15	4.15	8.24					
30	4.58	6.96	1.16				
45	8.26	8.71	0.7		3.3	1.61	
60	2.92		1.65	8.24			
90	7.84	4.99	1.38				
120	7.76			2.56			
150							
180				8.02			
210					1.36	2.95	
240							

Table 19. Identified degradation products of 1H-BT during photocatalysis by FPCR_TiO_2/CNT (degradation products confirmed by EIC – green, degradation products confirmed by MS – approximated concentration - ppm)

Time, min	$C_6H_5N_3O$ m/z=136.0505 RT:6.5 min| RT:6.7 min		$C_6H_5N_3O_2$ m/z=152.0455 RT:5.1 min| RT:5.9 min		$C_6H_5N_3O_3$ m/z=168.0404 RT:5.4 min| RT:6.3 min		$C_6H_3N_3O_2$ m/z=150.0298 RT:6.2 min
-30							
0							
15			1.64				
30		8.17	0.83				
45	0.73	7.3	1.64				
60	3.02	6.04	1.23				2.41
90	3.05	5.7	1.37	3.63			3.95
120	4.77	4.59	2.26	2.19			1.62
150	4.2	5.97	2.19	1.78			3.48
180	2.52	5.27	2.48	2.62			
305		3.69	5.23	4.19			

Table 20. Identified degradation products of 1H-BT during photocatalysis by CPC_TiO_2 (degradation products confirmed by EIC – green, degradation products confirmed by MS – approximated concentration - ppm)

Time, min	m/z=136.0505 RT:6.4, RT:6.7 min	$C_6H_5N_3O_2$ m/z=152.0455 RT:4.9 min	$C_6H_5N_3O_3$ m/z=168.0404 RT:5.1 min	$C_6H_7N_3O_4$ m/z=186.0509 RT:5.1 min
-30				
0				
15		/		
30		0.9	/	
45		2.215	9.62	
60		0.8	8.57	3.46
90		3.94	5.75	
120		3.175	8.05	
150		4.765	6.73	
180		0.835	7.675	
210		3.215	7.725	
240		0.915	6.62	

Table 21. Identified degradation products of 1H-BT during photocatalysis by CPC_TiO_2/CNT (degradation products confirmed by EIC – green, degradation products confirmed by MS – approximated concentration - ppm)

Time, min	m/z=136.0505 RT:6.6 min, RT: 6.9 min	$C_6H_5N_3O_2$ m/z=152.0455 RT:4.9 min	$C_6H_5N_3O_3$ m/z=168.0404 RT:5.1 min	$C_6H_7N_3O_4$ m/z= 186.0509 RT:5.1 min
-30				
0				
15				
30				
45			10.71	
60		5.94	10.71	
90		6.22	10.71	
120		4.47	10.71	
150		6.10	10.41	
180		7.84	10.28	
210		6.71	9.37	
240		4.52	10.49	

6.1.2.1 Degradation products of 1H-BT in FPCR

The first degradation product $C_6H_5N_3O$ (m/z=136.0505), appears after 15 minutes of photocatalysis by **FPCR_TiO$_2$**. Its occurrence was reported in the literature [102,157,166,172,200,203] as the result of the hydroxylation of the benzene ring. As can be seen in Annex 7, two dominant peaks at RT: 6.5 (**DP1a**) and RT: 6.7 min (**DP1b**) are occurring, and $C_6H_5N_3O$ was confirmed by MS spectrum. The occurrence of two $C_6H_5N_3O$ isomers, 4-OHBT and 5-OHBT, was reported as the most probable in the literature [157,197,200,203]. The first peak corresponded to 5-OHBT, and the second nearby to 4-OHBT isomer, which can be correlated with the findings in this dissertation. Even though 1-OHBT was reported as the third possible isomer [200], in another study, it was discussed it is less probable to exist, as was the case in this dissertation [157]. However, the appearance of other peaks in EIC (m/z= 136.0505, 137.053) indicated the existence of intermediates or transient species with different structures. In the interval of 30-120 minutes at RT:2.0 min, a peak with very low abundance is detected, indicating it could be a transient species. On the other hand, continuous increase of abundance can be noticed with peaks in RT:7.8-11.0 min indicating presence of degradation product with at least 4 different structures. Over the time, their abundance had increased as well as the occurrence of smaller peaks, suggesting that there were more species in the system along the photocatalysis. Moreover, the same two isomers $C_6H_5N_3O$ (RT:6.5, RT:6.7 min), **DP1a** and **DP1b**, were identified and confirmed by MS spectrum (Annex 12) during the photocatalysis by **FPCR_TiO$_2$/CNT**. As well, results of EIC (m/z= 136.0505, 137.053) indicated existence of species with different structures. The peak at RT:1.9 min with very low abundance is present throughout 305 minutes of photocatalysis. However, a lack of peaks after 7.8 minute (Annex 12) suggests that species which are formed during the photocatalysis by FPCR_TiO_2 were adsorbed due to the addition of CNT. For instance, it was reported [172] that graphene addition contributes to the adsorption of 1H-BT due to the π-π interactions, as well as contributes to the enhancement of photocatalysis due to the synergistic effect. Furthermore, multiwalled CNTs (MWCNTs) are used as a sorbent in solid-phase extraction (SPE) for pre-concentration of BTs from real water samples [204].

The second degradation product $C_6H_5N_3O_2$ (m/z=152.0455), was confirmed in both variations with reactors and photocatalysts. However, specific differences were observed. Therefore, two dominant peaks at RT:5.1 min (**DP2a**) and RT:5.9 min (**DP2b**) were identified during photocatalysis by **FPCR_TiO$_2$** (Annex 8) and **FPCR_TiO$_2$/CNT** (Annex 13). The

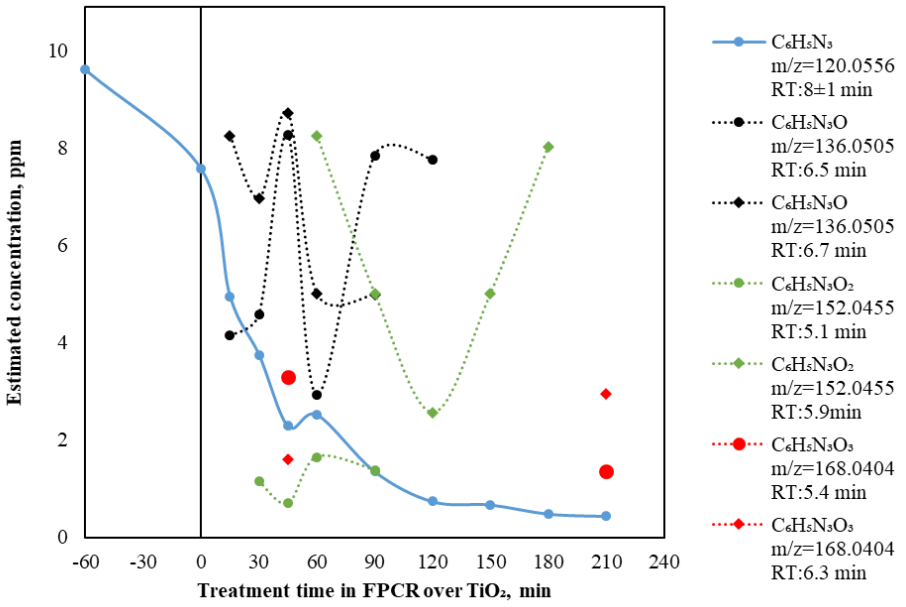
aforementioned suggests further benzene ring hydroxylation, as reported in the literature [102,109,157,166,203]. As well, a reduced number of peaks after RT:7 min (Annex 13) in the FPCR_TiO_2/CNT compared with the FPCR_TiO_2 was observed, as was the case with DP1a and DP1b, confirming adsorption onto CNT. Meanwhile, the occurrence of both DP1 and DP2 isomers later during the photocatalysis with CNT in the photocatalyst's formulation indicates that due to the adsorption of other structurally different intermediates onto CNT, formation of DP1 and DP2 was prolonged (Table 18, Table 19, Figure 22).

The third degradation product $C_6H_5N_3O_3$ (m/z= 168.0404, 169.0429), was confirmed in **FPCR_TiO_2**, while only m/z was identified in FPCR_TiO_2/CNT. The abundance of $C_6H_5N_3O_3$ (Annex 9) was sufficient for detecting two isomers (RT:5.4 min – **DP3a**, RT:6.3 min – **DP3b**) in the 45th and 210th minute of photocatalysis. At the same time, according to EIC, it was present in lower abundance. However, the same peaks were observed in FPCR_TiO2/CNT (Annex 17) in low abundances for concentration estimation based on the MS spectrum. Therefore, the mentioned was assigned to the adsorption onto CNT. In the literature, at least three structures were reported as the $C_6H_5N_3O_3$, two isomers of hydroxylated 1H-BT with three -OH groups [109,162], as well as triazole acetic [109,157] and triazole carboxylic acid [162] formed due to the benzene ring breakage. Observed DP3a and DP3b could be assigned to isomers with three -OH groups since OH radicals govern the photocatalysis when TiO_2 is used [157]. Yet, the addition of CNT contributes to the adsorption and smaller abundances in the system. What can be noticed from the peaks (EIC) is that abundance of DP3a and DP3b is slightly increasing over time in the setup with the CNT, from the 15th and 150th minutes of photocatalysis. Other peaks observed in both designs were at RT: 2.1 min and RT: 4.7 min. Thus, their abundance was emphasized in the FPCR_TiO_2/CNT compared with FPCR_TiO_2, implying the influence of CNT toward different reaction degradation pathways. Above mentioned presupposes the presence of at least two additional intermediate species or degradation products throughout the 15-305th minute of photocatalysis.

The fourth degradation product, $C_6H_3N_3O_2$ (m/z= 150.0298, 151.0323), was confirmed in **FPCR_TiO_2/CNT** (Annex 15) at RT:6.2 min (**DP4**). The peak at the same RT confirmed the existence of the same degradation product in the **FPCR_TiO_2** (Annex 10). However, the abundances were insufficient for concentration estimation based on the MS spectrum. The degradation product $C_6H_3N_3O_2$ was reported by [157,162]. According to [162], $C_6H_3N_3O_2$ is formed due to the further reaction of $C_6H_5N_3O_2$ (para position of -OH groups) with •OH radicals

and H_2O releasement. So stated explains the small abundances of DP3a and DP3b in FPCR_TiO_2/CNT. On the other hand, a pretty significant peak at the RT:11.3 min was observed in both setups, FPCR_TiO_2 and FPCR_TiO_2/CNT, indicating the occurrence of additional degradation products with the different chemical formulas.

a)



b)

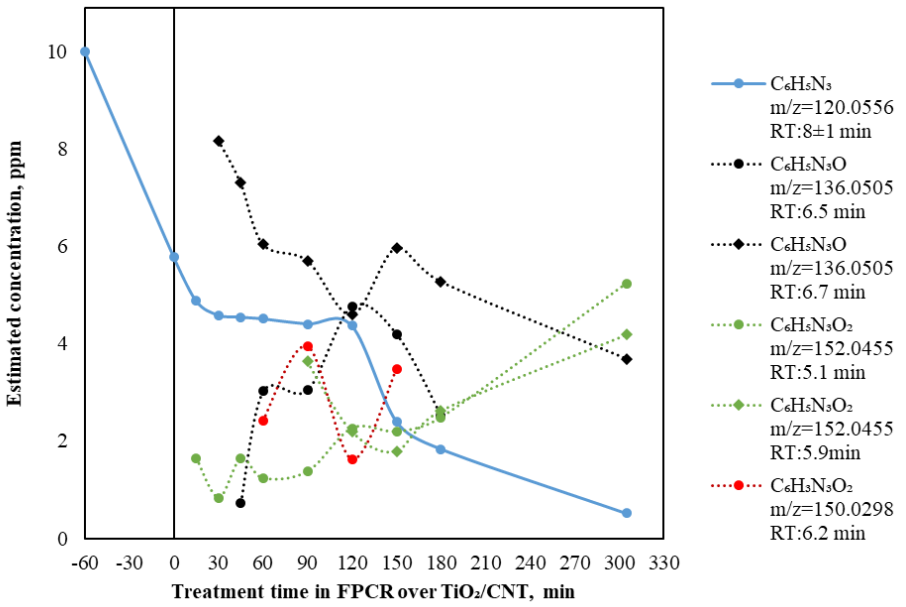


Figure 22. Estimated concentrations of 1H-BT and its degradation products during photocatalysis in a) FPCR_TiO_2, b) FPCR_TiO_2/CNT

Based on the above discussion, common reaction pathways of 1H-BT degradation in the FPCR reactor with TiO_2 and TiO_2/CNT were proposed in Figure 23. In addition, a similar degradation pathway was reported by [109].

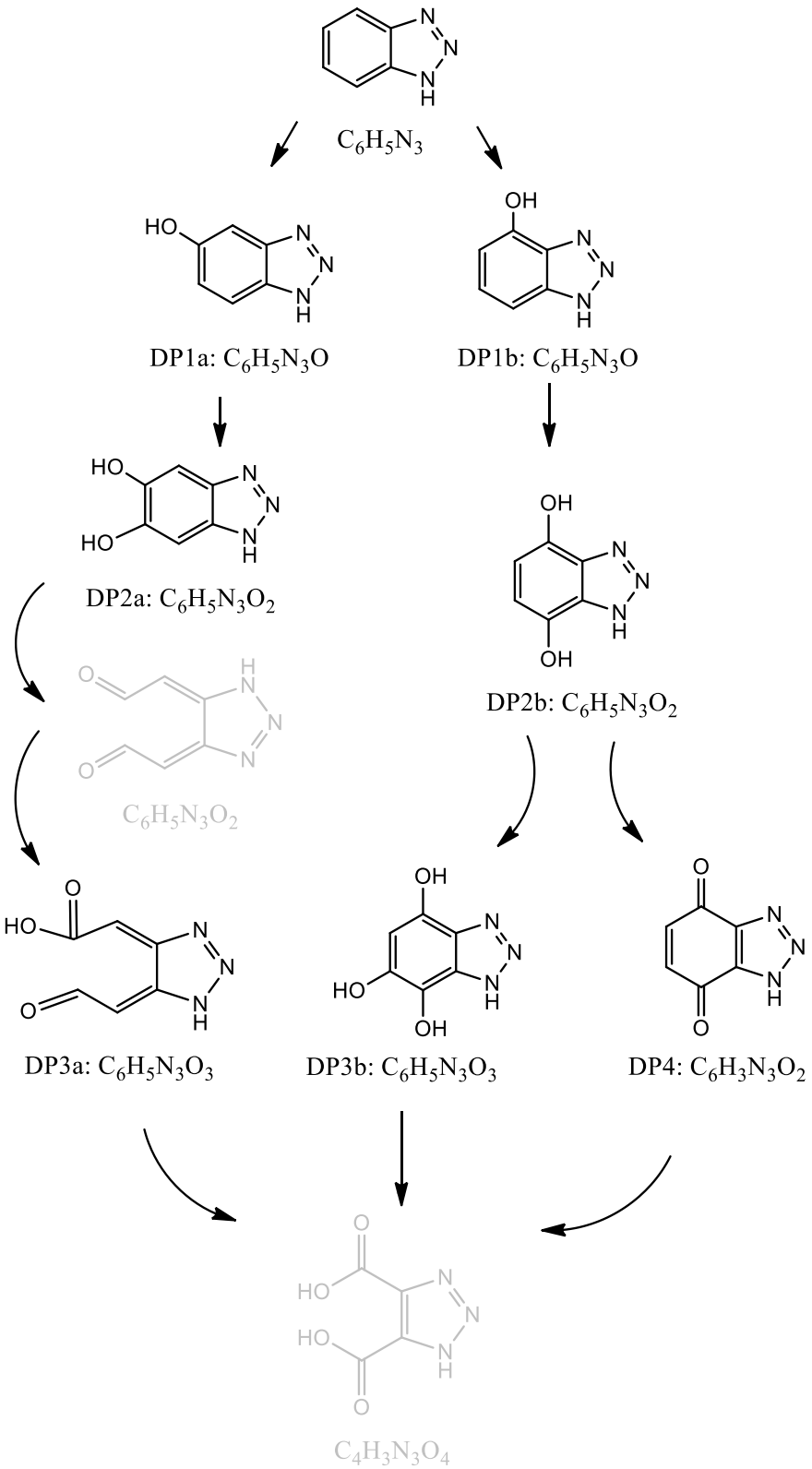


Figure 23. Proposed degradation pathway during photocatalysis in FPCR_TiO_2 and FPCR_TiO_2/CNT

6.1.2.2 Degradation products of 1H-BT in CPC reactor

Meanwhile, even though the EIC (m/z=136.0505, 137.053) was identified after photocatalysis by **CPC_TiO$_2$** (Annex 17) and CPC_TiO$_2$/CNT (Annex 22), the existence of $C_6H_5N_3O$ was not confirmed by MS spectrum. Later implies the formation of degradation products with different structures. Namely, two dominant peaks were observed in **CPC_TiO$_2$** (RT:6.4, RT:6.7 min) and **CPC_TiO$_2$/CNT** (RT:6.6 min, RT: 6.9 min). Since the CPC reactor is designed to enhance the usability of irradiation [35], it could be concluded that reactor design and the addition of CNT contributed to the formation of four different structures. Also, a lack of peaks after RT:7 min in both the CPC_TiO$_2$ and CPC_TiO$_2$/CNT suggests that initial intermediate species formed during photocatalysis by FPCR_TiO$_2$ were not developed.

Furthermore, the second degradation product $C_6H_5N_3O_2$ (m/z=152.0455), was confirmed during the photocatalysis in both **CPC_TiO$_2$** (Annex 18) and **CPC_TiO$_2$/CNT** (Annex 23). However, different RT (RT:4.9 min) was confirmed for $C_6H_5N_3O_2$ (**DP6**), having one dominant peak for both CPC setups. The aforementioned indicates that hydroxylation of the benzene ring is not necessarily the dominant process in photocatalytic degradation. After RT:6 min, other peaks can be observed for the CPC_TiO$_2$ and CPC_TiO$_2$/CNT, indicating the reaction mechanism was more enhanced toward forming intermediates with m/z=152.0455 than intermediates with m/z=136.0505. While in the FPCR, the photocatalyst's modification with CNT was governed by the adsorption process, in the CPC reactor, an increase in the abundance of DP6 indicates photocatalytic enhancement. According to [202], excitation of 1H-BT by visible light irradiation enables the transfer of e− onto the photocatalyst conduction band, thus enhancing the reduction of O_2. Therefore, the reaction mechanism is governed by triazole opening by combining h^+ and $\bullet O_2^-$. Moreover, oxygen reduction is enhanced due to the larger CNT surface area and greater formation of electrons e^- [35]. An important implication of these findings is that degradation of 1H-BT in the CPC reactor is governed by $\bullet O_2^-$ radicals due to irradiation capturing and furtherly increased by the addition of CNT. It also implies that the degradation process was initiated by triazole opening, as reported by [202].

As was the case in previous degradation products detected during the photocatalysis in the CPC reactor, different RTs were observed for degradation product $C_6H_5N_3O_3$ (m/z= 168.0404, 169.0429) in CPC setup compared to FPCR setup. At RT:5.1 min $C_6H_5N_3O_3$ (**DP7**) was confirmed for both **CPC_TiO$_2$** (Annex 19) and **CPC_TiO$_2$/CNT** (Annex 24). Apart from the mentioned peak, two typical peaks were observed, with different structures, a barely visible

peak at RT:4.3 min and a few peaks between RT:8 min and RT:11 min with decreasing trend. Additional observation due to different reactor setups and the abundance increase of DP7 (Table 20, Table 21, Figure 24) in CPC_TiO_2/CNT compared to the CPC_TiO_2 confirms previously discussed enhancements and the mechanism's pathway.

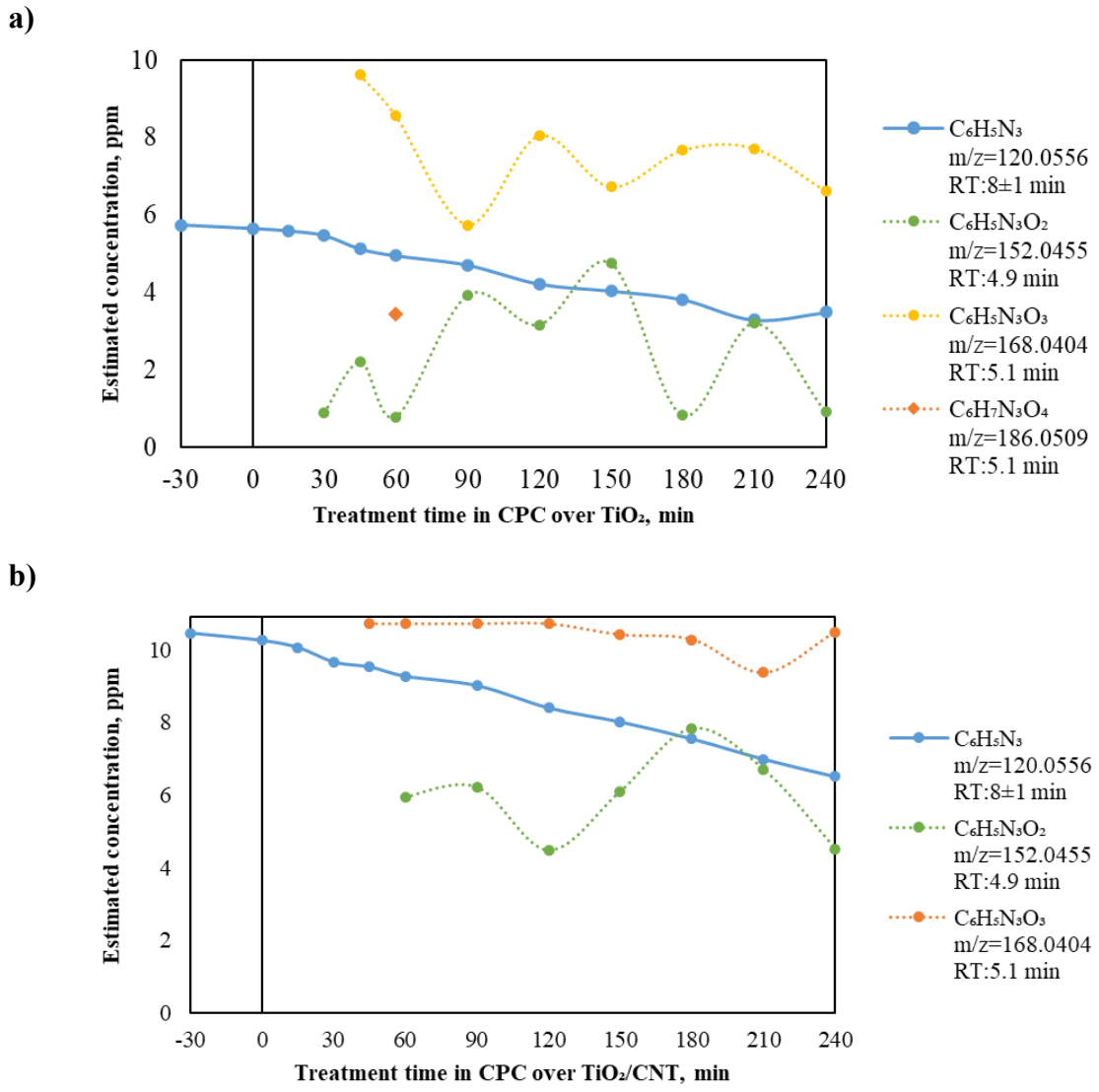


Figure 24. Estimated concentrations of 1H-BT and its degradation products during photocatalysis in a) CPC with TiO_2, b) CPC with TiO_2/CNT

Regarding the fourth degradation product $C_6H_7N_3O_4$ (m/z= 186.0509, 187.0535), it was confirmed in **CPC_TiO_2** (Annex 20) at RT:5.1 min (**DP8**) after 60 minutes of photocatalysis. Nevertheless, the DP8 is present in smaller abundances throughout the 15-to-210-time interval of photocatalysis. The peak at the same RT was observed in the **CPC_TiO_2/CNT** (Annex 25). However, abundances were insufficient for concentration estimation based on the MS spectrum. The structure $C_6H_7N_3O_4$ was reported in the literature [109,162] as the product of ozonolysis.

The benzene breakage is due to the electrophilic addition of O_3 onto the benzene ring. The formation of O_3 in the system could be possible due to enhanced irradiation capturing. Other than DP8, a peak at RT:1.3 min can be noticed as well as a couple of peaks between RT:8 min and RT:14 min with decreasing trend in both CPC setups.

Based on the above discussion, common reaction pathways of 1H-BT degradation in the CPC reactor with TiO_2 and TiO_2/CNT were proposed in Figure 25. In addition, a similar degradation pathway was reported by [162,202].

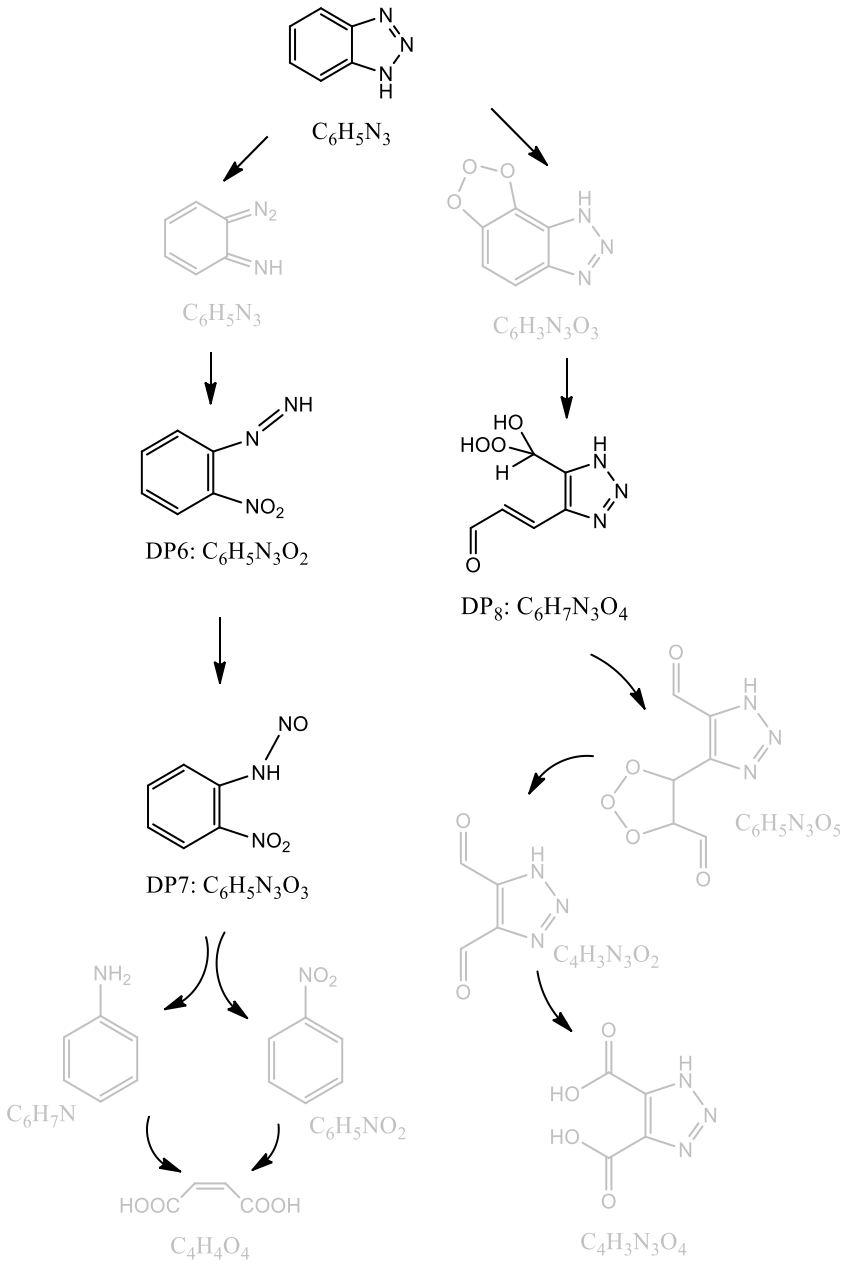


Figure 25. Proposed degradation pathway during photocatalysis in cpc_TiO_2 and FPCR_TiO_2/CNT

6.2 Photocatalytic degradation of 1H-BT

Before discussing photocatalytic degradation, a couple of words will be said about photolysis. In the environment, 1H-BT is subjected to direct and indirect photolysis according to first-order kinetics reaction mechanism under UV light [105,157,205]. However, when using UV-A and UV-B lamps as a source of irradiation, slow photolysis of 1H-BT was observed in the literature [101,180,205]. Furthermore, it was reported that the relatively long persistence of 1H-BT in the environment is because of its insensitivity to visible light [102]. However, photolysis is relevant in conditions such as surface waters. Furthermore, the reaction of 1H-BT with other reactive species can lead to the formation of toxic compounds if there is a lack of mineralization [101].

Likewise, it was reported that photolysis depends on the molar extinction coefficient of the compound itself. According to the 1H-BT values, photolysis of 1H-BT is effective under UV-C light, while that is not the case for UV-A and UV-B light. However, combined with a photocatalyst, UV-A and UV-B light is effective in 1H-BT removal [103], which emphasizes the importance of photocatalysis.

6.2.1 Impact of photocatalyst's modification on 1H-BT degradation intensification

As discussed earlier, MWCNTs can be used as sorbent in SPE as a pre-treatment for BTs concentrations from surface waters. Therefore, before photocatalysis, an equilibrium was established. For the CPC reactor, equilibrium establishing was 30 minutes long (Figure 26.a) in correspondence with the previous report [180]. Namely, adsorption of 1H-BT was negligible in the CPC setup with immobilised TiO_2 and TiO_2/CNT, where 2 % and 4 % were reported, respectively. In this dissertation, adsorption contribution was 2 % for both photocatalysts in the CPC reactor.

Meanwhile, due to the larger surface of photocatalysts in FPCR (15.6x) regarding the CPC reactor, the equilibrium time lasted for 1 hour (Figure 26.b). When TiO_2 was used as a photocatalyst (4 %), adsorption was negligible. On the other hand, significant adsorption was observed onto TiO_2/CNT photocatalyst at 42 %. For instance, 82 % of 1H-BT was reported to be adsorbed when 10 % of graphene was added to the photocatalyst's formulation [172]. Likewise, it was reported that CNT acts as an adsorbent in catalyst composites [66]. Furthermore, the composites of CNT and TiO_2 were proven promising photocatalysts [48,61].

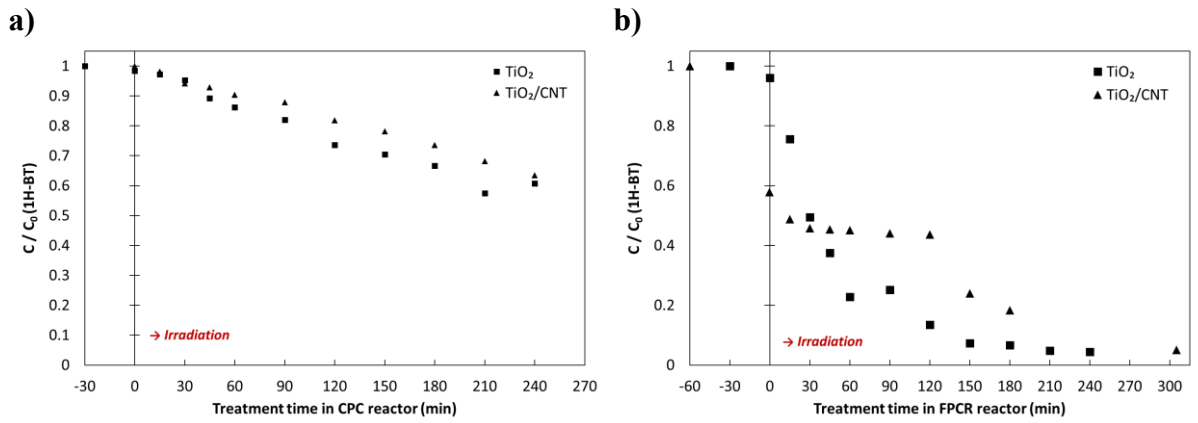


Figure 26. Photocatalytic degradation of 1H-BT (C_0=10 ppm) in the a) CPC reactor and b) FPCR – comparison of different photocatalyst's formulation usage (TiO_2 and TiO_2/CNT)

The photocatalysis lasted for 240 minutes in the CPC reactor, with both photocatalyst formulations, TiO_2 and TiO_2/CNT. Achieved degradation rates were 38 % and 36 %, respectively. When the CPC_TiO_2 was used, the achieved rate followed the literature finding [180]. The initial concentration of $[1H\text{-}BT]_0$=5 ppm during 2 h of photocatalysis was 32 % degraded, while in this dissertation, 38 % of $[1H\text{-}BT]_0$=10 ppm was degraded in 4 h. On the other hand, in the same study [180], only 26 % of 1H-BT was reported when TiO_2/CNT was used, while 36 % was achieved in this study. Given can be explained due to different reaction mechanisms in CPC_TiO_2/CNT, as was previously discussed in this dissertation. A higher concentration of 1H-BT enables 1H-BT excitation and, along with CNT, enhances the formation of $\bullet O_2^-$ radicals and shifts the reaction mechanism toward 1H-BT triazole opening [35,202]. Furthermore, given reaction mechanisms, a degradation product with the same m/z as 1H-BT can be formed (see Annex 6). The aforementioned explains why the trend of photocatalytic degradation by CPC_TiO_2 seems more efficient than CPC_ TiO_2/CNT. Therefore, an observed trend can be considered a confirmation of the proposed reaction mechanism.

Regarding photocatalytic degradation in the FPCR reactor, photocatalysis by TiO_2 lasted 240 minutes, while photocatalysis by TiO_2/CNT lasted longer (300 minutes). As previously discussed, hydroxylation governs the reaction mechanism of 1H-BT degradation in FPCR. Also, due to the larger surface of a photocatalyst's carrier, degradation by TiO_2 was 95 % effective during the 240 minutes. Since adsorption was negligible, it can be concluded that

photocatalysis was governed by hydroxylation. Furthermore, adsorption was significant in the FPCR_ TiO_2/CNT due to a greater photocatalyst's surface area and adsorption of hydroxylated species onto CNT [206]. Immediately after the irradiation, equilibrium establishing due to the desorption lasting up to 120^{th} min. By the end of the 300^{th} min, 91 % of 1H-BT was degraded.

In a research study [207], the ageing of both photocatalysts was analysed. Results have revealed the dependence of the TiO_2/CNT immobilisation preparation process with lower photocatalytic activity compared to TiO_2 due to uneven dispersion of CNT particles. On the other hand, regarding the durability of TiO_2/CNT and TiO_2, it was observed that during 90 days in water, the photocatalyst's mass loss was 6 % and 11 % for TiO_2 and TiO_2/CNT, respectively. Furthermore, reduced photocatalytic activity is observed as well. However, with the ageing of photocatalysts in the air, improvements in photocatalytic activity were achieved.

6.2.2 Impact of different photocatalytic reactor setups on 1H-BT degradation intensification

In this dissertation, the open type of the photocatalytic reactor, the FPCR and the closed type, the CPC reactor, were discussed. The advantage of FPCR is the usage of incoming irradiation, yet evaporation of volatile compounds and particle release is highly probable [35]. For example, variations of the FPCR reactors have been successfully applied to treat industrial or agricultural wastewater [208], such as for dye degradation or water disinfection [35]. Meanwhile, the CPC reactor has become known as state-of-the-art in design [98]. Its application was reported for various compounds, such as chlorophenols, dyes, pesticides, chlorinated solvents, bacteria, fungi, and parasite removal [35]. Therefore, what can be observed (Figure 27) is faster degradation of 1H-BT in the FPCR reactor than in the CPC reactor, demonstrating that photocatalysis is a surface phenomenon. Furthermore, kinetic modelling was applied to examine the impact of various reactor setups correctly, and it is discussed further in the text.

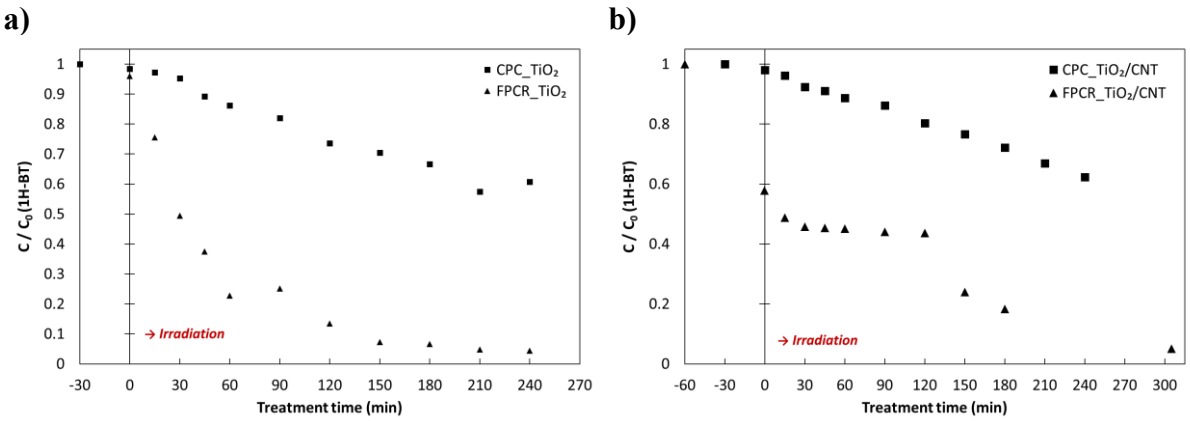


Figure 27. Photocatalytic degradation of 1H-BT (C_0=10 ppm) with a) TiO_2 and b) TiO_2/CNT photocatalyst's formulation – comparison of the FPCR and CPC reactor

6.2.3 Impact of different irradiation setups on 1H-BT degradation intensification

Photocatalysis depends on the effective irradiation wavelength of the photocatalyst, i.e. band gap energy [20]. Therefore, various designs of lamps are used as irradiation sources [28]. During the experiments with compact fluorescent lamps in the CPC reactor, an increase in the temperature was observed. It was reported that temperature increase promotes the recombination of electron/hole pairs and desorption of adsorbed reactants, reducing photocatalytic activity [100]. On the other hand, visible evaporation was observed in the FPCR setup due to its open concept. Results shown in Figure 28 indicate more efficient degradation under fluorescent lamps in the case of photocatalytic degradation by CPC_TiO_2. Moreover, it is worth mentioning that temperature increase reduces oxygen solubility, thus disturbing the reaction mechanism of superoxide radical's formation. Therefore, faster degradation is governed by the higher proportion of UV light in the compact fluorescent lamp (UV-A=1558 mW/cm^2, UV-B=509 mW/cm^2, UV-C=161 mW/cm^2) regarding linear lamps (UV-A=70 mW/cm^2, UV-B=200 mW/cm^2, UV-C=6 mW/cm^2), since total irradiation is similar, 67.8 W/m^2 and 68.3 W/m^2.

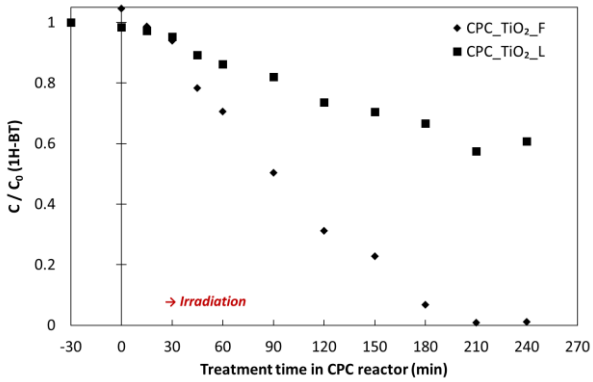


Figure 28. Photocatalytic degradation of 1H-BT (C_0=10 ppm) in CPC_TiO_2 under linear (L) and compact fluorescent (F) irradiation source

6.2.4 Modelling of Photocatalytic Degradation

A more detailed analysis of photocatalytic degradation, namely due to the different intensification parameters of the reactor and photocatalyst, was achieved by applying mathematical modelling. Model setups are given in the section on Materials and methodology. Intrinsic degradation rate constant k_i, as well as intensification factors due to the different photocatalyst's formulation Y_{cat} and photocatalytic reactor Y_{RD}, were obtained and are given in Table 22 for 1H-BT.

Table 22. Intrinsic parameters obtained by mathematical modelling for photocatalytic degradation of 1H-BT

	k_i ($s^{-1}W^{-0.5}m^{1.5}$)	Y_{cat} (-)	Y_{RD}
1H-BT	3.54×10^{-10}	0.769	25

Given results are slightly different than the one reported in the literature [180] under the same CPC setup conditions (k_i=1.1972×10^{-9} $s^{-1}W^{-0.5}m^{1.5}$). The given indicates the impact of the compound concentration in the system. With twice the concentration value (5 vs. 10 ppm), the degradation rate in the CPC reactor was 3.3 times faster. Based on the obtained intrinsic parameters, the prediction was plotted and compared with the experimental data in Figure 29. While modelled data fit well with the experimental data for the CPC setup with both photocatalysts, adsorption contribution in the FPCR reactor data is better aligned with the experimental data recorded later during the photocatalysis.

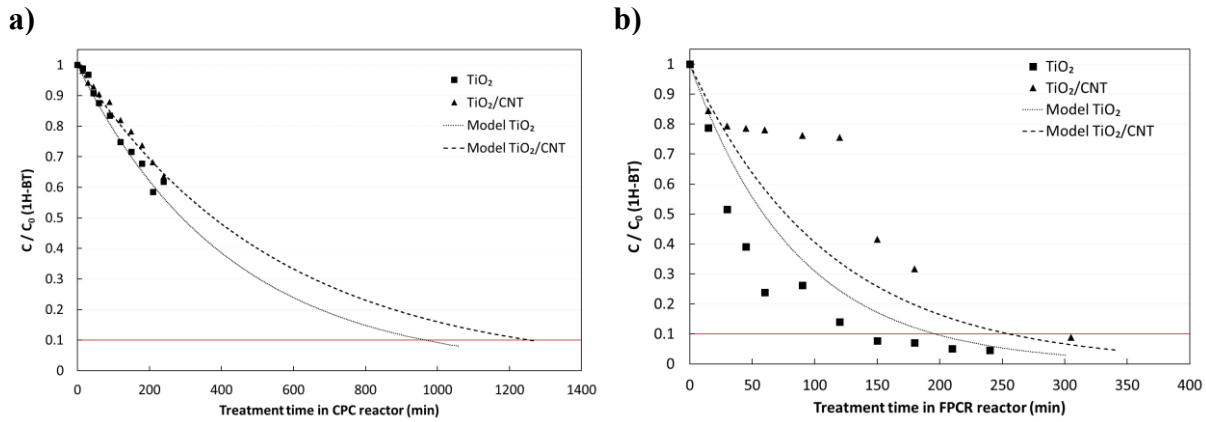


Figure 29. Photocatalytic degradation of 1H-BT (C_0=10 ppm) in the a) CPC reactor and b) FPCR – comparison of different photocatalyst's formulation usage (TiO_2 and TiO_2/CNT), experimental and modelled

Furthermore, the prediction of the time necessary for the pollutant's degradation is possible by using the modelling approach. For example, a 90 % degradation of 1H-BT can be achieved within one day. More detailed data can be found in Table 23.

Table 23. The efficiency of 1H-BT photocatalytic degradation (C_0=10 ppm) in different setups based on developed model prediction

		50 %		90 %	
Photoreactors	Photocatalysts	(h)	(min)	(h)	(min)
CPC	TiO_2	4.9	295	16.5	988
	TiO_2/CNT	6.3	3782	20.9	1256
FPCR	TiO_2	0.3	21	1.2	70
	TiO_2/CNT	1.8	106	5.7	341

6.3 Environmental impact estimation

6.3.1 Toxicity Estimation Software Tool (T.E.S.T.)

Other than achieving a successful removal rate, it is vital to establish if more toxic compounds are generated throughout the process. For that purpose, oral rat LD_{50}, developmental mutagenicity, bioaccumulation and mutagenicity were evaluated by the consensus method of T.E.S.T. The results are shown in the following Table 24 and Table 25.

Table 24. Results of toxicity estimation according to consensus method T.E.S.T. for proposed degradation products during photocatalysis in FPCR with both photocatalysts

Compound	Oral rat LD_{50} (mg/kg)	Developmental mutagenicity	Bioaccumulation	Mutagenicity
1H-BT	522.54	0.63 development toxicant	10.8	0.54 positive
DP1a	/	0.56 development toxicant	12.9	0.54 positive
DP1b	/	0.52 development toxicant	5.04	0.54 positive
DP2a	/	0.60 development toxicant	3.8	0.55 positive
DP2b	/	0.62 development toxicant	6.22	0.55 positive
DP3a	/	0.48 developmental non-toxicant	/	0.53 positive
DP3b	/	0.43 developmental non-toxicant	1.62	0.56 positive
DP4	/	0.75 development toxicant	9.3	0.49 negative
1H-1,2,3-triazole-4,5-dicarboxylic acid	/	0.53 development toxicant	0.085	0.44 negative

Depending on the literature, 50 % of the lethal impact on rats after 1H-BT oral ingestion varies, from being toxic ($LD_{50} < 400$ mg/kg) [151] to relatively low toxic material ($LD_{50} > 900$ mg/kg) [209]. In this paper, based on the software database search, an average value was reported (LD_{50} = 522.54 mg/kg) which classifies 1H-BT as moderately toxic for the rat population in accordance with the data reported in [111].

As was observed in the literature [109,157], hydroxylated degradation products created at the beginning of the process in the FPCR reactor tend to develop toxicity. However, with further degradation, degradation products with a negative mutagenic effect and the possibility of developing toxicity could occur. However, a decreasing trend of bioaccumulation has been observed. It contributes to the formation of less harmful products to the environment.

Regarding the degradation products proposed during the photocatalysis in the CPC reactor, bioaccumulation, as well as the development of the mutagenicity for the initial degradation products, has been smaller than the ones observed during the degradation in the FPCR. Therefore, despite the increase of toxicity developing for the products later in the degradation

process, mutagenicity was observed as negative. Consequently, it indicates that CPC reactor usage contributes to forming less harmful degradation products.

Table 25. Results of toxicity estimation according to consensus method T.E.S.T. for proposed degradation products during photocatalysis in CPC reactor with both photocatalysts

Compound	Oral rat LD_{50} (mg/kg)	Developmental mutagenicity	Bioaccumulation	Mutagenicity
6-diazocyclohexa-2,4-dienimine	/	0.44 developmental non-toxicant	/	/
DP6	/	0.5 developmental non-toxicant	/	/
DP7	/	0.34 developmental non-toxicant	/	0.72 positive
Aniline	250.11	0.53 development toxicant	5.38	0.36 negative
Nitrobenzene	349.40	0.26 developmental non-toxicant	4.38	0.37 negative
Maleic acid	707.55	0.79 development toxicant	0.53	0.19 negative
8H-[1,2,3]trioxolo[4',5':3,4]benzo[1,2-d][1,2,3]triazole	/	0.74 development toxicant	34.9	0.63 positive
DP8	/	0.43 developmental non-toxicant	/	/
4-(5-formyl-1,2,3-trioxolan-4-yl)-1H-1,2,3-triazole-5-carbaldehyde	/	0.61 development toxicant	/	/
1H-1,2,3-triazole-4,5-dicarbaldehyde	/	0.65 development toxicant	/	0.21 negative
1H-1,2,3-triazole-4,5-dicarboxylic acid	/	0.53development toxicant	0.085	0.44 negative

6.3.2 Ecological Structure Activity Relationships (ECOSAR)

Another tool used for ecotoxicity estimation is ECOSAR. For the compounds, it is possible to estimate the median effective concentration (EC_{50}), which is expected to have a specific effect on 50 % of test organisms. In comparison, lethal concentration causes death in 50 % of the tested population (LC_{50}), usually aquatic organisms such as daphnids or green algae [165].

Therefore, the estimation of ecotoxicity on fish, daphnids and green algae was checked by ECOSAR for proposed degradation products and results are shown in Table 26 and Table 27.

While hydroxylated products formed during the photocatalysis in the FPCR are less ecotoxic for aquatic species (Table 26), that was not the case with the initially formed degradation products in the CPC reactor (Table 27). However, in both cases, further mineralisation enables the formation of products less harmful to aquatic life.

Table 26. Results of ecotoxicity estimation for aquatic species according to ECOSAR for proposed degradation products during photocatalysis in FPCR reactor with both photocatalysts

Compound	**Fish 96 h, LC_{50} mg/L**	**Daphnid 48 h, LC_{50} mg/L**	**Green algae 96 h, EC_{50} mg/L**
1H-BT	40.7	244	8.19
DP1a	88.9	688	16.3
DP1b	/	/	/
DP2a	2.22×10^{3}	1.11×10^{3}	484
DP2b	/	/	/
DP3a	/	/	/
DP3b	1.53×10^{4}	7.04×10^{3}	$2{,}2\times10^{3}$
DP4	/	/	/
1H-1,2,3-triazole-4,5-dicarboxylic acid	1.37×10^{6}	5.7×10^{5}	1.18×10^{5}

Table 27. Results of ecotoxicity estimation for aquatic species according to ECOSAR for proposed degradation products during photocatalysis in CPC reactor with both photocatalysts

Compound	**Fish 96 h, LC_{50} mg/L**	**Daphnid 48 h, LC_{50} mg/L**	**Green algae 96 h, EC_{50} mg/L**
6-diazocyclohexa-2,4-dienimine	/	/	/
DP6	26.7	16.3	16.1
DP7	86.9	9.60	9.22
Aniline	40.3	1.67	5.10
Nitrobenzene	150	83.5	57.8
Maleic acid	5.33×10^{4}	2.53×10^{4}	8.96×10^{3}
8H-[1,2,3]trioxolo[4',5':3,4]benzo[1,2-d][1,2,3]triazole	1.12×10^{3}	2.16×10^{4}	147
DP8	/	/	/
4-(5-formyl-1,2,3-trioxolan-4-yl)-1H-1,2,3-triazole-5-carbaldehyde	1.53×10^{6}	5.76×10^{5}	7.96×10^{4}
1H-1,2,3-triazole-4,5-dicarbaldehyde	9.25×10^{4}	3.88×10^{4}	8.25×10^{4}
1H-1,2,3-triazole-4,5-dicarboxylic acid	1.37×10^{6}	5.7×10^{5}	1.18×10^{5}

6.4 Life cycle assessment (LCA)

6.4.1 Goal and scope

Life cycle assessment (LCA) is frequently used in the framework of process scaling. Therefore, the goal of LCA in this dissertation was to assess the environmental impacts of 1H-BT photocatalytic degradation in dependence on different intensification approaches. The purpose of the LCA study was to identify critical aspects of the process, minimize environmental burdens, and propose feasible options for scale-up. The emphasis was on the energy scenario and toxicological effects. To achieve the stated, comparative LCA was conducted with the system boundaries shown in Figure 30. The functional unit, the base for the comparison, was determined as the time necessary to achieve 90 % efficient degradation of 1H-BT.

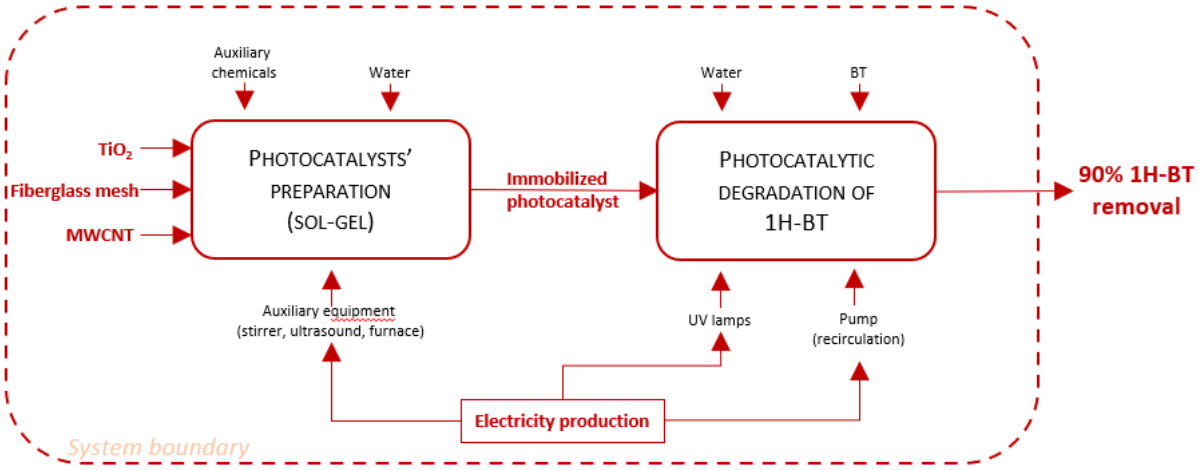


Figure 30. System boundaries for the LCA

Overall, eight scenarios were discussed. The overview of the scenarios and main variations parameters are schematically shown in Figure 31.

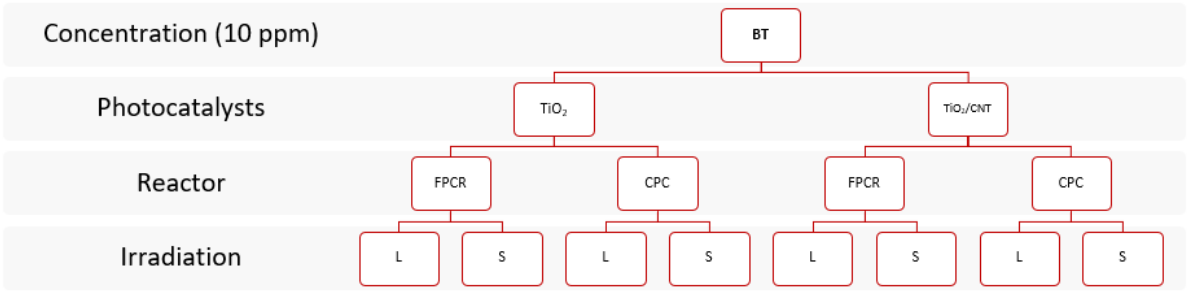


Figure 31. Overview of the scenarios for the comparative LCA (L states for the linear artificial source of light, while S for the Sun)

6.4.2 Inventory

The inventory analysis has been modelled in open-source software, OpenLCA. Primary data were collected and incorporated into the analysis by experiments; photocatalysts' sol-gel preparation and BT's degradation (Table 28). In addition, the Ecoinvent database has obtained secondary data to fill the inventory for electricity and transport. The time necessary to achieve 90 % of efficient degradation of 1H-BT was determined according to the values shown in Figure 32.

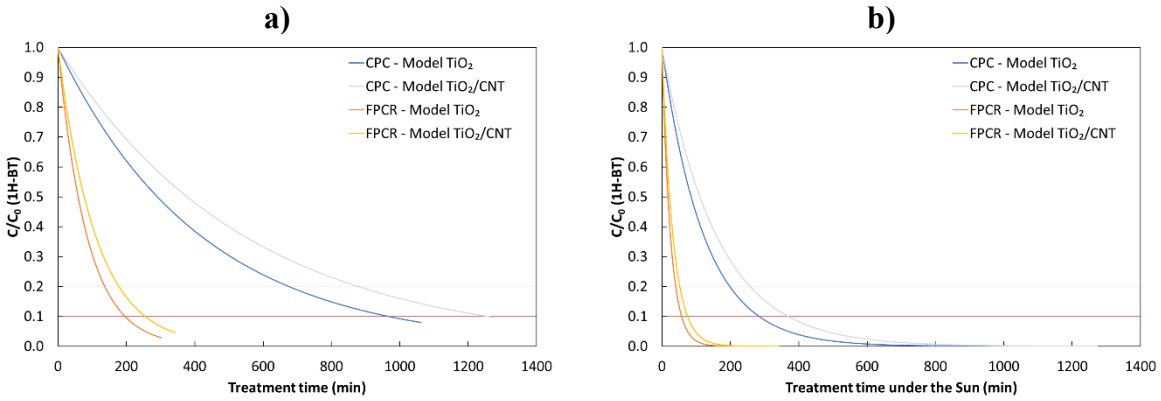


Figure 32. Modell of photocatalytic degradation by CPC&FPCR_TiO_2 and CPC&FPCR_TiO_2/CNT over a time to achieve 90 % degradation efficiency of 1H-BT under a) artificial irradiation source, b) natural Sun

Table 28. Data that were obtained by experiments

Category	Component
Photocatalysts' preparation	
Input	
Chemicals (sol-gel)	Titanium dioxide
	Multiwalled carbon nanotubes
	Deionized water
	Sodium hydroxide (10 M)
	Ethanol
	Acetic acid
	TEOS
Materials	Fibreglass mesh (CPC)
	Fibreglass mesh (FPCR)
Energy	Electricity consumption (magnetic stirrer)
	Electricity consumption (ultrasound bath)
	Electricity consumption (calcination furnace)
Output	
Waste	Sol-gel solution
Emissions	Ethanol
	Acetic acid
Product	Immobilised photocatalyst TiO_2
	Immobilised photocatalyst TiO_2/CNT
Photocatalytic degradation of BT	
Input	
Material	Distilled water
	1H-benzotriazole
	Immobilised photocatalyst TiO_2 approximated with mass
	Immobilised photocatalyst TiO_2 (FPCR)
	Immobilised photocatalyst TiO_2/CNT
	Peristaltic pump
	Ultraviolet linear lamp
	Ultraviolet fluorescent lamp
Energy	Electricity consumption (peristaltic pump)
	Electricity consumption (linear lamps)
	Electricity consumption (fluorescent lamps)
Output	
Emissions	Model solution of BT
	Model solution evaporation
	1H-benzotriazole
By-products	Carbon dioxide
Functional unit	

6.4.3 Life cycle impact assessment (LCIA)

LCIA has been conducted by the IMPACT 2002+ method since it covers a significant number of impact categories. Overall, fifteen impact categories are aquatic acidification, aquatic ecotoxicity, aquatic eutrophication, carcinogens, global warming, ionizing radiation, land occupation, mineral extraction, non-carcinogens, non-renewable energy, ozone layer depletion, respiratory inorganics, respiratory organics, terrestrial acid/nutri and terrestrial ecotoxicity.

Furthermore, USEtox 2 method was used to determine impacts related to the toxicity. Results are reported through three impact categories, freshwater ecotoxicity, human toxicity – and human toxicity - non-cancer.

Regarding the impact, for the set boundaries, impact on the environment was observed in four categories: aquatic ecotoxicity, carcinogens, global warming and terrestrial ecotoxicity. The results are shown in Figure 33. What can be noticed is that usage of CPC as a reactor is less harmful to the environment than FPCR reactor. Stated can be explained by the open reactor concept and the possible evaporation of particles into the environment. Furthermore, a larger photocatalyst's surface area and more material were used during the photocatalyst's preparation for the FPCR then for the CPC reactor.

However, when the boundaries of LCA study are broadened toward raw material extraction, the observed impact is negligible. On the following Figure 34, the comparison of the results concerning the different boundaries is shown. Apart from the mentioned impact categories, the impact is visible in all the other impact categories given by the methodology (Table 29). The aforementioned emphasizes the importance of a proper presentation of boundaries which are set for the LCA study. However, it is worth emphasizing that even in that case, scenarios in which Sun is used as an irradiation source have a less negative impact on the environment, which makes solar photocatalysis scalable for degradation under natural sunlight.

Regarding the results obtained by USEtox 2 LCIA methodology (Figure 35), it can be noticed that slightly less negative impact on the environment is by FPCR_TiO_2/CNT in the category of impact on the human toxicity-non cancer compared with other scenarios with FPCR reactor. Given can be due to the adsorption process onto the CNT. Furthermore, what can be seen is that usage of the CPC reactor with both photocatalyst formulations has a less negative impact on the environment than FPCR for freshwater ecotoxicity and human cancerous toxicity. The closed concept of the reactor can explain the abovementioned.

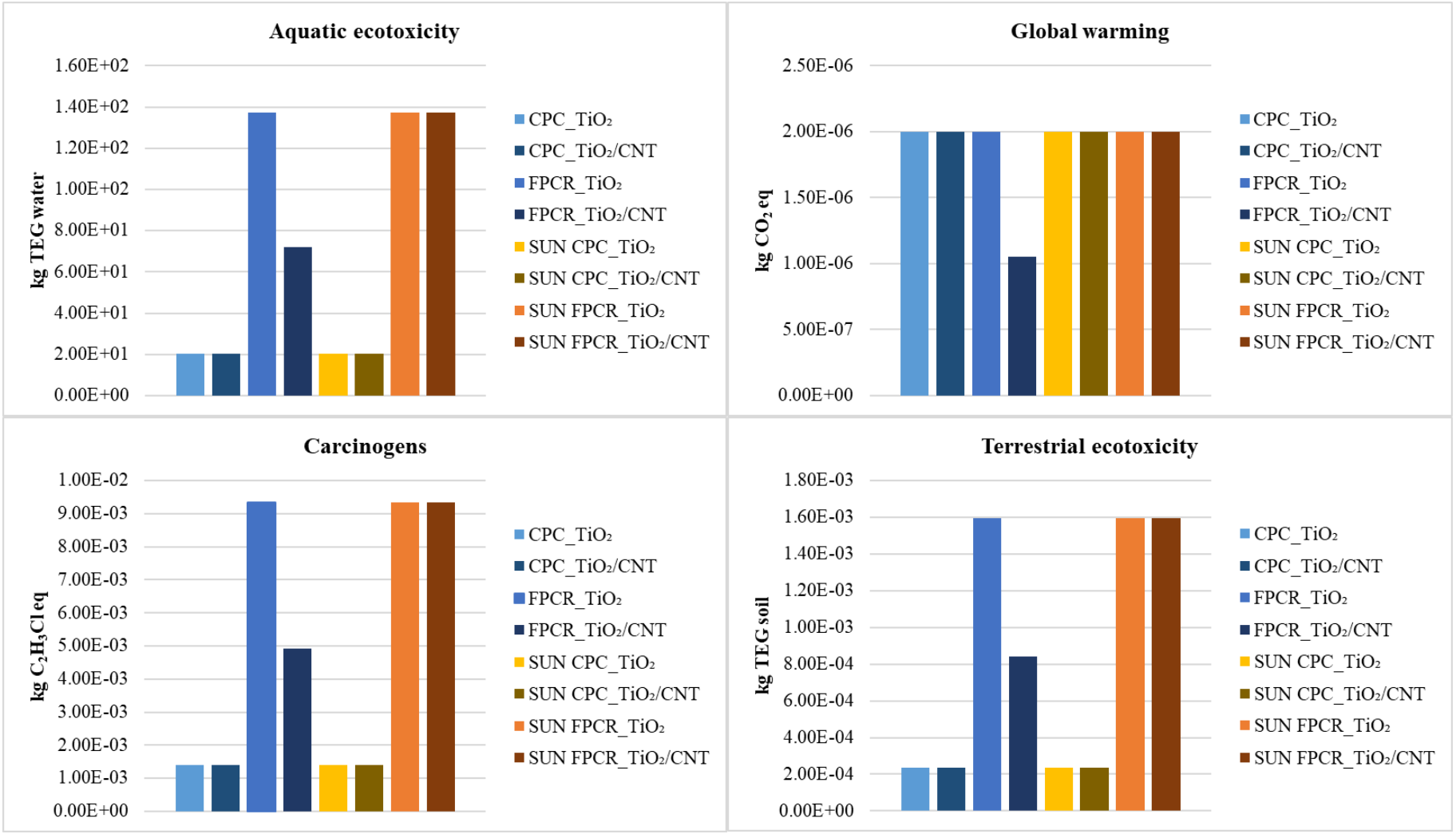


Figure 33. Results of the LCIA by IMPACT 2002+methodology in four impact categories, aquatic ecotoxicity, carcinogens, global warming and terrestrial ecotoxicity

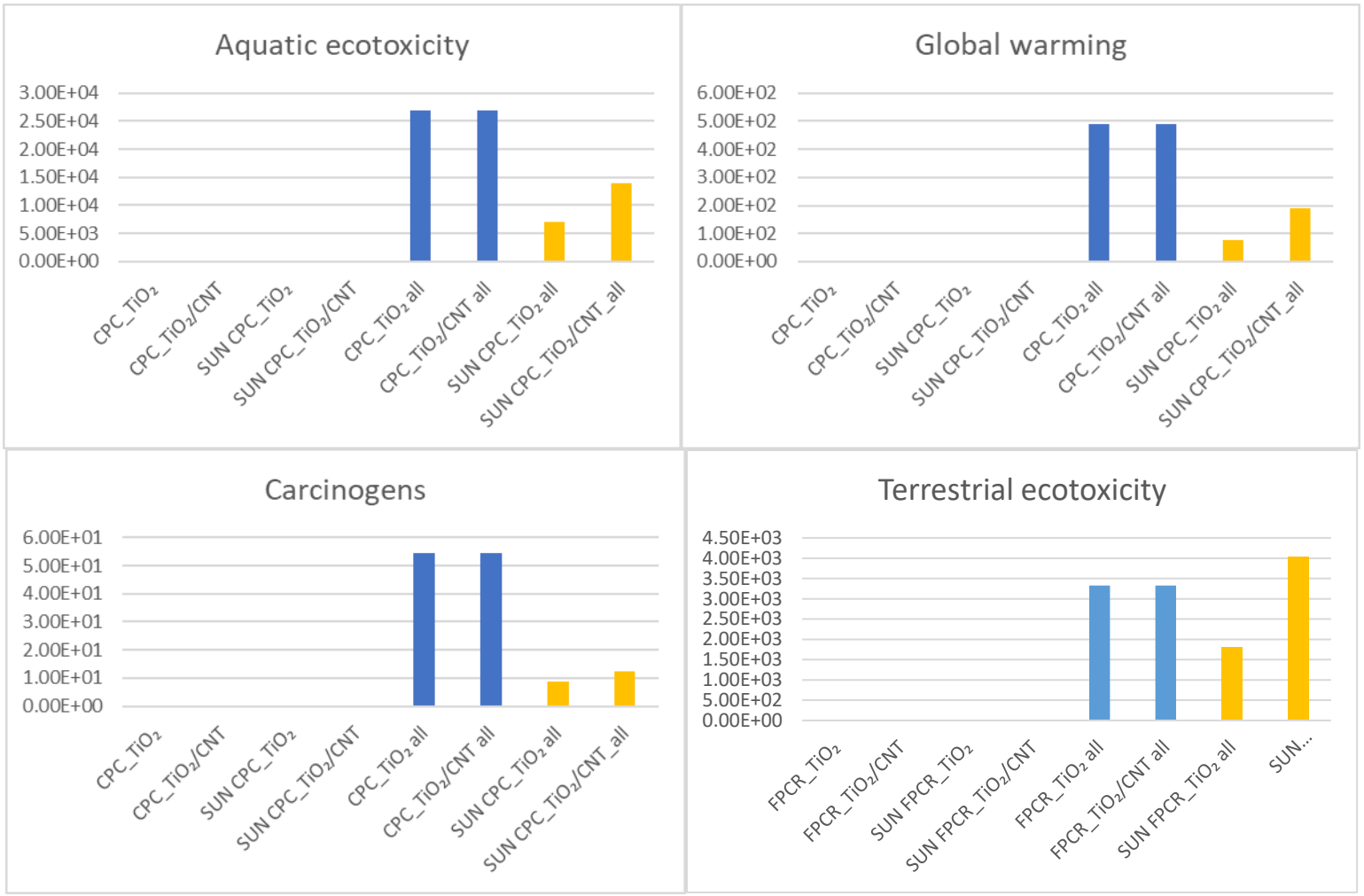


Figure 34. Results of the LCIA by IMPACT 2002+methodology in four impact categories with widened LCA boundaries, freshwater ecotoxicity, human toxicity – and human toxicity - non-cancer

Table 29. Overview of the obtained results on the environmental impact with widened boundaries toward raw materials extraction

Indicator	CPC_TiO_2	CPC_TiO_2/CNT	SUN CPC_TiO_2	SUN CPC_TiO_2/CNT	FPCR_TiO_2	FPCR_TiO_2/CNT	SUN FPCR_TiO_2	SUN FPCR_TiO_2/CNT	Unit
Aquatic acidification	5.63E-01	5.63E-01	1.81E-01	9.70E-01	5.68E-01	3.29E+00	1.87E-01	5.48E+00	kg SO_2 eq
Aquatic ecotoxicity	2.69E+04	2.69E+04	6.96E+03	1.39E+04	2.71E+04	4.96E+04	7.17E+03	5.36E+04	kg TEG water
Aquatic eutrophication	3.01E-02	3.01E-02	2.61E-02	4.35E-02	3.02E-02	7.93E-02	2.63E-02	1.43E-01	kg PO_4 P^- lim
Carcinogens	5.44E+01	5.44E+01	8.88E+00	1.24E+01	5.44E+01	6.64E+01	8.90E+00	3.29E+01	kg C_2H_3Cl eq
Global warming	4.91E+02	4.92E+02	7.69E+01	1.91E+02	4.92E+02	8.88E+02	7.76E+01	8.40E+02	kg CO_2 eq
Ionizing radiation	1.63E+02	1.63E+02	6.26E+01	8.09E+02	1.68E+02	2.78E+03	6.75E+01	5.08E+03	Bq C^{-14} eq
Land occupation	4.22E-01	4.22E-01	2.66E-01	1.16E+00	4.29E-01	3.47E+00	2.73E-01	6.30E+00	morg.arable
Mineral extraction	1.84E+01	1.84E+01	1.70E+01	2.36E+01	1.84E+01	3.33E+01	1.71E+01	6.10E+01	MJ surplus
Non-carcinogens	1.08E+01	1.08E+01	7.00E+00	2.57E+01	1.09E+01	7.39E+01	7.11E+00	1.33E+02	kg C_2H_3Cl eq
Non-renewable energy	8.84E+03	8.84E+03	1.34E+03	2.97E+03	8.85E+03	1.45E+04	1.35E+03	1.23E+04	MJ primary
Ozone layer depletion	3.51E-05	3.51E-05	5.38E-06	1.20E-05	3.51E-05	5.82E-05	5.43E-06	4.99E-05	kg CFC-11 eq
Respiratory inorganics	1.06E-01	1.06E-01	3.96E-02	2.32E-01	1.07E-01	7.69E-01	4.08E-02	1.33E+00	kg $PM_{2.5}$ eq
Respiratory organics	1.38E-01	1.38E-01	2.44E-02	5.62E-02	1.38E-01	2.47E-01	2.46E-02	2.38E-01	kg C_2H_4 eq
Terrestrial acid/nutri	2.17E+00	2.17E+00	5.47E-01	3.44E+00	2.18E+00	1.22E+01	5.65E-01	2.00E+01	kg SO_2 eq
Terrestrial ecotoxicity	3.33E+03	3.33E+03	1.80E+03	4.03E+03	3.34E+03	1.01E+04	1.82E+03	1.68E+04	kg TEG soil

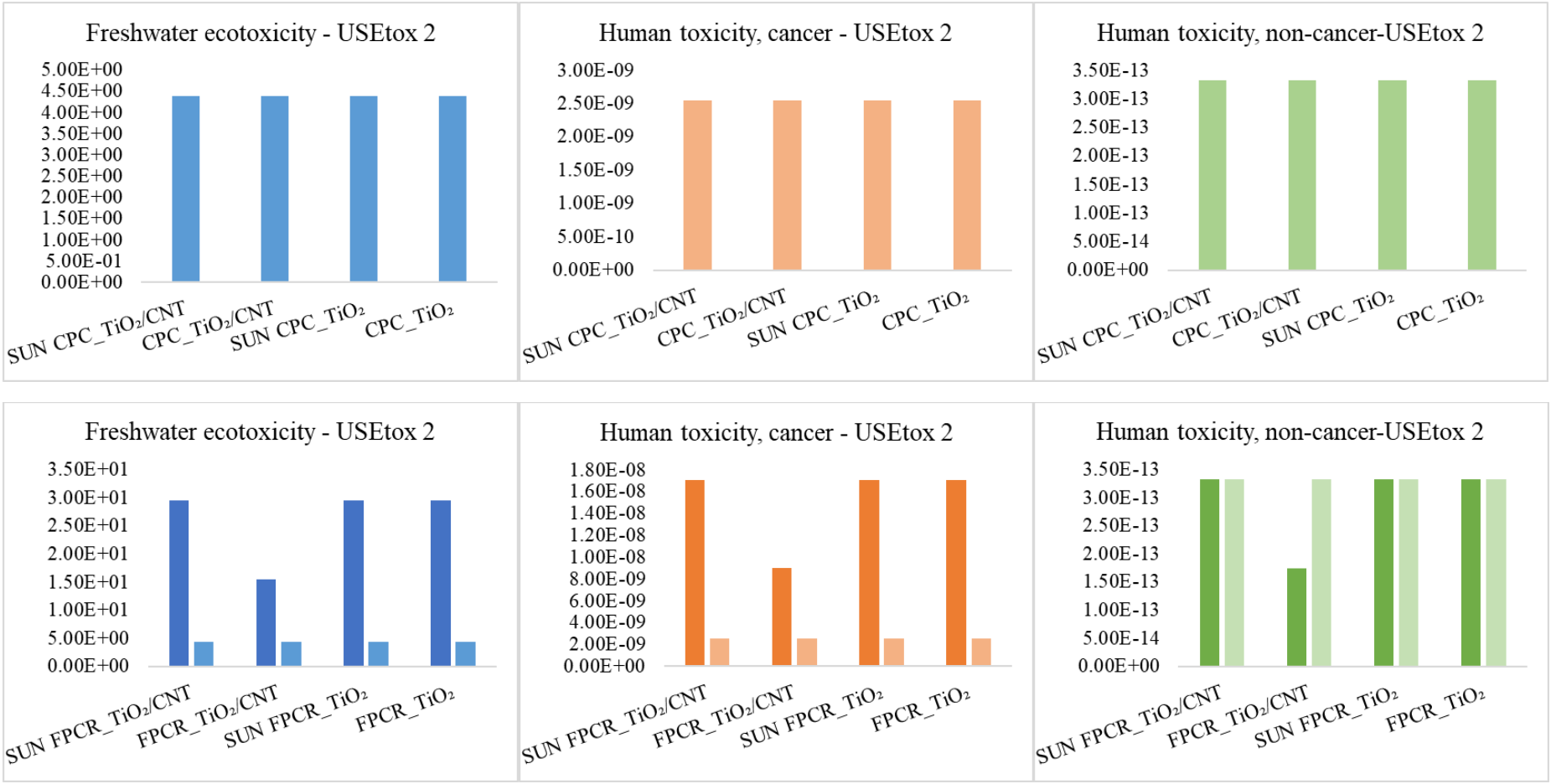


Figure 35. Results of the LCIA by USEtox 2 methodology in three impact categories

6.5 Perspectives for a scale-up in real systems

Having the Sun as a freely available resource all over the Earth's surface has significant potential from economic and environmental points of view, especially for using solar light to drive photocatalysis. Nonetheless, the irradiation power and spectra are greatly influenced by latitude, longitude, date time, pollution, and weather conditions. Therefore, photocatalytic reactors are strongly correlated with specific applications and solar average radiation flux available at a particular location. Accordingly, the scale-up of the system requires taking into account irradiation variability, date and times of the process operation [35]. According to the results obtained in this dissertation, the CPC reactor with TiO_2/CNT would be proposed as the best option for further scaling. The choice of the reactor is not surprising since CPC was reported as state-of-the-art [49]. As well, prior to experimental conducting, it would be expected to achieve better degradation of 1H-BT with TiO_2/CNT photocatalysts since it was designed to boost degradation in visible spectra, which was reported in the literature [49,180]. However, that was not the case regarding 1H-BT photocatalytic degradation. The analysis of degradation products pointed at CNT contribution to mechanisms of increased radical formation when applied in the CPC reactor while degradation products with the same fragmentation can hide the actual degradation rate. With a larger photocatalyst surface, CNT acted as an adsorbent, thus contributing to the toxicity decrease due to adsorption. Therefore, even though degradation of 1H-BT was observed to be faster by application of TiO_2, the main reasons for the abovementioned suggestion about perspectives for the system scale-up would be low photoactivity under visible light; reported reaction mechanisms of degradation by application of TiO_2/CNT in CPC reactor; lower negative impact on the environment confirmed by LCA analysis.

7 CONCLUSIONS

The efficient removal of micropollutants from the environment is a significant challenge nowadays. In the framework of this dissertation, three main objectives were set up:

1. to develop mathematical model including irradiation terms and a rate of photon absorption over photocatalyst surface (local or global) and fluid dynamics in chosen reactors to obtain intrinsic reaction rate;
2. to determine 1H-BT photocatalytic degradation pathways in correlation with different intensification approach under neutral pH conditions and
3. to propose optimal parameters for a real-scale photocatalytic process based on a comparative life cycle assessment of various photocatalysis intensification approaches and the use of natural sunlight.

Based on the objectives, four hypotheses were formulated:

H1. The 1H-BT degradation is more effective with TiO_2/CNT photocatalyst under simulated solar light compared to TiO_2;
H2. Existing kinetic models with a local volumetric rate of photon absorption can be modified for 1H-BT degradation in FPCR and CPC reactors;
H3. Photocatalytic degradation products of 1H-BT degradation are negligible compared to ones obtained by photolysis alone and
H4. Photocatalysis under natural irradiation with UV/vis intensified photocatalyst is optimal for scale-up and real-scale application based on the comparative life cycle assessment.

Therefore, regarding the first hypothesis, based on observed experimental data and 1H-BT concentration decreasing, it could be concluded that photocatalysis with TiO_2/CNT is not more efficient than photocatalysis with TiO_2 in both cases when FPCR and CPC reactor was applied. Nevertheless, further analysis by the newest high-resolution techniques, a hybrid Q-TOF, enabled identifying degradation products formed during photocatalysis. With unique insight, it was possible to identify that modification of TiO_2 with CNT had triggered different reaction mechanisms in the CPC reactor. The degradation product with the same fragmentation pattern as the 1H-BT can occur in the system due to triazole ring breakage. On the other hand, the reaction pathway of 1H-BT degradation in FPCR was governed by hydroxylation and benzene

ring breakage. Furthermore, the larger surface of the immobilised photocatalyst in the FPCR (15.6x) compared to the CPC reactor demonstrated that photocatalysis is a surface phenomenon; therefore, the addition of CNT had increased adsorption. Regarding the degradation product's toxicity, mentioned was favourable since hydroxylated species pose a slightly greater negative impact on the environment. Therefore, it can be said that 1H-BT degradation is not necessarily more effective with TiO_2/CNT compared to TiO_2 under simulated solar light. However, from the aspects of reaction mechanisms, TiO_2/CNT contributes to photocatalysis enhancement and environmentally friendlier photocatalysis.

Regarding the second hypothesis, a kinetic model with mass balance was developed and successfully applied for 1H-BT degradation independently on reactor setup and different photocatalysts formulation. The introduction of intrinsic parameters enabled the determination of the intrinsic reaction rate constant for 1H-BT (k_i=3.54×10^{-10} s^{-1}W$^{-0.5}$m$^{1.5}$) applicable in all setups, while the contribution of photocatalyst's formulation and reactor setups was described with appropriate indexes, Y_{cat}=0.769 and Y_{RD}=25, respectively.

As was discussed in the dissertation, 1H-BT is subjected to photolysis under UV, namely UV-C light, while that is not the case with UV-A and UV-B light. However, with the assistance of photocatalysts, it is possible to degrade 1H-BT using UV/vis light and obtain less harmful degradation products.

And lastly, natural irradiation is favourable for the degradation process due to less energy consumption and the higher proportion of irradiation.

Therefore, the constant of the intrinsic reaction rate for 1H-BT was determined by which the first objective of this dissertation was achieved. Moreover, the mechanism's degradation pathways were proposed in correlation with different intensification processes. Namely, while in the FPCR setup, hydroxylation is the dominant reaction pathway of benzene cleavage with emphasized adsorption when TiO_2/CNT was used, in the CPC reactor degradation pathway goes toward nucleophilic addition reaction and triazole cleavage. As mentioned, the second objective of this dissertation was achieved. And finally, based on the comparative LCA, photocatalysis under natural sunlight in the CPC reactor was proposed as the optimum for scaling.

8 LITERATURE

1. Kosek, K.; Luczkiewicz, A.; Fudala-Książek, S.; Jankowska, K.; Szopińska, M.; Svahn, O.; Tränckner, J.; Kaiser, A.; Langas, V.; Björklund, E. Implementation of Advanced Micropollutants Removal Technologies in Wastewater Treatment Plants (WWTPs) - Examples and Challenges Based on Selected EU Countries. *Environ. Sci. Policy* **2020**, *112*, 213–226, doi:10.1016/j.envsci.2020.06.011.

2. Mahmoud, W.M.M.; Rastogi, T.; Kümmerer, K. Application of Titanium Dioxide Nanoparticles as a Photocatalyst for the Removal of Micropollutants Such as Pharmaceuticals from Water. *Curr. Opin. Green Sustain. Chem.* **2017**, *6*, 1–10, doi:10.1016/j.cogsc.2017.04.001.

3. Lado Ribeiro, A.R.; Moreira, N.F.F.; Li Puma, G.; Silva, A.M.T. Impact of Water Matrix on the Removal of Micropollutants by Advanced Oxidation Technologies. *Chem. Eng. J.* **2019**, *363*, 155–173, doi:10.1016/j.cej.2019.01.080.

4. Byrne, C.; Subramanian, G.; Pillai, S.C. Recent Advances in Photocatalysis for Environmental Applications. *J. Environ. Chem. Eng.* **2018**, *6*, 3531–3555, doi:10.1016/j.jece.2017.07.080.

5. Ameta, R.; Solanki, M.S.; Benjamin, S.; Ameta, S.C. Photocatalysis. In *Advanced Oxidation Processes for Waste Water Treatment*; Elsevier, 2018; pp. 135–175 ISBN 9780128105252.

6. Khalid, N.R.; Majid, A.; Tahir, M.B.; Niaz, N.A.; Khalid, S. Carbonaceous-TiO2 Nanomaterials for Photocatalytic Degradation of Pollutants: A Review. *Ceram. Int.* **2017**, *43*, 14552–14571, doi:10.1016/j.ceramint.2017.08.143.

7. Saharan, V.K.; Pinjari, D. V.; Gogate, P.R.; Pandit, A.B. Advanced Oxidation Technologies for Wastewater Treatment. In *Industrial Wastewater Treatment, Recycling and Reuse*; Elsevier, 2014; pp. 141–191.

8. Cindrić, I. Fotokataliza Organskih Tvari Primjenom Titanova (IV) Oksida Modificiranog Bojilima i Pigmentima, Sveučilište u Zagrebu, 2018.

9. Grčić, I.; Marčec, J.; Radetić, L.; Radovan, A.-M.; Melnjak, I.; Jajčinović, I.; Brnardić,

I. Ammonia and Methane Oxidation on TiO2 Supported on Glass Fiber Mesh under Artificial Solar Irradiation. *Environ. Sci. Pollut. Res.* **2020**, doi:10.1007/s11356-020-09561-y.

10. Fernández-Castro, P.; Vallejo, M.; San Román, M.F.; Ortiz, I. Insight on the Fundamentals of Advanced Oxidation Processes. Role and Review of the Determination Methods of Reactive Oxygen Species. *J. Chem. Technol. Biotechnol.* **2015**, *90*, 796–820, doi:10.1002/jctb.4634.

11. Legrini, O.; Oliveros, E.; Braun, A.M. Photochemical Processes for Water Treatment. *Chem. Rev.* **1993**, *93*, 671–698, doi:10.1021/cr00018a003.

12. Deng, Y.; Zhao, R. Advanced Oxidation Processes (AOPs) in Wastewater Treatment. *Curr. Pollut. Reports* **2015**, *1*, 167–176, doi:10.1007/s40726-015-0015-z.

13. Islam, M.T.; Dominguez, A.; Turley, R.S.; Kim, H.; Sultana, K.A.; Shuvo, M.A.I.; Alvarado-Tenorio, B.; Montes, M.O.; Lin, Y.; Gardea-Torresdey, J.; et al. Development of Photocatalytic Paint Based on TiO2 and Photopolymer Resin for the Degradation of Organic Pollutants in Water. *Sci. Total Environ.* **2020**, *704*, 135406, doi:10.1016/j.scitotenv.2019.135406.

14. Orozco-Hernández, L.; Gómez-Oliván, L.M.; Elizalde-Velázquez, A.; Natividad, R.; Fabian-Castoño, L.; SanJuan-Reyes, N. 17-β-Estradiol: Significant Reduction of Its Toxicity in Water Treated by Photocatalysis. *Sci. Total Environ.* **2019**, *669*, 955–963, doi:10.1016/j.scitotenv.2019.03.190.

15. Wang, J.; Zhuan, R. Degradation of Antibiotics by Advanced Oxidation Processes: An Overview. *Sci. Total Environ.* **2020**, *701*, 135023, doi:10.1016/j.scitotenv.2019.135023.

16. Trawiński, J.; Skibiński, R. Studies on Photodegradation Process of Psychotropic Drugs: A Review. *Environ. Sci. Pollut. Res.* **2017**, *24*, 1152–1199, doi:10.1007/s11356-016-7727-5.

17. Schneider, J.; Bahnemann, D.; Ye, Y.; Li Puma, G.; Dionysiou, D.D. *Photocatalysis*; Schneider, J., Bahnemann, D., Ye, J., Li Puma, G., Dionysiou, D.D., Eds.; Energy and Environment Series; Royal Society of Chemistry: Cambridge, 2016; ISBN 978-1-78262-041-9.

18. Dionysiou, D.; Puma, G.L.; Ye, J.; Schneider, J.; Bahnemann, D. Contents. In; 2016; pp. P007-P025 ISBN 9781782621089.

19. Augugliaro, V.; Palmisano, G.; Palmisano, L.; Soria, J. Heterogeneous Photocatalysis and Catalysis. In *Heterogeneous Photocatalysis*; Elsevier, 2019; pp. 1–24.

20. Herrmann, J.-M. Photocatalysis. In *Kirk-Othmer Encyclopedia of Chemical Technology*; John Wiley & Sons, Inc.: Hoboken, NJ, USA, 2017; pp. 1–44 ISBN 9780128105252.

21. Espíndola, J.C.; Vilar, V.J.P. Innovative Light-Driven Chemical/Catalytic Reactors towards Contaminants of Emerging Concern Mitigation: A Review. *Chem. Eng. J.* **2020**, *394*, 124865, doi:10.1016/j.cej.2020.124865.

22. Frederichi, D.; Scaliante, M.H.N.O.; Bergamasco, R. Structured Photocatalytic Systems: Photocatalytic Coatings on Low-Cost Structures for Treatment of Water Contaminated with Micropollutants—a Short Review. *Environ. Sci. Pollut. Res.* **2021**, *28*, 23610–23633, doi:10.1007/s11356-020-10022-9.

23. Khan, M.M.; Pradhan, D.; Sohn, Y. Springer Series on Polymer and Composite Materials Nanocomposites for Visible Light-Induced Photocatalysis. *Nanocomposites Visible Light. Photocatal.* **2017**, 19–40, doi:10.1007/978-3-319-62446-4.

24. Demeestere, K.; Dewulf, J.; Van Langenhove, H. Heterogeneous Photocatalysis as an Advanced Oxidation Process for the Abatement of Chlorinated, Monocyclic Aromatic and Sulfurous Volatile Organic Compounds in Air: State of the Art. *Crit. Rev. Environ. Sci. Technol.* **2007**, *37*, 489–538, doi:10.1080/10643380600966467.

25. Pelaez, M.; Nolan, N.T.; Pillai, S.C.; Seery, M.K.; Falaras, P.; Kontos, A.G.; Dunlop, P.S.M.; Hamilton, J.W.J.; Byrne, J.A.A.; O'Shea, K.; et al. A Review on the Visible Light Active Titanium Dioxide Photocatalysts for Environmental Applications. *Appl. Catal. B Environ.* **2012**, *125*, 331–349, doi:10.1016/j.apcatb.2012.05.036.

26. Liang, R.; Hu, A.; Hatat-Fraile, M.; Zhou, N. Fundamentals on Adsorption, Membrane Filtration, and Advanced Oxidation Processes for Water Treatment. In; 2014; Vol. 22, pp. 1–45.

27. Herrmann, J.-M. Heterogeneous Photocatalysis: Fundamentals and Applications to the

Removal of Various Types of Aqueous Pollutants. *Catal. Today* **1999**, *53*, 115–129, doi:10.1016/S0920-5861(99)00107-8.

28. F. Jović, V.T.; Jović, F.; Tomašić, V. Heterogena Fotokataliza: Osnove i Primjena Za Obradu Onečišćenog Zraka. *Kem. Ind.* **2011**, *60*, 387–403.

29. Li, X.; Yu, J.; Jaroniec, M. Hierarchical Photocatalysts. *Chem. Soc. Rev.* **2016**, *45*, 2603–2636, doi:10.1039/c5cs00838g.

30. Malato, S.; Fernández-Ibáñez, P.; Maldonado, M.I.; Blanco, J.; Gernjak, W. Decontamination and Disinfection of Water by Solar Photocatalysis: Recent Overview and Trends. *Catal. Today* **2009**, *147*, 1–59, doi:10.1016/j.cattod.2009.06.018.

31. Belver, C.; Bedia, J.; Gómez-Avilés, A.; Peñas-Garzón, M.; Rodriguez, J.J. Semiconductor Photocatalysis for Water Purification. In *Nanoscale Materials in Water Purification*; Elsevier, 2019; pp. 581–651.

32. Woan, K.; Pyrgiotakis, G.; Sigmund, W. Photocatalytic Carbon-Nanotube-Ti02 Composites. *Adv. Mater.* **2009**, *21*, 2233–2239, doi:10.1002/adma.200802738.

33. Hurum, D.C.; Agrios, A.G.; Gray, K.A.; Rajh, T.; Thurnauer, M.C. Explaining the Enhanced Photocatalytic Activity of Degussa P25 Mixed-Phase TiO 2 Using EPR. *J. Phys. Chem. B* **2003**, *107*, 4545–4549, doi:10.1021/jp0273934.

34. Nasr, M.; Eid, C.; Habchi, R.; Miele, P.; Bechelany, M. Recent Progress on Titanium Dioxide Nanomaterials for Photocatalytic Applications. *ChemSusChem* **2018**, *11*, 3023–3047, doi:10.1002/cssc.201800874.

35. Marugán, J.; López-Muñoz, M.J.; Fernández-Ibáñez, P.; Malato, S. Solar Photocatalysis: Fundamentals, Reactors and Applications. In *Photocatalysis: Applications*; Dionysiou, D.D., Li Puma, G., Ye, J., Schneider, J., Bahnemann, D., Eds.; The Royal Society of Chemistry 2016: Cambridge, 2016; pp. 92–129 ISBN 978-1-78262-710-4.

36. Saqib, N. us; Adnan, R.; Shah, I. A Mini-Review on Rare Earth Metal-Doped TiO2 for Photocatalytic Remediation of Wastewater. *Environ. Sci. Pollut. Res.* **2016**, *23*, 15941–15951, doi:10.1007/s11356-016-6984-7.

37. Marschall, R.; Wang, L. Non-Metal Doping of Transition Metal Oxides for Visible-Light

Photocatalysis. *Catal. Today* **2014**, *225*, 111–135, doi:10.1016/j.cattod.2013.10.088.

38. Wang, D.-H.; Jia, L.; Wu, X.-L.; Lu, L.-Q.; Xu, A.-W. One-Step Hydrothermal Synthesis of N-Doped TiO 2 /C Nanocomposites with High Visible Light Photocatalytic Activity. *Nanoscale* **2012**, *4*, 576–584, doi:10.1039/C1NR11353D.

39. Cao, S.; Zhao, Z.; Jin, X.; Sheng, W.; Li, S.; Ge, Y.; Dong, M.; Wu, W.; Fang, L. Unique Double-Shelled Hollow Silica Microspheres: Template-Guided Self-Assembly, Tunable Pore Size, High Thermal Stability, and Their Application in Removal of Neutral Red. *J. Mater. Chem.* **2011**, *21*, 19124, doi:10.1039/c1jm13011k.

40. Ihara, T. Visible-Light-Active Titanium Oxide Photocatalyst Realized by an Oxygen-Deficient Structure and by Nitrogen Doping. *Appl. Catal. B Environ.* **2003**, *42*, 403–409, doi:10.1016/S0926-3373(02)00269-2.

41. Shi, J.; Lee, D.-K.; Yoo, H.-I.; Janek, J.; Becker, K.-D. Oxidation Kinetics of Nitrogen Doped TiO2−δ Thin Films. *Phys. Chem. Chem. Phys.* **2012**, *14*, 12930, doi:10.1039/c2cp42559a.

42. Zheng, Z.; Zhao, J.; Yuan, Y.; Liu, H.; Yang, D.; Sarina, S.; Zhang, H.; Waclawika, E.R.; Zhu, H. Tuning the Surface Structure of Nitrogen-Doped TiO 2 Nanofibres-An Effective Method to Enhance Photocatalytic Activities of Visible-Light-Driven Green Synthesis and Degradation. *Chem. - A Eur. J.* **2013**, *19*, 5731–5741, doi:10.1002/chem.201203961.

43. Kim, J.-G.; Shi, D.; Kong, K.-J.; Heo, Y.-U.; Kim, J.H.; Jo, M.R.; Lee, Y.C.; Kang, Y.-M.; Dou, S.X. Structurally and Electronically Designed TiO 2 N x Nanofibers for Lithium Rechargeable Batteries. *ACS Appl. Mater. Interfaces* **2013**, *5*, 691–696, doi:10.1021/am302197y.

44. Etacheri, V.; Seery, M.K.; Hinder, S.J.; Pillai, S.C. Highly Visible Light Active TiO 2−x N x Heterojunction Photocatalysts. *Chem. Mater.* **2010**, *22*, 3843–3853, doi:10.1021/cm903260f.

45. Wu, L.; Yu, J.C.; Fu, X. Characterization and Photocatalytic Mechanism of Nanosized CdS Coupled TiO2 Nanocrystals under Visible Light Irradiation. *J. Mol. Catal. A Chem.* **2006**, *244*, 25–32, doi:10.1016/j.molcata.2005.08.047.

46. Bessekhouad, Y.; Chaoui, N.; Trzpit, M.; Ghazzal, N.; Robert, D.; Weber, J.V. UV–Vis versus Visible Degradation of Acid Orange II in a Coupled CdS/TiO2 Semiconductors Suspension. *J. Photochem. Photobiol. A Chem.* **2006**, *183*, 218–224, doi:10.1016/j.jphotochem.2006.03.025.

47. Etacheri, V.; Michlits, G.; Seery, M.K.; Hinder, S.J.; Pillai, S.C. A Highly Efficient TiO 2– x C x Nano-Heterojunction Photocatalyst for Visible Light Induced Antibacterial Applications. *ACS Appl. Mater. Interfaces* **2013**, *5*, 1663–1672, doi:10.1021/am302676a.

48. Marques, R.R.N.; Sampaio, M.J.; Carrapiço, P.M.; Silva, C.G.; Morales-Torres, S.; Dražić, G.; Faria, J.L.; Silva, A.M.T. Photocatalytic Degradation of Caffeine: Developing Solutions for Emerging Pollutants. *Catal. Today* **2013**, *209*, 108–115, doi:10.1016/j.cattod.2012.10.008.

49. Malinowski, S.; Presečki, I.; Jajčinović, I.; Brnardić, I.; Mandić, V.; Grčić, I. Intensification of Dihydroxybenzenes Degradation over Immobilized TiO2 Based Photocatalysts under Simulated Solar Light. *Appl. Sci.* **2020**, *10*, 7571, doi:10.3390/app10217571.

50. Jajčinović, I.; Brnardić, I.; Kožuh, S.; Tolić, K. The Impact of Multiwalled Carbon Nanotubes on the Photocatalytic Properties of Immobilized TiO2. In Proceedings of the Proceedings Book 18th International Foundrymen Conference: Coexistence of material science and sustainable technology in economic growth; Sisak, 2019; pp. 247–254.

51. Guo, M.Y.; Liu, F.; Leung, Y.H.; Ng, A.M.C.; Djurišić, A.B.; Chan, W.K. TiO2–Carbon Nanotube Composites for Visible Photocatalysts – Influence of TiO2 Crystal Structure. *Curr. Appl. Phys.* **2013**, *13*, 1280–1287, doi:10.1016/j.cap.2013.03.022.

52. Sundar, K.P.; Kanmani, S. Progression of Photocatalytic Reactors and It's Comparison: A Review. *Chem. Eng. Res. Des.* **2020**, *154*, 135–150, doi:10.1016/j.cherd.2019.11.035.

53. Pichat, P. *Photocatalysis and Water Purification*; Pichat, P., Ed.; Wiley-VCH Verlag GmbH & Co. KGaA: Weinheim, Germany, Germany, 2013; ISBN 9783527645404.

54. Tan, L.-L.; Wong, V.L.; Phang, S.J. Recent Advances on TiO2 Photocatalysis for Wastewater Degradation: Fundamentals, Commercial TiO2 Materials, and

Photocatalytic Reactors. In *Handbook of Nanotechnology Applications*; Lau, W.J., Piyachomkwan, K., Faungnawakij, K., Ruktanonchai, U.R., Eds.; Elsevier, 2021; pp. 25–65 ISBN 978-0-12-821506-7.

55. Srikanth, B.; Goutham, R.; Badri Narayan, R.; Ramprasath, A.; Gopinath, K.P.; Sankaranarayanan, A.R. Recent Advancements in Supporting Materials for Immobilised Photocatalytic Applications in Waste Water Treatment. *J. Environ. Manage.* **2017**, *200*, 60–78, doi:10.1016/j.jenvman.2017.05.063.

56. Ghoreishian, S.M.; Badii, K.; Norouzi, M.; Malek, K. Effect of Cold Plasma Pre-Treatment on Photocatalytic Activity of 3D Fabric Loaded with Nano-Photocatalysts: Response Surface Methodology. *Appl. Surf. Sci.* **2016**, *365*, 252–262, doi:10.1016/j.apsusc.2015.12.155.

57. Lin, L.; Wang, H.; Xu, P. Immobilized TiO2-Reduced Graphene Oxide Nanocomposites on Optical Fibers as High Performance Photocatalysts for Degradation of Pharmaceuticals. *Chem. Eng. J.* **2017**, *310*, 389–398, doi:10.1016/j.cej.2016.04.024.

58. Lin, L.; Wang, H.; Luo, H.; Xu, P. Enhanced Photocatalysis Using Side-Glowing Optical Fibers Coated with Fe-Doped TiO2 Nanocomposite Thin Films. *J. Photochem. Photobiol. A Chem.* **2015**, *307–308*, 88–98, doi:10.1016/j.jphotochem.2015.04.010.

59. Mahadik, M.A.; Shinde, S.S.; Mohite, V.S.; Kumbhar, S.S.; Moholkar, A.V.; Rajpure, K.Y.; Ganesan, V.; Nayak, J.; Barman, S.R.; Bhosale, C.H. Visible Light Catalysis of Rhodamine B Using Nanostructured Fe2O3, TiO2 and TiO2/Fe2O3 Thin Films. *J. Photochem. Photobiol. B Biol.* **2014**, *133*, 90–98, doi:10.1016/j.jphotobiol.2014.01.017.

60. Zhao, D.; Yang, X.; Chen, C.; Wang, X. Enhanced Photocatalytic Degradation of Methylene Blue on Multiwalled Carbon Nanotubes–TiO2. *J. Colloid Interface Sci.* **2013**, *398*, 234–239, doi:10.1016/j.jcis.2013.02.017.

61. Wongaree, M.; Chiarakorn, S.; Chuangchote, S. Photocatalytic Improvement under Visible Light in TiO2 Nanoparticles by Carbon Nanotube Incorporation. *J. Nanomater.* **2015**, *2015*, 1–10, doi:10.1155/2015/689306.

62. Elghniji, K.; Ksibi, M.; Elaloui, E. Sol–Gel Reverse Micelle Preparation and Characterization of N-Doped TiO2: Efficient Photocatalytic Degradation of Methylene

Blue in Water under Visible Light. *J. Ind. Eng. Chem.* **2012**, *18*, 178–182, doi:10.1016/j.jiec.2011.11.011.

63. Pyrgiotakis, G.; Lee, S.-H.; Sigmund, W. Advanced Photocatalysis with Anatase Nano-Coated Multi-Walled Carbon Nanotubes. *MRS Proc.* **2005**, *876*, R5.7, doi:10.1557/PROC-876-R5.7.

64. Morales, E.R.; Mathews, N.R.; Reyes-Coronado, D.; Magaña, C.R.; Acosta, D.R.; Alonso-Nunez, G.; Martinez, O.S.; Mathew, X. Physical Properties of the CNT:TiO2 Thin Films Prepared by Sol–Gel Dip Coating. *Sol. Energy* **2012**, *86*, 1037–1044, doi:10.1016/j.solener.2011.06.027.

65. Oh, W.-C.; Zhang, F.-J.; Chen, M.-L. Preparation of MWCNT/TiO2 Composites by Using MWCNTs and Titanium(IV) Alkoxide Precursors in Benzene and Their Photocatalytic Effect and Bactericidal Activity. *Bull. Korean Chem. Soc.* **2009**, *30*, 2637–2642, doi:10.5012/bkcs.2009.30.11.2637.

66. Wang, W.; Serp, P.; Kalck, P.; Faria, J.L. Visible Light Photodegradation of Phenol on MWNT-TiO2 Composite Catalysts Prepared by a Modified Sol–Gel Method. *J. Mol. Catal. A Chem.* **2005**, *235*, 194–199, doi:10.1016/j.molcata.2005.02.027.

67. Bai, H.; Zan, X.; Zhang, L.; Sun, D.D. Multi-Functional CNT/ZnO/TiO2 Nanocomposite Membrane for Concurrent Filtration and Photocatalytic Degradation. *Sep. Purif. Technol.* **2015**, *156*, 922–930, doi:10.1016/j.seppur.2015.10.016.

68. Bakos, L.P.; Justh, N.; Moura da Silva Bezerra da Costa, U.C.; László, K.; Lábár, J.L.; Igricz, T.; Varga-Josepovits, K.; Pasierb, P.; Färm, E.; Ritala, M.; et al. Photocatalytic and Gas Sensitive Multiwalled Carbon Nanotube/TiO2-ZnO and ZnO-TiO2 Composites Prepared by Atomic Layer Deposition. *Nanomaterials* **2020**, *10*, 252, doi:10.3390/nano10020252.

69. Jung, J.-Y.; Lee, D.; Lee, Y.-S. CNT-Embedded Hollow TiO2 Nanofibers with High Adsorption and Photocatalytic Activity under UV Irradiation. *J. Alloys Compd.* **2015**, *622*, 651–656, doi:10.1016/j.jallcom.2014.09.068.

70. Despotović, V. Fotolitička i Fotokatalitička Razgradnja Odabranih Herbicida u Vodenoj Sredini, Prirodno-matematički fakultet, Univerzitet u Novom Sadu, 2014.

71. Herrmann, J.M. Fundamentals and Misconceptions in Photocatalysis. *J. Photochem. Photobiol. A Chem.* **2010**, *216*, 85–93, doi:10.1016/j.jphotochem.2010.05.015.

72. Hoffmann, M.R.; Martin, S.T.; Choi, W.; Bahnemann, D.W. Environmental Applications of Semiconductor Photocatalysis. *Chem. Rev.* **1995**, *95*, 69–96, doi:10.1021/cr00033a004.

73. Wang, D.; Mueses, M.A.; Márquez, J.A.C.; Machuca-Martínez, F.; Grčić, I.; Peralta Muniz Moreira, R.; Li Puma, G. Engineering and Modeling Perspectives on Photocatalytic Reactors for Water Treatment. *Water Res.* **2021**, *202*, 117421, doi:10.1016/j.watres.2021.117421.

74. Boyjoo, Y.; Sun, H.; Liu, J.; Pareek, V.K.; Wang, S. A Review on Photocatalysis for Air Treatment: From Catalyst Development to Reactor Design. *Chem. Eng. J.* **2017**, *310*, 537–559, doi:10.1016/j.cej.2016.06.090.

75. Oliveira de Brito Lira, J.; Riella, H.G.; Padoin, N.; Soares, C. An Overview of Photoreactors and Computational Modeling for the Intensification of Photocatalytic Processes in the Gas-Phase: State-of-Art. *J. Environ. Chem. Eng.* **2021**, *9*, 105068, doi:10.1016/j.jece.2021.105068.

76. Alfano, O.M.; Cassano, A.E. Scaling-Up of Photoreactors. In *Advances in Chemical Engineering: Photocatalytic Technologies*; de Lasa, H.I., Serrano Rosales, B., Eds.; Springer International Publishing, 2009; Vol. 36, pp. 229–287 ISBN 9780123747631.

77. Cassano, A.E.; Alfano, O.M. Design and Analysis of Homogeneous and Heterogeneous Photoreactors. In *Chemical Engineering*; John Wiley & Sons, Ltd: Chichester, UK, 2005; pp. 125–169.

78. Fernandez-Ibañez, P.; McMichael, S.; Tolosana-Moranchel, A.; Byrne, J.A. Chapter 2 Photocatalytic Reactors Design for Water Applications. In *Photocatalysis*; De Gruyter, 2021; pp. 37–76.

79. Abdel-Maksoud, Y.; Imam, E.; Ramadan, A. TiO2 Solar Photocatalytic Reactor Systems: Selection of Reactor Design for Scale-up and Commercialization—Analytical Review. *Catalysts* **2016**, *6*, 138, doi:10.3390/catal6090138.

80. Crittenden, J.C.; Zhang, Y.; Hand, D.W.; Perram, D.L.; Marchand, E.G. Solar Detoxification of Fuel-Contaminated Groundwater Using Fixed-Bed Photocatalysts. *Water Environ. Res.* **1996**, *68*, 270–278, doi:10.2175/106143096X127703.

81. Miranda-García, N.; Suárez, S.; Sánchez, B.; Coronado, J.M.; Malato, S.; Maldonado, M.I. Photocatalytic Degradation of Emerging Contaminants in Municipal Wastewater Treatment Plant Effluents Using Immobilized TiO2 in a Solar Pilot Plant. *Appl. Catal. B Environ.* **2011**, *103*, 294–301, doi:10.1016/j.apcatb.2011.01.030.

82. Remoundaki, E.; Vidali, R.; Kousi, P.; Hatzikioseyian, A.; Tsezos, M. Photolytic and Photocatalytic Alterations of Humic Substances in UV (254 Nm) and Solar Cocentric Parabolic Concentrator (CPC) Reactors. *Desalination* **2009**, *248*, 843–851, doi:10.1016/j.desal.2009.08.002.

83. Jiménez, M.; Ignacio Maldonado, M.; Rodríguez, E.M.; Hernández-Ramírez, A.; Saggioro, E.; Carra, I.; Sánchez Pérez, J.A. Supported TiO 2 Solar Photocatalysis at Semi-Pilot Scale: Degradation of Pesticides Found in Citrus Processing Industry Wastewater, Reactivity and Influence of Photogenerated Species. *J. Chem. Technol. Biotechnol.* **2015**, *90*, 149–157, doi:10.1002/jctb.4299.

84. Navntoft, C.; Araujo, P.; Litter, M.I.; Apella, M.C.; Fernández, D.; Puchulu, M.E.; Hidalgo, M. del V.; Blesa, M.A. Field Tests of the Solar Water Detoxification SOLWATER Reactor in Los Pereyra, Tucumán, Argentina. *J. Sol. Energy Eng.* **2007**, *129*, 127–134, doi:10.1115/1.2391318.

85. Nakano, K.; Obuchi, E.; Takagi, S.; Yamamoto, R.; Tanizaki, T.; Taketomi, M.; Eguchi, M.; Ichida, K.; Suzuki, M.; Hashimoto, A. Photocatalytic Treatment of Water Containing Dinitrophenol and City Water over TiO2/SiO2. *Sep. Purif. Technol.* **2004**, *34*, 67–72, doi:10.1016/S1383-5866(03)00176-X.

86. Bekbölet, M.; Lindner, M.; Weichgrebe, D.; Bahnemann, D.W. Photocatalytic Detoxification with the Thin-Film Fixed-Bed Reactor (TFFBR): Clean-up of Highly Polluted Landfill Effluents Using a Novel TiO2-Photocatalyst. *Sol. Energy* **1996**, *56*, 455–469, doi:10.1016/0038-092X(96)00020-5.

87. Zayani, G.; Bousselmi, L.; Mhenni, F.; Ghrabi, A. Solar Photocatalytic Degradation of Commercial Textile Azo Dyes: Performance of Pilot Plant Scale Thin Film Fixed-Bed

Reactor. *Desalination* **2009**, *246*, 344–352, doi:10.1016/j.desal.2008.03.059.

88. Kanki, T.; Hamasaki, S.; Sano, N.; Toyoda, A.; Hirano, K. Water Purification in a Fluidized Bed Photocatalytic Reactor Using TiO2-Coated Ceramic Particles. *Chem. Eng. J.* **2005**, *108*, 155–160, doi:10.1016/j.cej.2005.01.014.

89. Shavisi, Y.; Sharifnia, S.; Hosseini, S.N.; Khadivi, M.A. Application of TiO2/Perlite Photocatalysis for Degradation of Ammonia in Wastewater. *J. Ind. Eng. Chem.* **2014**, *20*, 278–283, doi:10.1016/j.jiec.2013.03.037.

90. Mozia, S.; Brożek, P.; Przepiórski, J.; Tryba, B.; Morawski, A.W. Immobilized TiO 2 for Phenol Degradation in a Pilot-Scale Photocatalytic Reactor. *J. Nanomater.* **2012**, *2012*, 1–10, doi:10.1155/2012/949764.

91. Chan, A.H.C.; Chan, C.K.; Barford, J.P.; Porter, J.F. Solar Photocatalytic Thin Film Cascade Reactor for Treatment of Benzoic Acid Containing Wastewater. *Water Res.* **2003**, *37*, 1125–1135, doi:10.1016/S0043-1354(02)00465-7.

92. Thu, H.B.; Karkmaz, M.; Puzenat, E.; Guillard, C.; Herrmann, J.-M. From the Fundamentals of Photocatalysis to Its Applications in Environment Protection and in Solar Purification of Water in Arid Countries. *Res. Chem. Intermed.* **2005**, *31*, 449–461, doi:10.1163/1568567053956671.

93. Rao, N.N.; Chaturvedi, V.; Li Puma, G. Novel Pebble Bed Photocatalytic Reactor for Solar Treatment of Textile Wastewater. *Chem. Eng. J.* **2012**, *184*, 90–97, doi:10.1016/j.cej.2012.01.004.

94. Hanaor, D.A.H.; Sorrell, C.C. Sand Supported Mixed-Phase TiO 2 Photocatalysts for Water Decontamination Applications. *Adv. Eng. Mater.* **2014**, *16*, 248–254, doi:10.1002/adem.201300259.

95. Adamek, E.; Baran, W.; Ziemiańska-Błaszczyk, J.; Sobczak, A. Immobilisation of TiO2-P25 on a Glass Fibre Mat: Preparation, Photocatalytic Activity and Stability. *Sol. Energy* **2019**, *188*, 1232–1242, doi:10.1016/j.solener.2019.07.034.

96. Azadi, S.; Karimi-Jashni, A.; Javadpour, S.; Amiri, H. Photocatalytic Treatment of Landfill Leachate Using Cascade Photoreactor with Immobilized W-C-Codoped TiO2

Nanoparticles. *J. Water Process Eng.* **2020**, *36*, 101307, doi:10.1016/j.jwpe.2020.101307.

97. Matsuoka, M.; Toyao, T.; Horiuchi, Y.; Takeuchi, M.; Anpo, M. Wastewater Treatment Using Highly Functional Immobilized TiO2 Thin-Film Photocatalysts. In *Photocatalysis and Water Purification: From Fundamentals to Recent Applications*; Pichat, P., Ed.; Wiley-VCH Verlag GmbH & Co. KGaA: Weinheim, Germany, 2013; pp. 179–198 ISBN 978-3-527-64542-8.

98. Rodriguez-Acosta, J.W.; Mueses, M.Á.; Machuca-Martínez, F. Mixing Rules Formulation for a Kinetic Model of the Langmuir-Hinshelwood Semipredictive Type Applied to the Heterogeneous Photocatalytic Degradation of Multicomponent Mixtures. *Int. J. Photoenergy* **2014**, *2014*, 1–9, doi:10.1155/2014/817538.

99. Carp, O.; Huisman, C.L.; Reller, A. Photoinduced Reactivity of Titanium Dioxide. *Prog. Solid State Chem.* **2004**, *32*, 33–177, doi:10.1016/j.progsolidstchem.2004.08.001.

100. Gaya, U.I.; Abdullah, A.H. Heterogeneous Photocatalytic Degradation of Organic Contaminants over Titanium Dioxide: A Review of Fundamentals, Progress and Problems. *J. Photochem. Photobiol. C Photochem. Rev.* **2008**, *9*, 1–12, doi:10.1016/j.jphotochemrev.2007.12.003.

101. Minella, M.; De Laurentiis, E.; Pellegrino, F.; Prozzi, M.; Dal Bello, F.; Maurino, V.; Minero, C. Photocatalytic Transformations of 1H-Benzotriazole and Benzotriazole Derivates. *Nanomaterials* **2020**, *10*, 1835, doi:10.3390/nano10091835.

102. Shi, Z.-Q.; Liu, Y.-S.; Xiong, Q.; Cai, W.-W.; Ying, G.-G. Occurrence, Toxicity and Transformation of Six Typical Benzotriazoles in the Environment: A Review. *Sci. Total Environ.* **2019**, *661*, 407–421, doi:10.1016/j.scitotenv.2019.01.138.

103. Lee, J.-E.; Kim, M.-K.; Lee, J.-Y.; Lee, Y.-M.; Zoh, K.-D. Degradation Kinetics and Pathway of 1H-Benzotriazole during UV/Chlorination Process. *Chem. Eng. J.* **2019**, *359*, 1502–1508, doi:10.1016/j.cej.2018.11.026.

104. Weidauer, C.; Davis, C.; Raeke, J.; Seiwert, B.; Reemtsma, T. Sunlight Photolysis of Benzotriazoles – Identification of Transformation Products and Pathways. *Chemosphere* **2016**, *154*, 416–424, doi:10.1016/j.chemosphere.2016.03.090.

105. Bahnmüller, S.; Loi, C.H.; Linge, K.L.; Gunten, U. von; Canonica, S. Degradation Rates of Benzotriazoles and Benzothiazoles under UV-C Irradiation and the Advanced Oxidation Process UV/H2O2. *Water Res.* **2015**, *74*, 143–154, doi:10.1016/j.watres.2014.12.039.

106. Reemtsma, T.; Miehe, U.; Duennbier, U.; Jekel, M. Polar Pollutants in Municipal Wastewater and the Water Cycle: Occurrence and Removal of Benzotriazoles. *Water Res.* **2010**, *44*, 596–604, doi:10.1016/j.watres.2009.07.016.

107. Dai, Q.; Chen, W.; Luo, J.; Luo, X. Abatement Kinetics of Highly Concentrated 1H-Benzotriazole in Aqueous Solution by Ozonation. *Sep. Purif. Technol.* **2017**, *183*, 327–332, doi:10.1016/j.seppur.2017.03.059.

108. Alotaibi, M.D.; McKinley, A.J.; Patterson, B.M.; Reeder, A.Y. Benzotriazoles in the Aquatic Environment: A Review of Their Occurrence, Toxicity, Degradation and Analysis. *Water, Air, Soil Pollut.* **2015**, *226*, 226, doi:10.1007/s11270-015-2469-4.

109. Yin, W.; Shao, H.; Huo, Z.; Wang, S.; Zou, Q.; Xu, G. Degradation of Anticorrosive Agent Benzotriazole by Electron Beam Irradiation: Mechanisms, Degradation Pathway and Toxicological Analysis. *Chemosphere* **2022**, *287*, 132133, doi:10.1016/j.chemosphere.2021.132133.

110. Katritzky, A.R.; Yannakopoulou, K.; Anders, E.; Stevens, J.; Szafran, M. Ab Initio and Semiempirical Calculations on the Tautomeric Equilibria of N-Unsubstituted and N-Substituted Benzotriazoles. *J. Org. Chem.* **1990**, *55*, 5683–5687, doi:10.1021/jo00309a009.

111. National Center for Biotechnology Information 1H-Benzotriazole Available online: https://pubchem.ncbi.nlm.nih.gov/compound/1H-Benzotriazole (accessed on 6 October 2022).

112. Dennis Hall, C.; Panda, S.S. The Benzotriazole Story. In *Advances in Heterocyclic Chemistry: Heterocyclic Chemistry in the 21st Centur*; Scriven, E.F.V., Ramsden, C.A., Eds.; Academic Press, 2016; Vol. 119, pp. 1–23 ISBN 9780128046951.

113. Bajaj, K.; Sakhuja, R. Benzotriazole: Much More Than Just Synthetic Heterocyclic Chemistry. In *The Chemistry of Benzotriazole Derivatives. Topics in Heterocyclic*

Chemistry; Monbaliu, J.-C.M., Ed.; Springer, Cham: New York, 2015; Vol. 43, pp. 235–283 ISBN 978-3-319-31552-2.

114. US Goverment 21CFR178.3910 Surface Lubricants Used in the Manufacture of Metallic Articles. Available online: https://www.accessdata.fda.gov/scripts/cdrh/cfdocs/cfCFR/CFRSearch.cfm?fr=178.3910.

115. Ye, Y. Micropollutant Degradation in Water by Photochemical Processes, Wageningen University, 2018.

116. Chavoshani, A.; Hashemi, M.; Mehdi Amin, M.; Ameta, S.C. Introduction. In *Micropollutants and Challenges*; Elsevier, 2020; pp. 1–33.

117. Asimakopoulos, A.G.; Ajibola, A.; Kannan, K.; Thomaidis, N.S. Occurrence and Removal Efficiencies of Benzotriazoles and Benzothiazoles in a Wastewater Treatment Plant in Greece. *Sci. Total Environ.* **2013**, *452–453*, 163–171, doi:10.1016/j.scitotenv.2013.02.041.

118. Stasinakis, A.S.; Thomaidis, N.S.; Arvaniti, O.S.; Asimakopoulos, A.G.; Samaras, V.G.; Ajibola, A.; Mamais, D.; Lekkas, T.D. Contribution of Primary and Secondary Treatment on the Removal of Benzothiazoles, Benzotriazoles, Endocrine Disruptors, Pharmaceuticals and Perfluorinated Compounds in a Sewage Treatment Plant. *Sci. Total Environ.* **2013**, *463–464*, 1067–1075, doi:10.1016/j.scitotenv.2013.06.087.

119. Herzog, B.; Lemmer, H.; Helmreich, B.; Horn, H.; Müller, E. Monitoring Benzotriazoles: A 1 Year Study on Concentrations and Removal Efficiencies in Three Different Wastewater Treatment Plants. *Water Sci. Technol.* **2014**, *69*, 710–717, doi:10.2166/wst.2013.766.

120. Nödler, K.; Licha, T.; Bester, K.; Sauter, M. Development of a Multi-Residue Analytical Method, Based on Liquid Chromatography–Tandem Mass Spectrometry, for the Simultaneous Determination of 46 Micro-Contaminants in Aqueous Samples. *J. Chromatogr. A* **2010**, *1217*, 6511–6521, doi:10.1016/j.chroma.2010.08.048.

121. Weiss, S.; Reemtsma, T. Determination of Benzotriazole Corrosion Inhibitors from Aqueous Environmental Samples by Liquid Chromatography-Electrospray Ionization-

Tandem Mass Spectrometry. *Anal. Chem.* **2005**, *77*, 7415–7420, doi:10.1021/ac051203e.

122. Weiss, S.; Jakobs, J.; Reemtsma, T. Discharge of Three Benzotriazole Corrosion Inhibitors with Municipal Wastewater and Improvements by Membrane Bioreactor Treatment and Ozonation. *Environ. Sci. Technol.* **2006**, *40*, 7193–7199, doi:10.1021/es061434i.

123. Voutsa, D.; Hartmann, P.; Schaffner, C.; Giger, W. Benzotriazoles, Alkylphenols and Bisphenol A in Municipal Wastewaters and in the Glatt River, Switzerland. *Environ. Sci. Pollut. Res. - Int.* **2006**, *13*, 333–341, doi:10.1065/espr2006.01.295.

124. Liu, Y.-S.; Ying, G.-G.; Shareef, A.; Kookana, R.S. Simultaneous Determination of Benzotriazoles and Ultraviolet Filters in Ground Water, Effluent and Biosolid Samples Using Gas Chromatography–Tandem Mass Spectrometry. *J. Chromatogr. A* **2011**, *1218*, 5328–5335, doi:10.1016/j.chroma.2011.05.100.

125. Loi, C.H.; Busetti, F.; Linge, K.L.; Joll, C.A. Development of a Solid-Phase Extraction Liquid Chromatography Tandem Mass Spectrometry Method for Benzotriazoles and Benzothiazoles in Wastewater and Recycled Water. *J. Chromatogr. A* **2013**, *1299*, 48–57, doi:10.1016/j.chroma.2013.04.073.

126. Janna, H.; Scrimshaw, M.D.; Williams, R.J.; Churchley, J.; Sumpter, J.P. From Dishwasher to Tap? Xenobiotic Substances Benzotriazole and Tolyltriazole in the Environment. *Environ. Sci. Technol.* **2011**, *45*, 3858–3864, doi:10.1021/es103267g.

127. Carpinteiro, I.; Abuin, B.; Ramil, M.; Rodríguez, I.; Cela, R. Simultaneous Determination of Benzotriazole and Benzothiazole Derivatives in Aqueous Matrices by Mixed-Mode Solid-Phase Extraction Followed by Liquid Chromatography–Tandem Mass Spectrometry. *Anal. Bioanal. Chem.* **2012**, *402*, 2471–2478, doi:10.1007/s00216-012-5718-z.

128. Herrero, P.; Borrull, F.; Pocurull, E.; Marcé, R.M. Efficient Tandem Solid-Phase Extraction and Liquid Chromatography-Triple Quadrupole Mass Spectrometry Method to Determine Polar Benzotriazole, Benzothiazole and Benzenesulfonamide Contaminants in Environmental Water Samples. *J. Chromatogr. A* **2013**, *1309*, 22–32, doi:10.1016/j.chroma.2013.08.018.

129. Herrero, P.; Borrull, F.; Pocurull, E.; Marcé, R.M. A Quick, Easy, Cheap, Effective, Rugged and Safe Extraction Method Followed by Liquid Chromatography-(Orbitrap) High Resolution Mass Spectrometry to Determine Benzotriazole, Benzothiazole and Benzenesulfonamide Derivates in Sewage Sludge. *J. Chromatogr. A* **2014**, *1339*, 34–41, doi:10.1016/j.chroma.2014.02.081.

130. Herrero, P.; Borrull, F.; Marcé, R.M.; Pocurull, E. A Pressurised Hot Water Extraction and Liquid Chromatography–High Resolution Mass Spectrometry Method to Determine Polar Benzotriazole, Benzothiazole and Benzenesulfonamide Derivates in Sewage Sludge. *J. Chromatogr. A* **2014**, *1355*, 53–60, doi:10.1016/j.chroma.2014.05.086.

131. Karthikraj, R.; Kannan, K. Mass Loading and Removal of Benzotriazoles, Benzothiazoles, Benzophenones, and Bisphenols in Indian Sewage Treatment Plants. *Chemosphere* **2017**, *181*, 216–223, doi:10.1016/j.chemosphere.2017.04.075.

132. Chung, K.H.-Y.; Lin, Y.-C.; Lin, A.Y.-C. The Persistence and Photostabilizing Characteristics of Benzotriazole and 5-Methyl-1H-Benzotriazole Reduce the Photochemical Behavior of Common Photosensitizers and Organic Compounds in Aqueous Environments. *Environ. Sci. Pollut. Res.* **2018**, *25*, 5911–5920, doi:10.1007/s11356-017-0900-7.

133. Heeb, F.; Singer, H.; Pernet-Coudrier, B.; Qi, W.; Liu, H.; Longrée, P.; Müller, B.; Berg, M. Organic Micropollutants in Rivers Downstream of the Megacity Beijing: Sources and Mass Fluxes in a Large-Scale Wastewater Irrigation System. *Environ. Sci. Technol.* **2012**, *46*, 8680–8688, doi:10.1021/es301912q.

134. Zhang, Z.; Yang, H.; Wu, G.; Li, Z.; Song, T.; Li, X. qian Probing the Difference between BH3 Groove of Mcl-1 and Bcl-2 Protein: Implications for Dual Inhibitors Design. *Eur. J. Med. Chem.* **2011**, *46*, 3909–3916, doi:10.1016/j.ejmech.2011.05.062.

135. van Leerdam, J.A.; Hogenboom, A.C.; van der Kooi, M.M.E.; de Voogt, P. Determination of Polar 1H-Benzotriazoles and Benzothiazoles in Water by Solid-Phase Extraction and Liquid Chromatography LTQ FT Orbitrap Mass Spectrometry. *Int. J. Mass Spectrom.* **2009**, *282*, 99–107, doi:10.1016/j.ijms.2009.02.018.

136. Loos, R.; Gawlik, B.M.; Locoro, G.; Rimaviciute, E.; Contini, S.; Bidoglio, G. EU-Wide Survey of Polar Organic Persistent Pollutants in European River Waters. *Environ. Pollut.*

2009, *157*, 561–568, doi:10.1016/j.envpol.2008.09.020.

137. Loos, R.; Tavazzi, S.; Mariani, G.; Suurkuusk, G.; Paracchini, B.; Umlauf, G. Analysis of Emerging Organic Contaminants in Water, Fish and Suspended Particulate Matter (SPM) in the Joint Danube Survey Using Solid-Phase Extraction Followed by UHPLC-MS-MS and GC–MS Analysis. *Sci. Total Environ.* **2017**, *607–608*, 1201–1212, doi:10.1016/j.scitotenv.2017.07.039.

138. Cancilla, D.A.; Martinez, J.; van Aggelen, G.C. Detection of Aircraft Deicing/Antiicing Fluid Additives in a Perched Water Monitoring Well at an International Airport. *Environ. Sci. Technol.* **1998**, *32*, 3834–3835, doi:10.1021/es980489k.

139. Loos, R.; Locoro, G.; Comero, S.; Contini, S.; Schwesig, D.; Werres, F.; Balsaa, P.; Gans, O.; Weiss, S.; Blaha, L.; et al. Pan-European Survey on the Occurrence of Selected Polar Organic Persistent Pollutants in Ground Water. *Water Res.* **2010**, *44*, 4115–4126, doi:10.1016/j.watres.2010.05.032.

140. Breedveld, G.D.; Roseth, R.; Sparrevik, M.; Hem, L.J. Persistence of the De-Icing Additive Benzotriazole at an Abandoned Airport. *Water, Air, Soil Pollut. Focus* **2003**, *3*, 91–101, doi:https://doi.org/10.1023/A:1023961213839.

141. Zhang, Z.; Ren, N.; Li, Y.-F.; Kunisue, T.; Gao, D.; Kannan, K. Determination of Benzotriazole and Benzophenone UV Filters in Sediment and Sewage Sludge. *Environ. Sci. Technol.* **2011**, *45*, 3909–3916, doi:10.1021/es2004057.

142. Nakata, H.; Murata, S.; Filatreau, J. Occurrence and Concentrations of Benzotriazole UV Stabilizers in Marine Organisms and Sediments from the Ariake Sea, Japan. *Environ. Sci. Technol.* **2009**, *43*, 6920–6926, doi:10.1021/es900939j.

143. Wang, L.; Asimakopoulos, A.G.; Moon, H.-B.; Nakata, H.; Kannan, K. Benzotriazole, Benzothiazole, and Benzophenone Compounds in Indoor Dust from the United States and East Asian Countries. *Environ. Sci. Technol.* **2013**, *47*, 4752–4759, doi:10.1021/es305000d.

144. Barbosa, M.O.; Moreira, N.F.F.; Ribeiro, A.R.; Pereira, M.F.R.; Silva, A.M.T. Occurrence and Removal of Organic Micropollutants: An Overview of the Watch List of EU Decision 2015/495. *Water Res.* **2016**, *94*, 257–279,

doi:10.1016/j.watres.2016.02.047.

145. LeFevre, G.H.; Müller, C.E.; Li, R.J.; Luthy, R.G.; Sattely, E.S. Rapid Phytotransformation of Benzotriazole Generates Synthetic Tryptophan and Auxin Analogs in Arabidopsis. *Environ. Sci. Technol.* **2015**, *49*, 10959–10968, doi:10.1021/acs.est.5b02749.

146. LeFevre, G.H.; Lipsky, A.; Hyland, K.C.; Blaine, A.C.; Higgins, C.P.; Luthy, R.G. Benzotriazole (BT) and BT Plant Metabolites in Crops Irrigated with Recycled Water. *Environ. Sci. Water Res. Technol.* **2017**, *3*, 213–223, doi:10.1039/C6EW00270F.

147. Yao, L.; Zhao, J.-L.; Liu, Y.-S.; Yang, Y.-Y.; Liu, W.-R.; Ying, G.-G. Simultaneous Determination of 24 Personal Care Products in Fish Muscle and Liver Tissues Using QuEChERS Extraction Coupled with Ultra Pressure Liquid Chromatography-Tandem Mass Spectrometry and Gas Chromatography-Mass Spectrometer Analyses. *Anal. Bioanal. Chem.* **2016**, *408*, 8177–8193, doi:10.1007/s00216-016-9924-y.

148. Yao, L.; Lv, Y.-Z.; Zhang, L.-J.; Liu, W.-R.; Zhao, J.-L.; Liu, Y.-S.; Zhang, Q.-Q.; Ying, G.-G. Determination of 24 Personal Care Products in Fish Bile Using Hybrid Solvent Precipitation and Dispersive Solid Phase Extraction Cleanup with Ultrahigh Performance Liquid Chromatography-Tandem Mass Spectrometry and Gas Chromatography-Mass Spectrometry. *J. Chromatogr. A* **2018**, *1551*, 29–40, doi:10.1016/j.chroma.2018.04.003.

149. Yao, L.; Zhao, J.-L.; Liu, Y.-S.; Zhang, Q.-Q.; Jiang, Y.-X.; Liu, S.; Liu, W.-R.; Yang, Y.-Y.; Ying, G.-G. Personal Care Products in Wild Fish in Two Main Chinese Rivers: Bioaccumulation Potential and Human Health Risks. *Sci. Total Environ.* **2018**, *621*, 1093–1102, doi:10.1016/j.scitotenv.2017.10.117.

150. Seeland, A.; Oetken, M.; Kiss, A.; Fries, E.; Oehlmann, J. Acute and Chronic Toxicity of Benzotriazoles to Aquatic Organisms. *Environ. Sci. Pollut. Res.* **2012**, *19*, 1781–1790, doi:10.1007/s11356-011-0705-z.

151. Cancilla, D.A.; Holtkamp, A.; Matassa, L.; Fang, X. Isolation and Characterization of Microtox®-Active Components from Aircraft de-Icing/Anti-Icing Fluids. *Environ. Toxicol. Chem.* **1997**, *16*, 430–434, doi:10.1002/etc.5620160306.

152. Damalas, D.E.; Bletsou, A.A.; Agalou, A.; Beis, D.; Thomaidis, N.S. Assessment of the Acute Toxicity, Uptake and Biotransformation Potential of Benzotriazoles in Zebrafish (Danio Rerio) Larvae Combining HILIC- with RPLC-HRMS for High-Throughput Identification. *Environ. Sci. Technol.* **2018**, *52*, 6023–6031, doi:10.1021/acs.est.8b01327.

153. Asimakopoulos, A.G.; Wang, L.; Thomaidis, N.S.; Kannan, K. Benzotriazoles and Benzothiazoles in Human Urine from Several Countries: A Perspective on Occurrence, Biotransformation, and Human Exposure. *Environ. Int.* **2013**, *59*, 274–281, doi:10.1016/j.envint.2013.06.007.

154. Mazioti, A.A.; Stasinakis, A.S.; Psoma, A.K.; Thomaidis, N.S.; Andersen, H.R. Hybrid Moving Bed Biofilm Reactor for the Biodegradation of Benzotriazoles and Hydroxy-Benzothiazole in Wastewater. *J. Hazard. Mater.* **2017**, *323*, 299–310, doi:10.1016/j.jhazmat.2016.06.035.

155. Yuan, H.; Herzog, B.; Helmreich, B.; Lemmer, H.; Müller, E. Determination of Optimal Conditions for 5-Methyl-Benzotriazole Biodegradation with Activated Sludge Communities by Dilution of the Inoculum. *Sci. Total Environ.* **2014**, *487*, 756–762, doi:10.1016/j.scitotenv.2013.10.111.

156. Herzog, B.; Huber, B.; Lemmer, H.; Horn, H.; Müller, E. Analysis and in Situ Characterization of Activated Sludge Communities Capable of Benzotriazole Biodegradation. *Environ. Sci. Eur.* **2013**, *25*, 31, doi:10.1186/2190-4715-25-31.

157. Chen, Y.; Ye, J.; Li, C.; Zhou, P.; Liu, J.; Ou, H. Degradation of 1 H -Benzotriazole by UV/H 2 O 2 and UV/TiO 2 : Kinetics, Mechanisms, Products and Toxicology. *Environ. Sci. Water Res. Technol.* **2018**, *4*, 1282–1294, doi:10.1039/C8EW00116B.

158. Kim, D.K.; He, Y.; Jeon, J.; O'Shea, K.E. Irradiation of Ultrasound to 5-Methylbenzotriazole in Aqueous Phase: Degradation Kinetics and Mechanisms. *Ultrason. Sonochem.* **2016**, *31*, 227–236, doi:10.1016/j.ultsonch.2016.01.006.

159. Zúñiga-Benítez, H.; Soltan, J.; Peñuela, G. Ultrasonic Degradation of 1-H-Benzotriazole in Water. *Water Sci. Technol.* **2014**, *70*, 152–159, doi:10.2166/wst.2014.210.

160. Ahmadi, M.; Rahmani, K.; Rahmani, A.; Rahmani, H. Removal of Benzotriazole by

Photo-Fenton like Process Using Nano Zero-Valent Iron: Response Surface Methodology with a Box-Behnken Design. *Polish J. Chem. Technol.* **2017**, *19*, 104–112, doi:10.1515/pjct-2017-0015.

161. Ahmed, Y.; Zhong, J.; Yuan, Z.; Guo, J. Simultaneous Removal of Antibiotic Resistant Bacteria, Antibiotic Resistance Genes, and Micropollutants by a Modified Photo-Fenton Process. *Water Res.* **2021**, *197*, 117075, doi:10.1016/j.watres.2021.117075.

162. Zhang, Y.; Ji, H.; Liu, W.; Wang, Z.; Song, Z.; Wang, Y.; Liu, C.; Xu, B.; Qi, F. Synchronous Degradation of Aqueous Benzotriazole and Bromate Reduction in Catalytic Ozonation: Effect of Matrix Factor, Degradation Mechanism and Application Strategy in Water Treatment. *Sci. Total Environ.* **2020**, *727*, 138696, doi:10.1016/j.scitotenv.2020.138696.

163. Mawhinney, D.B.; Vanderford, B.J.; Snyder, S.A. Transformation of 1 H -Benzotriazole by Ozone in Aqueous Solution. *Environ. Sci. Technol.* **2012**, *46*, 7102–7111, doi:10.1021/es300338e.

164. Prosen, H.; Malinović, B.; Korenčić, E.; Markelj, J.; Vranješ, S.; Đuričić, T. Electrooxidation of Polar Benzotriazole - The Impact of Supporting Electrolyte. *J. Chem. Technol. Environ.* **2020**, *1*, 28–33, doi:https://doi.org/10.7251/JCTE2001028P.

165. Nika, M.-C.; Bletsou, A.A.; Koumaki, E.; Noutsopoulos, C.; Mamais, D.; Stasinakis, A.S.; Thomaidis, N.S. Chlorination of Benzothiazoles and Benzotriazoles and Transformation Products Identification by LC-HR-MS/MS. *J. Hazard. Mater.* **2017**, *323*, 400–413, doi:10.1016/j.jhazmat.2016.03.035.

166. Yang, T.; Mai, J.; Wu, S.; Liu, C.; Tang, L.; Mo, Z.; Zhang, M.; Guo, L.; Liu, M.; Ma, J. UV/Chlorine Process for Degradation of Benzothiazole and Benzotriazole in Water: Efficiency, Mechanism and Toxicity Evaluation. *Sci. Total Environ.* **2021**, *760*, 144304, doi:10.1016/j.scitotenv.2020.144304.

167. Pandis, P.K.; Kalogirou, C.; Kanellou, E.; Vaitsis, C.; Savvidou, M.G.; Sourkouni, G.; Zorpas, A.A.; Argirusis, C. Key Points of Advanced Oxidation Processes (AOPs) for Wastewater, Organic Pollutants and Pharmaceutical Waste Treatment: A Mini Review. *ChemEngineering* **2022**, *6*, 8, doi:10.3390/chemengineering6010008.

168. Coha, M.; Farinelli, G.; Tiraferri, A.; Minella, M.; Vione, D. Advanced Oxidation Processes in the Removal of Organic Substances from Produced Water: Potential, Configurations, and Research Needs. *Chem. Eng. J.* **2021**, *414*, 128668, doi:10.1016/j.cej.2021.128668.

169. Čižmar, T.; Panžić, I.; Salamon, K.; Grčić, I.; Radetić, L.; Marčec, J.; Gajović, A. Low-Cost Synthesis of Cu-Modified Immobilized Nanoporous TiO2 for Photocatalytic Degradation of 1H-Benzotriazole. *Catalysts* **2019**, *10*, 19, doi:10.3390/catal10010019.

170. Čižmar, T.; Kojić, V.; Rukavina, M.; Brkljačić, L.; Salamon, K.; Grčić, I.; Radetić, L.; Gajović, A. Hydrothermal Synthesis of FeOOH and Fe2O3 Modified Self-Organizing Immobilized TiO2 Nanotubes for Photocatalytic Degradation of 1H-Benzotriazole. *Catalysts* **2020**, *10*, 1371, doi:10.3390/catal10121371.

171. Marčec, J. Photocatalytic Oxidation of 1H-Benzotriazole: Kinetics and Degradation Pathways, University of Zagreb, 2022.

172. Frindy, S.; Li, Y.; Sillanpää, M. Synthesis of Novel α-Fe2O3-Bi2S3-Gr for Efficient Photocatalytic Degradation of Environmental Pollutants under Visible-LED Light Irradiation. *Sep. Purif. Technol.* **2022**, *284*, 120241, doi:10.1016/j.seppur.2021.120241.

173. Xu, J.; Li, L.; Guo, C.; Zhang, Y.; Wang, S. Removal of Benzotriazole from Solution by BiOBr Photocatalysis under Simulated Solar Irradiation. *Chem. Eng. J.* **2013**, *221*, 230–237, doi:10.1016/j.cej.2013.01.081.

174. Li, Z.; He, Z.; Lai, H.; He, Y.; Zhu, Z.; Chen, Y.; Jin, T. A Novel High-Efficiency Photocatalyst Ta2O5/PtCl2 Nanosheets for Benzotriazole Degradation. *J. Environ. Chem. Eng.* **2021**, *9*, 106345, doi:10.1016/j.jece.2021.106345.

175. Ahmadi, M.; Ghanbari, F.; Moradi, M. Photocatalysis Assisted by Peroxymonosulfate and Persulfate for Benzotriazole Degradation: Effect of PH on Sulfate and Hydroxyl Radicals. *Water Sci. Technol.* **2015**, *72*, 2095–2102, doi:10.2166/wst.2015.437.

176. Garg, S.; Yadav, M.; Chandra, A.; Sapra, S.; Gahlawat, S.; Ingole, P.P.; Pap, Z.; Hernadi, K. Biofabricated BiOI with Enhanced Photocatalytic Activity under Visible Light Irradiation. *RSC Adv.* **2018**, *8*, 29022–29030, doi:10.1039/C8RA05661G.

177. Yao, Y.; Luan, J. Preparation, Property Characterization of Gd2YSbO7/ZnBiNbO5 Heterojunction Photocatalyst for Photocatalytic Degradation of Benzotriazole under Visible Light Irradiation. *Catalysts* **2022**, *12*, 159, doi:10.3390/catal12020159.

178. Dyamenahalli, K.; Famili, A.; Shandas, R. Characterization of Shape-Memory Polymers for Biomedical Applications. In *Shape Memory Polymers for Biomedical Applications*; Yahia, L., Ed.; Elsevier: Cambridge, 2015; pp. 35–63.

179. Passos, M.L.C.; Sarraguça, M.C.; Saraiva, M.L.M.F.S.; Prasada Rao, T.; Biju, V.M. Organic Compounds. In *Reference Module in Chemistry, Molecular Sciences and Chemical Engineering*; Elsevier, 2018; pp. 236–243.

180. Radetić, L.; Marčec, J.; Brnardić, I.; Čižmar, T.; Grčić, I. Study of Photocatalytic Oxidation of Micropollutants in Water and Intensification Case Study. *Catalysts* **2022**, *12*, doi:10.3390/catal12111463.

181. Ramart-Lucas, M.; Hoch, J.; Grumez, M. 1H-Benzotriazole Available online: https://webbook.nist.gov/cgi/cbook.cgi?ID=C95147&Mask=400 (accessed on 6 October 2022).

182. Schymanski, E.L.; Singer, H.P.; Longrée, P.; Loos, M.; Ruff, M.; Stravs, M.A.; Ripollés Vidal, C.; Hollender, J. Strategies to Characterize Polar Organic Contamination in Wastewater: Exploring the Capability of High Resolution Mass Spectrometry. *Environ. Sci. Technol.* **2014**, *48*, 1811–1818, doi:10.1021/es4044374.

183. Gago-Ferrero, P.; Schymanski, E.L.; Bletsou, A.A.; Aalizadeh, R.; Hollender, J.; Thomaidis, N.S. Extended Suspect and Non-Target Strategies to Characterize Emerging Polar Organic Contaminants in Raw Wastewater with LC-HRMS/MS. *Environ. Sci. Technol.* **2015**, *49*, 12333–12341, doi:10.1021/acs.est.5b03454.

184. Agilent-Technologies *Basics of LC/MS*; Santa Clara, USA, 1998;

185. Agilent-Technologies Agilent 6200 Series TOF and 6500 Series Q-TOF LC/MS System 2015, 144.

186. Zhou, L.; Fan, D.; Yin, W.; Gu, W.; Wang, Z.; Liu, J.; Xu, Y.; Shi, L.; Liu, M.; Ji, G. Comparison of Seven in Silico Tools for Evaluating of Daphnia and Fish Acute Toxicity:

Case Study on Chinese Priority Controlled Chemicals and New Chemicals. *BMC Bioinformatics* **2021**, *22*, 151, doi:10.1186/s12859-020-03903-w.

187. Melnikov, F.; Kostal, J.; Voutchkova-Kostal, A.; Zimmerman, J.B.; T. Anastas, P. Assessment of Predictive Models for Estimating the Acute Aquatic Toxicity of Organic Chemicals. *Green Chem.* **2016**, *18*, 4432–4445, doi:10.1039/C6GC00720A.

188. Martin, T.M. User's Guide for T.E.S.T. (Toxicity Estimation Software Tool) 2020, 63.

189. Martin, T.M.; Harten, P.; Venkatapathy, R.; Das, S.; Young, D.M. A Hierarchical Clustering Methodology for the Estimation of Toxicity. *Toxicol. Mech. Methods* **2008**, *18*, 251–266, doi:10.1080/15376510701857353.

190. Gorre, M.; Heijungs, R.; Huppes, G.; Kleijn, R.; de Koning, A.; van Oers, L.; Wegener Sleeswijk, A.; Suh, S.; Udo de Haes, H.A.; de Bruijn, H.; et al. *Handbook on Life Cycle Assessment*; Guine, J., Ed.; 2nd ed.; Kluwer Academic Publishers: New York, 2004;

191. Foteinis, S.; Borthwick, A.G.L.; Frontistis, Z.; Mantzavinos, D.; Chatzisymeon, E. Environmental Sustainability of Light-Driven Processes for Wastewater Treatment Applications. *J. Clean. Prod.* **2018**, *182*, 8–15, doi:10.1016/j.jclepro.2018.02.038.

192. Pini, M.; Bondioli, F.; Montecchi, R.; Neri, P.; Ferrari, A.M. Environmental and Human Health Assessment of Life Cycle of NanoTiO2 Functionalized Porcelain Stoneware Tile. *Sci. Total Environ.* **2017**, *577*, 113–121, doi:10.1016/j.scitotenv.2016.10.115.

193. Ravelli, D.; Dondi, D.; Fagnoni, M.; Albini, A. Titanium Dioxide Photocatalysis: An Assessment of the Environmental Compatibility for the Case of the Functionalization of Heterocyclics. *Appl. Catal. B Environ.* **2010**, *99*, 442–447, doi:10.1016/j.apcatb.2010.05.010.

194. Muñoz, I.; Rieradevall, J.; Torrades, F.; Peral, J.; Domènech, X. Environmental Assessment of Different Solar Driven Advanced Oxidation Processes. *Sol. Energy* **2005**, *79*, 369–375, doi:10.1016/j.solener.2005.02.014.

195. Rodríguez, R.; Espada, J.J.; Pariente, M.I.; Melero, J.A.; Martínez, F.; Molina, R. Comparative Life Cycle Assessment (LCA) Study of Heterogeneous and Homogenous Fenton Processes for the Treatment of Pharmaceutical Wastewater. *J. Clean. Prod.* **2016**,

124, 21–29, doi:10.1016/j.jclepro.2016.02.064.

196. Agüera, A.; Ramos, M. del M.G.; Fernández-Alba, A.R. Chemical Evaluation of Water Treatment Processes by LC–(Q)TOF-MS. In *Comprehensive Analytical Chemistry*; 2012; pp. 61–109.

197. Huntscha, S.; Hofstetter, T.B.; Schymanski, E.L.; Spahr, S.; Hollender, J. Biotransformation of Benzotriazoles: Insights from Transformation Product Identification and Compound-Specific Isotope Analysis. *Environ. Sci. Technol.* **2014**, *48*, 4435–4443, doi:10.1021/es405694z.

198. Trenholm, R.A.; Vanderford, B.J.; Lakshminarasimman, N.; McAvoy, D.C.; Dickenson, E.R. V. Identification of Transformation Products for Benzotriazole, Triclosan, and Trimethoprim by Aerobic and Anoxic-Activated Sludge. *J. Environ. Eng.* **2020**, *146*, 04020094, doi:10.1061/(ASCE)EE.1943-7870.0001691.

199. Ye, J.; Hu, H.; Chen, Y.Y.; Chen, Y.Y.; Ou, H. Degradation of 1H-Benzotriazole Using Vacuum Ultraviolet: A Prospective Treatment Method for Micro-Pollutants. *Water Sci. Technol.* **2019**, *80*, 773–783, doi:10.2166/wst.2019.320.

200. Felis, E.; Sochacki, A.; Magiera, S. Degradation of Benzotriazole and Benzothiazole in Treatment Wetlands and by Artificial Sunlight. *Water Res.* **2016**, *104*, 441–448, doi:10.1016/j.watres.2016.08.037.

201. Ding, Y.; Yang, C.; Zhu, L.; Zhang, J. Photoelectrochemical Activity of Liquid Phase Deposited TiO2 Film for Degradation of Benzotriazole. *J. Hazard. Mater.* **2010**, *175*, 96–103, doi:10.1016/j.jhazmat.2009.09.037.

202. Luan, J.; Huang, P. Photophysical and Photocatalytic Properties of BiSnSbO6 under Visible Light Irradiation. *Materials (Basel).* **2018**, *11*, 491, doi:10.3390/ma11040491.

203. Borowska, E.; Felis, E.; Kalka, J. Oxidation of Benzotriazole and Benzothiazole in Photochemical Processes: Kinetics and Formation of Transformation Products. *Chem. Eng. J.* **2016**, *304*, 852–863, doi:10.1016/j.cej.2016.06.123.

204. Speltini, A.; Maraschi, F.; Sturini, M.; Contini, M.; Profumo, A. Dispersive Multi-Walled Carbon Nanotubes Extraction of Benzenesulfonamides, Benzotriazoles, and

Benzothiazoles from Environmental Waters Followed by Microwave Desorption and HPLC-HESI-MS/MS. *Anal. Bioanal. Chem.* **2017**, *409*, 6709–6718, doi:10.1007/s00216-017-0627-9.

205. Ye, J.; Zhou, P.; Chen, Y.; Ou, H.; Liu, J.; Li, C.; Li, Q. Degradation of 1H-Benzotriazole Using Ultraviolet Activating Persulfate: Mechanisms, Products and Toxicological Analysis. *Chem. Eng. J.* **2018**, *334*, 1493–1501, doi:10.1016/j.cej.2017.11.101.

206. Hu, C.; Zhang, R.; Xiang, J.; Liu, T.; Li, W.; Li, M.; Duo, S.; Wei, F. Synthesis of Carbon Nanotube/Anatase Titania Composites by a Combination of Sol–Gel and Self-Assembly at Low Temperature. *J. Solid State Chem.* **2011**, *184*, 1286–1292, doi:10.1016/j.jssc.2011.03.040.

207. Marić, T. Aging of Photocatalysis Based on Titanium(IV) Oxide and Carbon Nanotubes, University of Zagreb, 2020.

208. Khan, S.J.; Reed, R.H.; Rasul, M.G. Thin-Film Fixed-Bed Reactor for Solar Photocatalytic Inactivation of Aeromonas Hydrophila: Influence of Water Quality. *BMC Microbiol.* **2012**, *12*, 285, doi:10.1186/1471-2180-12-285.

209. Guo, X.; An, M.; Yang, P.; Li, H.; Su, C. Effects of Benzotriazole on Anodized Film Formed on AZ31B Magnesium Alloy in Environmental-Friendly Electrolyte. *J. Alloys Compd.* **2009**, *482*, 487–497, doi:10.1016/j.jallcom.2009.04.053.

LIST OF FIGURES

FIGURE 1. SCHEMATIC REPRESENTATION OF THE "BAND GAP MODEL." (1) PHOTOINDUCED ELECTRON-HOLE PAIR FORMATION; (2) CHARGE TRANSFER ONTO THE SURFACE; (3) REDOX REACTIONS; (4) RECOMBINATION. VB AND CB REPRESENT THE VALENCE BAND AND CONDUCTION BAND, RESPECTIVELY [24] 4

FIGURE 2. BAND GAPS WITH VALENCE AND CONDUCTION BAND GAP EDGES OF COMMON SEMICONDUCTORS AND STANDARD REDOX POTENTIALS (VERSUS NHE: NORMAL HYDROGEN ELECTRODE) OF THE ($O2/•O2^-$) AND ($•OH/OH^-$) REDOX COUPLE [24] 6

FIGURE 3. THE PRINCIPLE OF ENERGY GAP NARROWING [4] 10

FIGURE 4. SCHEMATIC REPRESENTATION OF THE PHOTOCATALYTIC ACTIVITY OF A CNT SEMICONDUCTOR OXIDE [35] 12

FIGURE 5. SCHEMATIC REPRESENTATION OF ELECTRON/HOLES PAIRS FORMATION ON THE PHOTOCATALYST [71] 15

FIGURE 6. THE PROPOSED MECHANISMS FOR THE CNT-MEDIATED ENHANCEMENT OF PHOTOCATALYSIS. A) CNTS ACT AS ELECTRON SINKS AND SCAVENGE AWAY THE ELECTRONS HINDERING RECOMBINATION. B) PHOTONS GENERATE AN ELECTRON-HOLE PAIR IN THE CNT. BASED ON THE RELEVANT POSITIONS OF THE BANDS, AN ELECTRON (OR THE HOLE) IS INJECTED IN THE TiO_2 GENERATING AN $O2^-$ OR A $\bullet OH$ SPECIES. [32] 17

FIGURE 7. STRUCTURAL FORMULA OF 1H-BENZOTRIAZOLE [111] 27

FIGURE 8. THE IMAGE OF PHOTOCATALYSTS: TiO_2 PHOTOCATALYTIC FILM ON GLASS FIBRE MESH (WHITE) AND TiO_2/CNT PHOTOCATALYTIC FILM ON GLASS FIBRE MESH (BLACK) FOR A) THE FPCR AND B) CPC REACTOR 37

FIGURE 9. A SCHEME OF THE CUSTOM-MADE PANEL WITH THREE FULL SPECTRA LAMPS AND CORRESPONDING REFLECTIVE MIRRORS 38

FIGURE 10. SCHEME OF THE EXPERIMENTAL SETUP FOR THE FPCR REACTOR (1-REACTOR WITH A PHOTOCATALYST, 2-SAMPLING TANK, 3-PERISTALTIC PUMP, AND 4-IRRADIATION SOURCE, CUSTOM-MADE PANEL). 39

FIGURE 11. THE SETUP FOR THE CPC REACTOR (2 QUARTZ TUBES CONNECTED WITH A PTFE U-TUBE PLACED IN A COMPOUND PARABOLIC MIRROR) 40

FIGURE 12. REPRESENTATION OF THE SCHEME A) AND LAB B) EXPERIMENTAL SETUPS FOR THE CPC REACTOR. THE SCHEME NUMBERS REPRESENT 1-CPC REACTOR WITH A PHOTOCATALYST, 2-SAMPLING TANK & MAGNETIC STIRRER, 3-PERISTALTIC PUMP, AND 4-IRRADIATION SOURCE (CUSTOM-MADE PANEL). 40

FIGURE 13. EXPERIMENTAL SETUPS OF A) THE FPCR AND B) THE CPC REACTOR WITH COMPACT FLUORESCENT LAMPS AS THE IRRADIATION SOURCE 41

FIGURE 14. UV/VIS SPECTROPHOTOMETER (AVANTES AVALIGHT-DH-S-BALSPECTROMETER) 43

FIGURE 15. UV/VIS SPECTRA OF THE 1H-BT WITH MAXIMUM PEAK AT 256 NM [181] 43

FIGURE 16. DETERMINATION OF 1H-BT CALIBRATION CURVE A) BASED ON THE UV-VIS SPECTROGRAM B) WITH FIVE POINTS 44

FIGURE 17. SCHEME OF AGILENT 6530 Q-TOF LC/MS [185] 46

FIGURE 18. THE SCHEME OF API-ESI [184] 47

FIGURE 19. DEVICES FOR THE IRRADIATION MEASUREMENTS; A) UVX RADIOMETER WITH B) SENSORS AND C) SOLARIMETER HT204 48
FIGURE 20. CHROMATOGRAPHS WITH EXTRACTED PEAKS OF 1H-BT (A) AND ASSOCIATED CALIBRATION CURVE WITH FIVE POINTS (10, 8, 6, 4 AND 2 PPM) (B) 55
FIGURE 21. OVERVIEW OF PROPOSED 1H-BT DEGRADATION PATHWAYS REPORTED IN LITERATURE [102,109,157,166,172,173,177,200–203] 59
FIGURE 22. ESTIMATED CONCENTRATIONS OF 1H-BT AND ITS DEGRADATION PRODUCTS DURING PHOTOCATALYSIS IN A) FPCR_TiO_2, B) FPCR_TiO_2/CNT 65
FIGURE 23. PROPOSED DEGRADATION PATHWAY DURING PHOTOCATALYSIS IN FPCR_TiO_2 AND FPCR_TiO_2/CNT 66
FIGURE 24. ESTIMATED CONCENTRATIONS OF 1H-BT AND ITS DEGRADATION PRODUCTS DURING PHOTOCATALYSIS IN A) CPC WITH TiO_2, B) CPC WITH TiO_2/CNT 68
FIGURE 25. PROPOSED DEGRADATION PATHWAY DURING PHOTOCATALYSIS IN CPC_TiO_2 AND FPCR_TiO_2/CNT 69
FIGURE 26. PHOTOCATALYTIC DEGRADATION OF 1H-BT (C_0=10 PPM) IN THE A) CPC REACTOR AND B) FPCR – COMPARISON OF DIFFERENT PHOTOCATALYST'S FORMULATION USAGE (TiO_2 AND TiO_2/CNT) 71
FIGURE 27. PHOTOCATALYTIC DEGRADATION OF 1H-BT (C_0=10 PPM) WITH A) TiO_2 AND B) TiO_2/CNT PHOTOCATALYST'S FORMULATION – COMPARISON OF THE FPCR AND CPC REACTOR 73
FIGURE 28. PHOTOCATALYTIC DEGRADATION OF 1H-BT (C_0=10 PPM) IN CPC_TiO_2 UNDER LINEAR (L) AND COMPACT FLUORESCENT (F) IRRADIATION SOURCE 74
FIGURE 29. PHOTOCATALYTIC DEGRADATION OF 1H-BT (C_0=10 PPM) IN THE A) CPC REACTOR AND B) FPCR – COMPARISON OF DIFFERENT PHOTOCATALYST'S FORMULATION USAGE (TiO_2 AND TiO_2/CNT), EXPERIMENTAL AND MODELLED 75
FIGURE 30. SYSTEM BOUNDARIES FOR THE LCA 79
FIGURE 31. OVERVIEW OF THE SCENARIOS FOR THE COMPARATIVE LCA (L STATES FOR THE LINEAR ARTIFICIAL SOURCE OF LIGHT, WHILE S FOR THE SUN) 79
FIGURE 32. MODELL OF PHOTOCATALYTIC DEGRADATION BY CPC&FPCR_TiO_2 AND CPC&FPCR_TiO_2/CNT OVER A TIME TO ACHIEVE 90 % DEGRADATION EFFICIENCY OF 1H-BT UNDER A) ARTIFICIAL IRRADIATION SOURCE, B) NATURAL SUN 80
FIGURE 33. RESULTS OF THE LCIA BY IMPACT 2002+METHODOLOGY IN FOUR IMPACT CATEGORIES, AQUATIC ECOTOXICITY, CARCINOGENS, GLOBAL WARMING AND TERRESTRIAL ECOTOXICITY 83
FIGURE 34. RESULTS OF THE LCIA BY IMPACT 2002+METHODOLOGY IN FOUR IMPACT CATEGORIES WITH WIDENED LCA BOUNDARIES, FRESHWATER ECOTOXICITY, HUMAN TOXICITY – AND HUMAN TOXICITY - NON-CANCER 84
FIGURE 35. RESULTS OF THE LCIA BY USETOX 2 METHODOLOGY IN THREE IMPACT CATEGORIES 86

LIST OF TABLES

TABLE 1 OXIDATION POTENTIAL OF A FEW OXIDIZING AGENTS [11] 3

TABLE 2. SEMICONDUCTORS WITH CORRESPONDING BAND GAP ENERGY VALUES [30] 6

TABLE 3. PROPERTIES OF ANATASE AND RUTILE [25] 7

TABLE 4. REVIEW OF NANOSTRUCTURES AND ASSOCIATED NANOPARTICLE FORMS WITH THE CORRESPONDING METHOD OF OBTAINING [34] 8

TABLE 5. SUMMARY OF TiO_2 MODIFICATION APPROACHES TOWARDS PHOTOACTIVITY IN VISIBLE LIGHT SPECTRA [35] 9

TABLE 6. SUMMARY OF MAIN ADVANTAGES AND DISADVANTAGES OF SUSPENDED AND IMMOBILISED PHOTOCATALYSTS [35,54] 13

TABLE 7. EXAMPLES OF PHOTOREACTORS WITH SUSPENDED AND IMMOBILISED PHOTOCATALYSTS [54] 18

TABLE 8. IMMOBILISED TiO_2 REACTORS THROUGHPUT AND DEGRADATION EFFICIENCIES [79] 20

TABLE 9. PROPERTIES OF 1H-BENZOTRIAZOLE [111] 28

TABLE 10. CONCENTRATIONS OF 1H-BT BEFORE AND AFTER WWTPS IN DIFFERENT COUNTRIES [102] 29

TABLE 11. CONCENTRATIONS OF 1H-BT IN FRUITS AND VEGETABLES [145,146] 31

TABLE 12 OVERVIEW OF THE STUDIES RESEARCHING THE REMOVAL OF 1H-BT BY PHOTOCATALYSIS [171] 35

TABLE 13. PHOTOMETRICAL DATA OF THE FIRST IRRADIATION SOURCE - ULTRA LINEAR FLUORESCENT LAMPS 38

TABLE 14. TECHNICAL DATA OF THE SECOND IRRADIATION SOURCE - COMPACT FLUORESCENT LAMP 39

TABLE 15. OVERVIEW OF THE PLANNED EXPERIMENTS 41

TABLE 16. MASS SPECTRA OF 1H-BT WITH ION DISTRIBUTIONS IN POSITIVE MODE OBTAINED BY ISOTOPE DISTRIBUTION CALCULATOR 54

TABLE 17. AN OVERVIEW OF SUPPLEMENT MATERIALS REGARDING THE IDENTIFICATION OF DEGRADATION PRODUCTS 58

TABLE 18. IDENTIFIED DEGRADATION PRODUCTS OF 1H-BT DURING PHOTOCATALYSIS BY FPCR_TiO_2 (DEGRADATION PRODUCTS CONFIRMED BY EIC – GREEN, DEGRADATION PRODUCTS CONFIRMED BY MS – APPROXIMATED CONCENTRATION - PPM) 61

TABLE 19. IDENTIFIED DEGRADATION PRODUCTS OF 1H-BT DURING PHOTOCATALYSIS BY FPCR_TiO_2/CNT (DEGRADATION PRODUCTS CONFIRMED BY EIC – GREEN, DEGRADATION PRODUCTS CONFIRMED BY MS – APPROXIMATED CONCENTRATION - PPM) 61

TABLE 20. IDENTIFIED DEGRADATION PRODUCTS OF 1H-BT DURING PHOTOCATALYSIS BY CPC_TiO_2 (DEGRADATION PRODUCTS CONFIRMED BY EIC – GREEN, DEGRADATION PRODUCTS CONFIRMED BY MS – APPROXIMATED CONCENTRATION - PPM) 62

TABLE 21. IDENTIFIED DEGRADATION PRODUCTS OF 1H-BT DURING PHOTOCATALYSIS BY CPC_TiO_2/CNT (DEGRADATION PRODUCTS CONFIRMED BY EIC – GREEN, DEGRADATION PRODUCTS CONFIRMED BY MS – APPROXIMATED CONCENTRATION - PPM) 62

TABLE 22. INTRINSIC PARAMETERS OBTAINED BY MATHEMATICAL MODELLING FOR PHOTOCATALYTIC DEGRADATION OF 1H-BT 74

TABLE 23. EFFICIENCY OF 1H-BT PHOTOCATALYTIC DEGRADATION (C_0=10 PPM) IN DIFFERENT SETUPS BASED ON DEVELOPED MODEL PREDICTION 75
TABLE 24. RESULTS OF TOXICITY ESTIMATION ACCORDING TO CONSENSUS METHOD T.E.S.T. FOR PROPOSED DEGRADATION PRODUCTS DURING PHOTOCATALYSIS IN FPCR WITH BOTH PHOTOCATALYSTS 76
TABLE 25. RESULTS OF TOXICITY ESTIMATION ACCORDING TO CONSENSUS METHOD T.E.S.T. FOR PROPOSED DEGRADATION PRODUCTS DURING PHOTOCATALYSIS IN CPC REACTOR WITH BOTH PHOTOCATALYSTS 77
TABLE 26. RESULTS OF ECOTOXICITY ESTIMATION FOR AQUATIC SPECIES ACCORDING TO ECOSAR FOR PROPOSED DEGRADATION PRODUCTS DURING PHOTOCATALYSIS IN FPCR REACTOR WITH BOTH PHOTOCATALYSTS 78
TABLE 27. RESULTS OF ECOTOXICITY ESTIMATION FOR AQUATIC SPECIES ACCORDING TO ECOSAR FOR PROPOSED DEGRADATION PRODUCTS DURING PHOTOCATALYSIS IN CPC REACTOR WITH BOTH PHOTOCATALYSTS 78
TABLE 28. DATA THAT WERE OBTAINED BY EXPERIMENTS 81
TABLE 29. OVERVIEW OF THE OBTAINED RESULTS ON THE ENVIRONMENTAL IMPACT WITH WIDENED BOUNDARIES TOWARD RAW MATERIALS EXTRACTION 85

LIST OF ABBREVIATION

WWTPs	*Wastewater treatment plants*
AOPs	*Advanced oxidation processes*
POPs	*Persistent organic pollutants*
CNT	*Carbon nanotubes*
MWCNT	*Multiwalled carbon nanotubes*
UV	*Ultraviolet spectrum*
e^-	*Electron*
h^+	*Positively charged hole*
e^-/h^+	*Electron hole pair*
VB	*Valence band*
CB	*Conduction band*
E_g	*Band gap energy*
E_a	*Apparent activation energy*
LH	*Langmuir-Hinshelwood mechanisms*
ER	*Eley-Rideal mechanisms*
CVD	*Chemical vapour deposition*
CPD	*Cold plasma discharge*
PAHD	*Polymer assisted hydrothermal decomposition*
CPC	*Compound parabolic collector*
TFFBR	*Thin-film fixed-bed reactor*
FPCR	*Flat plate cascade reactor*
BTs	*Benzotriazoles*
1H-BT	*1H-benzotriazole*
5-MBT	*5-methylbenzotriazole*
4-TTri	*4-tolitriazole*
5-TTri	*5-tolitriazole*
MBBR	*Moving Bed Biofilm Reactor*
MBR	*Membrane bioreactor*
COD	*Chemical oxygen demand*

TOC	*Total organic carbon*
UV/vis	*Ultraviolet-visible*
Q-TOF LC/MS	*Quadrupole time-of-flight mass spectrometry coupled with liquid chromatography system*
LC/MS	*Liquid chromatography with mass spectrometry*
MS	*Mass spectrum*
ESI	*Electrospray ionization*
EIC	*Extracted ion chromatography*
RT	*Retention time*
DP	*Degradation product*
QSARs	*Quantitative Structure-Activity Relationships*
T.E.S.T.	*Toxicity Estimation Software Tool*
ECOSAR	*Ecological Structure Activity Relationships*
LC_{50}	*Lethal concentration causes death in 50 % of the tested population*
LD_{50}	*Lethal dose causes death in 50 % of the tested population*
EC_{50}	*median effective concentration expected to have effect on 50 % of test organisms*
LCA	*Life cycle assessment*
ISO	*International Standard Organisation*
LCIA	*Life cycle impact assessment*
USA	*United stated of America*
OECD	*The Organization for Economic Cooperation and Development*
COST	*European Cooperation in Science and Technology*
EFCATS	*European Federation of Catalysis Societies*
SE	*Southeast*
CROSBI	*Croatian Scientific Bibliography*

*A**bbreviations** of chemical's structures*

TiO_2	*Titanium dioxide*	TiO_2/CNT	*Nanocomposite of TiO_2 and CNT*
ZnO	*Zinc oxide*	TiO_2_CPC	*CPC reactor with TiO_2 as used photocatalyst*
CeO_2	*Cerium dioxide*	TiO_2_FPCR	*FPCR reactor with TiO_2 as used photocatalyst*
ZrO_2	*Zirconium dioxide*	TiO_2/CNT_CPC	*CPC reactor with TiO_2/CNT as used photocatalyst*
SnO_2	*Tin dioxide*	TiO_2/CNT_FPCR	*FPCR reactor with TiO_2/CNT as used photocatalyst*
Sb_2O_4	*Antimony oxide*	$\bullet OH$	*Hydroxyl radical*
ZnS	*Zinc sulfide*	$\bullet O_2^-$	*Superoxide radical*
WO_3,	*Tungsten trioxide*	$\bullet HO_2$	*Hydroperoxyl radical*
$BiVO_4$	*Bismuth vanadate*	O_3	*Ozone*
Fe_2O_3	*Hematit*	H_2O_2	*Hydrogen peroxide*
CdS	*Cadmium sulfide*	*BTEX*	*Benzene, toluene, ethylbenzene, and xylene*
GaP	*Gallium phosphide*	*MeOH*	*methanol*
V_2O_5	*Vanadium pentoxide*	*FA, HCOOH*	*formic acid*
Bi_2S_3	*Bismuth Sulfide*	*1-, 4-, 5-OHBT*	*1 or 4 or 5-hydoxy-1,2,3 benzotriazole*
SiO_2	*Silicon dioxide, quartz*	$C_6H_5N_3$	*1H-benzotriazole*
α-Fe_2O_3/Bi_2S_3	*Nanocomposite of α-Fe_2O_3 and Bi_2S_3*	$C_6H_5N_3O$	*1H-benzo[d][1,2,3]triazol-1-ol*
$BiSnSbO_6$	*Composite of Bi_2O_3, SnO_2 and Sb_2O_5*	$C_6H_5N_3O_2$	*1H-benzo[d][1,2,3]triazol-1,6-diol*
$Gd_2YSbO_7/ZnBiNbO_5$	*heterojunction photocatalyst*	$C_6H_5N_3O_3$	*1H-benzo[d][1,2,3]triazole-4,5,7-triol*
$TiCl_4$	*Titanium tetrachloride*	$C_6H_3N_3O_2$	*1H-benzo[d][1,2,3]trizole-4,7-dione*
DBS	*(1,3:2,4) Dibenzylidene sorbitol*	$C_6H_7N_3O_4$	*(E)-3-(5-(hydroperoxyl(hydroxy)methyl)-1H-1,2,3-trizol-4-yl)acrylaldehyde*
NaOH	*Sodium hydroxide*	*HCHO*	*Formaldehyde*
EDDS	*ethylenediamine-N,N'-disuccinic acid*	H_2O	*water*
EDTA	*Ethylenediaminetetraacetic acid*	CO_2	*carbon dioxide*
		NH_3	*Ammonia*
		NH_4^+	*Ammonium cation*

ANNEXES

ANNEX 1. IDENTIFICATION OF 1H-BT IN SAMPLES FOR CALIBRATION CURVE: A) 2 PPM, B) 4 PPM, C) 6 PPM, D) 8 PPM, AND E) 10 PPM. CHROMATOGRAMS WITH EXTRACTED PRECURSOR ION (EIC) M/Z=120.0556 (FIRST IMAGE), WITH EXTRACTED ION FRAGMENT M/Z=121.0581 (SECOND IMAGE) AND MASS SPECTRUM (THIRD IMAGE) 124

ANNEX 2. IDENTIFICATION OF 1H-BT (C_0=10 PPM) WITH PRECURSOR ION M/Z=120.0556 AND FRAGMENT ION M/Z= 121.0581 IN SAMPLES – PHOTOCATALYTIC DEGRADATION BY TiO_2 IN CPC REACTOR 125

ANNEX 3. IDENTIFICATION OF 1H-BT (C_0=10 PPM) WITH PRECURSOR ION M/Z=120.0556 AND FRAGMENT ION M/Z= 121.0581 IN SAMPLES – PHOTOCATALYTIC DEGRADATION BY TiO_2/CNT IN CPC REACTOR 126

ANNEX 4. IDENTIFICATION OF 1H-BT (C_0=10 PPM) WITH PRECURSOR ION M/Z=120.0556 AND FRAGMENT ION M/Z= 121.0581 IN SAMPLES – PHOTOCATALYTIC DEGRADATION BY TiO_2 IN FPCR REACTOR 127

ANNEX 5. IDENTIFICATION OF 1H-BT (C_0=10 PPM) WITH PRECURSOR ION M/Z=120.0556 AND FRAGMENT ION M/Z= 121.0581 IN SAMPLES – PHOTOCATALYTIC DEGRADATION BY TiO_2/CNT IN FPCR REACTOR 128

ANNEX 6. OVERVIEW OF PROPOSED 1H-BT DEGRADATION PATHWAYS REPORTED IN LITERATURE ALONG WITH THE PRECURSOR AND FRAGMENT IONS (POSITIVE MODE) 129

ANNEX 7. EXTRACTED ION CHROMATOGRAMS (M/Z= 136.0505, 137.053) OF $C_6H_5N_3O$. THE DEGRADATION PRODUCT WAS IDENTIFIED IN SAMPLES OF PHOTOCATALYTIC DEGRADATION BY FPCR_TiO_2 ([1H-BT]$_0$=10 PPM) 137

ANNEX 8. EXTRACTED ION CHROMATOGRAMS (M/Z=152.0455, 153.0479) OF $C_6H_5N_3O_2$. THE DEGRADATION PRODUCT WAS IDENTIFIED IN SAMPLES OF PHOTOCATALYTIC DEGRADATION BY FPCR_TiO_2 ([1H-BT]$_0$=10 PPM) 138

ANNEX 9. EXTRACTED ION CHROMATOGRAMS (M/Z= 168.0404, 169.0429) OF $C_6H_5N_3O_3$. THE DEGRADATION PRODUCT WAS IDENTIFIED IN SAMPLES OF PHOTOCATALYTIC DEGRADATION BY FPCR_TiO_2 ([1H-BT]$_0$=10 PPM) 139

ANNEX 10. EXTRACTED ION CHROMATOGRAMS (M/Z= 150.0298, 151.0323) OF $C_6H_3N_3O_2$. THE DEGRADATION PRODUCT WAS IDENTIFIED IN SAMPLES OF PHOTOCATALYTIC DEGRADATION BY FPCR_TiO_2 ([1H-BT]$_0$=10 PPM) 140

ANNEX 11. CONFIRMED DEGRADATION PRODUCTS A) $C_6H_5N_3O$, B) $C_6H_5N_3O_2$ AND C) $C_6H_5N_3O_3$ BY MASS SPECTRUM IN SAMPLES OF PHOTOCATALYTIC DEGRADATION BY FPCR_TiO_2 ([1H-BT]$_0$=10 PPM) 141

ANNEX 12. EXTRACTED ION CHROMATOGRAMS (M/Z= 136.0505, 137.053) OF $C_6H_5N_3O$. THE DEGRADATION PRODUCT WAS IDENTIFIED IN SAMPLES OF PHOTOCATALYTIC DEGRADATION BY FPCR_TiO_2/CNT ([1H-BT]$_0$=10 PPM) 142

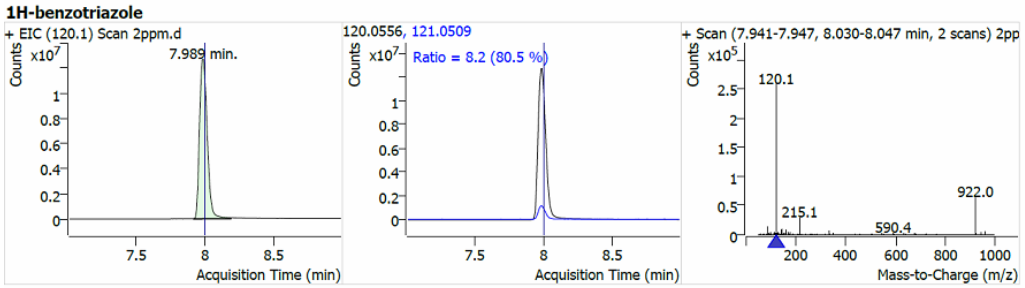
ANNEX 13. EXTRACTED ION CHROMATOGRAMS (M/Z=152.0455, 153.0479) OF $C_6H_5N_3O_2$. THE DEGRADATION PRODUCT WAS IDENTIFIED IN SAMPLES OF PHOTOCATALYTIC DEGRADATION BY FPCR_TiO_2/CNT ([1H-BT]$_0$=10 PPM) 143

ANNEX 14. EXTRACTED ION CHROMATOGRAMS (M/Z= 168.0404, 169.0429) OF $C_6H_5N_3O_3$. THE DEGRADATION PRODUCT WAS IDENTIFIED IN SAMPLES OF PHOTOCATALYTIC DEGRADATION BY FPCR_TiO_2/CNT ([1H-BT]$_0$=10 PPM) 144

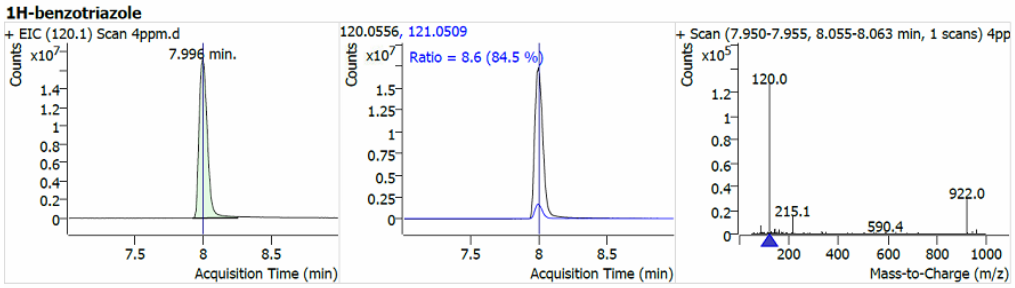
ANNEX 15. EXTRACTED ION CHROMATOGRAMS (M/Z= 150.0298, 151.0323) OF $C_6H_3N_3O_2$. THE DEGRADATION PRODUCT WAS IDENTIFIED IN SAMPLES OF PHOTOCATALYTIC DEGRADATION BY FPCR_TiO_2/CNT ([1H-BT]$_0$=10 PPM) 145
ANNEX 16. CONFIRMED DEGRADATION PRODUCTS A) $C_6H_5N_3O$, B) $C_6H_5N_3O_2$ AND C) $C_6H_3N_3O_2$ BY MASS SPECTRUM IN SAMPLES OF PHOTOCATALYTIC DEGRADATION BY FPCR_TiO_2/CNT ([1H-BT]$_0$=10 PPM) .. 146
ANNEX 17. EXTRACTED ION CHROMATOGRAMS (M/Z= 136.0505, 137.053) OF $C_6H_5N_3O$. THE DEGRADATION PRODUCT WAS IDENTIFIED IN SAMPLES OF PHOTOCATALYTIC DEGRADATION BY CPC_TiO_2 ([1H-BT]$_0$=10 PPM) 147
ANNEX 18. EXTRACTED ION CHROMATOGRAMS (M/Z=152.0455, 153.0479) OF $C_6H_5N_3O_2$. THE DEGRADATION PRODUCT WAS IDENTIFIED IN SAMPLES OF PHOTOCATALYTIC DEGRADATION BY CPC_TiO_2 ([1H-BT]$_0$=10 PPM) 148
ANNEX 19. EXTRACTED ION CHROMATOGRAMS (M/Z= 168.0404, 169.0429) OF $C_6H_5N_3O_3$. THE DEGRADATION PRODUCT WAS IDENTIFIED IN SAMPLES OF PHOTOCATALYTIC DEGRADATION BY CPC_TiO_2 ([1H-BT]$_0$=10 PPM) 149
ANNEX 20. EXTRACTED ION CHROMATOGRAMS (M/Z= 186.0509, 187.0535) OF $C_6H_7N_3O_4$. THE DEGRADATION PRODUCT WAS IDENTIFIED IN SAMPLES OF PHOTOCATALYTIC DEGRADATION BY CPC_TiO_2 ([1H-BT]$_0$=10 PPM) 150
ANNEX 21. CONFIRMED DEGRADATION PRODUCTS A) $C_6H_5N_3O_2$, B) $C_6H_5N_3O_3$ AND C) $C_6H_7N_3O_4$ BY MASS SPECTRUM IN SAMPLES OF PHOTOCATALYTIC DEGRADATION BY CPC_TiO_2 ([1H-BT]$_0$=10 PPM) 151
ANNEX 22. EXTRACTED ION CHROMATOGRAMS (M/Z= 136.0505, 137.053) OF $C_6H_5N_3O$. THE DEGRADATION PRODUCT WAS IDENTIFIED IN SAMPLES OF PHOTOCATALYTIC DEGRADATION BY CPC_TiO_2/CNT ([1H-BT]$_0$=10 PPM) 152
ANNEX 23. EXTRACTED ION CHROMATOGRAMS (M/Z=152.0455, 153.0479) OF $C_6H_5N_3O_2$. THE DEGRADATION PRODUCT WAS IDENTIFIED IN SAMPLES OF PHOTOCATALYTIC DEGRADATION BY CPC_TiO_2/CNT ([1H-BT]$_0$=10 PPM) 153
ANNEX 24. EXTRACTED ION CHROMATOGRAMS (M/Z= 168.0404, 169.0429) OF $C_6H_5N_3O_3$. THE DEGRADATION PRODUCT WAS IDENTIFIED IN SAMPLES OF PHOTOCATALYTIC DEGRADATION BY CPC_TiO_2/CNT ([1H-BT]$_0$=10 PPM) 154
ANNEX 25. EXTRACTED ION CHROMATOGRAMS (M/Z= 186.0509, 187.0535) OF $C_6H_7N_3O_4$. THE DEGRADATION PRODUCT WAS IDENTIFIED IN SAMPLES OF PHOTOCATALYTIC DEGRADATION BY CPC_TiO_2/CNT ([1H-BT]$_0$=10 PPM) 155
ANNEX 26. CONFIRMED DEGRADATION PRODUCTS A) $C_6H_5N_3O_2$, B) AND C) $C_6H_5N_3O_3$ BY MASS SPECTRUM IN SAMPLES OF PHOTOCATALYTIC DEGRADATION BY CPC_TiO_2/CNT ([1H-BT]$_0$=10 PPM) 156

Annex 1. Identification of 1H-BT in samples for calibration curve: a) 2 ppm, b) 4 ppm, c) 6 ppm, d) 8 ppm, and e) 10 ppm. Chromatograms with extracted precursor ion (EIC) m/z=120.0556 (first image), with extracted ion fragment m/z=121.0581 (second image) and mass spectrum (third image)

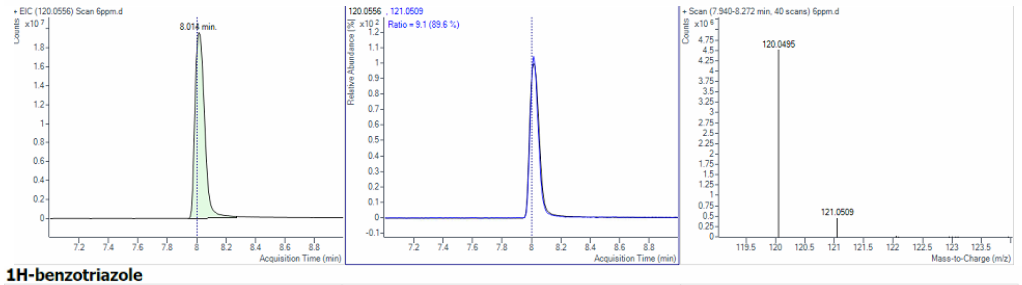
a)



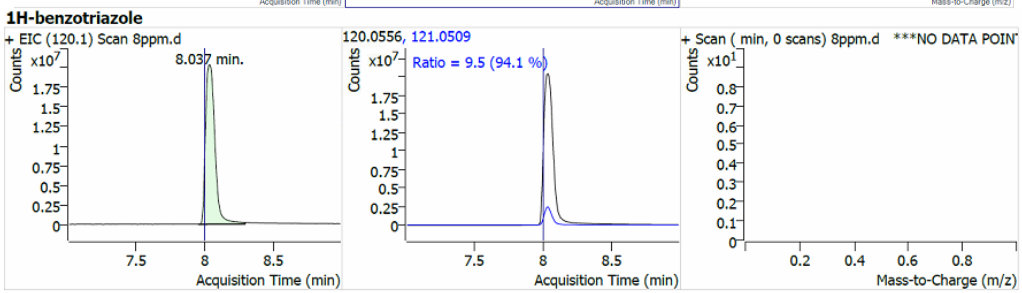
b)



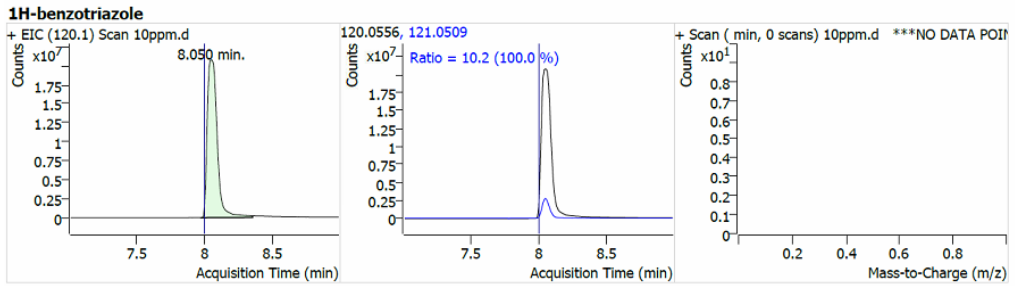
c)



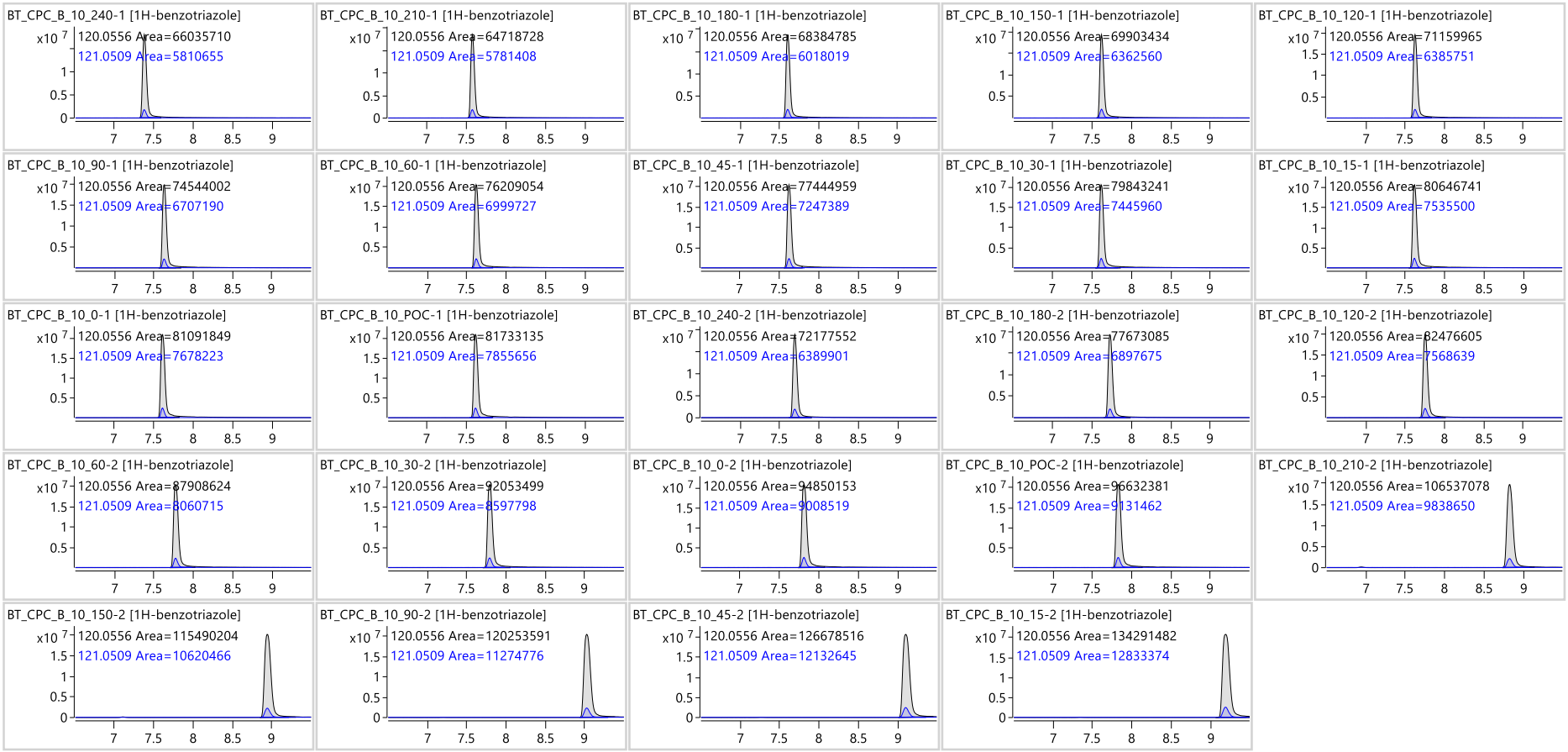
d)



e)

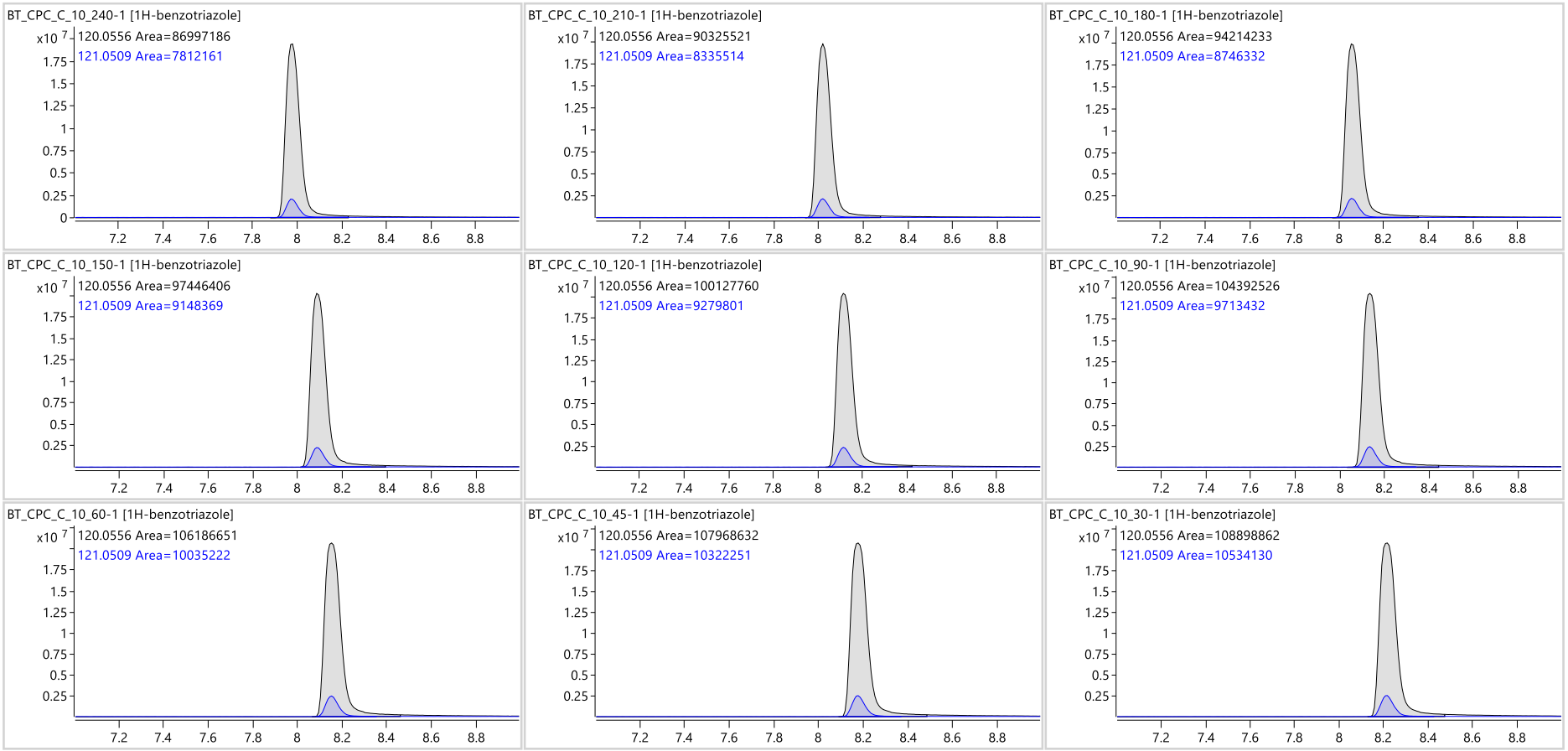


Annex 2. Identification of 1H-BT (C_0=10 ppm) with precursor ion m/z=120.0556 and fragment ion m/z= 121.0581 in samples – photocatalytic degradation by TiO_2 in CPC reactor



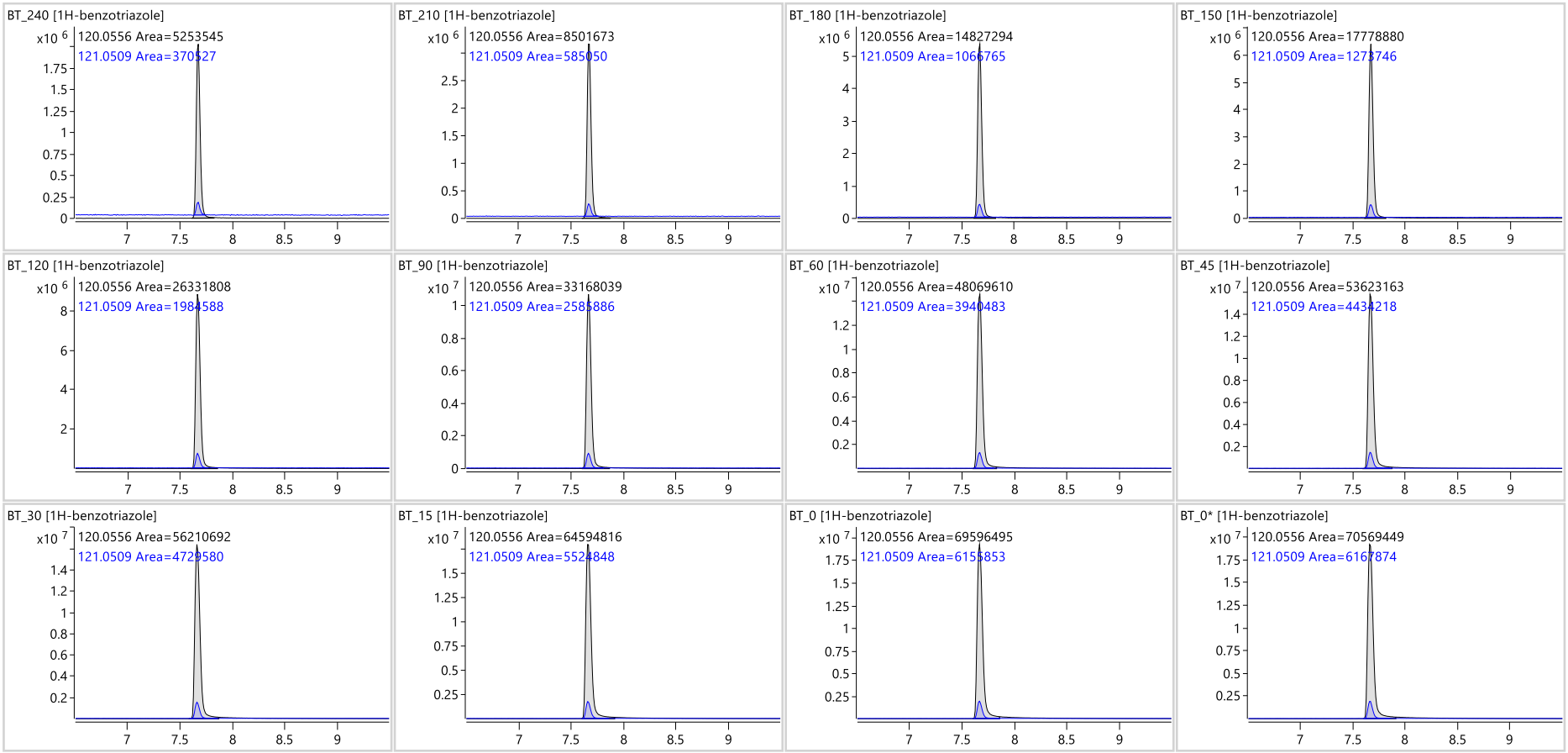
* Samples were taken in the following time intervals 240, 210, 180, 150, 120, 90, 60, 45, 30, 15, 0, -30 min.

Annex 3. Identification of 1H-BT (C_0=10 ppm) with precursor ion m/z=120.0556 and fragment ion m/z= 121.0581 in samples – photocatalytic degradation by TiO_2/CNT in CPC reactor



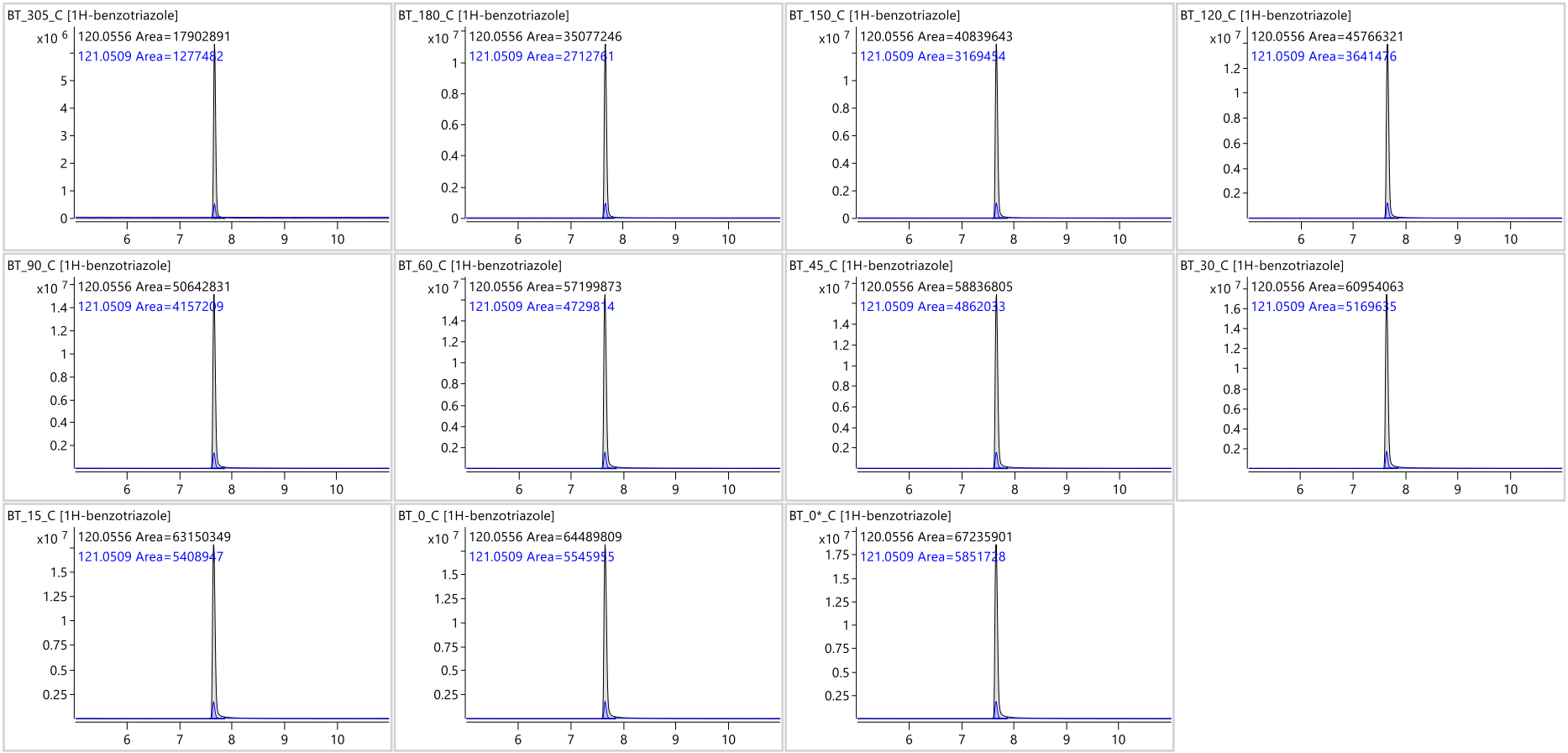
* Samples were taken in the following time intervals 240, 210, 180, 150, 120, 90, 60, 45, 30, 15, 0, -30 min.

Annex 4. Identification of 1H-BT (C_0=10 ppm) with precursor ion m/z=120.0556 and fragment ion m/z= 121.0581 in samples – photocatalytic degradation by TiO_2 in FPCR reactor



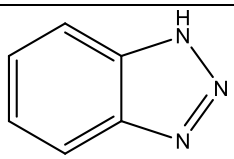
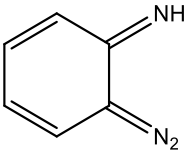
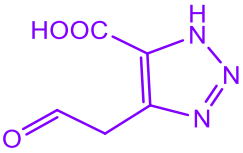
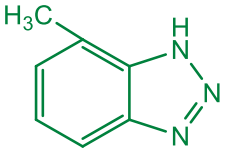
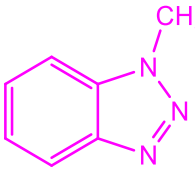
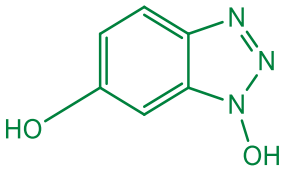
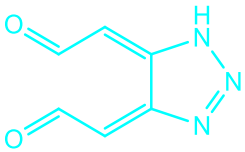
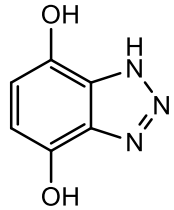
* Samples were taken in the following time intervals 240, 210, 180, 150, 120, 90, 60, 45, 30, 15, 0, -30 min.

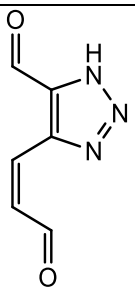
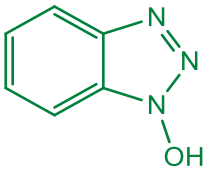
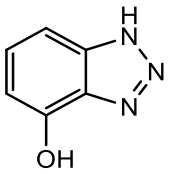
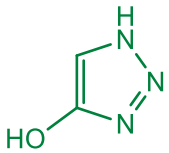
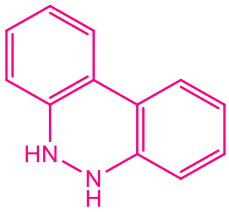
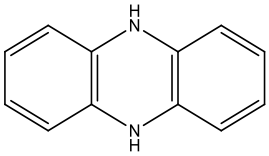
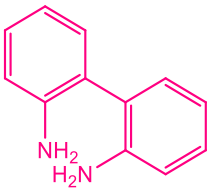
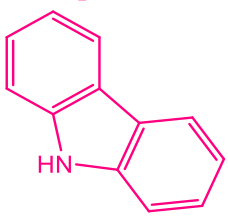
Annex 5. Identification of 1H-BT (C_0=10 ppm) with precursor ion m/z=120.0556 and fragment ion m/z= 121.0581 in samples – photocatalytic degradation by TiO_2/CNT in FPCR reactor

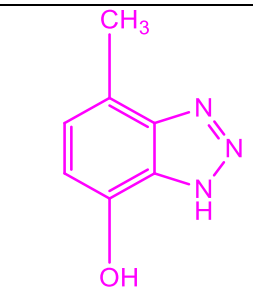
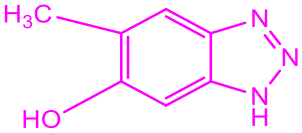
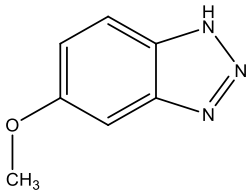
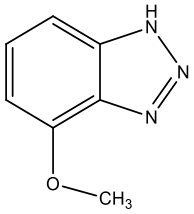
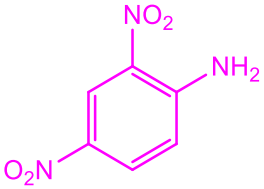
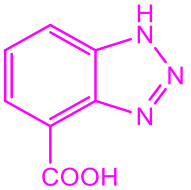
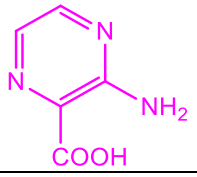


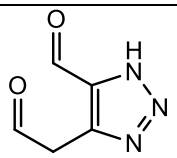
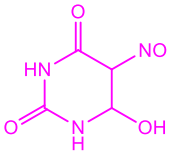
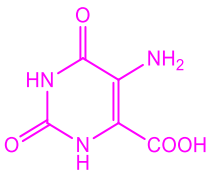
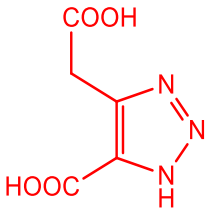
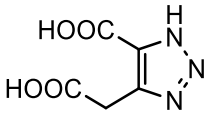
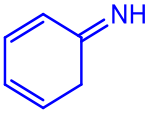
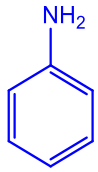
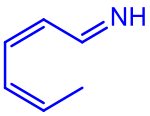
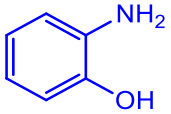
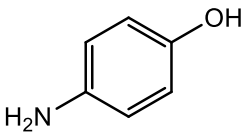
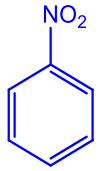
* Samples were taken in the following time intervals 305, 180, 150, 120, 90, 60, 45, 30, 15, 0, -30 min.

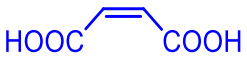
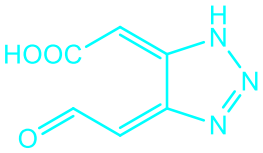
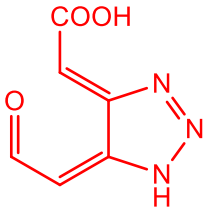
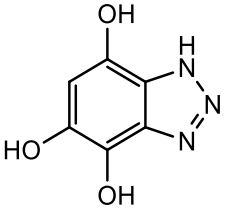
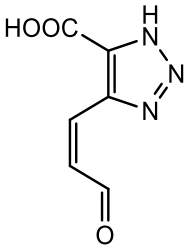
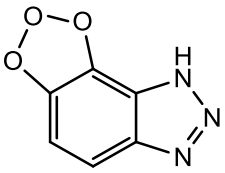
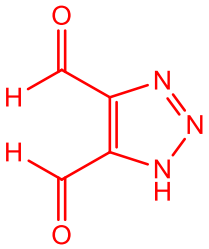
Annex 6. Overview of proposed 1H-BT degradation pathways reported in literature along with the precursor and fragment ions (positive mode)

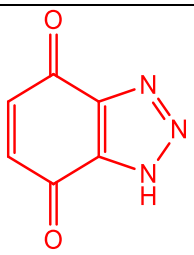
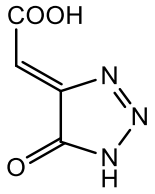
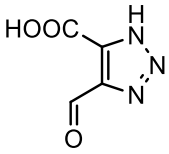
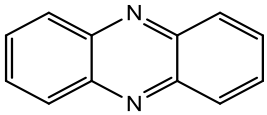
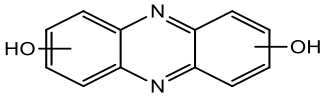
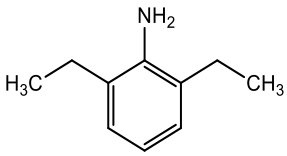
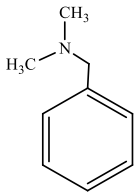
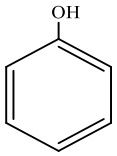
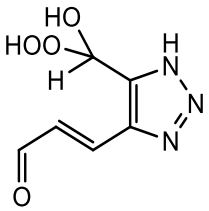
Chemical structure	Name Molecular formula Molecular weight [g/mol]	Precursor and fragment ions (positive mode)	Detected in FPCR		Detected in CPC		Reference
			TiO_2	TiO_2/CNT	TiO_2	TiO_2/CNT	
	1H-benzotriazole $C_6H_5N_3$ 119.12	120.0556, 121.0581, 122.0604					*[172]*
	6-diazocyclohexa-2,4-dienimine $C_6H_5N_3$ 119.12						*[102,201]*
	4-(2-oxoethyl)-1H-1,2,3-triazole-5 carboxylic acid $C_5H_5N_3O_3$ 155.11	156.0404, 157.0427, 158.0447					*[172]*
	4-methyl-1H-benzo[d][1,2,3]triazole 7-methyl-1H-benzo[d][1,2,3]triazole $C_7H_7N_3$ 133.15	134.0713, 135.0739, 136.0763					*[200]* *[177]*
	1-methyl-1H-benzo[d][1,2,3]triazole $C_7H_7N_3$ 133.15						
	1H-benzo[d][1,2,3]triazol-1,6-diol $C_6H_5N_3O_2$ 151.12						*[200]*
	(2E',2'E)-2,2'-(1H-1,2,3-triazole-4,5-diylidene)diacetaldehyde $C_6H_5N_3O_2$ 151.12	152.0455, 153.0479, 154.0499					*[109]*
	1H-benzo[d][1,2,3]triazole-4,7-diol $C_6H_5N_3O_2$ 151.12						*[162,203]*

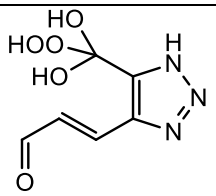
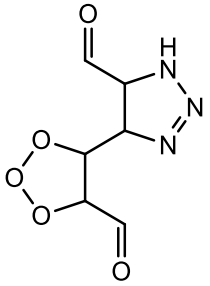
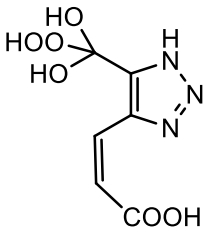
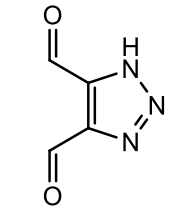
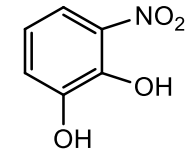
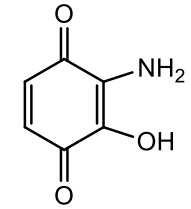
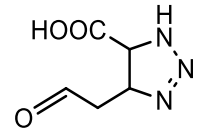
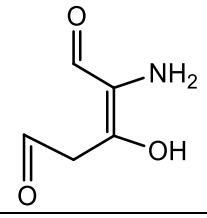
Chemical structure	Name Molecular formula Molecular weight [g/mol]	Precursor and fragment ions (positive mode)	Detected in FPCR		Detected in CPC		Reference
			TiO_2	TiO_2/CNT	TiO_2	TiO_2/CNT	
	(Z)-4-(3-oxoprop-1-en-1-yl)-1H-1,2,3-trizole-5-carbaldehyde $C_6H_5N_3O_2$ 151.12						*[162]*
	1H-benzo[d][1,2,3]triazol-1-ol $C_6H_5N_3O$ 135.12	136.0505, 137.053, 138.0551					*[200]*
	1H-benzo[d][1,2,3]triazol-4-ol $C_6H_5N_3O$ 135.12						*[162]* *[203]*
	1H-1,2,3-triazol-4-ol $C_2H_3N_3O$ 85.06	86.0349, 87.0362, 88.0387					*[200]*
	5,6-dihydrobenzo[c]cinnoline $C_{12}H_{10}N_2$ 182.22	183.0917, 184.0947, 185.0977					*[173]*
	5,10-dihxdrophenazine $C_{12}H_{10}N_2$ 182.22						*[173]*
	[1,1'-biphenyl]-2,2'-diamine $C_{12}H_{12}N_2$ 184.24	185.1073, 186.1104, 187.1134					*[173]*
	9H-carbazole $C_{12}H_9N$ 167.21	168.0808, 169.084, 170.0872					*[173]*

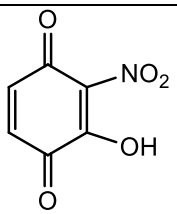
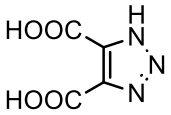
Chemical structure	Name Molecular formula Molecular weight [g/mol]	Precursor and fragment ions (positive mode)	Detected in FPCR		Detected in CPC		Reference
			TiO_2	TiO_2/CNT	TiO_2	TiO_2/CNT	
	4-methyl-1H-benzo[d][1,2,3]triazol-7-ol $C_7H_7N_3O$ 149.15						*[177]*
	5-methyl-1H-benzo[d][1,2,3]triazol-6-ol	150.0662, 151.0688, 152.071					
	4-methoxy-1H-benzo[d][1,2,3]triazole						*[198]*
	5-methoxy-1H-benzo[d][1,2,3]triazole $C_7H_7N_3O$ 149.15						
	2,4-dinitroaniline $C_6H_5N_3O_4$ 183.12	184.0353, 185.0378, 186.0397					*[177]*
	2-methyl-5-nitro-1H-imidazole $C_4H_5N_3O_2$ 127.10	128.0455, 129.0476, 130.0497					*[177]*
	1H-benzo[d][1,2,3]triazole-4-carboxylic acid $C_7H_5N_3O_2$ 163.13	164.0455, 165.0481, 166.0501					*[177]*
	3-aminopyrazine-2-carboxylic acid $C_5H_5N_3O_2$ 139.11	140.0455, 141.0478, 142.0498					*[177]*

Chemical structure	**Name Molecular formula Molecular weight [g/mol]**	**Precursor and fragment ions (positive mode)**	**Detected in FPCR**		**Detected in CPC**		**Reference**
			TiO_2	**TiO_2/CNT**	**TiO_2**	**TiO_2/CNT**	
	4-(2-oxoethyl)-1H-1,2,3-triazole-5-carbaldehyde $C_5H_5N_3O_2$ 139.11						***[162]***
	6-hydroxy-5-nitrosodihydropyrimidine-2,4(1H,3H)-dione $C_4H_5N_3O_4$ 159.10	160.0353, 161.0375, 162.0395					***[177]***
	5-amino-2,6-dioxo-1,2,3,6-tetrahydropyrimidine-4-carboxylic acid $C_5H_5N_3O_4$ 171.11						***[177]***
	4-(carboxymethyl)-1H-1,2,3-trizole-5-carboxylic acid $C_5H_5N_3O_4$ 171.11	172.0353, 173.0377, 174.0396					***[157,203]***
	4-(carboxymethyl)-1H-1,2,3-triazole-5-carboxylic acid $C_5H_5N_3O_4$ 171.11						***[162,203]***
	cyclohexa-2,4-dienimine C_6H_7N 93.13						***[202]***
	aniline C_6H_7N 93.13	94.0651, 95.0682, 96.0712					***[102,201]***
	(2Z,4Z)-hexa-2,4-dien-1-imine C_6H_9N 95.14	96.0808, 97.0838, 98.0869					***[202]***
	2-aminophenol C_6H_7NO 109.13	110.06, 111.0631, 112.0652					***[202]*** ***[102]***
	4-aminophenol C_6H_7NO 109.13						***[102]***
	nitrobenzene $C_6H_5NO_2$ 123.11	124.0393, 125.0424, 126.0442					***[202]***

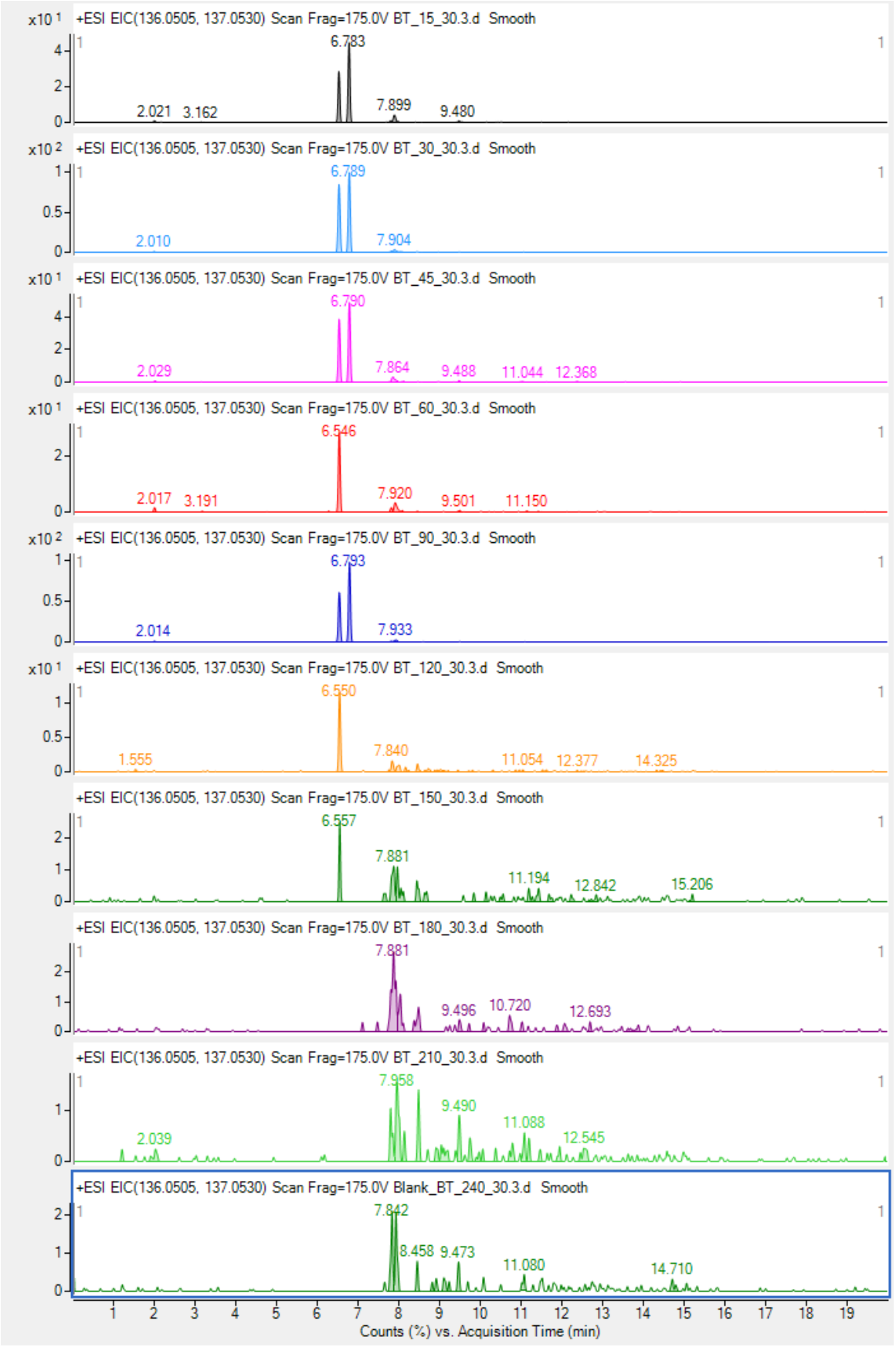
Chemical structure	Name Molecular formula Molecular weight [g/mol]	Precursor and fragment ions (positive mode)	Detected in FPCR		Detected in CPC		Reference
			TiO_2	TiO_2/CNT	TiO_2	TiO_2/CNT	
	(E)-3-aminoprop-2-en-1-ol C_3H_7NO 73.09	74.06, 75.0629, 76.0645					*[202]*
	maleic acid $C_4H_4O_4$ 116.07	117.0182, 118.0217, 119.0227					*[202]*
	(E)-2-((E)-4-(2-oxoethylidene)-1H-1,2,3-trizol-5(4H)-ylidene)acetic acid $C_6H_5N_3O_3$ 167.12						*[109]*
	(Z)-2-((E)-5-(2-oxothylidene)-1h-1,2,3-triazol-4(5H)-ylidene)acetic acid $C_6H_5N_3O_3$ 167.12						*[157,203]*
	1H-benzo[d][1,2,3]triazole-4,5,7-triol $C_6H_5N_3O_3$ 167.12	168.0404, 169.0429, 170.0448					*[162]*
	(Z)-4-(3-oxoprop-1-en-1-yl)-1H-1,2,3-trizole-5-carboxylic acid $C_6H_5N_3O_3$ 167.12						*[162]*
	8H-[1,2,3]trioxolo[4',5':3,4]benzo[1,2-d][1,2,3]trizole $C_6H_5N_3O_3$ 167.12						*[162]*
	1H-1,2,3-trizole-4,5-dicarbaldehyde $C_4H_3N_3O_2$ 125.09	126.0298, 127.0319, 128.034					*[157]*

Chemical structure	Name Molecular formula Molecular weight [g/mol]	Precursor and fragment ions (positive mode)	Detected in FPCR		Detected in CPC		Reference
			TiO_2	TiO_2/CNT	TiO_2	TiO_2/CNT	
	1H-benzo[d][1,2,3]trizole-4,7-dione $C_6H_3N_3O_2$ 149.11	150.0298, 151.0323, 152.0343					*[157]* *[162]*
	(Z)-2-(5-oxo-1H-1,2,3-triazol-4(5H)-ylidene)acetic acid $C_4H_3N_3O_3$ 141.08	142.0247, 143.0269, 144.0289					*[102]*
	4-formyl-1H-1,2,3-triazole-5-carboxylic acid $C_4H_3N_3O_3$ 141.08						*[162]*
	phenazine $C_{12}H_8N_2$ 180.21	181.076, 182.0791, 183.0821					*[102]*
	phenazine-2,8-diol $C_{12}H_8N_2O_2$ 212.20	213.0659, 214.0689, 215.0713					*[102]*
	2,6-diethylaniline $C_{10}H_{15}N$ 149.23	150.1277, 151.1309, 152.1341					*[102]*
	N,N-dimethyl-1-phenylmethanamine $C_9H_{13}N$ 135.21	136.1121, 137.1153, 138.1184					*[102]*
	phenol C_6H_6O 94.11	95.0491, 96.0525, 97.0546					*[102]*
	(E)-3-(5-(hydroperoxyl(hydroxy)methyl)-1H-1,2,3-trizol-4-yl)acrylaldehyde $C_6H_7N_3O_4$ 185.14	186.0509, 187.0535, 188.0553					*[162]*

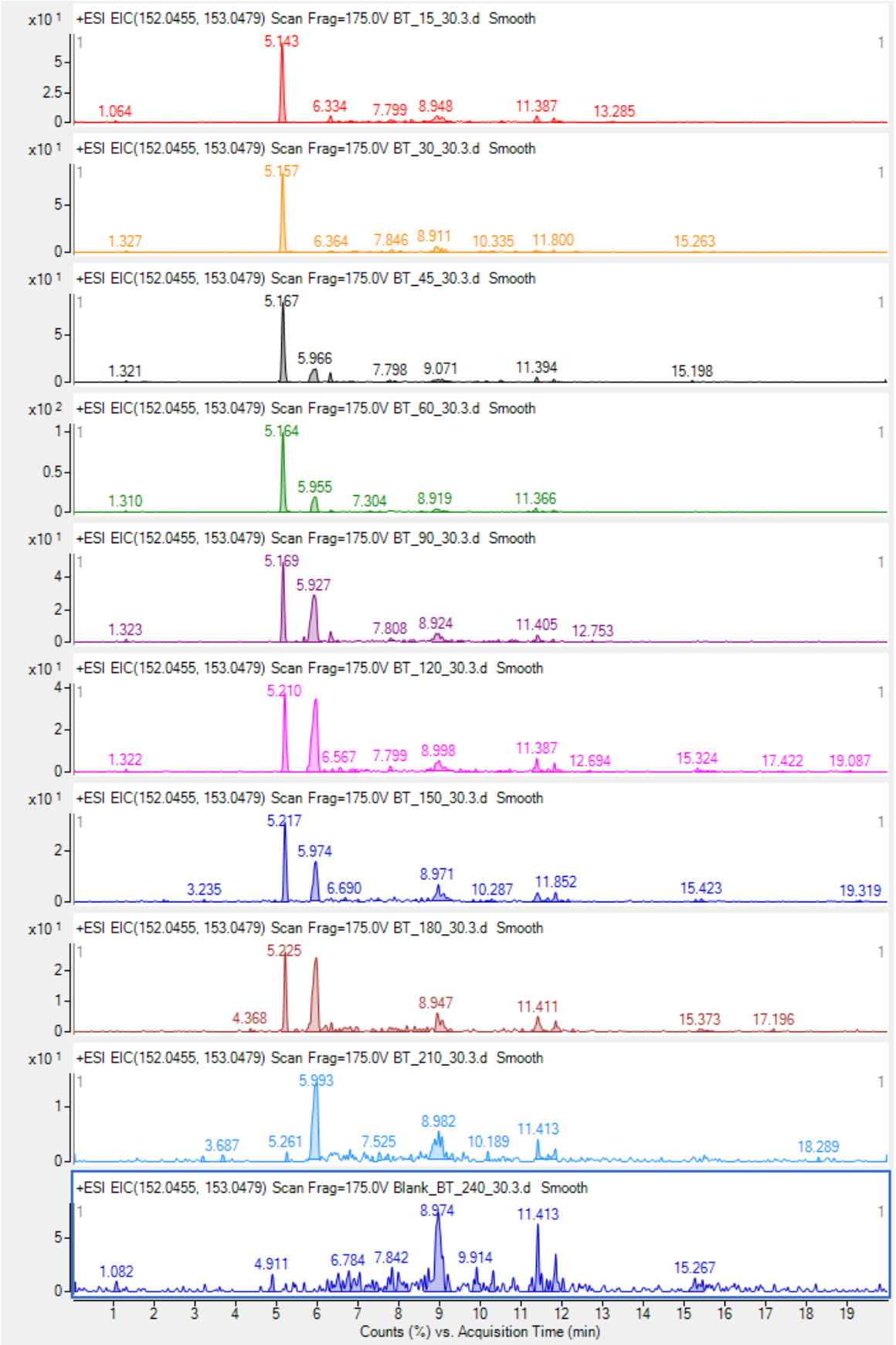
Chemical structure	Name Molecular formula Molecular weight [g/mol]	Precursor and fragment ions (positive mode)	Detected in FPCR		Detected in CPC		Reference
			TiO_2	TiO_2/CNT	TiO_2	TiO_2/CNT	
	(E)-3-(5-(hydroperoxydihydroxymethyl)-1H-1,2,3-trizol-4-yl)acrylaldehyde $C_6H_7N_3O_5$ 201.14						*[162]*
	4-(5-formyl-1,2,3-trioxolan-4-yl)-4,5-dihydro-1H-1,2,3-triazole-5-carbaldehyde $C_6H_7N_3O_5$ 201.14	202.0458, 203.0484, 204.0502					*[162]*
	(Z)-3-(5-(hydroperoxydihydroxymethyl)-1H-1,2,3-trizol-4-yl)acrylic acid $C_6H_7N_3O_6$ 217.14	218.0408, 219.0433, 220.0451					*[162]*
	1H-1,2,3-triazole-4,5-dicarbaldehyde $C_4H_3N_3O_2$ 125.09	126.0298, 127.0319, 128.034					*[162]*
	3-nitrobenzene-1,2-diol $C_6H_5NO_4$ 155.11	156.0291, 157.0322, 158.0338					*[162]*
	2-amino-3-hydroxycyclohexa-2,5-diene-1,4-dione $C_6H_5NO_3$ 139.11	140.0342, 141.0373, 142.0389					*[162]*
	4-(2-oxoethyl)-4,5-dihydro-1H-1,2,3-triazole-5-carboxylic acid $C_5H_7N_3O_3$ 157.13	158.056, 159.0584, 160.0603					*[162]*
	(Z)-2-amino-3-hydroxypent-2-enedial $C_5H_7NO_3$ 129.11	130.0499, 131.0529, 132.0545					*[162]*

Chemical structure	**Name** **Molecular formula** **Molecular weight [g/mol]**	**Precursor and fragment ions (positive mode)**	**Detected in FPCR**		**Detected in CPC**		**Reference**
			TiO_2	**TiO_2/CNT**	**TiO_2**	**TiO_2/CNT**	
	2-hydroxy-3-nitrocyclohexa-2,5-diene-1,4-dione $C_6H_3NO_5$ 169.09	170.0084, 171.0115, 172.013					***[162]***
	1H-1,2,3-triazole-4,5-dicarboxylic acid $C_4H_3N_3O_4$ 157.08	158.0196, 159.0218, 160.0239					***[162]***

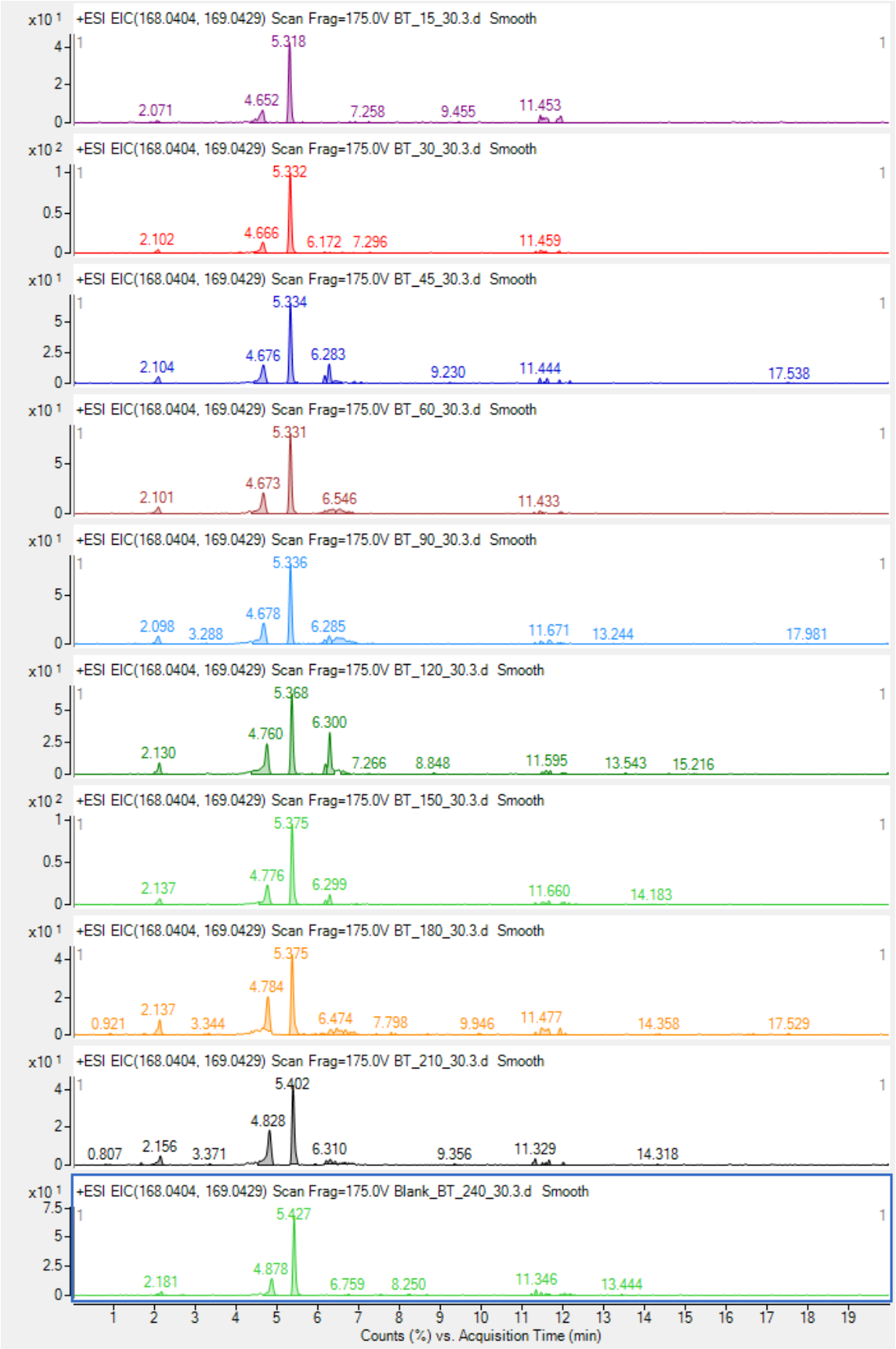
Annex 7. Extracted ion chromatograms (m/z= 136.0505, 137.053) of $C_6H_5N_3O$. The degradation product was identified in samples of photocatalytic degradation by FPCR_TiO_2 ([1H-BT]$_0$=10 ppm)



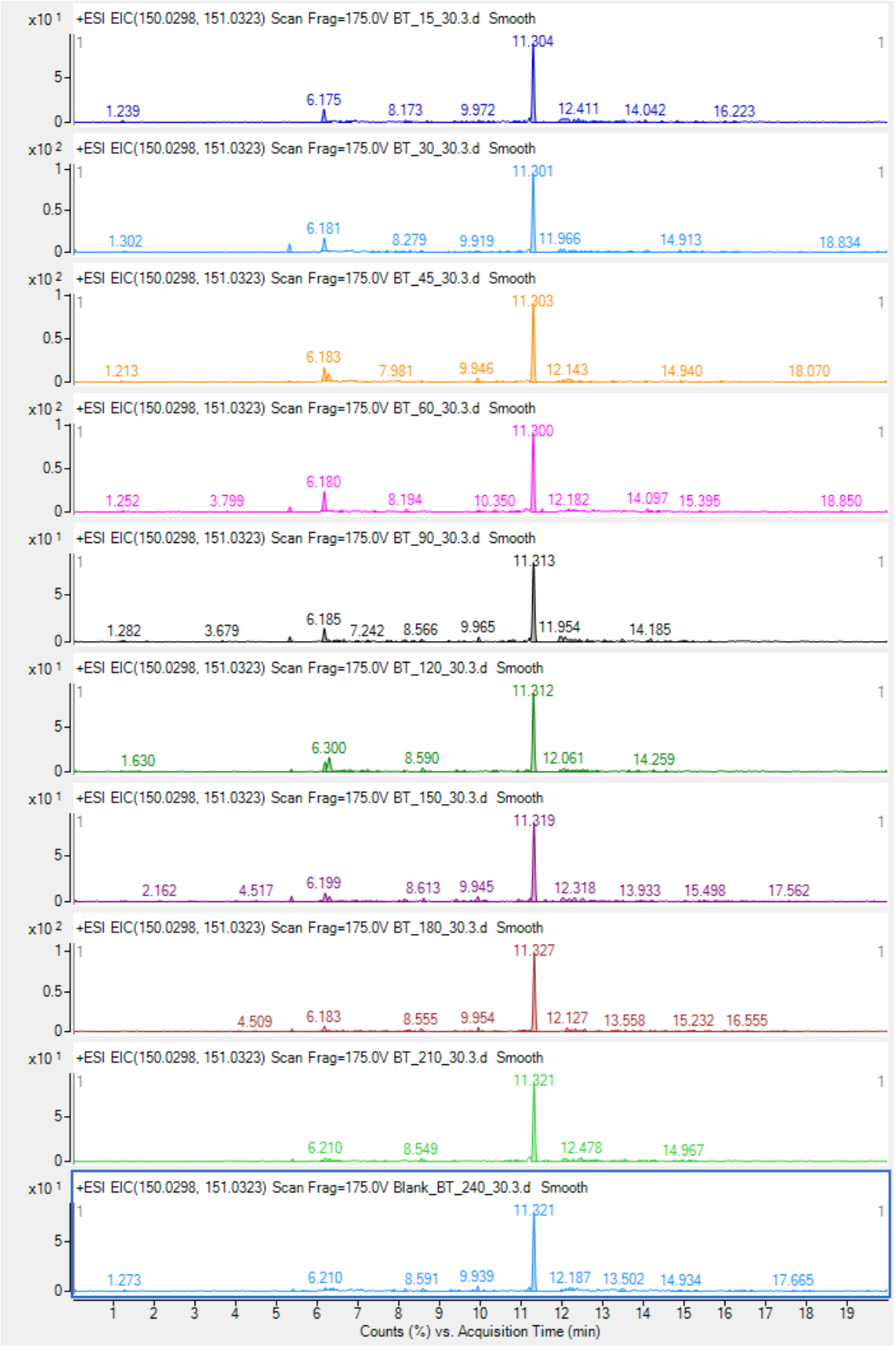
Annex 8. Extracted ion chromatograms (m/z=152.0455, 153.0479) of $C_6H_5N_3O_2$. The degradation product was identified in samples of photocatalytic degradation by FPCR_TiO_2 ([1H-BT]$_0$=10 ppm)



Annex 9. Extracted ion chromatograms (m/z= 168.0404, 169.0429) of $C_6H_5N_3O_3$. The degradation product was identified in samples of photocatalytic degradation by FPCR_TiO_2 ([1H-BT]$_0$=10 ppm)

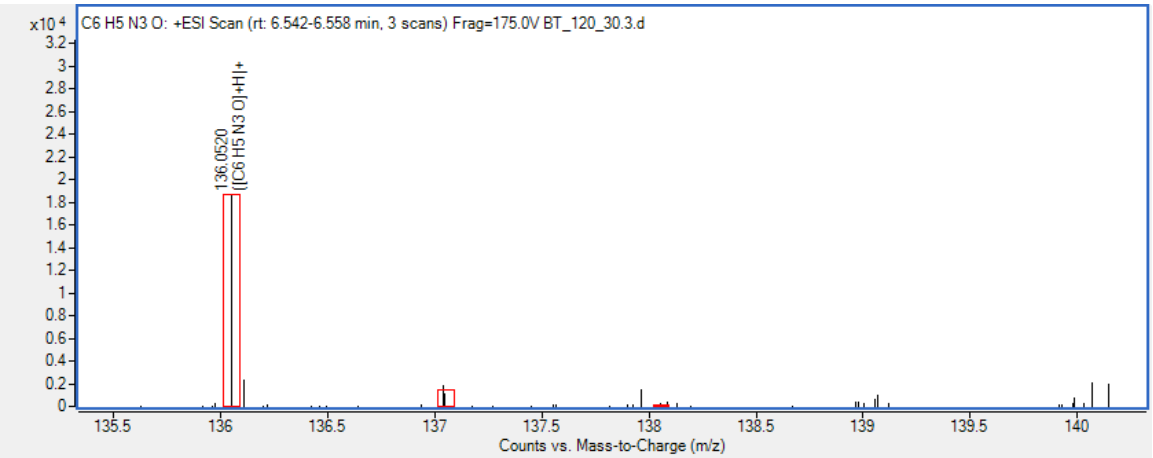


Annex 10. Extracted ion chromatograms (m/z= 150.0298, 151.0323) of $C_6H_3N_3O_2$. The degradation product was identified in samples of photocatalytic degradation by FPCR_TiO_2 ([1H-BT]$_0$=10 ppm)

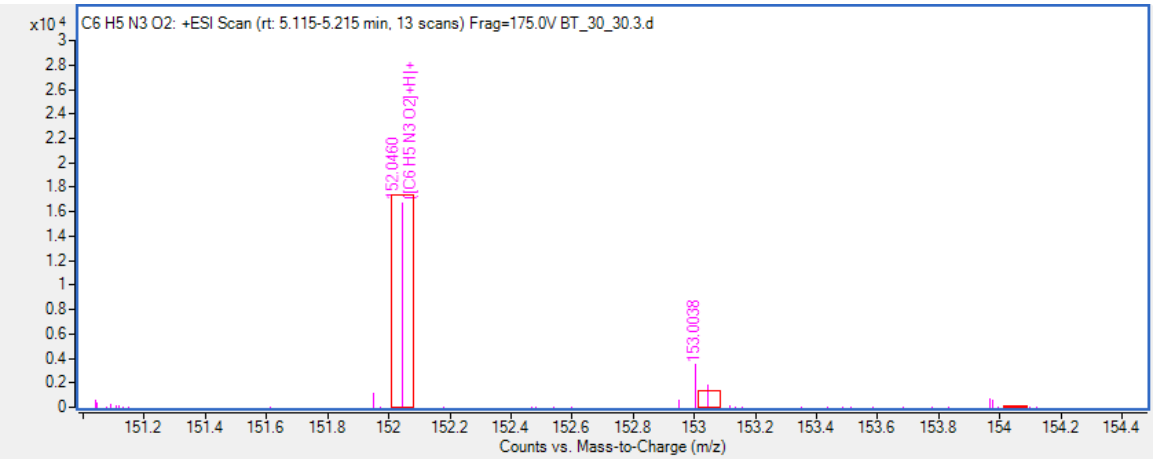


Annex 11. Confirmed degradation products a) $C_6H_5N_3O$, b) $C_6H_5N_3O_2$ and c) $C_6H_5N_3O_3$ by mass spectrum in samples of photocatalytic degradation by FPCR_TiO_2 ([1H-BT]$_0$=10 ppm)

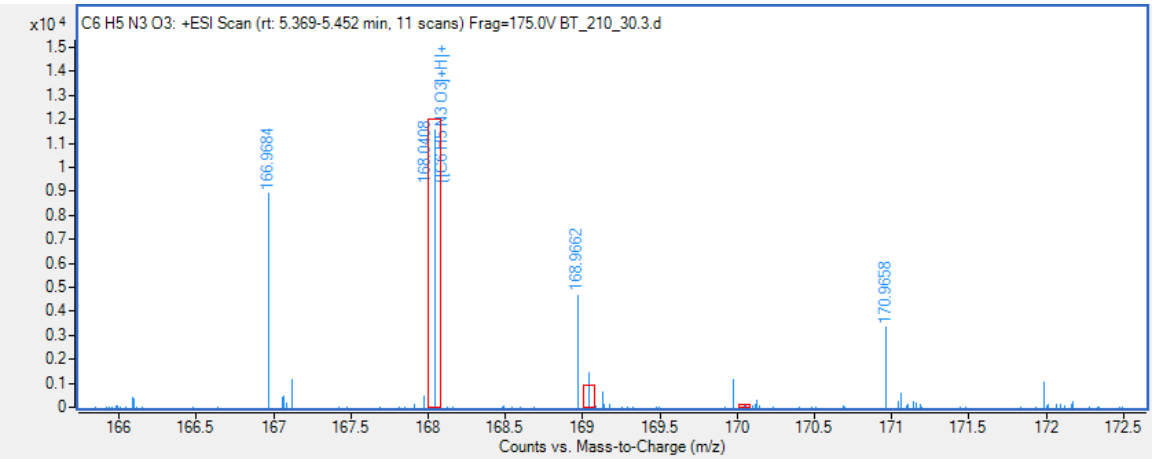
a) $C_6H_5N_3O$ (m/z= 136.0505, 137.053)



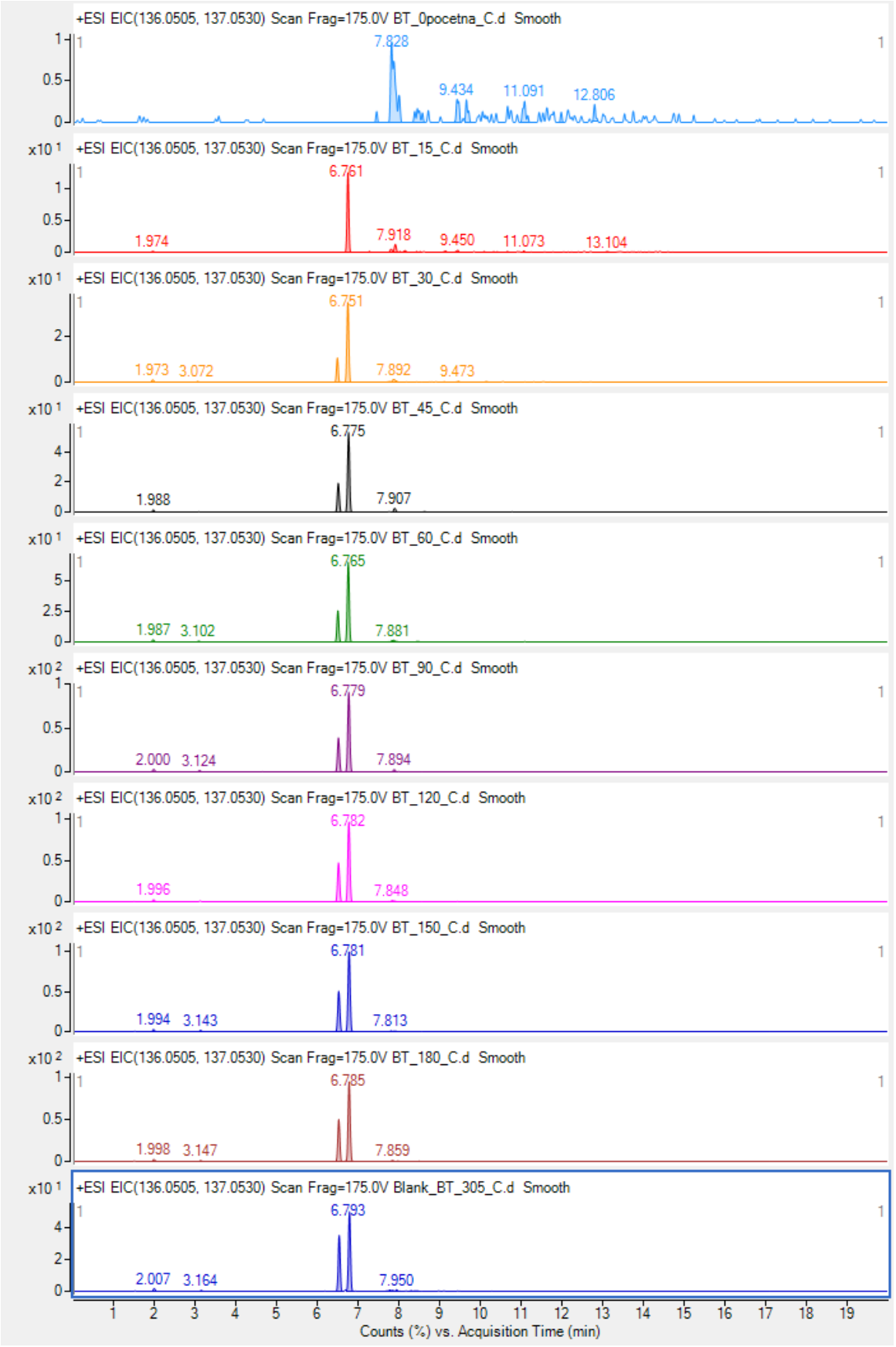
b) $C_6H_5N_3O_2$ (m/z= 152.0455, 153.0479)



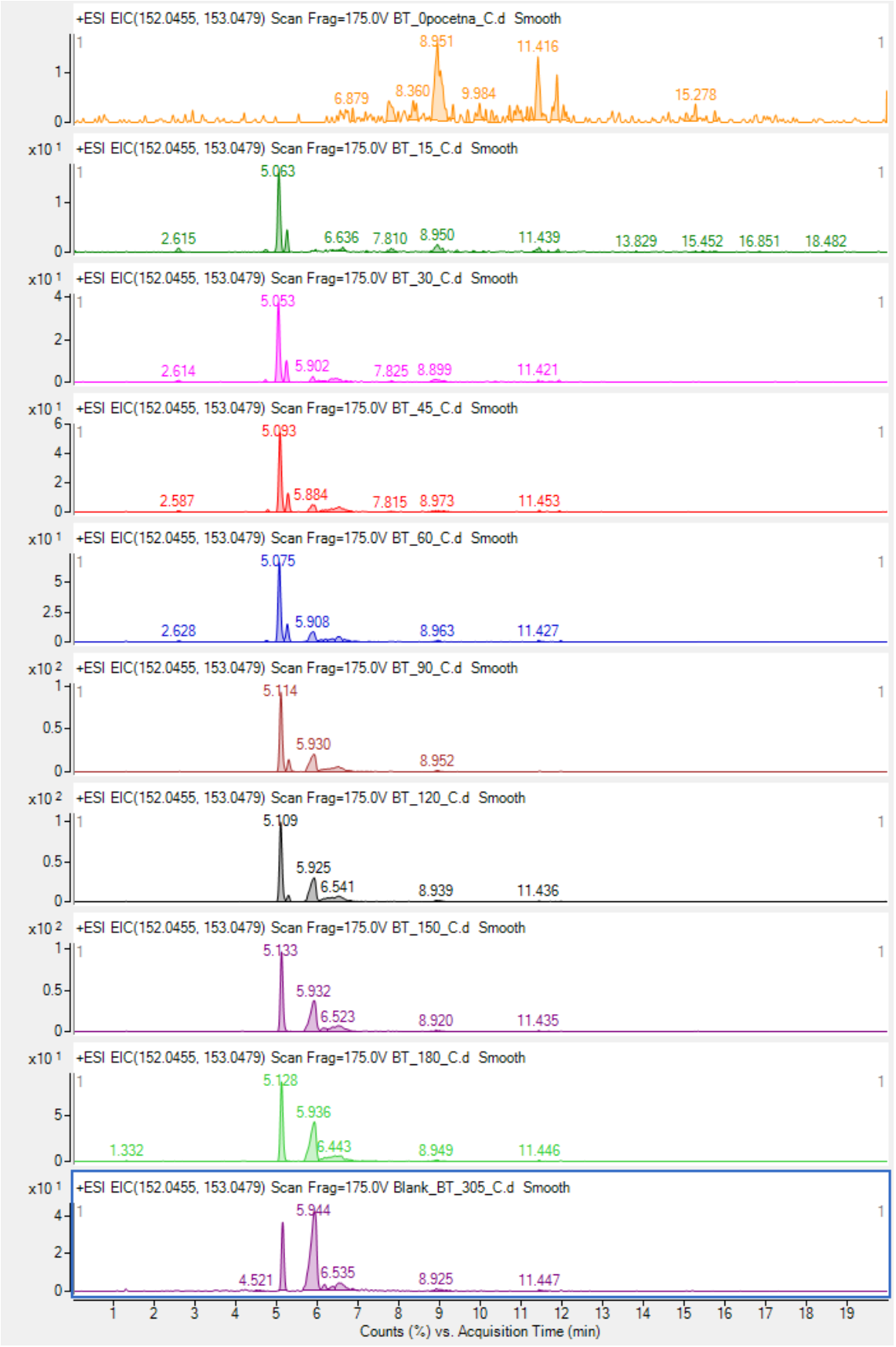
c) $C_6H_5N_3O_3$ (m/z= 168.0404, 169.0429)



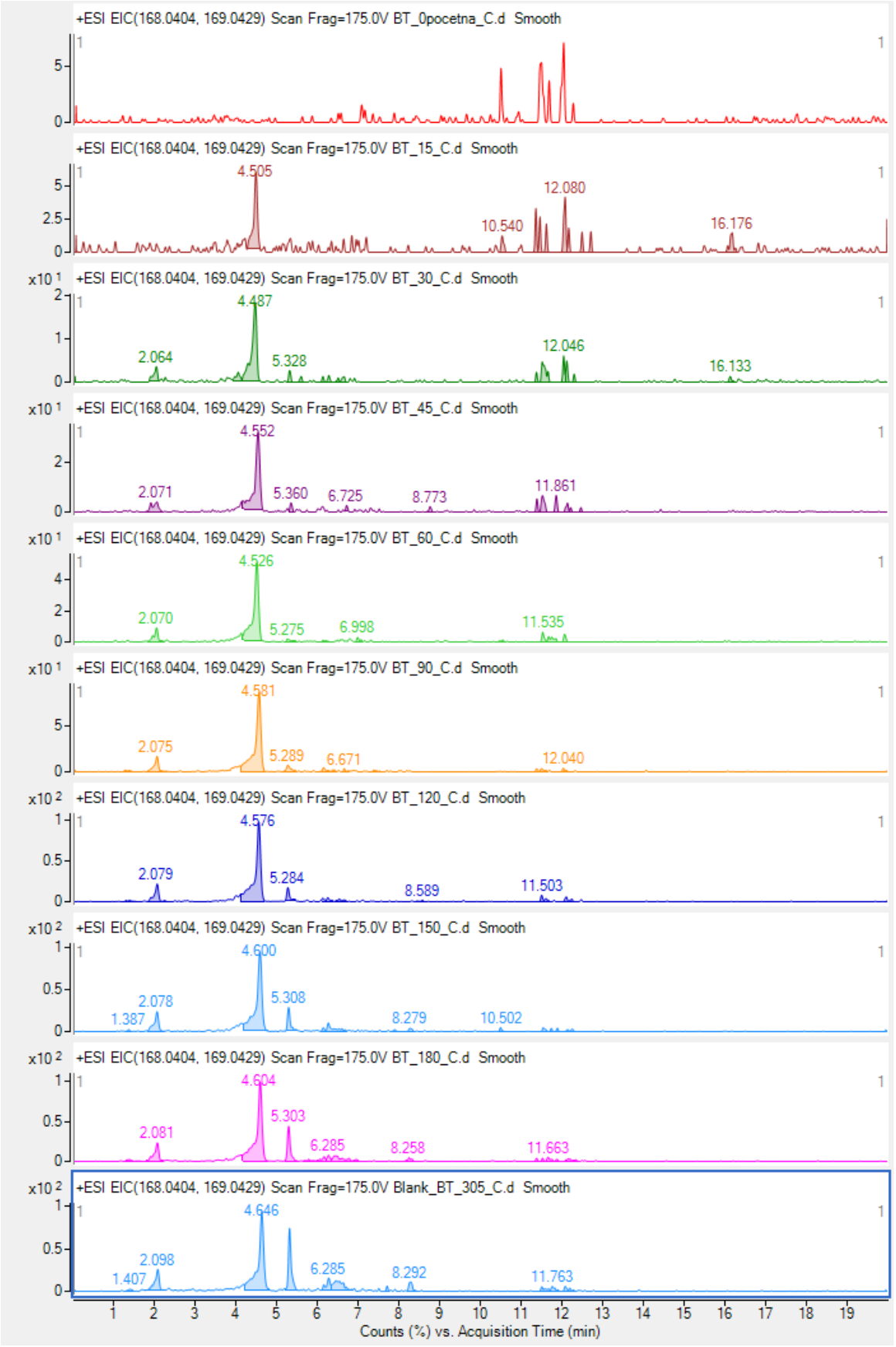
Annex 12. Extracted ion chromatograms (m/z= 136.0505, 137.053) of $C_6H_5N_3O$. The degradation product was identified in samples of photocatalytic degradation by FPCR_TiO_2/CNT ($[1H\text{-}BT]_0$=10 ppm)



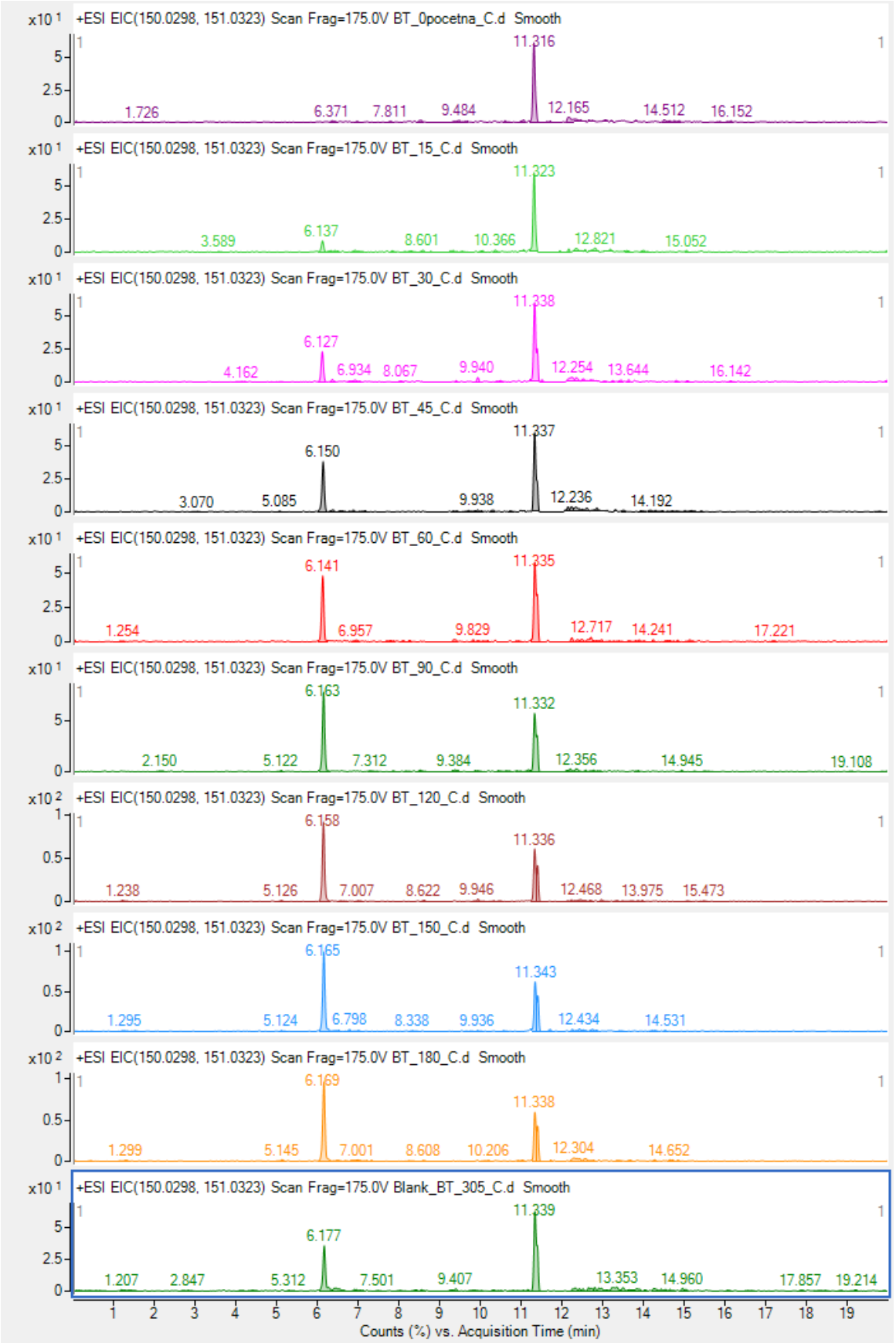
Annex 13. Extracted ion chromatograms (m/z=152.0455, 153.0479) of $C_6H_5N_3O_2$. The degradation product was identified in samples of photocatalytic degradation by FPCR_TiO_2/CNT ($[1H\text{-}BT]_0$=10 ppm)



Annex 14. Extracted ion chromatograms (m/z= 168.0404, 169.0429) of $C_6H_5N_3O_3$. The degradation product was identified in samples of photocatalytic degradation by FPCR_TiO_2/CNT ([1H-BT]$_0$=10 ppm)

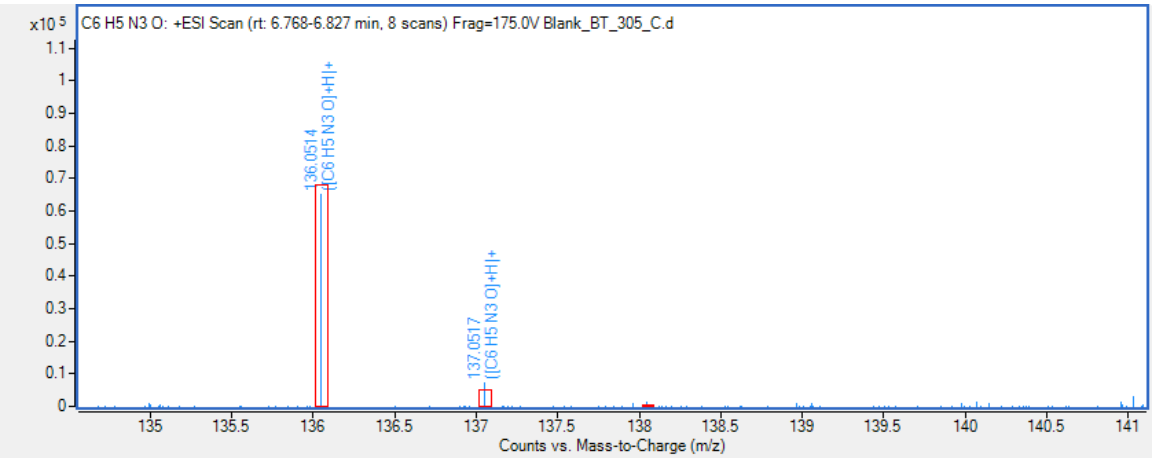


Annex 15. Extracted ion chromatograms (m/z= 150.0298, 151.0323) of $C_6H_3N_3O_2$. The degradation product was identified in samples of photocatalytic degradation by FPCR_TiO_2/CNT ([1H-BT]$_0$=10 ppm)

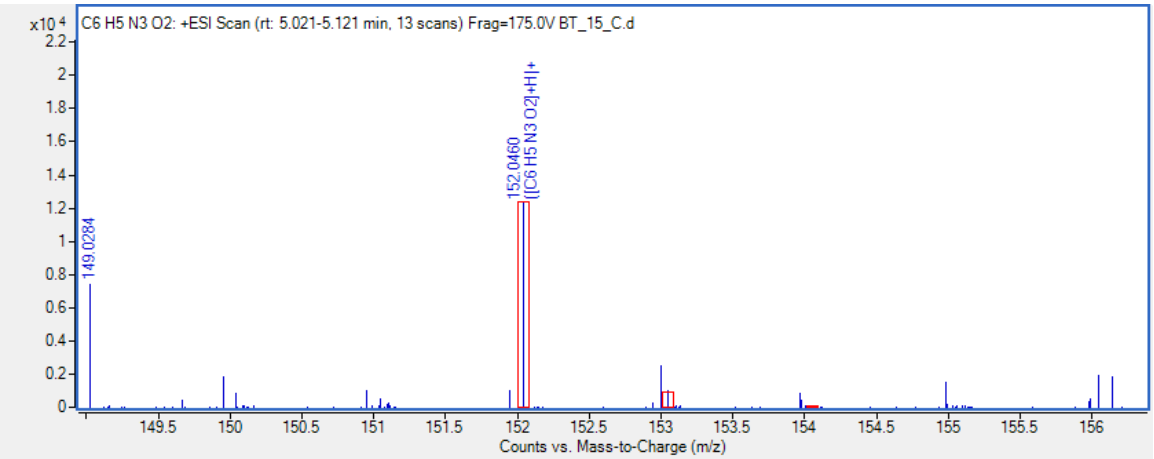


Annex 16. Confirmed degradation products a) $C_6H_5N_3O$, b) $C_6H_5N_3O_2$ and c) $C_6H_3N_3O_2$ by mass spectrum in samples of photocatalytic degradation by FPCR_TiO_2/CNT ($[1H\text{-}BT]_0$=10 ppm)

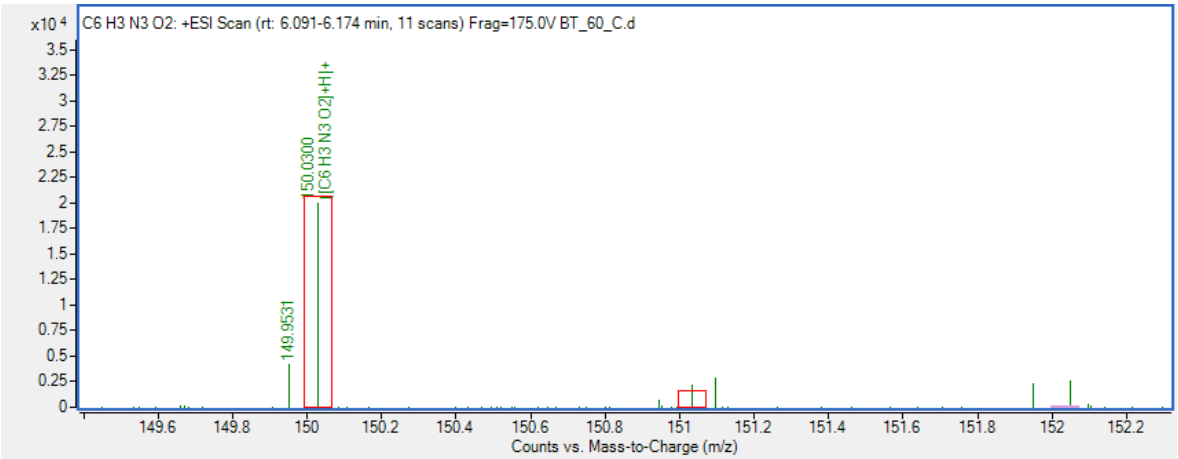
a) $C_6H_5N_3O$ (m/z= 136.0505, 137.053)



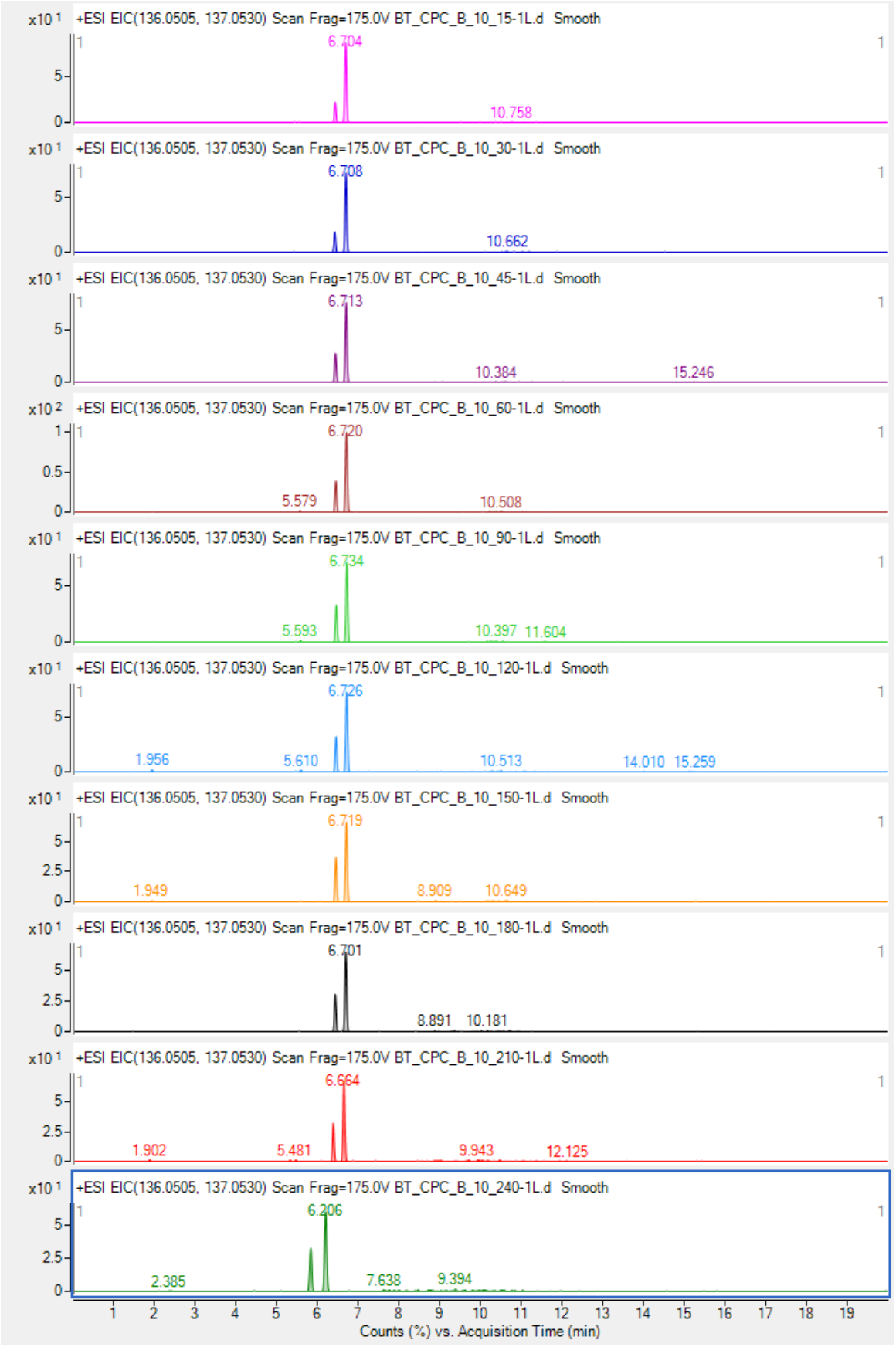
b) $C_6H_5N_3O_2$ (m/z= 152.0455, 153.0479)



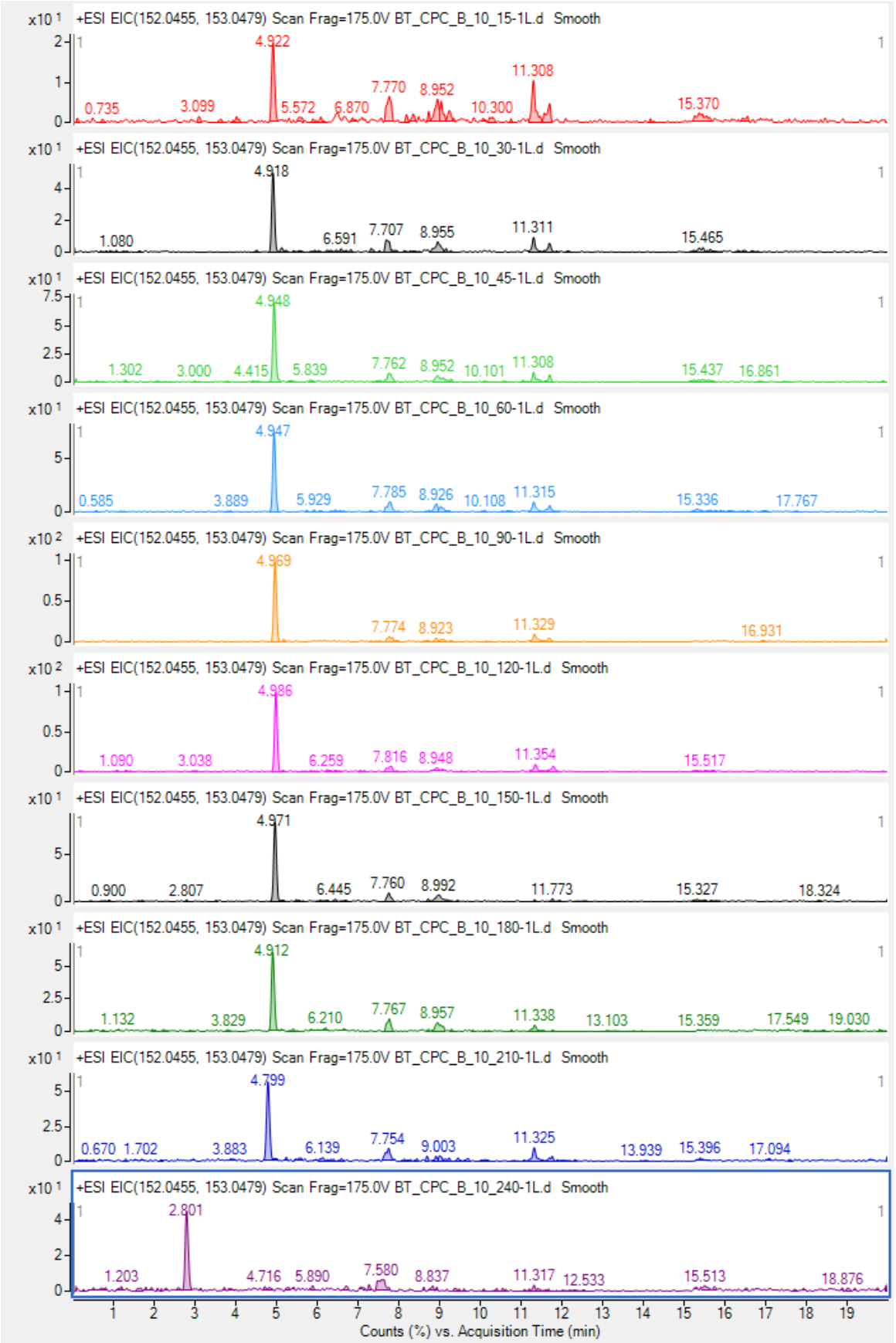
c) $C_6H_3N_3O_2$ (m/z= 150.0298, 151.0323)



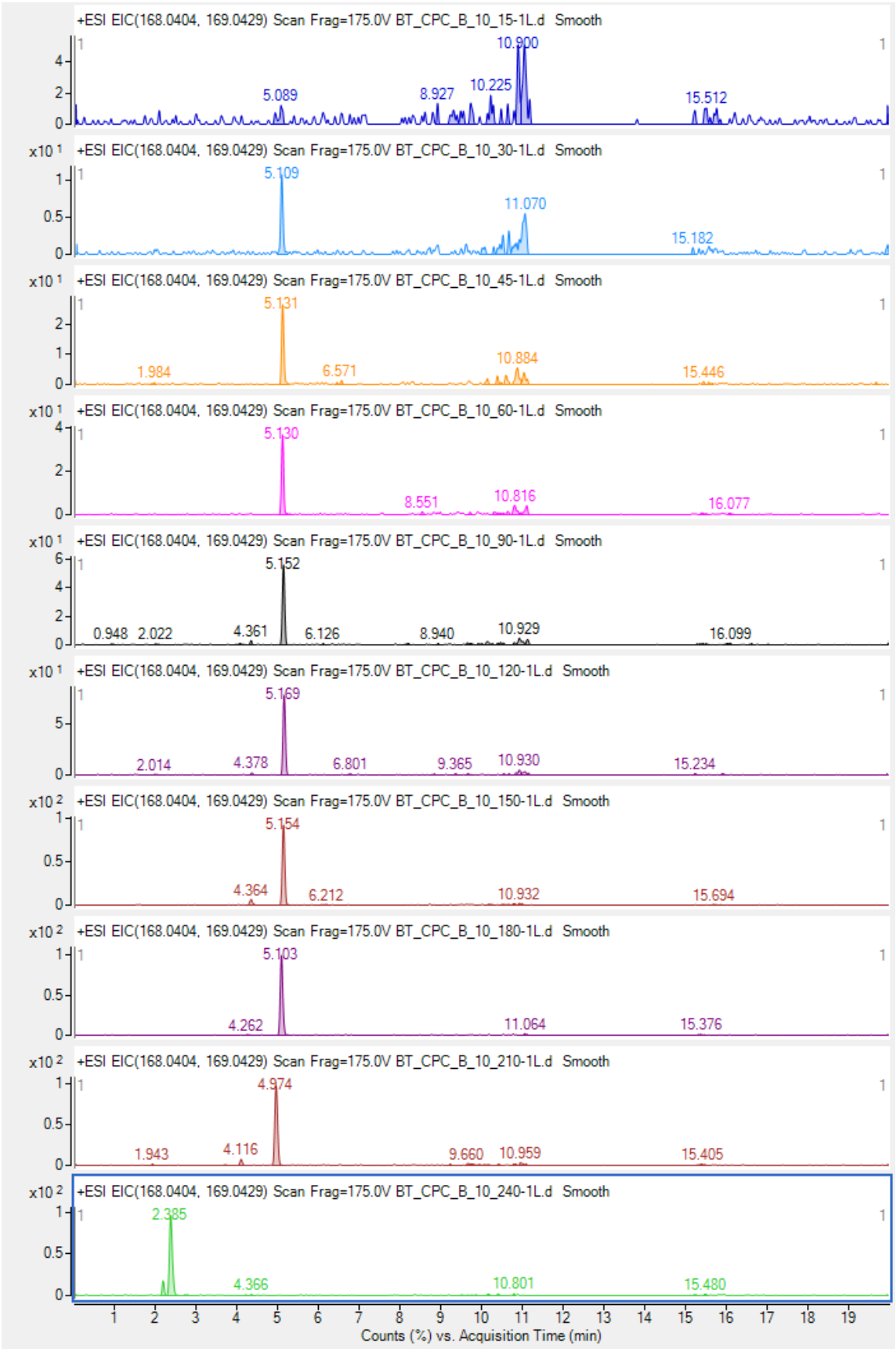
Annex 17. Extracted ion chromatograms (m/z= 136.0505, 137.053) of $C_6H_5N_3O$. The degradation product was identified in samples of photocatalytic degradation by CPC_TiO_2 ($[1H\text{-}BT]_0$=10 ppm)



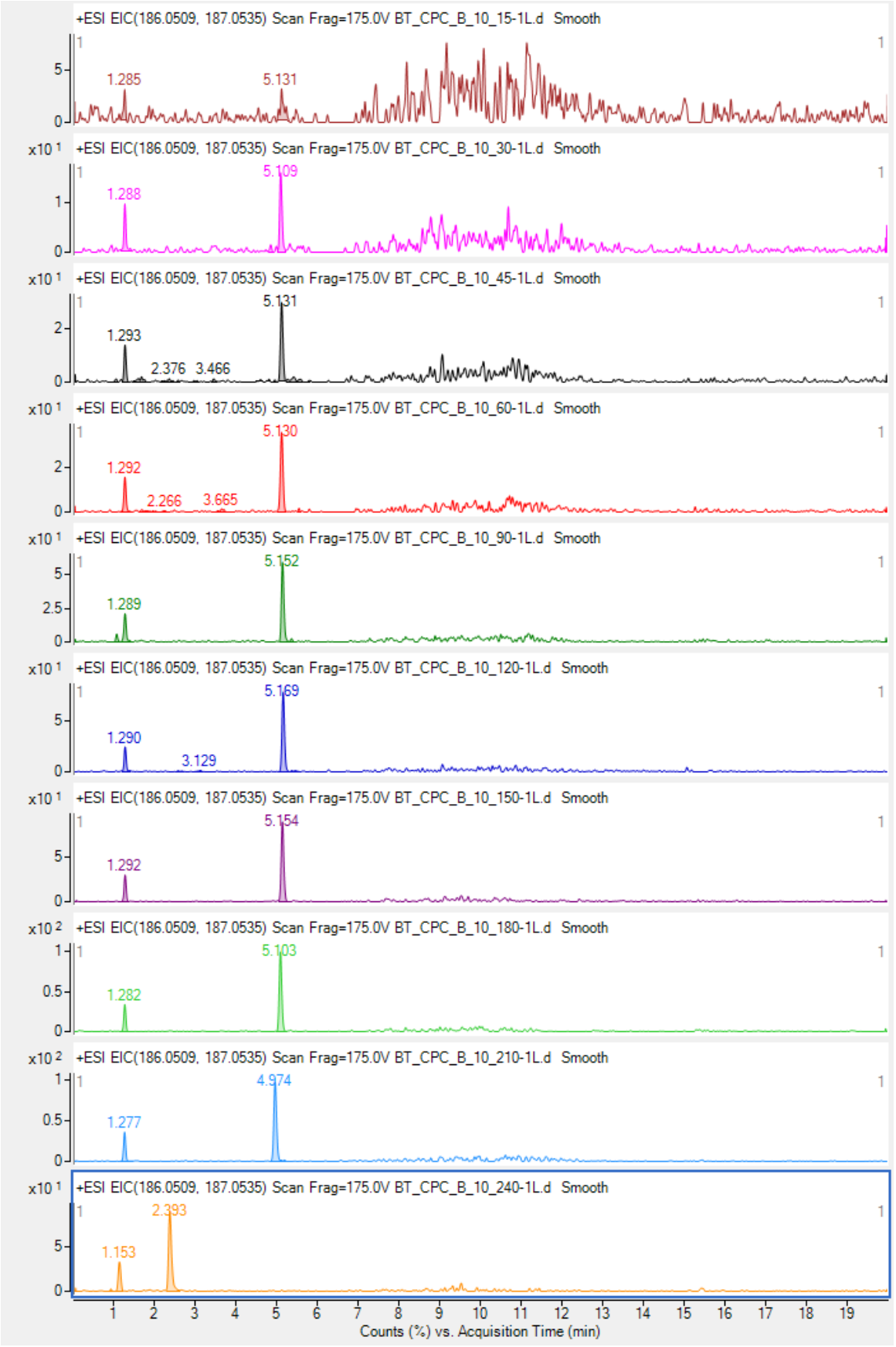
Annex 18. Extracted ion chromatograms (m/z=152.0455, 153.0479) of $C_6H_5N_3O_2$. The degradation product was identified in samples of photocatalytic degradation by CPC_TiO_2 ([1H-BT]$_0$=10 ppm)



Annex 19. Extracted ion chromatograms (m/z= 168.0404, 169.0429) of $C_6H_5N_3O_3$. The degradation product was identified in samples of photocatalytic degradation by CPC_TiO_2 ([1H-BT]$_0$=10 ppm)

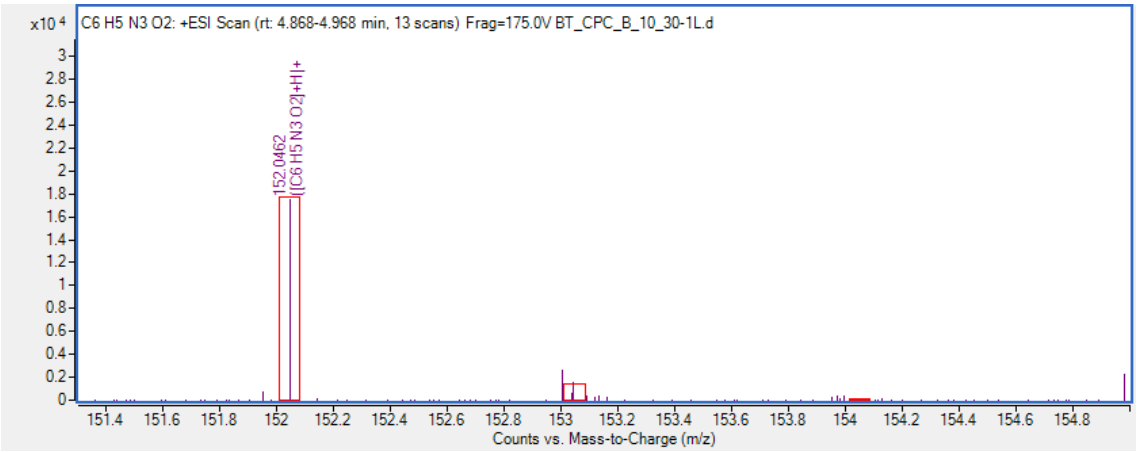


Annex 20. Extracted ion chromatograms (m/z= 186.0509, 187.0535) of $C_6H_7N_3O_4$. The degradation product was identified in samples of photocatalytic degradation by CPC_TiO_2 ($[1H\text{-}BT]_0$=10 ppm)

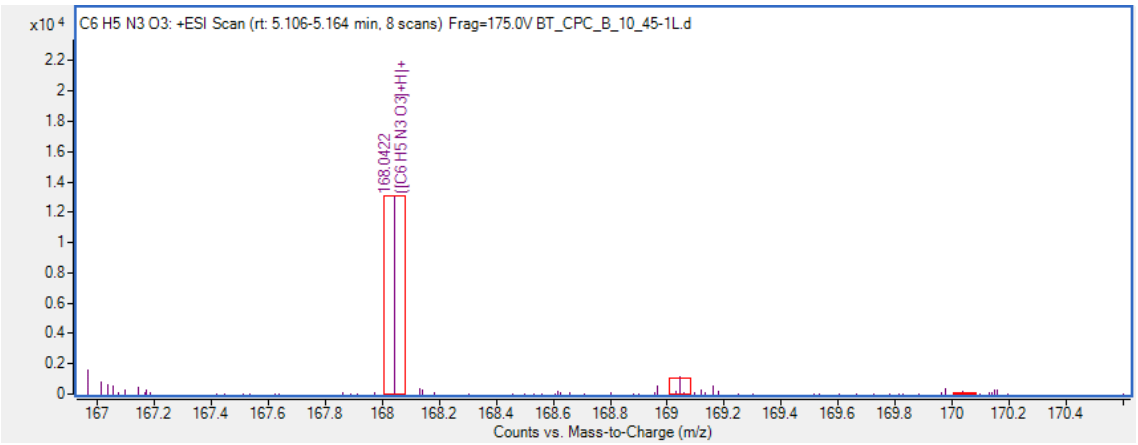


Annex 21. Confirmed degradation products a) $C_6H_5N_3O_2$, b) $C_6H_5N_3O_3$ and c) $C_6H_7N_3O_4$ by mass spectrum in samples of photocatalytic degradation by CPC_TiO_2 ($[1H\text{-}BT]_0$=10 ppm)

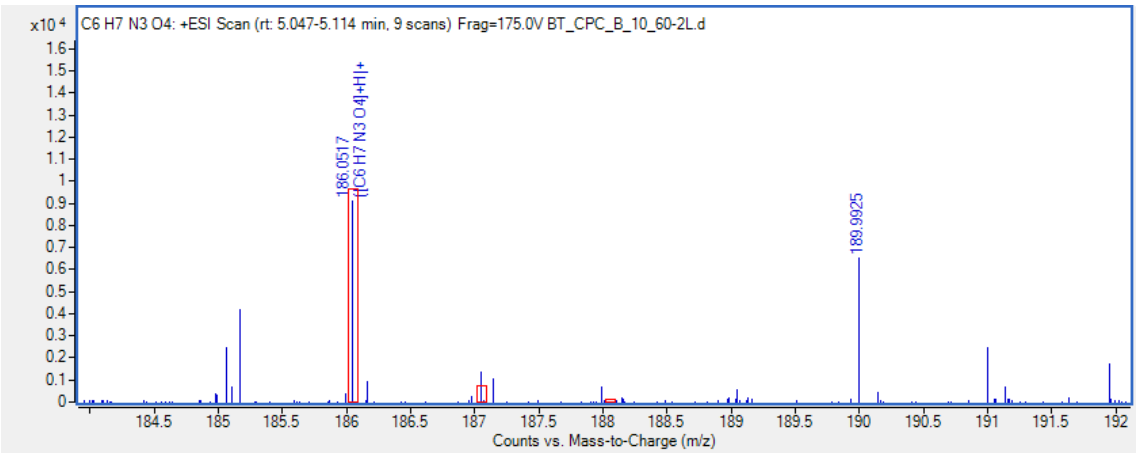
a) $C_6H_5N_3O_2$ (m/z= 152.0455, 153.0479)



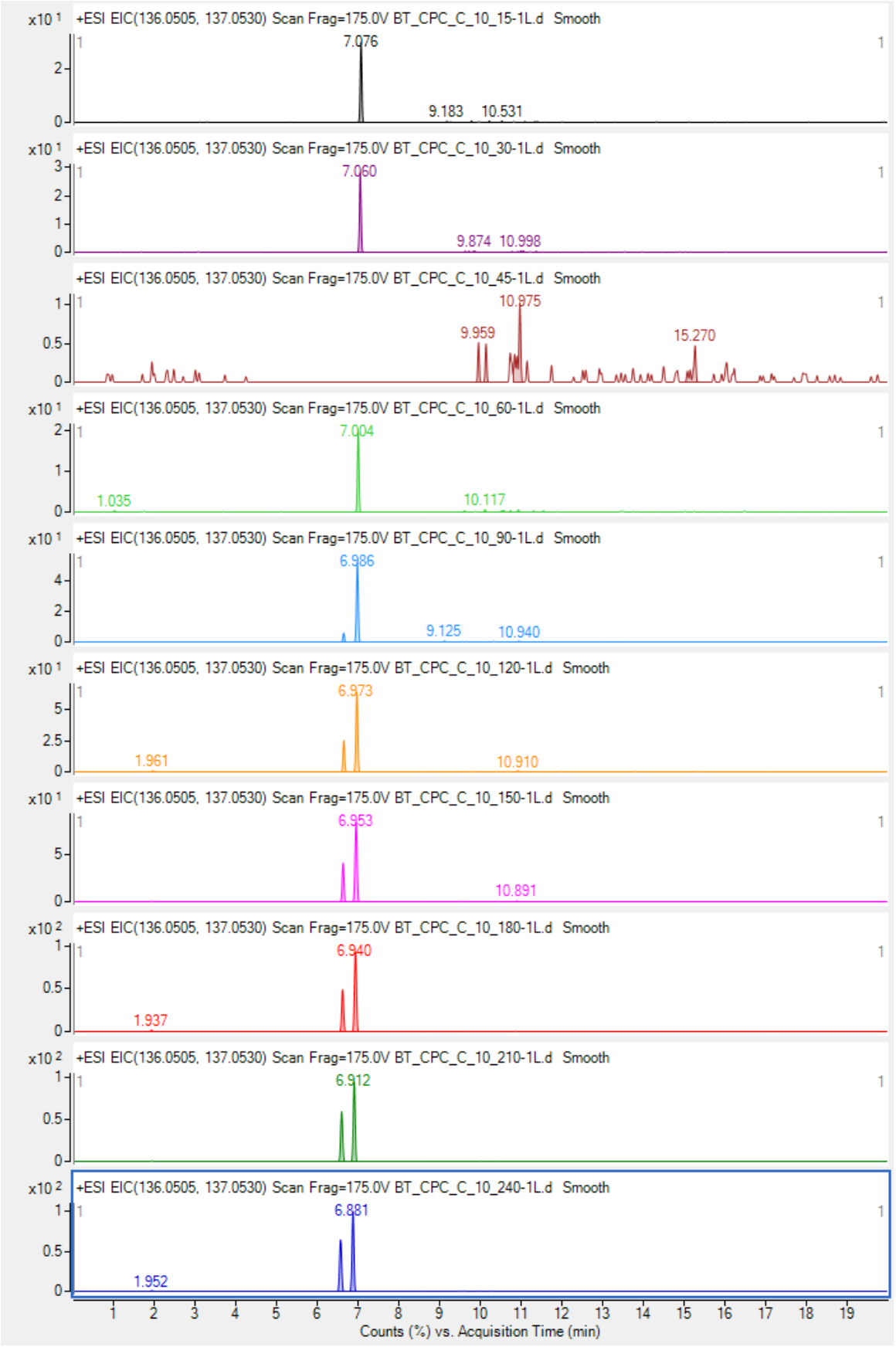
b) $C_6H_5N_3O_3$ (m/z= 168.0404, 169.0429)



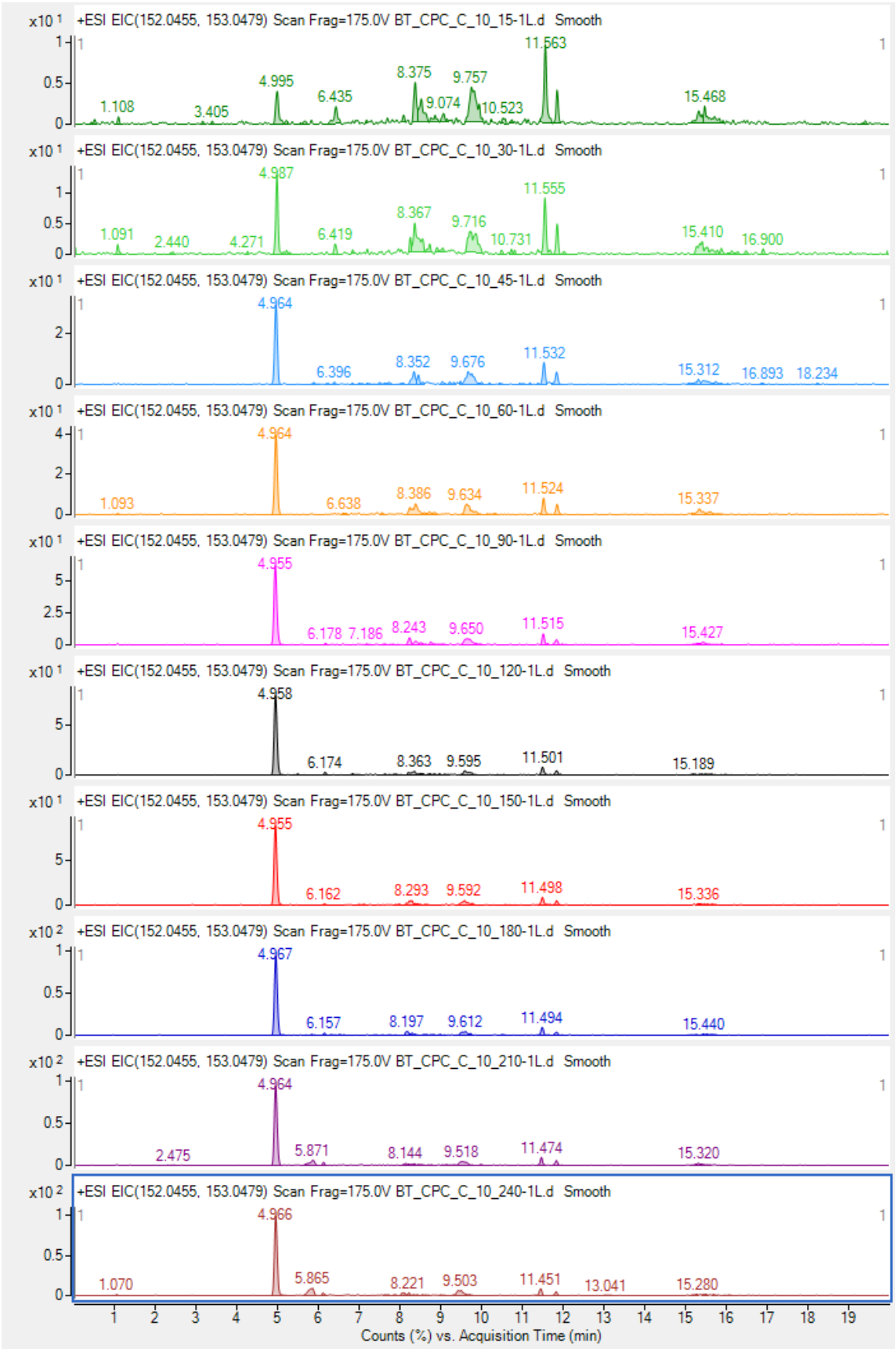
c) $C_6H_7N_3O_4$ (m/z= 186.0509, 187.0535)



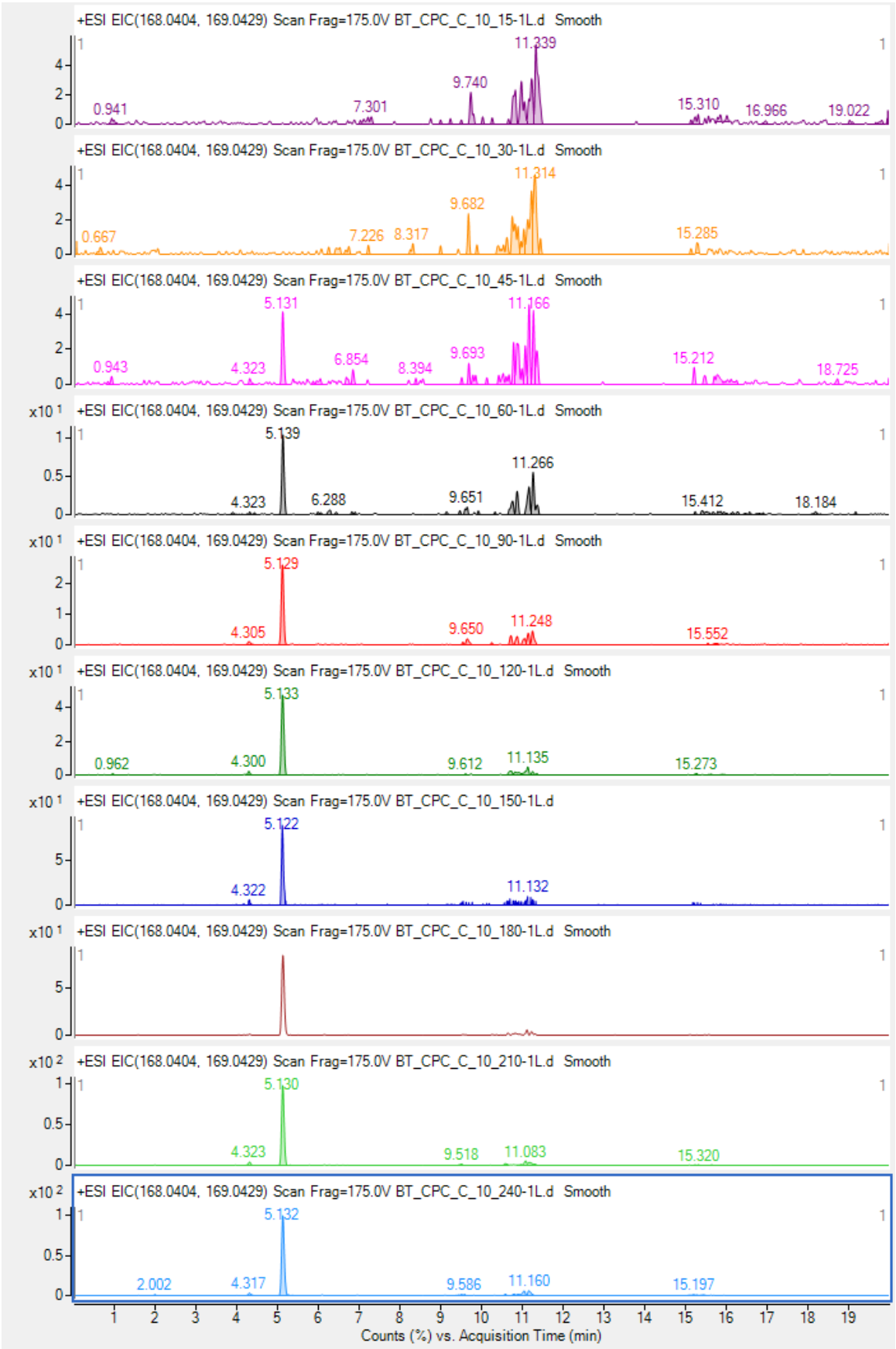
Annex 22. Extracted ion chromatograms (m/z= 136.0505, 137.053) of $C_6H_5N_3O$. The degradation product was identified in samples of photocatalytic degradation by CPC_TiO_2/CNT ($[1H\text{-}BT]_0$=10 ppm)



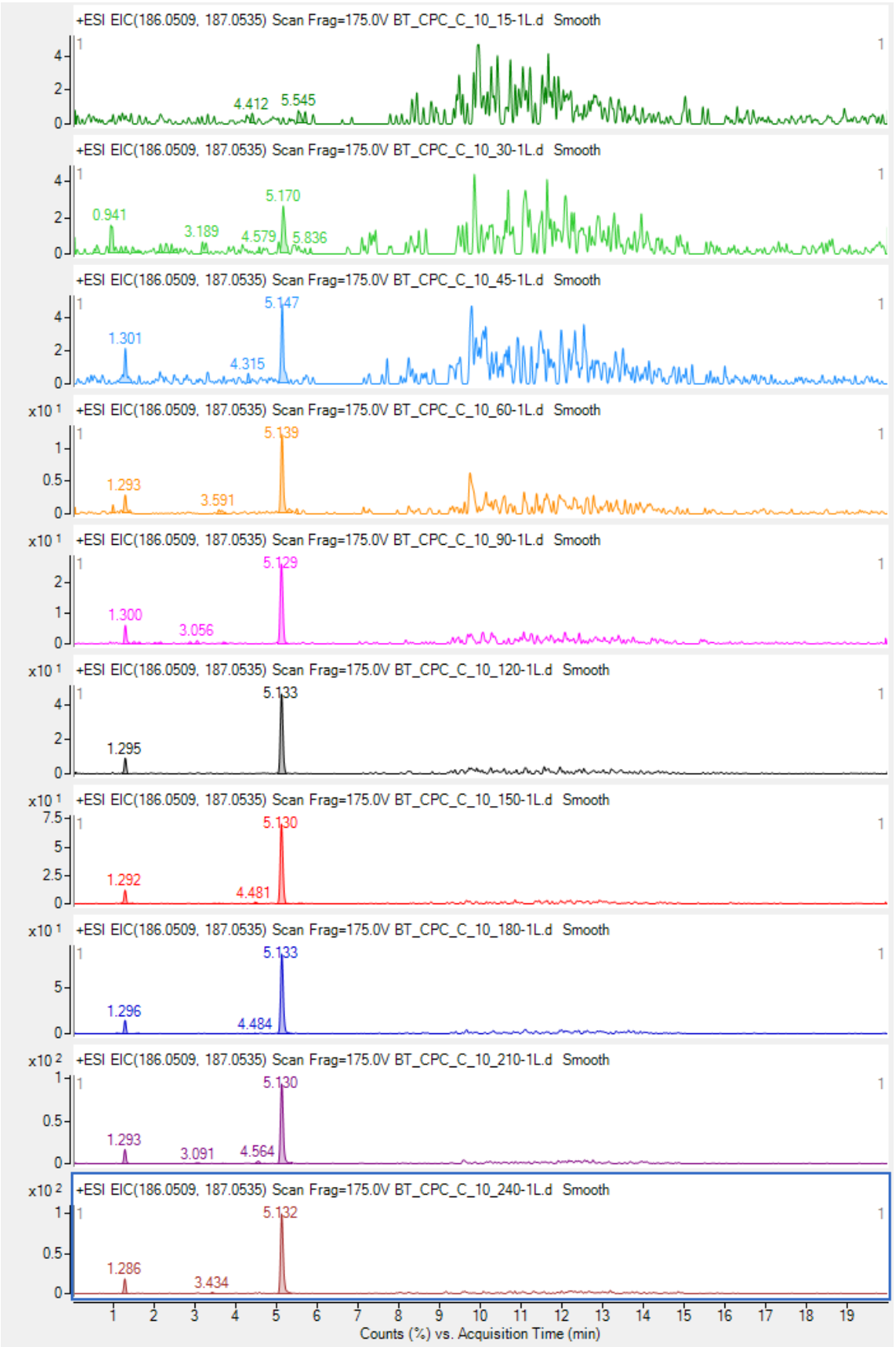
Annex 23. Extracted ion chromatograms (m/z=152.0455, 153.0479) of $C_6H_5N_3O_2$. The degradation product was identified in samples of photocatalytic degradation by CPC_TiO_2/CNT ($[1H\text{-}BT]_0$=10 ppm)



Annex 24. Extracted ion chromatograms (m/z= 168.0404, 169.0429) of $C_6H_5N_3O_3$. The degradation product was identified in samples of photocatalytic degradation by CPC_TiO_2/CNT ($[1H\text{-}BT]_0$=10 ppm)

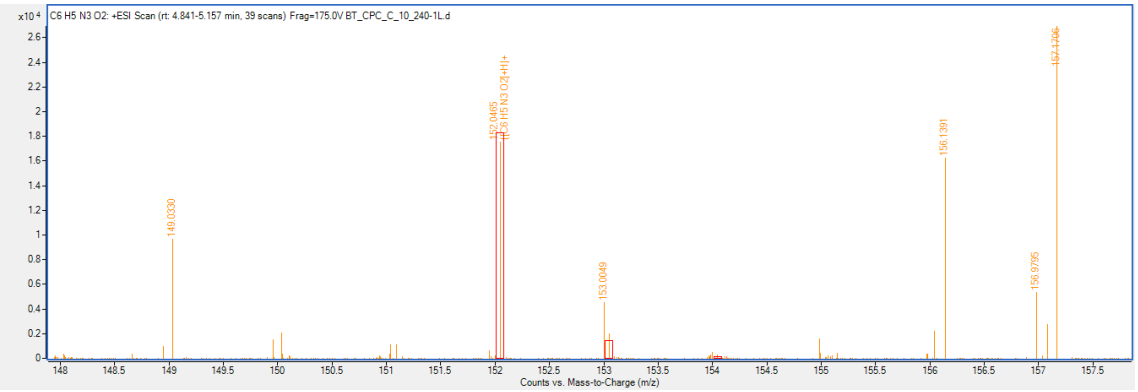


Annex 25. Extracted ion chromatograms (m/z= 186.0509, 187.0535) of $C_6H_7N_3O_4$. The degradation product was identified in samples of photocatalytic degradation by CPC_TiO_2/CNT ($[1H\text{-}BT]_0$=10 ppm)

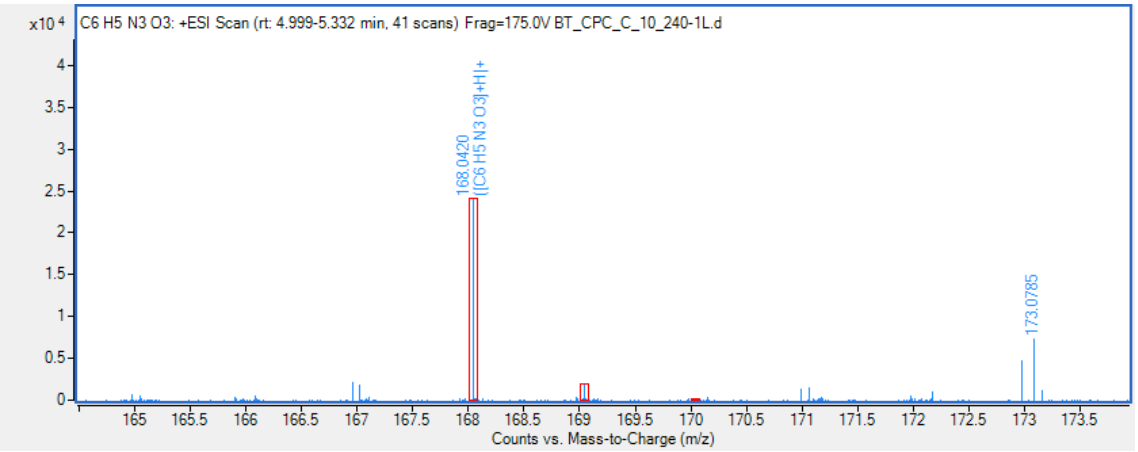


Annex 26. Confirmed degradation products a) $C_6H_5N_3O_2$, b) and c) $C_6H_5N_3O_3$ by mass spectrum in samples of photocatalytic degradation by CPC_TiO_2/CNT ([1H-BT]$_0$=10 ppm)

a) $C_6H_5N_3O_2$ (m/z= 152.0455, 153.0479)



b) $C_6H_5N_3O_3$ (m/z= 168.0404, 169.0429)



CURRICULUM VITAE

Lucija Radetić was born on February 22, 1991, in Požega, Croatia. After her undergraduate studies, she completed her graduate studies in Geoengineering, majoring in Environmental Engineering at the Faculty of Geotechnical Engineering in 2015. After graduation, she was enrolled as an associate and later employed as an assistant at the Geotechnical Faculty. Throughout scientific work, she has widened her primary field of interest from waste management to the life cycle assessment and application of solar photocatalysis for water and air purification, the best available technologies. Her research focuses on detecting photocatalytic degradation by-products in water samples by hybrid Q-TOF (LC/MS). To improve her skills, she has participated in 5 training schools organized by COST actions and EFCATS. She had won two gold medals for innovations presented by teamwork at the ARCA international fair in the field of solar photocatalysis application. She was one of seven finalists in the start-up competition organized by the international company BASF for SE Europe. She is enrolled in the classes and co-author in papers with students.

She is an author or co-author of 10 papers published in journals, seven articles published in conference proceedings and over 20 conference abstracts. In addition, she was actively involved in the NanoPeroPhotoSens project under the leadership of Andreja Gajović, PhD, from the Institute Ruđer Bošković funded by Croatian Science Foundation and is involved in the OS-Mi project (K.K.01.1.1.04.0006) under the supervision of associate professor Ivana Grčić, PhD, supported by European funds, within which the following topic of the dissertation was written.

The list of scientific articles can be found on CROSBI. The link is the following:

https://www.bib.irb.hr/pretraga?operators=and|Radeti%C4%87,%20Lucija%20%2836196%29|text|profile